Shaping tubes in cells

Martin Lenz

THESE DE DOCTORAT DE
L'UNIVERSITE PIERRE ET MARIE CURIE

Spécialité

Physique
(École Doctorale de Physique de la Région Parisienne - ED 107)

Présentée par

M. Martin Lenz

Pour obtenir le grade de

DOCTEUR de l'UNIVERSITÉ PIERRE ET MARIE CURIE

Sujet de la thèse :

Shaping tubes in cells

soutenue le 13 octobre 2009

devant le jury composé de :

M. Jean-François Joanny, Professeur à l'Université Paris 6	Directeur de thèse
M. Jacques Prost, Directeur de Recherches au CNRS	Co-directeur de thèse
M. Luca Peliti, Professeur à l'Università di Napoli « Federico II »	Rapporteur
M. Samuel A. Safran, Professeur au Weizmann Institute of Science	Rapporteur
M. Alain Comtet, Professeur à l'Université Paris 6	Examinateur
M. François Gallet, Professeur à l'Université Paris 7	Président

Remerciements

Je me suis un jour entendu dire que l'on n'est pas prêt à terminer son doctorat avant de détester son directeur de thèse. Si tel est bien le cas, je suis infiniment reconnaissant à Jean-François Joanny et Jacques Prost de m'avoir autorisé à soutenir si tôt, car je crois qu'arriver à maturité m'aurait pris beaucoup plus que ces trois ans. Au-delà de la physique qu'ils m'ont enseignée, j'ai le sentiment d'avoir appris d'eux toute une attitude vis-à-vis de la science faite de curiosité, de dévouement et de confiance dans l'avenir. Quoiqu'il advienne de moi par la suite, je suis convaincu que mes réalisations futures porteront leur marque.

Merci ensuite à Aurélien Roux, vers qui Jean-François et Jacques ont eu l'excellente idée de me diriger dès le début de mon doctorat et avec qui j'ai eu le plaisir d'établir une relation amicale tout autant que scientifique. L'environnement remarquable du Laboratoire Physicochimie Curie m'a d'ailleurs permis de tisser de nombreux liens expériences-théorie tout aussi agréables et fructueux avec Patricia Bassereau, Timo Betz, Gerbrand Koster, Sandrine Morlot et Cécile Sykes. Je tiens également à remercier Arnaud Échard de son ouverture d'esprit et de son enthousiasme à aller vers les théoriciens, malgré leur (ou plutôt mon) ignorance crasse des bases de la biologie.

Many of the best memories of my time in Curie are of moments—OK, coffee breaks—spent with the other members of the theory group, and especially Markus Basan, Andrew Callan-Jones and Thomas Risler. It was a blessing to be part of such an open and ever-moving team, and to benefit from interaction with visitors and former members—those with Imre Derényi and Daniel J. G. Crow have been particularly fruitful. Overall, it has been a great asset and pleasure for me to be surrounded by such friendly, selfless and helpful labmates, and I can only hope that I will be lucky enough to spend the rest of my career in groups that measure up to this one.

Sortant de l'univers de Curie, mon choix de m'engager dans la voie de la recherche doit beaucoup à mes parents, que je remercie d'avoir toujours su m'encourager à poser des questions, et de m'avoir convaincu que le temps passé à chercher les réponses n'est jamais perdu.

Enfin, je voudrais exprimer toute ma tendresse et ma reconnaissance à Claire, sans le soutien et la confiance de laquelle ma thèse, ainsi que bien d'autres choses, se seraient déroulées de manière très différente.

Publications associated with the thesis

1. **Martin Lenz**, Jacques Prost, and Jean-François Joanny. Mechanochemical action of the dynamin protein. *Phys. Rev. E* 78(1):011911, July 2008.

2. **Martin Lenz**, Daniel J G Crow, and Jean-François Joanny. Membrane buckling induced by curved filaments. *Phys. Rev. Lett.* 103(3):038101, July 2009.

3. Timo Betz, **Martin Lenz**, Jean-François Joanny, and Cécile Sykes. ATP-dependent mechanics of red blood cells. *Proc. Natl. Acad. Sci. U.S.A.* 106(36):15320–15325, September 2009.

4. **Martin Lenz**, Sandrine Morlot, and Aurélien Roux. Physical requirements for membrane fission: common facts from various examples. *FEBS Lett.* 583(23):3839–3846, December 2009

5. Aurélien Roux, Gerbrand Koster, **Martin Lenz**, Benoît Sorre, Jean-Baptiste Manneville, Pierre Nassoy, and Patricia Bassereau. Membrane curvature controls dynamin polymerization. *Proc. Natl. Acad. Sci. U.S.A.* 107(9):4141–4146, March 2010

6. Markus Basan, Timon Idema, **Martin Lenz**, Jean-François Joanny, and Thomas Risler. A reaction-diffusion model of the cadherin-catenin system: a possible mechanism for contact inhibition and implications for tumorigenesis. *Biophys. J.* 98(12):2770–2779, June 2010

7. **Martin Lenz**, Jacques Prost, and Jean-François Joanny. Actin cross-linkers and the shape of stereocilia. *Biophys. J.* 99(8):2423–2433, October 2010

8. Sandrine Morlot, **Martin Lenz (equal contributions)**, Jacques Prost, Jean-François Joanny and Aurélien Roux. Deformation of dynamin helices damped by membrane friction. *Biophys. J.* 99(11):3580–3588, December 2010

Keywords

biophysics; protein-membrane interactions; dynamin;
ESCRT-III; stereocilia; out-of-equilibrium

Mots-clés

biophysique; interactions protéines-membrane; dynamine;
ESCRT-III; stéréocils; hors équilibre

Laboratoire Physicochimie Curie
Institut Curie/UMR 168 CNRS/UPMC
11, rue Pierre et Marie Curie
75005 Paris, France

Contents

Chapter 1

Foreword: membrane and proteins

Life is sparse. Even in the most densely populated ecosystems, biological matter occupies only a small fraction of the available space, and living organisms are separated by large volumes of comparatively simple inanimate matter. Because of this, all known forms of life from bacteria to mammals have some kind of enclosure that prevents them from diluting away into the surrounding dead world. Although different types of living cells—a very evocative term to designate the building block of life—have evolved different kinds of enclosures depending on their surroundings, one ingredient of their confining structure is universal throughout the whole biota. This ingredient is the cell membrane, a bilayer of amphiphilic molecules tightly bound together into a flexible sheet by hydrophobic interactions. Although the cell membrane provides an excellent confinement, no enclosure can be expected to be perfectly hermetic. Therefore, on long enough time scales, the membrane will let the living matter through and the organism it encircles will wither away and die unless some pump-like mechanism compensates the losses. Moreover, no reasonable definition of life should allow us to term "living" a purely passive compartment, no matter how watertight: we expect biological matter to feed, grow and reproduce. These functions are carried out by proteins, a versatile type of organic polymers that maintain and expand the architecture of the cell by performing a variety of tasks, including the production of other proteins—with the assistance of nucleic acids. Note however that the delicate production and coordination of proteins can only take place in a well-controlled closed environment, which is in turn provided by the cell membrane. These intricate reciprocal interactions between membrane and proteins are the broad area of research considered in this thesis. In the present chapter, we introduce some general aspects of this field and explain why the shaping of membrane tubes is a central event of this interplay.

The cell membrane is primarily constituted of a type of organic molecules known as phospholipids. Perhaps the most important property of phospholipids for the cell membrane is that they are amphiphilic molecules, meaning that one part of the molecule has hydrophilic properties while the other is hydrophobic. The structure of phospholipids comprises one hydrophilic head and two hydrophobic tails. When put in an aqueous medium, the hydrophobic tails tend to cluster together to minimize their contact with water. Because phospholipids have a roughly cylindrical shape, they tend to form planar aggregates, where the heads arrange into two parallel planes to shield the tails from

water. These structures known as "lipid bilayers" are the prototype of cell membranes [Fig. 1.1(a)]. Phospholipids interact mostly through hydrophobic bonds between their tails, and are thus relatively mobile with respect to one another within the bilayer. In many biological situations, the cell membrane actually behaves as a two-dimensional liquid.

The protein-membrane interactions discussed in this thesis critically involve membrane deformations. Such deformations have an energetic cost. In order to evaluate it, we model the membrane as an infinitely thin liquid sheet, and consider this effective surface on length scales much larger than the bilayer's thickness. The first type of deformation that we consider are bending deformations. Such deformations confer a curved shape to the initially planar membrane. This shape is locally characterized by its two principal radii of curvature r_1 and r_2, as shown in Fig. 1.1(b). For a homogeneous membrane of fixed topology, we only need to consider the total curvature $c = 1/r_1 + 1/r_2$ of the surface. Bending a lipid bilayer exposes the hydrophobic tails to the surrounding water, and therefore a membrane with $c \neq 0$ has a higher energy than a flat one. Moreover, if the bilayer is assumed to be symmetric with respect to its middle plane, curving it downwards or upwards should cost the same amount of energy, meaning that the energy of the membrane should be even in c. Therefore, for small deformations, the local cost of bending the membrane is proportional to c^2, and we denote the proportionality coefficient by $\kappa/2$. It is also possible to deform the membrane while keeping it flat by stretching it. In practice, it is very difficult to stretch the cell membrane and the amplitude of such deformations is often negligible. When a cell expands some region of its membrane, it thus imports phospholipids from the neighboring regions rather than stretching those already there. This can be taken into account by considering that the membrane is in contact with a reservoir of phospholipids. Unless the membrane contained in the reservoir is extremely floppy, retrieving it from there has an energetic cost as it implies working against the tension of the membrane reservoir. We denote the energetic cost per unit area by σ. These two effects are described by the Helfrich Hamiltonian, which gives the free energy of a weakly deformed, homogenous, inextensible membrane of arbitrary shape but fixed topology put into contact with a reservoir of lipids [3]:

$$\mathcal{H} = \iint \left(\frac{\kappa}{2}c^2 + \sigma\right) \mathrm{d}S. \tag{1.1}$$

The coefficient κ is known as the membrane's "bending modulus". The first term in the integral represents the bending energy of the membrane, and is proportional to c^2 integrated over the whole surface area of the membrane. The second term is the constant σ, known as the membrane's "tension". It is integrated over the surface of the membrane, which yields a constant energetic cost per unit area as required.

Membrane deformations are very common in cells, as they often use lipid bilayers for much more than just preventing their contents from spilling. Fig. 1.1(c) illustrates some of the membrane trafficking eukaryotic cells set into motion to transport tightly membrane-bound proteins, also known as "integral membrane proteins". Throughout these processes, membrane compartments bud out, invaginate, become severed or fuse. All of these operations are performed by proteins, such as those indicated in color in Fig. 1.1(c).

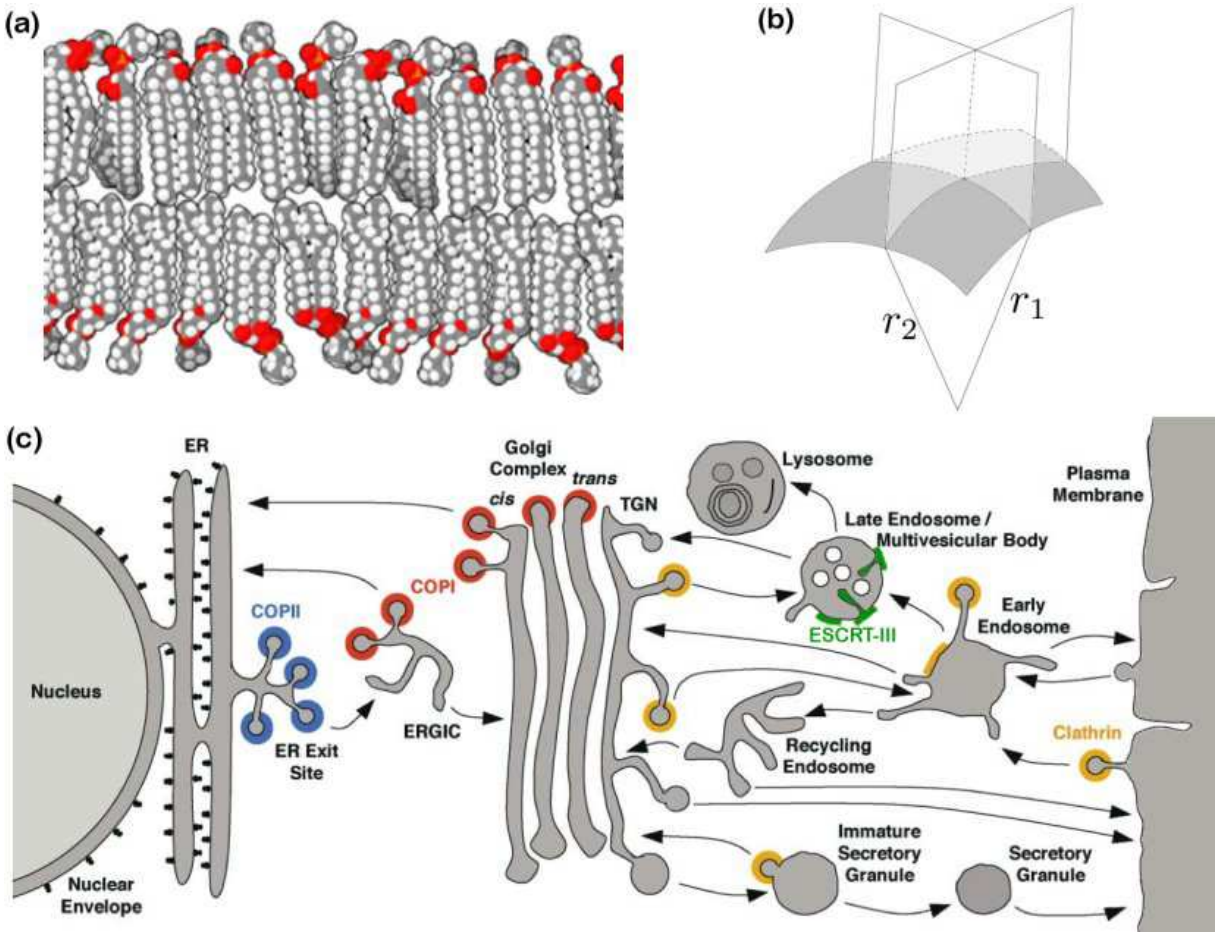

Figure 1.1: Structure and function of the cell membrane. (a) Schematic cross-section of a bilayer made up of the phospholipid phosphatidylcholine. The hydrophilic heads of the lipids (identifiable by their oxygen—red—atoms) stick out of the bilayer and into the water while their hydrophobic tails form the bulk of the membrane. (b) Schematic of the local state of a curved surface (representing the membrane) showing its two principal radii of curvature r_1 and r_2. Figure adapted from Ref. [1]. (c) Some intracellular transport pathways in eukaryotic cells. The outside of the cell and the subcellular compartments are represented in gray. The topological inside of the cell—which is known as its "cytoplasm"—is white. All the white-gray interfaces are delimited by lipid bilayers. Transport between them is carried out by small membrane compartments—also termed "vesicles"—propelled by motor proteins. Integral membrane proteins are produced at the endoplasmic reticulum (ER). They are then transported to the Golgi complex, which they traverse until they reach the trans-Golgi network (TGN). From there, they are addressed and sent to the region of the cell where they are needed *e.g.* the cell's external membrane, also known as "plasma membrane". When the time comes for them to be disposed of, they get labeled for degradation and are sent to the endosomes' membrane. They then get concentrated in membrane invaginations, which pinch off the endosomal membrane to become intralumenal vesicles (pictured as white circles inside the Late Endosome/Multivesicular Body). The endosomes thus become multivesicular bodies. The intralumenal vesicles and the associated integral proteins are then degraded as the multivesicular bodies become lysosomes. Figure adapted from Ref. [2].

Deformations of the membrane by proteins are however not unique to intracellular transport. In many cases, proteins define the shape of the cell itself. One of the most important proteins of this type is actin. Actin is a small soluble globular protein that can exist either in a monomeric form, termed G-actin for "globular actin" [Fig. 1.2(a)], or in a polymerized state, termed F-actin for "filamentous actin". Actin polymers are relatively rigid and give mechanical support to the cell—they are part of its "cytoskeleton". Both forms of actin can be associated to either adenosine triphosphate (ATP) or adenosine diphosphate (ADP). ATP is a more energetic molecule than ADP and spontaneously hydrolyzes into ADP, but the cell constantly spends energy restoring G-actin into its ATP-associated state. It thereby maintains a constant ATP-associated G-actin pool in the cytoplasm. The structure of F-actin is polar, and it continuously incorporates ATP-associated G-actin from its so-called "barbed end", visible at the top of Fig. 1.2(b). The G-actin thus incorporated in the polymer hydrolyzes ATP and turns into ADP-associated F-actin. The polymer continuously depolymerizes from its "pointed end", at the bottom of Fig. 1.2(b), and thus gets rid of ADP-associated actin. This has an interesting consequence for the dynamics of the actin filaments: assume that the actin monomers within the filament are motionless in some reference frame and that actin polymerization balances its depolymerization. Then the filament has a constant length and moves relative to the reference frame, as its ends are constantly changing position because of the actin turnover. This motion of the filament's center of mass relative to its monomers is known as "treadmilling". If it takes place inside a cell, the filament ends up touching the plasma membrane. In some cases, the actin filament is not deflected by the lipid bilayer, but other filaments bind to it and join its pushing action against the membrane. Actin filaments thus exert a force on the membrane, a phenomenon ultimately fueled by the active recycling of ADP-associated G-actin into ATP-associated G-actin [4]. Under appropriate conditions (including the presence of actin-associated proteins), the growth of actin filaments dramatically modifies the shape of the cell, often in ways required for its function [Fig. 1.2(c)].

Having reviewed varied, yet representative examples of protein-induced membrane deformations, we argue that membrane tubes are central to these crucial events in the cell cycle. We encountered such tubes in the examples presented above. Consider for instance the proteins COPI, COPII and clathrin, represented respectively in red, blue and yellow in Fig. 1.1(c). These proteins pinch the membrane out into spherical vesicles. At the end of this process, these vesicles end up bound to the main membrane by small tubular necks. Such necks need to be severed for the vesicle to detach, which allows intracellular transport to proceed. Another example is the protein complex ESCRT-III, which invaginates the membrane into multivesicular bodies to form their intralumenal vesicles. This also leads to the formation of tubes, as represented in green in Fig. 1.1(c). Finally the protrusions generated by the pushing action of actin and displayed in Fig. 1.2(c) are tubular as well. It therefore seems reasonable to consider tubes as a generic feature of protein-membrane interactions. Indeed, the competition between membrane tension (which keeps membrane deformations small) and bending modulus (which keeps membrane deformations smooth) means that any pointwise modification of the membrane—be it pinching it out, invaginating it in or exerting a point force on it—is expected to generate a cylindrical structure.

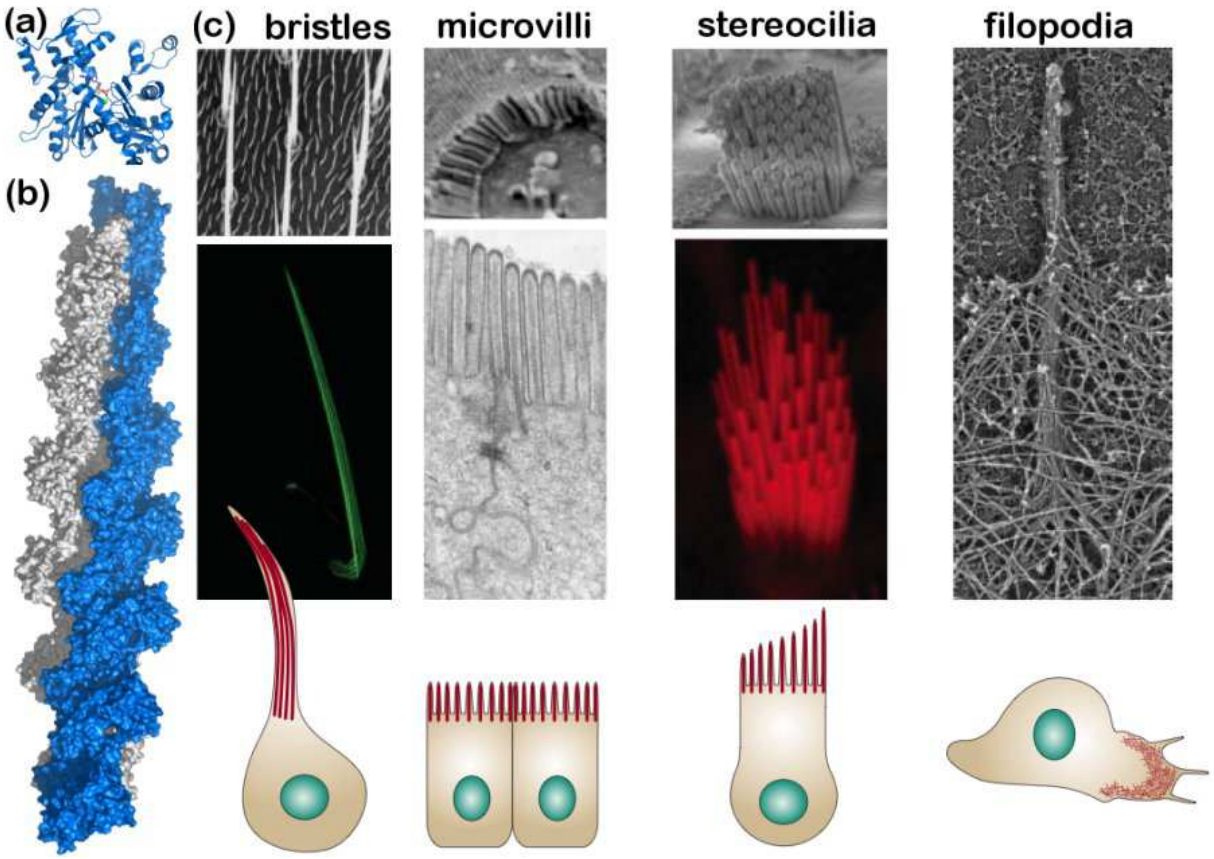

Figure 1.2: Actin and its role in cell deformations. (a) Structure of G-actin. The actin monomer has a diameter of about 5.5 nm. (b) Structure of F-actin. The filament has a helical shape, which consists of two intertwined strands. The diameter of the filament is approximately 7 nm, and its helical period about 37 nm. Its length can be up to several micrometers in cells. Both figures taken from Ref. [5]. (c) Actin-based cellular protrusions. Each panel shows electron microscopy (in shades of gray) and/or fluorescence microscopy (in color) pictures of a specific type of protrusion, as well as a schematic of the resulting overall cell shape (where the actin is represented in red, and the cell nucleus in green). Here we briefly introduce each of these protrusion types: Bristles are observed on the the thorax of *Drosophila melanogaster* and are involved in mechanosensing. Microvilli are involved in a wide variety of functions, including absorption, secretion, cellular adhesion, and mechanotransduction. Stereocilia are mechanosensing organelles of hair cells, which respond to fluid motion or fluid pressure changes in numerous types of animals for various functions, primarily hearing. Filopodia are slender cytoplasmic projections which extend from the leading edge of migrating cells. Figure taken from Ref. [6].

In this thesis, we approach this broad class of events not by referring to the detailed molecular interactions involved in specific situations, but by identifying a few crucial geometrical and thermodynamic features. The out-of-equilibrium character of these phenomena is also often essential for their understanding, and we describe them in as general theoretical terms as possible. Meanwhile, we compare our predictions to experimental

results whenever the opportunity is present. In order to reach both of these goals, we divide our study into three parts, each being on the one hand representative of a class of geometrical configurations that the cell has to deal with, and on the other focused on a characteristic example of this class. Our first part revolves around dynamin, which we further introduce in chapter 2. Dynamin is generally used to shape tubes whose outer surface is in contact with the cytoplasm of the cell, as when clathrin creates a membrane bud destined to be severed off the membrane, for instance during endocytosis [Fig. 1.1(c), yellow patches]. The first function of dynamin is to encircle the membrane and pay the bending energy cost of shrinking it into a very narrow tube, as demonstrated in chapter 3. In chapter 4, we show how an active conformational change allows dynamin to further deform the tube, eventually leading to its breakage. In the second part of the thesis, we tackle the topologically opposite problem, where the cell needs to create a tube *away from* the cytoplasm. In chapter 5, we show that the buildup of elastic stresses in ESCRT-III [Fig. 1.1(c), green patches] clusters allows the cell to punch holes into its membrane. The third part focuses on tubes created not by membrane-bound proteins, but by a force resulting from the growth of a filament. Chapter 6 demonstrates that the mechanism by which the cell binds actin filaments together has a crucial influence on the shape and size of actin-based protrusions such as filopodia, and in particular stereocilia [Fig. 1.2(c)]. Finally, in chapter 7, we recapitulate our results and discuss possible future research directions. Five appendices follow. Appendices A, B and C are dedicated to the derivation of specific results and to the discussion of preliminary experiments, while Appendix D reproduces publications associated with this thesis dealing with topics not discussed in the main text. Finally, Appendix E is a summary of the thesis in French.

Part I

Dynamin

Chapter 2

Membrane severing by dynamin: a twofold problem

In order to operate efficiently, living cells must constantly maintain concentration gradients of various chemical species and isolate some of their components. One of the many different biological processes required to maintain this traffic is membrane fission, by which a cell membrane compartment is split into two or more topologically distinct parts. A fundamental protein involved in most membrane fission events is dynamin, which has been proposed to be a "universal membrane fission protein" [7].

In the human body, dynamin is present under three isoforms: dynamin I is expressed in neurons and neuroendocrine cells, dynamin II is ubiquitous and dynamin III is strongly expressed in the testis, but also present in heart, brain, and lung tissue [7]. Its function is essential, and although mutations in such an important protein are often lethal, defective dynamin or dynamin analogs have been shown to be involved in human diseases such as the optical atrophy type 1, the Charcot-Marie-Tooth disease and the dominant centronuclear myopathy [8, 9, 10]. In mice, a knock-out of dynamin I leads to striking defects in synapse organization, and results in a strong dysfunction of the neuronal activity [11]. In flies, the *shibire* temperature-sensitive mutant of the *Drosophila* dynamin analog is responsible for a temperature-induced paralytic phenotype [12].

The structure of dynamin and its analogs is conserved throughout eukaryotic cells, which is typical for such an important protein [Fig. 2.1(a)]. Fig. 2.1(b) presents a summary of the many cellular processes in animals and plants where members of the dynamin superfamily play a role. Classical dynamins are well known to be involved in the budding of clathrin-coated vesicles at the plasma membrane, cleavage furrow, Golgi apparatus and endosome, but also in budding events at caveolae and phagosomes where clathrin is not involved. Related proteins assume a host of functions and are involved in the division of organelles such as mitochondria and peroxisomes, and in the reorganization of mitochondria (probably in mitochondrial fusion). Others confer resistance against RNA viruses, for instance by interacting with viral ribonucleoproteins. In plants, dynamin-related proteins assume some of the same functions as in animals, but also participate in the formation of the cell plate or in chloroplast division.

The biological mode of action of dynamin is typified by the well-studied example of clathrin-coated endocytosis, illustrated in Fig. 2.2. Dynamin is recruited by clathrin-

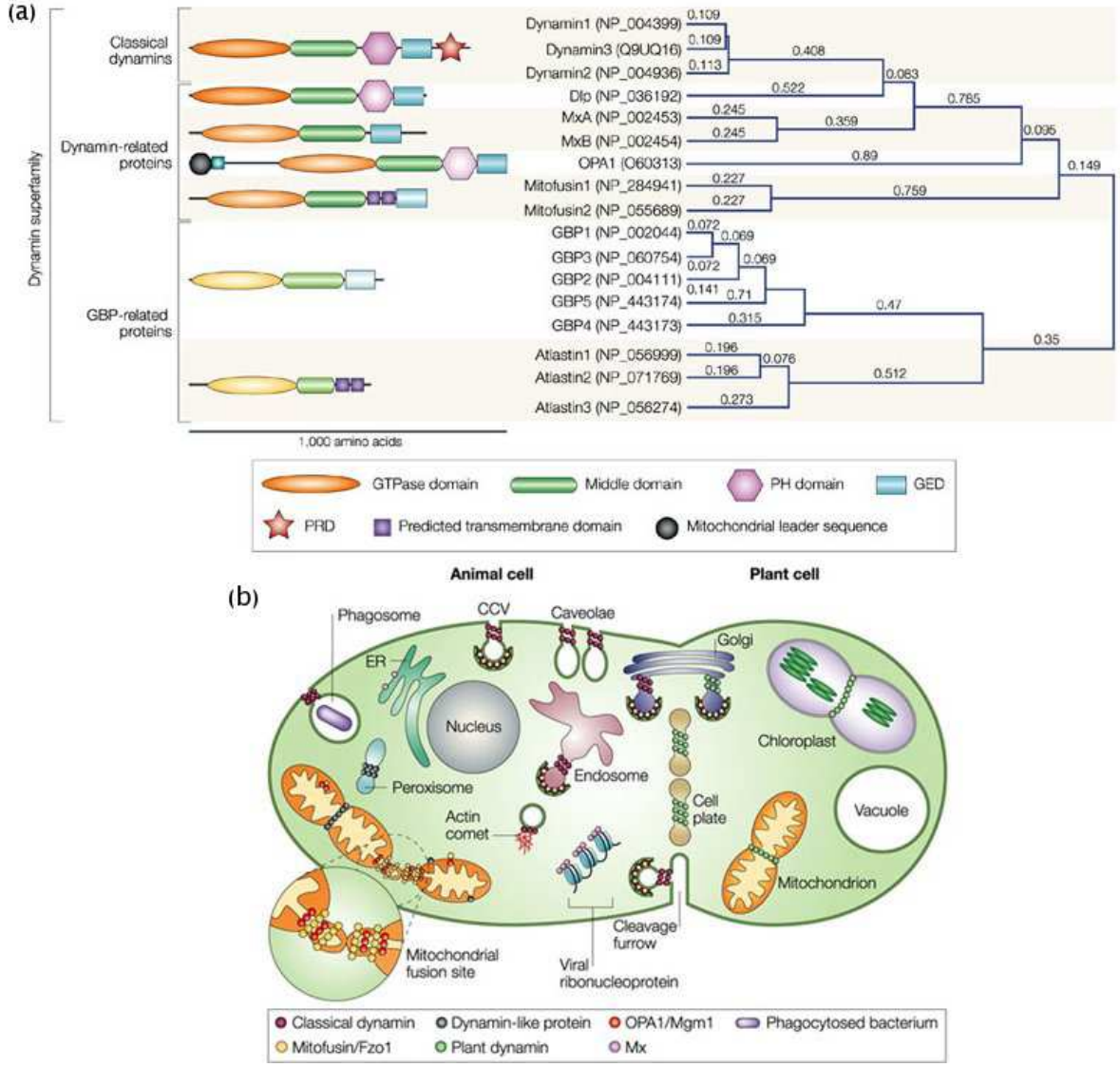

Figure 2.1: Dynamin-related proteins are ubiquitous in animal and plant cells. (a) Similarities between the structures of the members of the dynamin superfamily. All dynamins have a GTPase domain that binds and hydrolyzes GTP, as well as a middle domain and a GTPase effector domain (GED). These domains are involved in dynamin oligomerization and their interactions stimulate the GTPase activity. Most dynamins also contain a domain for interactions with lipid membranes. In classical dynamins, this role is played by a pleckstrin-homology (PH) domain, which displays specific interactions with the phospholipid phosphatidylinositol-4,5-bisphosphate (PIP_2). Their proline-rich domain (PRD) also interacts with lipids, as well as with Src-homology-3 (SH3) domains. Dynamin has a molecular weight of $\sim 100\,\mathrm{kDa}$. (b) Such proteins play a role in a wide variety of processes essential for the proper functioning of eukaryotic cells. Both figures taken from Ref. [7].

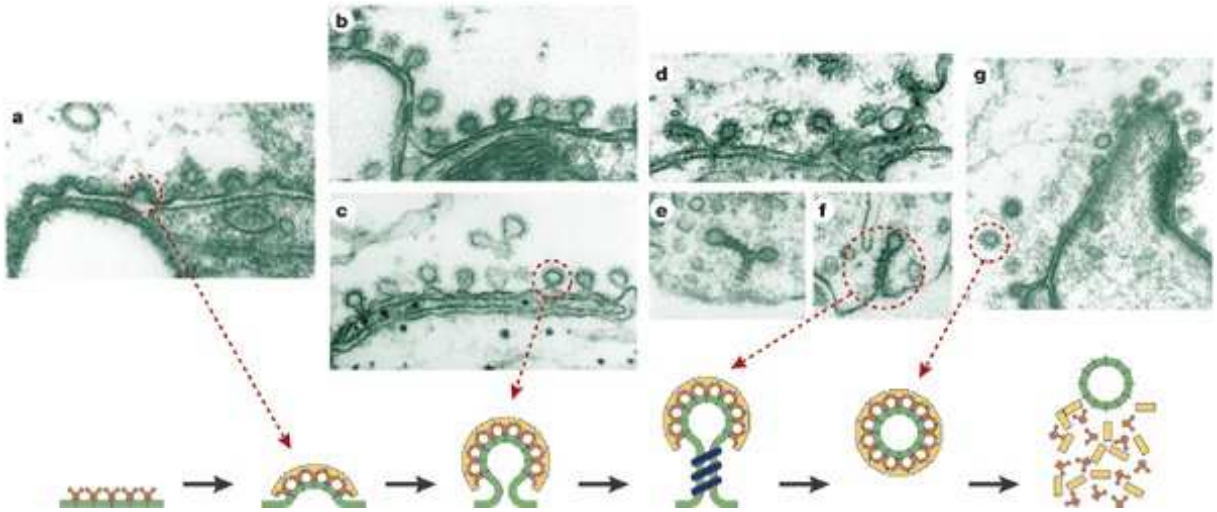

Figure 2.2: The successive steps of clathrin-coated endocytosis. The clathrin coat proteins deform the plasma membrane into a bud (a), thus forming deeply invaginated pits (b-c). Dynamin oligomerizes into short helices around the necks of these pits (d-f) and severs them upon GTP hydrolysis, thus releasing the endocytosis vesicle (g). Figure taken from Ref. [20].

coated vesicles, possibly through membrane-mediated elastic interactions [13], and self-assembles into short (a few helical repeats) helical constructs on the cell membrane necks localized at their base [14]. These membrane necks need to be severed to complete endocytosis. For this to happen, however, they need to undergo substantial deformations, which is energetically costly. Dynamin is a GTPase and therefore catalyses the hydrolysis of guanosine triphosphate (GTP) into guanosine diphosphate (GDP) and inorganic phosphate (Pi). This highly exoenergetic ($\sim 25\,k_BT$ per GTP molecule in a typical cellular environment) reaction is similar to the hydrolysis of ATP, which fuels actin treadmilling, most known molecular motors and many other cellular processes [15]. GTP hydrolysis could therefore be a source of energy sufficient to power membrane tube fission by self-assembled dynamin [7, 16, 17]. This interpretation is supported by the fact that in the presence of a GTPγS, a non-hydrolyzable analog of GTP, endocytosis is blocked at the stage illustrated in Fig. 2.2(d-f) [18]. A similar behavior is observed with dynamin mutants defective in GTP binding [19].

The *in vivo* action of dynamin can therefore be broken down into two steps: its self-assembly into a helical polymer, and a GTP-induced severing stage. In the next two sections, we present experiments conducted in biomimetic environments that yield insight into each of these.

2.1 Self-assembly

The helical polymers of dynamin observed in a cellular environment [Fig. 2.2(d-f)] can also form out of purified dynamin in a low-salt solution [21], or in a physiological salt so-

lution in the presence of the non-hydrolyzable GDP:AlF_4^- or GTPγS [22]. Dynamin has an affinity for negatively charged substrates, and preferentially inserts in membranes containing phosphatidic acid, phosphatidylinositol-4-phosphate and phosphatidylinositol-4,5-bisphosphate (PIP_2) [23]. Consistent with this, its polymerization is most easily observed around negatively charged templates such as microtubules, onto which dynamin was first isolated. Purified dynamin also polymerizes in the absence of GTP or any other nucleotide around negatively-charged lipid bilayers, either synthetic [24] or extracted from the brain [25], thus deforming liposomes into dynamin-coated tubes, simply termed "tubes" in the following. Moreover, dynamin has specific interactions with PIP_2 through its Pleckstrin Homology (PH) domain [see Fig. 2.1(a)], and its recruitment to the neck of endocytic buds is dependent on the local synthesis of this lipid [26].

The tubes formed under these biomimetic conditions can be extremely long, up to tens of micrometers, which corresponds to thousands of helical repeats. Electron micrographs reveal their structure, as shown in Fig. 2.3(A, C, E). They suggest that the basic subunit of the dynamin polymer is a dimer and that the tubes are hollow, *i.e.* filled with water [27, 28, 29].

Although the biochemical parameters of the membrane determining the formation of long dynamin tubes *in vitro*—and therefore possibly the rate of endocytosis *in vivo*—have been well studied, the influence of its physical characteristics, such as curvature or tension, are much less known. We characterize these effects in chapter 3 and argue that they could play an important role in the recruitment of the protein *in vivo*.

2.2 GTPase activity

Although dynamin helices break the underlying membrane only upon GTP hydrolysis, this step is intimately linked to the polymerization step. Indeed, self-assembly of dynamin has been linked to a dramatic increase of its GTPase activity [30, 31, 32]. Its GTP hydrolysis rate is also unusually high compared to other GTPases (Fig. 2.4). Unlike most of them, the primary function of dynamin might therefore not be related to signaling.

Further evidence of this hypothesis is obtained by incubating dynamin with GTP, and then imaging it in electron microscopy. This reveals a dramatic change of conformation of the helix, and experiments both on normal dynamin [24] and dynamin Δ-PRD [*i.e.* dynamin lacking its PRD domain—see Fig. 2.1(a)] [33] indicate that the inner radius of the tube (lipids included) goes from 10 to 5 nm, its outer radius from 25 to 20 nm and its pitch from 13 to 9 nm. Dynamin Δ-PRD is particularly convenient when a three-dimensional reconstruction of the helix is intended, as it yields very ordered helices. Unlike normal dynamin, dynamin Δ-PRD changes conformation when incubated with the non-hydrolyzable GTP analogs GMPPCP, GMPPNP and GTPγS [27]. In this situation the outer radius also goes from 25 to 20 nm and the pitch shrinks—although less than for normal dynamin—from 10.6 to 9.4 nm on average (Refs. [28, 29] and Fig. 2.3). The application of reconstruction techniques yields information about the detailed structure of the helix, and reveals that the number of dimers per turn of the helix goes from 14.2 to 13.2. These numbers imply that the arc length between the surface of two subunits go from 7.1 to 5.7 nm, and thus that subsequent turns of the helix do not simply slide

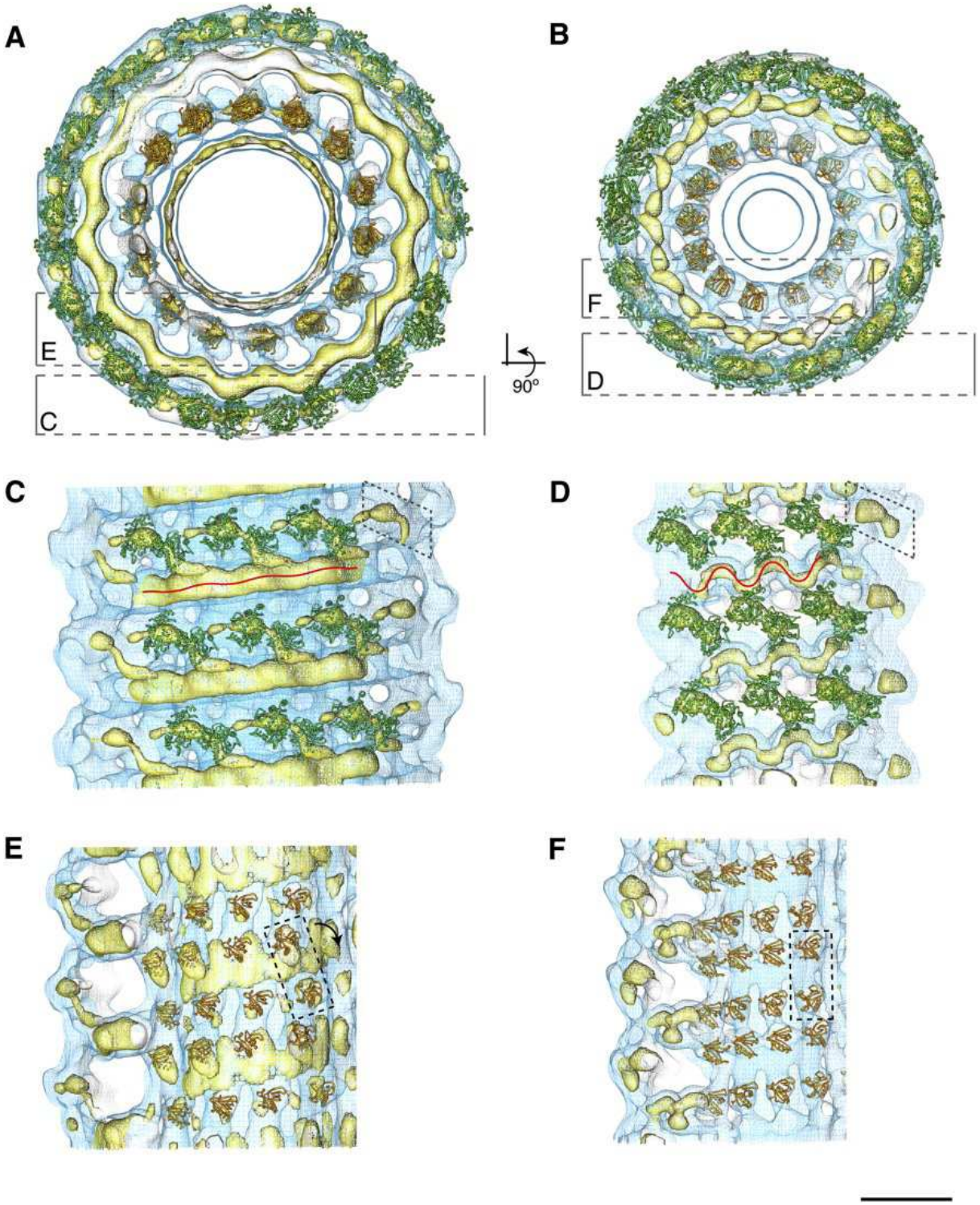

Figure 2.3: Reconstruction of the structure of dynamin Δ-PRD (lacking its PRD domain) assembled on negatively charged liposomes in its unconstricted (no nucleotides—A, C, E) and constricted (incubated with GMPPCP—B, D, F) states from electron micrographs. Two density thresholds are represented in blue and yellow. Green and orange represent fits of the GTPase and PH domains respectively. The points of view in C-F are indicated by dashed boxes and an arrow representing a rotation in A-B. Bar, 10 nm. Figure taken from Ref. [29]

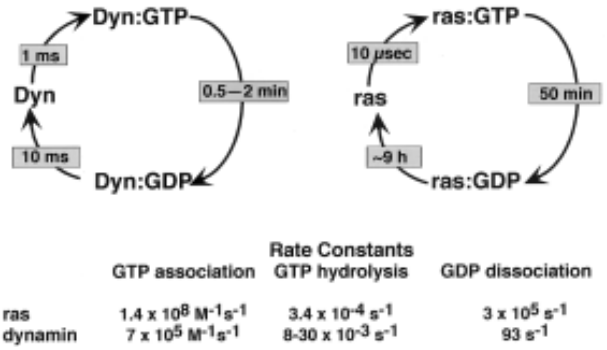

Figure 2.4: Comparison between the GTP hydrolysis cycles of dynamin and a typical GTPase, the small regulatory protein ras. The number given here for the GTP hydrolysis rate of dynamin is its basal rate (*i.e.* the hydrolysis rate in the non-polymerized state). Its stimulated rate (*i.e.* its hydrolysis rate in the polymerized state) is much higher, of order 1-5 s^{-1}. Figure taken from Ref. [16].

upon one another, but also that individual dimers contract, as shown by the red lines in Fig. 2.3(C) and (D). Whether or not this is representative of the behavior of normal dynamin upon GTP hydrolysis is not known. In another series of experiments [34, 35], a special mixture of lipids that forms nanorods of radius ~ 16 nm even in the absence of dynamin was used. Unlike in Refs. [24, 33], normal dynamin was added in the presence of various nucleotides, following which it formed helices with an outer radius ~ 20 nm around the nanorods. No change in the radius of the nanorods was observed. If the nucleotide used was GDP, the pitch of the helices was approximately 20 nm. If on the other hand GTPγS or GDP:AlF_4^- (which mimics the transition state between GTP and GDP) were used, helices with a pitch of 11 nm were observed. When experiments with GTP were conducted, tight helices were observed shortly after the activation of GTP hydrolysis by $MgCl_2$, and only loose ones were seen on longer time scales. These results suggest that the radius of dynamin stays constant during GTP hydrolysis and that its pitch increases, in conflict with the results of Refs. [24, 27, 28, 29, 33]. These discrepancies are discussed in chapter 4.

Whatever the precise details of the change of conformation of dynamin, it is widely recognized to be both linked to GTP hydrolysis (which is itself conditioned to the polymer's self-assembly) and indispensable for endocytosis [35]. Dynamin is therefore thought to function primarily as a mechanochemical enzyme, a unique status among GTPases. *In vitro* and in the absence of any other protein, its change of conformation is sufficient to drive tube breakage when the end points of the tube are attached to a substrate [24]. However, no fission of freely floating tubes is observed [33]. More recently, optical microscopy was used to investigate the dynamics of the tube's conformational change and breaking [36]. In these experiments, dynamin-coated membrane tubes are grown from a lamellar phase of brain polar lipids (or a synthetic mixture mimicking brain polar lipids) supplemented with PIP_2. GTP is then injected in the experimental chamber (typically in a few tenths of seconds). The initially rather floppy tubes then straighten, revealing a buildup of their tension. If one end of the tube is free to fluctuate, this tension results

in the retraction of the tube. If both ends are attached, the tube breaks. If polystyrene beads (radii 130-160 nm) are attached to the dynamin coat, rotation is observed after GTP injection, showing that GTP hydrolysis induces not only tension but also torques in the tubes. The typical time scales involved in the rotation of the beads and the breaking of the tubes are roughly 3 s after GTP injection. Note that the buildup of torques is further evidenced by the formation of plectonemic supercoils, as observed in electron microscopy [33, 36].

Although the mechanism by which dynamin breaks membrane tubules is still a much-debated question for which several models have been proposed [16], these experimental results point in the direction that it might critically depend on some physical parameters. As tube breaking seems to depend on the buildup of torques and tube tension as the helix undergoes a concerted conformational change. However, this view was recently challenged and it has been argued that long dynamin helices disassemble very quickly when put in the presence of GTP [37, 38, 39]. In chapter 4, we set out to develop a theoretical framework allowing the study of concerted conformational changes in helical tubes. This allows us to formulate general predictions and interpret unpublished experimental results to argue strongly in favor of a concerted conformational change. We also set the path for a systematic study of the factors inducing tube breaking.

Chapter 3

Dynamin polymerization

In this chapter, we deal with the first step of dynamin's action: its polymerization around a membrane substrate. This is a very complicated problem to study in a cellular environment, because of the complex geometry and of the other proteins involved. Therefore, in order to obtain a quantitative insight into this process, we study dynamin in an *in vitro* setup using purified components. Combining the data from this well-controlled system with a theoretical approach, we are able to extract reliable information concerning the seeding and growth of dynamin helices. Unless stated otherwise, all the experimental data presented in this chapter is as yet unpublished work by Aurélien Roux in the group of Patricia Bassereau in Institut Curie.

In Sec. 3.1, we present the experimental setup with which the aforementioned data was obtained, as well as the basic physical principles underlying its functioning. Sec. 3.2 concerns the equilibrium properties of the dynamin polymer; the theoretical results obtained in this section are supported by substantial experimental data. In the more speculative next two sections, we try to interpret preliminary results concerning transient regimes: Sec. 3.3 deals with the seeding of the dynamin polymer and Sec. 3.4 with its growth dynamics. Experimental proposals are made that could lead to a better understanding of the dynamin-membrane interactions. Finally, in Sec. 3.5, we discuss the biological implications of our results.

3.1 Experimental setup

The setup described here allows control over a single dynamin helix. A giant unilamellar lipid vesicle (GUV) containing biotinilated lipids as well as PIP_2 is held by a micropipette [Fig. 3.1(a)]. The pressure P_p within the pipette is imposed and is lower than the pressure P_c in the experimental chamber. Denoting the pipette and vesicle radii by r_p and r_v, the membrane tension by σ and the pressure inside the vesicle by P_v, we write Laplace's law at the spherical interfaces between the inside of the pipette and the vesicle and between the vesicle and the experimental chamber, respectively:

$$\begin{cases} P_v - P_p = 2\sigma/r_p \\ P_v - P_c = 2\sigma/r_v \end{cases} \Rightarrow \sigma = \frac{r_p r_v}{2} \frac{P_c - P_p}{r_v - r_p}. \tag{3.1}$$

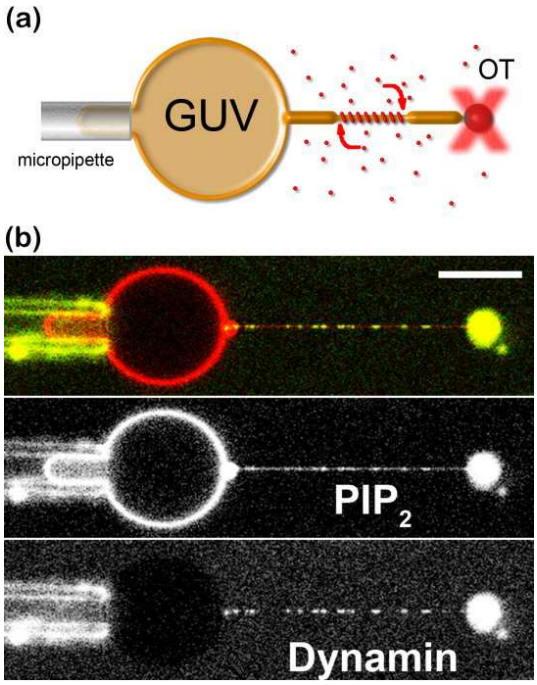

Figure 3.1: Experimental setup. (a) Schematic, see main text for description. (b) The membrane (labeled by GloPIP$_2$—red channel) and dynamin (Alexa 488-labeled—green channel) are imaged in confocal fluorescence microscopy. Inhomogeneities in the red channel are due to bleed through from the green channel to the red. Bar, 10 μm.

Therefore, assuming that the vesicle is large enough for r_v to vary negligibly over the course of the experiment, it is possible to set the tension of the vesicle by controlling P_p. This is done throughout this chapter.

In order to create a substrate suited for dynamin polymerization, a streptavidin-coated bead is brought into contact with the vesicle using optical tweezer (OT), allowing the membrane to stick to the bead by the formation of biotin-streptavidin bonds. When the bead is moved away, it remains attached to the vesicle by a thin cylindrical membrane tubule. Such a deformation of the membrane out of its initial spherical shape has an energetic cost, and the membrane exerts a restoring force on the bead accordingly. An easy way to observe this pulling effect is to turn the optical tweezer off: the tubule then quickly retracts and drags the bead back into contact with the vesicle. For small displacements of the bead, the confinement of the optical tweezer can be described as a harmonic trap, and the force exerted on the bead can therefore be measured by monitoring its displacement within the trap. This displacement is much smaller than the typical length of the tubules considered here. The optical tweezer exert a force f on the bead that balances the force exerted by the membrane. By considering the free energy cost of deforming the membrane, we are able to predict the value of this force. Neglecting thermal fluctuations, the energy of the membrane is given by Eq. (1.1). Let us write the free energy of a cylindrical bare membrane tubule of radius r_b and length L in contact with a membrane tension reservoir

(the vesicle, imposing a tension σ) and a force reservoir (the bead, imposing a force f):

$$F_b = 2\pi r_b \left(\frac{\kappa}{2r_b^2} + \sigma \right) L - fL, \tag{3.2}$$

where κ is the bending modulus of the membrane. Minimizing F_b with respect to r_b and L, we find that the radius of the tubule is set by the competition between the tension, which tends to suck the membrane to the vesicle and therefore deplete the tubule of lipids and make it narrower, and the bending modulus, which prevents the membrane from becoming too curved *i.e.* prevents the tubule from becoming too narrow. We also obtain the force needed to maintain a bare membrane tubule:

$$r_b = \sqrt{\frac{\kappa}{2\sigma}}, \quad f_b = 2\pi\sqrt{2\sigma\kappa}. \tag{3.3}$$

Moving away from well-established experimental procedures (for further details on this setup, see Ref. [40]), we introduce a purified dynamin solution in the experimental chamber. For high enough concentrations, dynamin spots appear on the tubule and grow with time [Fig. 3.1(b)]. This is evidence of the polymerization of a dynamin helix around the tubule, as mere adsorbed dynamin would be expected to cover the tubule homogeneously. Moreover, if the bead is released from the optical trap after covering the tubule with dynamin, full retraction of the tube is not observed, an indication of the rigidity of the dynamin polymer.

3.2 Thermodynamic study

Dynamin was one of the first proteins shown to tubulate protein-free charged liposomes [24]. At the end of this process, the tubules are encircled by dynamin helices, suggesting that dynamin polymerization provides the energy needed to deform the liposome membrane into a highly curved tubular structure. In this section, we investigate this interpretation by considering only the initial and final states of the polymerization process, thus avoiding speculations on its dynamics.

In Sec. 3.2.1, we propose a slight generalization of Eq. (3.2) allowing the description of dynamin-covered tubes. One important parameter of this description is the free energy associated with dynamin polymerization, which we measure in Sec. 3.2.2. In Sec. 3.2.3, we use this result to predict the dependence of dynamin polymerization on the initial curvature of its membrane substrate without any adjustable parameters, and confirm these results experimentally.

3.2.1 Dynamin-coated tubes

Dynamin has a tendency to spontaneously polymerize around membrane substrates. Here we propose an energetic description of this tendency and write the total free energy of the tubule in contact with the dynamin solution, the vesicle and the bead as

$$F = \mu_b(L - L_h) + \mu_h L_h - fL, \tag{3.4}$$

where $\mu_b = \frac{\pi\kappa}{r_b} + 2\pi\sigma r_b$ is the free energy per unit length of the bare membrane tubule, L_h is the length of tubule covered by the helix and the free energy per unit length for the dynamin-covered part reads

$$\mu_h = \frac{\pi\kappa}{r_0} + 2\pi r_0\sigma - \mathcal{P}(c, r_0). \tag{3.5}$$

Since the dynamin coat is very rigid [see discussion in the next chapter, and in particular Eq. (4.49)] and consistent with the very narrow dispersion in the radii of experimentally observed tubes [14, 24, 33, 41], we assume that r_0, the radius of the dynamin-coated membrane, is a constant imposed by the structure of the dynamin helix. More generally, in this section we do not take into account the energetic cost of deforming the helix, as it is considered so stiff that its deformation, and hence this cost, is negligible. The two first terms of the right-hand side of Eq. (3.5) obviously describe the cost of imposing the radius r_0 on the membrane while $\mathcal{P}(c, r_0)$ is the free energy gain per unit length that we associate with dynamin polymerization. This $\mathcal{P}$ includes the following effects:

- The binding energy of a dynamin dimer to an already existing helix—this quantity might depend on the salinity of the solution.
- The energy gain of dynamin upon binding the membrane—this quantity depends on the chemical composition of the membrane.
- The loss of entropy for dynamin dimers to leave the solution and go into the immobilized polymerized state—this quantity depends on the concentration c of the dynamin solution.
- The elastic cost of deforming the helix away from its preferred radius—this quantity depends on the inner radius r_0 of the dynamin helix.

In the hypothesis where r_0 is a constant and working at constant membrane and buffer composition, we only need to consider the dependence of $\mathcal{P}$ on the concentration c of dynamin in the solution.

Minimizing F with respect to r_b, we find that $\mu_b = f_b$ and that r_b has the same value as in Eq. (3.3).

3.2.2 Measurement of the polymerization free energy

Since dynamin gains free energy upon polymerization, we expect that it should be able to push against the bead with a force $\mathcal{P}(c)$, similar to microtubules growing against a wall [42]. By pushing against the bead, it should relieve some of the pulling force exerted by the membrane tubule. As mentioned above the force exerted on the bead is monitored throughout the experiments, and it should therefore be possible to observe this drop in the tubule force. Experimentally, we indeed observe such a force drop, as shown in Fig. 3.2(a-b). Note that if the tubule is only partially covered by dynamin, the force remains constant and equal to f_b. This is expected from our theoretical description, as can be seen by minimizing F with respect to L at fixed $L_h < L$—otherwise said, although dynamin grows, it cannot exert a force on the bead without leaning on the vesicle for

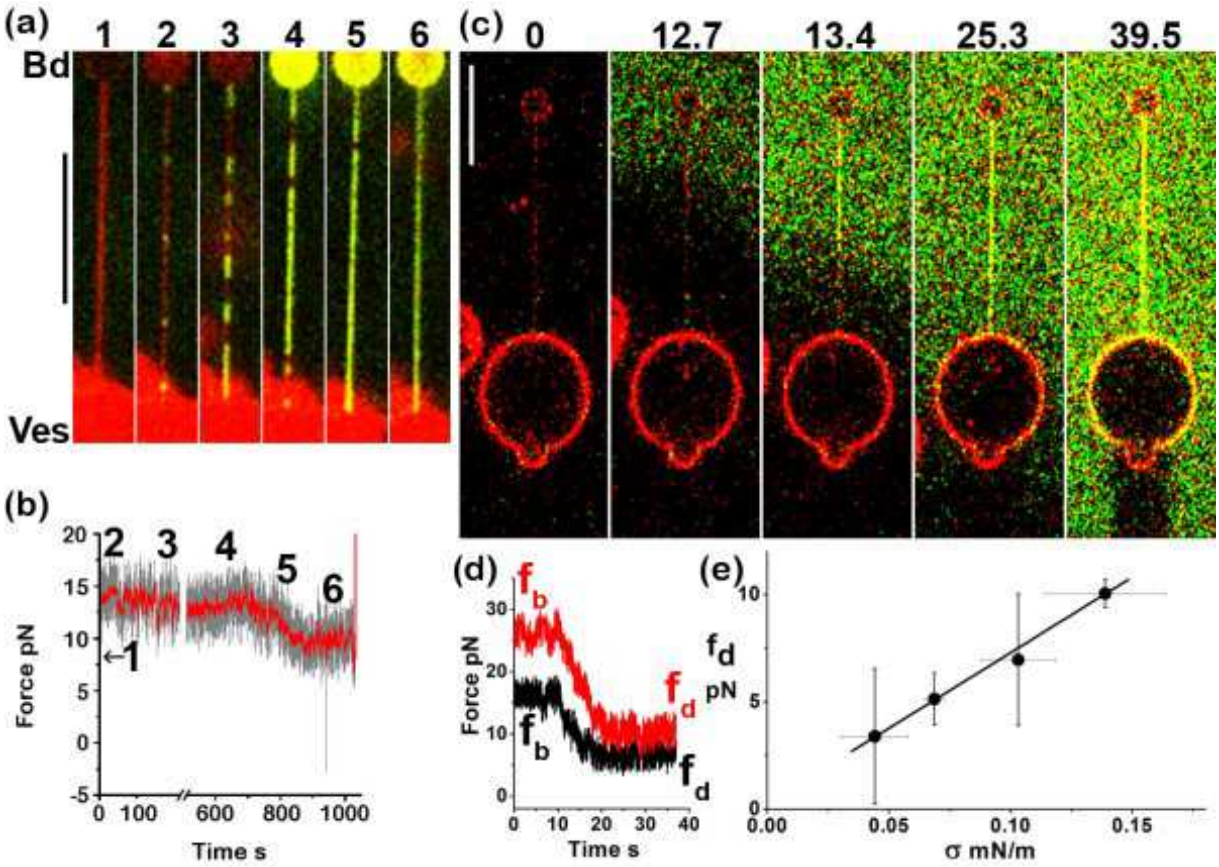

Figure 3.2: Coverage of the membrane tubule by dynamin induces a drop in the force. (a) Progressive coverage of a tubule by a dynamin helix in the presence of a 440 nM dynamin solution. Bd: bead, Ves: vesicle. (b) Force measurements throughout this process (gray, raw data; red, smoothed average). The numbers refer to the successive images of (a). The force drops when full coverage of the tubule by dynamin is achieved. (c) Rapid coverage of the tubule by dynamin upon injection of a 12 μM dynamin solution by an auxiliary pipette (outside of the field of view). Times are indicated in s. (d) Force measurement for two similar experiments, with two different membrane tensions. (e) Dependence on the membrane tension of the force associated with the dynamin-covered tube. Bars, 10 μm.

support. At full coverage, on the other hand, $L = L_h$ and the minimization yields a force $f_h = \mu_h$.

Moving to a higher dynamin concentration of 12 μM, where the polymerization process is quicker [Fig. 3.2(c)], but the force drop feature is conserved [Fig. 3.2(d)], we conduct experiments at various membrane tensions and obtain the dependence of $f_h = \mu_h$ on σ [Fig. 3.2(e)]. As predicted in Eq. (3.5), this dependence is linear, confirming our assumption that r_0 is independent of σ. Using $\kappa = 16 \pm 3 k_B T$ (measured before dynamin injection following the protocol of Ref. [43]), the fit coefficients yield a new measurement of the inner radius of the dynamin helix, $r_0 = 11.2 \pm 0.3$ nm, consistent with existing electron

microscopy data [14, 24, 33, 41], as well as

$$\mathcal{P}(12\,\mu\mathrm{M}) = 18.1 \pm 2\,\mathrm{pN}. \tag{3.6}$$

Since the dynamin polymer grows by $a = 9.3\,\text{Å}$ upon addition of one dimer (14 dimers per 13 nm turn), this means that the polymerization free energy of the dynamin helix equals $\mathcal{P}(12\,\mu\mathrm{M}) \times a = 3.8 k_B T$ per dimer. This is of the same order of magnitude as the polymerization free energies of other biopolymers: 5-10$k_B T$ for tubulin [42] and 0.5-1.5$k_B T$ for actin [44].

3.2.3 Polymerization phase diagram

Having measured $\mathcal{P}$, we are now in a position to test our thermodynamic views on dynamin polymerization. In this picture, dynamin polymerizes around the membrane tubule if and only if $\mu_h < \mu_b$ [see Eq. (3.4)]. Formulating this criterion in terms of the bare tubule radius yields:

$$r_-(c) = \frac{r_0}{1 + \sqrt{\frac{r_0 \mathcal{P}(c)}{\pi\kappa}}} < r_b < r_+(c) = \frac{r_0}{1 - \sqrt{\frac{r_0 \mathcal{P}(c)}{\pi\kappa}}}. \tag{3.7}$$

In other words, a bare membrane tubule can be encircled by dynamin only if its radius lies between the lower critical radius r_- and the upper critical radius r_+. Experimentally, it is indeed observed that dynamin polymerization depends on the bare tubule radius, as shown in Fig. 3.3(a). Note that the tubule radii accessible experimentally are always larger then r_-, so that in practice smaller tubules are always more suitable for dynamin polymerization.

The higher the concentration of dynamin, the more efficiently it tubulates the membrane. This is reflected by the dependence of $\mathcal{P}(c)$ on the concentration of the dynamin solution. Assuming that dynamin is very dilute, we can describe the solution as ideal:

$$\mathcal{P}(c) = \mathcal{P}(12\,\mu\mathrm{M}) + \frac{k_B T}{a} \ln\left(\frac{c}{12\,\mu\mathrm{M}}\right). \tag{3.8}$$

Putting Eqs. (3.7) and (3.8) together with Eq. (3.6), we predict a phase diagram for dynamin polymerization on membrane tubules that does not involve any adjustable parameters. In Fig. 3.3(b), we show that experiments agree with these predictions, thus validating our picture of a competition between dynamin binding energy and membrane elastic energy.

Under certain experimental conditions, dynamin polymerizes around initially flat membrane substrates (as opposed to the cylindrical tubules considered until now) [36]. Theoretically, this behavior is reflected by a negative value of f_h, *i.e.*, a situation where tubes grow unless opposed by a compressive force from the bead. This condition reads $f_h = \mu_h < 0$, or

$$\sigma < \frac{\mathcal{P}(c)}{2\pi r_0} - \frac{\kappa}{2 r_0^2}. \tag{3.9}$$

In order to be able to plot this condition on the phase diagram of Fig. 3.3(b), we equivalently express this condition on the membrane tension in terms of the bare membrane

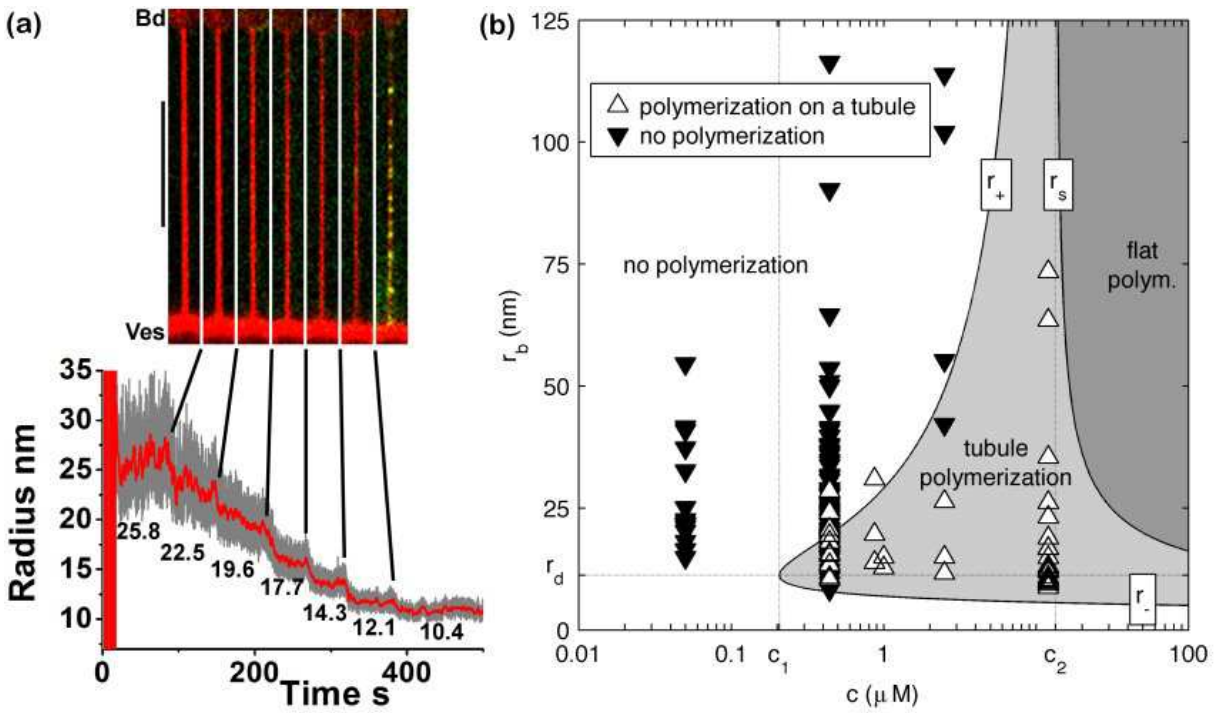

Figure 3.3: The initial radius of the membrane tubule determines whether dynamin polymerizes or not. (a) Membrane tubule in a homogeneous $c = 440\,\mathrm{nM}$ dynamin solution. The radius of the initially wide tubule is brought down progressively by applying steps in the aspiration [*i.e.* in P_p—see Eqs. (3.1) and (3.3)]. Polymerization is only observed once the radius falls below a certain critical radius (here $\simeq 11\,\mathrm{nm}$), which we denote by r_+ in Eq. (3.7). Bd: bead, Ves: vesicle. (b) Theoretical prediction for the dependence of the critical radii $r_\pm$ and the spontaneous tubulation radius r_s on c. The up and down triangles represent specific experiments where polymerization was respectively observed and not observed. An overlap of up and down triangles is observed in some parameter regimes, reflecting the imperfect reproducibility of our experiments due to fluctuations in the local dynamin concentration and in the lipid composition of the membranes. For $c < c_1$, dynamin never polymerizes around membrane tubules. For $c_1 < c < c_2$, dynamin polymerizes around wide ($r_b > r_0$) tubules only if their radius is smaller than $r_+(c)$. For $c_2 < c$, dynamin always polymerizes around wide tubules, and spontaneously tubulates floppy flat membranes [*i.e.* those with $r_b > r_s$—see Eqs. (3.9) and (3.10)]. Bar, $10\,\mu\mathrm{m}$.

radius:

$$r_b > r_s = \frac{r_0}{\sqrt{\frac{r_0 \mathcal{P}(c)}{\pi\kappa} - 1}}. \tag{3.10}$$

This threshold radius for spontaneous tubulation is not a very intuitive quantity to consider and should be understood in the following way: dynamin polymerizes on a flat membrane if the equilibrium radius of a hypothetical tubule extruded from this membrane is larger than r_s. Our description is thus compatible with the observation of spontaneous flat membrane tubulation by dynamin reported *e.g.* in Ref. [36]. Eq. (3.10) is a prediction

concerning the concentration and tension regimes where this should be observed experimentally. As yet, this regime has not been observed in our experiments, as the dynamin solutions we use are below c_2. Note that $\mathcal{P}$, and therefore c_2, depend on the lipid composition of the membrane, which accounts for the fact that other authors working with different lipid compositions observed the tubulation of flat membranes at concentrations lower than the ones used here. We could nonetheless validate Eq. (3.10) using a more concentrated dynamin solution. Doing so would prove that membrane tension alone can control dynamin polymerization, just like the experimental data presented in Fig. 3.3(b) shows that membrane curvature can control dynamin polymerization.

3.3 Seeding kinetics

In the previous section, we saw that at low dynamin concentrations, the initiation of dynamin polymerization occurs through a "seeding" stage. In this phase, the polymerized state of dynamin is the most favorable energetically but helices still only appear in sparse locations and then grow from there [Fig. 3.2(a)]. This is reminiscent of nucleation processes in first-order phase transitions, *e.g.* the liquefaction of water vapor. Under certain conditions, small domains of liquid water (the thermodynamically stable phase) are energetically disfavored and can only grow if a fluctuation of the vapor density makes them larger than a certain critical size above which their bulk stability overcomes the destabilizing surface effects. In the case of dynamin, the role of the metastable vapor is played by the bare membrane tubule with dynamin adsorbed on it. Because of the large radius of the tubule, helices have difficulties to form around it as fitting a dynamin polymer on a large tubule requires bending the polymer and therefore costs energy. Thus the role of surface tension (*i.e.* the energetic barrier) in the nucleation example is played by the energetic cost of locally taking the radius of the tubule down to r_0.

In this section, we speculate about the way dynamin crosses this energetic barrier, therefore making predictions about the kinetics of the seeding process. Although several effects are likely to play a role in practice, we somewhat artificially separate two extreme cases: in Sec. 3.3.1, we consider the case where the length and bending fluctuations of small dynamin oligomers account for the crossing of the barrier, whereas in Sec. 3.3.2 we assume that the thermal fluctuations of the membrane play a dominant role (Fig. 3.4). Because of the experimental difficulty to access the details of phenomena happening on such small length and time scales, we do not look for exact solutions of models involving straightforwardly measurable parameters. Rather, we focus on signatures of the two effects in terms of the scaling of the (experimentally observable) helix seeding rate as a function of (the experimentally tunable) c and σ.

3.3.1 Soft dynamin, stiff membrane

In this first model, we consider that the assembly of dynamin provides the energy necessary to create a pinch in the membrane of the type represented in Fig. 3.4(d). We therefore propose the simplified picture that dynamin first assembles into a small oligomer with a radius of curvature $r_b = \sqrt{\frac{\kappa}{2\sigma}}$ [Fig. 3.4(b)]. Let n denote its length (counted in number

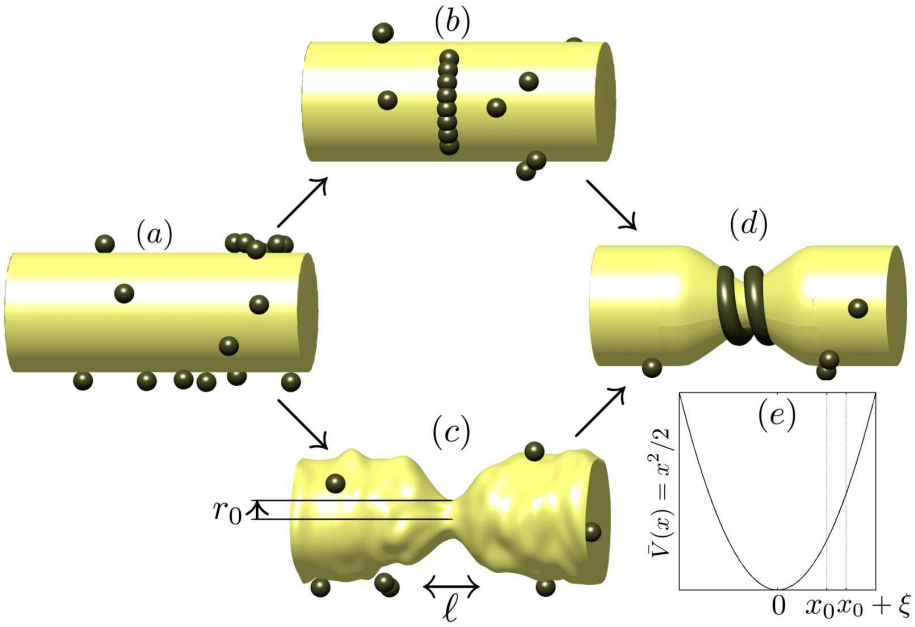

Figure 3.4: Schematics of the metastable (a) and stable (d) states of the dynamin-membrane system. (b) and (c) represent the two reaction intermediates considered here for the system to get out of the former and into the latter. (e) Simplified energy landscape for the "stiff dynamin, soft membrane" model.

of dynamin dimers). Since dynamin helices have a preferred radius $r_0 < r_b$, an elastic energy

$$E_{\text{oligo}} = n e_{\text{oligo}} = \frac{n k_{\text{oligo}}}{2} \left(\frac{1}{r_b} - \frac{1}{r_0} \right)^2 \tag{3.11}$$

is accumulated during the growth of such an underbent oligomer. This equation means that we express E_{oligo} as the bending energy of a worm-like chain with spontaneous curvature r_0^{-1} and persistence length $k_{\text{oligo}}/(k_B T \times \text{size of a dimer})$. Note that short, non-helical oligomers of dynamin might be much more flexible than a dynamin helix. Thus, even though we assumed in Sec. 3.2.1 that dynamin helices are extremely stiff and cannot accommodate a radius larger than r_0, small oligomers might be able to. Finally, we formulate the criterion that as soon as the accumulated energy E_{oligo} matches the energy $\approx \kappa$ necessary to create a pinch in the tubule [45], the oligomer collapses into a stable helix and growth is able to proceed [Fig. 3.4(d)]. This is of course a simplified representation of the actual situation, where the deformation of the membrane is progressive as the oligomer builds up. The equality of these two energies defines the critical oligomer size required for seeding

$$n^* \approx \frac{\kappa}{e_{\text{oligo}}} \approx \frac{\kappa}{k_{\text{oligo}} \left(r_b^{-1} - r_0^{-1} \right)^2}. \tag{3.12}$$

In order to understand the kinetics of seeding in this model, we therefore need to look at the aggregation dynamics of dynamin dimers on the surface of the bare tubule. We

are interested in the time it takes for the first oligomer of size n^* to appear. The change in free energy associated to the formation of a dimer-dimer bond reads:

$$e_{\text{bond}} = e_0 + e_{\text{oligo}}, \tag{3.13}$$

where e_0 is the bonding free energy on a tubule of radius r_d and is negative when polymerization is energetically favored on such a tubule. Infinitely strong bonds correspond to $e_0 \to -\infty$. We model the aggregation process in the following way: for times $t < 0$, N dynamin dimers are adsorbed on the tubule (this hypothesis is discussed further in Sec. 3.4.2). Providing that the dimer density on the tubule is not to high, N is proportional to the concentration c of the dynamin solution and to the length L of the tubule. The aggregation process is turned on at time $t = 0$, for instance by decreasing the value of r_b as in Fig. 3.3(a), thus making the formation of bonds more favorable energetically according to Eqs. (3.11) and (3.13). We assume that dynamin dimers form linear polymers, *i.e.* that they have two reaction sites that bond with other dimers' reaction sites with a rate constant k_{agg}. Note that k_{agg} can depend on the radius of the tubule, and therefore on σ, as well as on the temperature. Assuming fast diffusion and normalizing time by k_{agg}, we define the following reaction-limited aggregation process:

$$\frac{\mathrm{d}N_n}{\mathrm{d}t} = \frac{1}{2}\sum_{l+m=n}\left[\frac{(2N_l)(2N_m)}{N} - 2e^{\frac{e_{\text{bond}}}{k_BT}}N_n\right] - \sum_{m=0}^{+\infty}\left[\frac{(2N_m)(2N_n)}{N} - 2e^{\frac{e_{\text{bond}}}{k_BT}}N_{m+n}\right], \tag{3.14}$$

where N_n is the number of aggregates containing n dimers. In the right-hand side of this equation, terms quadratic in N_n account for aggregation events. Here we ignore circular oligomers, hence the factors 2 in these terms, corresponding to the fact that each aggregate has two dangling ends, hence two potential reaction sites. The terms linear in N_n, on the other hand, represent the fragmentation events. The reaction constants in front of them are proportional to $\exp(e_{\text{bond}}/k_BT)$, which is required to satisfy detailed balance. The factors of 2 in front of these fragmentation terms originate from the fact that there are two ways to break a n-mer into two pieces of prescribed size l and m such that $l + m = n$: either as a l-mer plus an m-mer, or as an m-mer plus a l-mer. We make the approximation that $N = \sum_n nN_n$ is conserved (which is a good approximation if exchanges with the solution are slow or if most dimers stay in a non-oligomerized state) and start from $N_1(t = 0) = N$.

This process corresponds to the special case RA_2 of the class of models introduced in Ref. [46]. Here we present some results from this reference. Let us define the "extent of reaction" $\delta(t)$ as the fraction of the reaction sites having reacted at time t. This quantity is sometimes also referred to as the "reaction rate". We can express the probability that a dimer selected at random is part of a n-mer in two ways:

1. as nN_n/N.

2. as the product of the following terms: the probability δ^{n-1} that $n - 1$ sites have reacted with some site on some other dimer; the probability $(1 - \delta)^2$ that the two sites at the dangling ends have not reacted; and a factor n representing our freedom to select any one of the dimers within the oligomer.

Equating those two expressions, we find the number of n-mers:

$$N_n = N\delta^{n-1}(1-\delta)^2. \tag{3.15}$$

We also write the rate equation for the chemical reactions between sites:

$$\frac{\mathrm{d}\delta}{\mathrm{d}t} = 2(1-\delta)^2 - e^{\frac{e_{\mathrm{bond}}}{k_B T}}\delta, \tag{3.16}$$

where the first term describes bonding reactions between two sites and the second breakage of bonds. The solution of this equation is

$$\delta(t) = \delta_0 \frac{1-e^{-\Delta t}}{1-\delta_0^2 e^{-\Delta t}}, \tag{3.17}$$

where the stationary solution is given by

$$\delta_0 = 1 + \frac{e^{\frac{e_{\mathrm{bond}}}{k_B T}} - \Delta}{4} \quad \text{with} \quad \Delta = \sqrt{e^{\frac{2e_{\mathrm{bond}}}{k_B T}} + 8e^{\frac{e_{\mathrm{bond}}}{k_B T}}}. \tag{3.18}$$

Combining Eq. (3.15) with Eq. (3.18), we find that at equilibrium N_n is an increasing function of n if and only if $e_{\mathrm{bond}} < 0$. This corresponds to a situation where long filaments are more stable than isolated dimers even on a tubule of radius r_b, and therefore to a case where the energy barrier considered here vanishes. The analog of this in the frame of first-order transition would be a situation where spinodal decomposition occurs. In this section, we focus on the case $e_{\mathrm{bond}} > 0$, and try to assess the time it takes for the first seed to appear. Rather than solving the full first-passage process it involves, we use the heuristic criterion that in large systems, the first seed appears for t_{seed} such that $N_{n^*}(t_{\mathrm{seed}}) \approx 1$. If the system is large enough [$N \to +\infty$, meaning $N_{n^*}^{\infty} = N_{n^*}(t = +\infty) \gg 1$], this happens for a small extent of reaction

$$\delta(t_{\mathrm{seed}}) \underset{N\to+\infty}{\sim} \frac{1}{N^{1/(n^*-1)}} \underset{N\to+\infty}{\to} 0, \quad \text{hence} \quad t_{\mathrm{seed}} \underset{N\to+\infty}{\sim} \frac{N^{-1/(n^*-1)}}{\delta_0 \Delta} \underset{N\to+\infty}{\to} 0. \tag{3.19}$$

This equation simplifies in the small temperature/high barrier limit $e^{\frac{e_{\mathrm{bond}}}{k_B T}} \gg 1$:

$$t_{\mathrm{seed}} \underset{\substack{N\to+\infty \\ T\to 0}}{\sim} N^{-1/(n^*-1)} \approx (cL)^{-1/(n^*-1)}, \tag{3.20}$$

This result has a rather simple interpretation: on short time scales, the number of $n = 1$ aggregates is roughly constant, and therefore of order cL. Thus the rate of formation of $n = 2$ aggregates is of order cL also, meaning that $N_2 \approx cLt$. Similarly, the average number of n^*-mers initially grows as $N_{n^*} \approx cLt^{n^*-1}$. Hence there is $N_{n^*} \approx 1$ aggregate of size n^* when t reaches the seeding time given in Eq. (3.20). Note that in this equation time is expressed in units of k_{agg}^{-1}, and that t_{seed} can thereby depend on σ and the temperature T. Experimentally, it should be possible to validate this mechanism by verifying that t_{seed} is a function of cL *i.e.* that it has the same dependence in c and in L. The form of this dependence should allow for the determination of n^*. Then the dependence of n^* on σ

could in principle be recovered, allowing an evaluation of the persistence length of short dynamin strands through Eq. (3.12).

In the case of a small system, the extent of reaction δ reaches its stationary value δ_0 way before t_{seed}. At any time, the average number of n^*-mers in the system is $N_{n^*}^{\infty} \ll 1$, meaning that there are no n^*-mers in the system a fraction $1 - N_{n^*}^{\infty}$ of the time and one n^*-mer a fraction $N_{n^*}^{\infty}$ of the time. Therefore to see a n^*-mer, we need to wait $1/N_{n^*}^{\infty}$ times the typical correlation time of the n^*-mer concentration. According to Eq. (3.17), this time is $1/\Delta$. Therefore:

$$t_{\text{seed}} \underset{N\to 0}{\approx} (N_{n^*}^{\infty}\Delta)^{-1} \approx \left[N\delta_0^{n^*-1}(1-\delta_0)^2\Delta\right]^{-1} \underset{\substack{N\to 0\\ T\to 0}}{\approx} (cL)^{-1} e^{\frac{(n^*-2)e_{\text{bond}}}{k_B T}}. \tag{3.21}$$

Again, the dependence of t_{seed} in T and σ in this expression is not completely known, as the time unit k_{agg}^{-1} depends on them. However, the dependence in n^* is completely explicit here as k_{agg}^{-1} does not depend on it. We can understand this dependence in simple terms: we have $\approx cL$ particles, each of which might aggregate with others and form an n^*-mer. Aggregation is however energetically disfavored, and the associated energetic barrier is $n^* e_{\text{bond}}$. According to Kramers' rate theory, we expect a rate of jumping over the barrier proportional to $\exp\left(-n^* e_{\text{bond}}/k_B T\right)$ for each particle [47]. Therefore the rate for *any* particle to cross the barrier is proportional to $cL\exp\left(-n^* e_{\text{bond}}/k_B T\right)$. Up to a prefactor, the t_{seed} of Eq. (3.21) is the inverse of this rate. Given the large value of the rightmost expression in this equation, seeding might not be observable on reasonable time scales in the low temperature limit. Not however that at any temperature, a seeding time proportional to $(cL)^{-1}$ is a signature of the small system regime of Eq. (3.21). Observing this dependence experimentally would be an indication that more interesting information could be gathered by increasing N and r_b (thus increasing e_{bond}) to reach the regime of Eq. (3.20).

It should be noted that the scaling laws presented here do not depend much on the precise mechanism by which the oligomers grow. Expressions similar to Eqs. (3.20) and (3.21) are recovered if dynamin is assumed to grow by addition of single dimers only, similar to the growth mechanism of other biopolymers [42, 44].

3.3.2 Stiff dynamin, soft membrane

We now consider the opposite extreme to the model presented above, and investigate a situation where dynamin is so stiff that it cannot oligomerize onto a substrate of radius larger than r_0. In such a situation, the membrane needs to locally fluctuate to a radius smaller than r_0 for seeding to happen. When a thermally excited pinch of this type occurs [Fig. 3.4(c)], dynamin must oligomerize around it before the fluctuation relaxes and dynamin assembly is made impossible again. We denote by $\mathcal{T}(c)$ the dynamin concentration-dependent characteristic time required for this oligomerization. One possible interpretation for $\mathcal{T}(c)$ is to view it as the time it takes for a full dynamin ring (made of 14 dimers) to form around the tubule. Once such a ring is formed, the pinch is stabilized by a sturdy dynamin ring that further thermal fluctuations cannot break.

In a nutshell, we are interested in the rate of long ($\geqslant \mathcal{T}$) small-radius ($< r_0$) fluctuations of the tubule. Because the tubule has many fluctuating degrees of freedom, this

problem is quite challenging in the general case. Here, we only consider a certain type of fluctuations, namely a typical pinch of radius r. Restricting ourselves to small deformations, the energetic cost of this pinch has to be quadratic in $(r - r_b)$. Thus we can write it as:

$$V(r) = \frac{k}{2}(r - r_b)^2. \tag{3.22}$$

Dimensionally, the stiffness k of the harmonic potential must be of order σ. In order to tackle the relaxation dynamics of the pinch, we need to know its length ℓ, defined in Fig. 3.4(c). Dimensionally, it must be of order r_b. By analogy with the relaxation of the peristaltic modes of a membrane tubule, we expect that the dominant dissipation mechanism in this system is the drainage of the water inside the tubule [48]. The typical time scale for this process is $\eta\sqrt{\kappa/\sigma^3}$, where η is the viscosity of water. The deterministic part of the pinch's relaxation is thus described by the equation

$$\frac{\mathrm{d}r}{\mathrm{d}t} = -\digamma(r - r_b), \tag{3.23}$$

with $\digamma \approx \frac{\sqrt{\sigma^3/\kappa}}{\eta}$.

For more clarity, we now convert these equations into a dimensionless form. We choose k_BT as our energy scale, $1/\digamma$ as our time scale and $\sqrt{k_BT/k}$ as our length scale. We moreover shift the origin of the position coordinate and change its sign such that in our new units the potential energy, time and position read

$$\bar{V} = \frac{V}{k_BT}, \quad \bar{t} = \digamma t, \quad x = \sqrt{\frac{k}{k_BT}}(r_b - r) \tag{3.24}$$

respectively. We also define $x_0 = \sqrt{k/k_BT}(r_b - r_0)$. In these units, the confining potential of Eq. (3.22) reads

$$\bar{V}(x) = \frac{x^2}{2}. \tag{3.25}$$

and the dynamical equation Eq. (3.23) becomes

$$\frac{\mathrm{d}x}{\mathrm{d}\bar{t}} = -x. \tag{3.26}$$

This simplified description therefore focuses on a section of the tubule of length $\approx r_b$, whose radius (described by the variable x) undergoes thermal fluctuations in the harmonic potential $\bar{V}(x)$ [Fig. 3.4(e)]. To this level of approximation, the fluctuation dynamics of the membrane is described by the following Fokker-Planck equation

$$\partial_{\bar{t}} P(x, \bar{t}) = \partial_x [x P(x, \bar{t})] + \partial_x^2 P(x, \bar{t}), \tag{3.27}$$

where $P(x, \bar{t})$ is the time-dependent probability density function for the random variable x. In the following, we place ourselves in the low-temperature limit $x_0 \gg 1 \Leftrightarrow k(r_b - r_0)^2/k_BT \gg 1$. Considering that $(r_b - r_0) \approx \sqrt{\kappa/\sigma}$, we have $k(r_b - r_0)^2 \approx \kappa$. The low-temperature limit is therefore reasonable as in practice $\kappa/k_BT \simeq 15$. In this limit, even if the variable x goes above x_0, it is very unlikely that it will go much further. Indeed,

since $x_0 \gg 1$ the restoring force in x_0 is much stronger than the fluctuating force due to thermal agitation. Thus above x_0 we can safely approximate the Fokker-Planck equation Eq. (3.27) by

$$\partial_{\bar{t}} P(x,\bar{t}) = x_0 \partial_x P(x,\bar{t}) + \partial_x^2 P(x,\bar{t}). \tag{3.28}$$

We introduce a few definitions in order to make the following reasoning more transparent. We are interested in excursions above a certain threshold x_0 of a brownian particle whose position x is described by Eq. (3.27). We call "ξ-excursions" the trajectories starting at position $x_0 + \xi$ and ending in x_0. We furthermore define "$(\xi, \bar{t})$-excursions" as ξ-excursions of duration $\bar{t}$. Now considering the brownian motion of the particle in the potential of Eq. (3.25) starting from $x < x_0 + \xi$, we say that the particle enters a ξ-excursion as soon as it reaches the position $x_0 + \xi$. The ξ-excursion ends as soon as the particle hits x_0. If the time between those two events is equal to $\bar{t}$, this excursion is a $(\xi, \bar{t})$-excursion according to the above definition. After the excursion is finished, the particle may enter another ξ-excursion upon hitting $x_0 + \xi$ again. In the following, we consider small ξs—we are actually interested in the $\xi \to 0$ limit. Therefore the motion of the particle during an excursion is well described by Eq. (3.28). Note that according to the discussion given in the beginning of this section, we should only be interested in the $(\xi = 0, \bar{t} \geqslant \bar{\mathcal{T}})$-excursions. Because of the fractal structure of the brownian motion, however, a particle in the vicinity of x_0 goes above and below it infinitely many times. If the starting point of the excursion is taken to be the same as its ending point, we will thus have to reason on an infinite number of excursions, which is not very convenient. Therefore, we discuss the general case $\xi > 0$ first, and then take the $\xi \to 0$ limit.

We consider a very long realization of the random walk described by Eq. (3.28). By "very long realization" we mean a realization much longer than the time between two $(\xi, \bar{t} \geqslant \bar{\mathcal{T}})$-excursions. Denoting the total duration of this realization by $\bar{T}_t$, we therefore work in the limit $\bar{T}_t \to +\infty$. For a given ξ, we define $\bar{T}_e(\xi)$ as the time spend in ξ-excursions of any duration. We denote by $N_e(\xi)$ the total number of ξ-excursions[1]. Let us pick an integer i at random between 1 and $N_e(\xi)$, and consider the ith ξ-excursion. The probability that this excursion is a $(\xi, \bar{t}_i)$-excursion with $\bar{t}_i \in [\bar{t}, \bar{t} + \mathrm{d}\bar{t}]$ is equal to the probability for a random walk described by Eq. (3.28) and starting in $x_0 + \xi$ to first hit x_0 after a time $\bar{t}_i$ such that $\bar{t}_i \in [\bar{t}, \bar{t} + \mathrm{d}\bar{t}]$. For a small $\mathrm{d}t$, this probability is given by [47]

$$\mathrm{d}p_\xi^i(\bar{t}) = \frac{\xi}{\sqrt{4\pi}} \exp\left[-\frac{(\xi - x_0\bar{t})^2}{4\bar{t}}\right] \frac{\mathrm{d}\bar{t}}{\bar{t}^{3/2}}. \tag{3.29}$$

Let us now pick a time at random among all times where the particle is in an excursion. Since excursion i has a duration $\bar{t}_i$, the probability that the particle is in excursion i at the time we picked is $\bar{t}_i / \bar{T}_e(\xi)$. Therefore, the joint probability that the particle is in excursion i at the time we picked *and* that $\bar{t}_i \in [\bar{t}, \bar{t} + \mathrm{d}\bar{t}]$ reads

$$\mathrm{d}q_\xi^i(\bar{t}) = \frac{\bar{t}}{\bar{T}_e(\xi)} \frac{\xi}{\sqrt{4\pi}} \exp\left[-\frac{(\xi - x_0\bar{t})^2}{4\bar{t}}\right] \frac{\mathrm{d}\bar{t}}{\bar{t}^{3/2}}. \tag{3.30}$$

[1] According to Eq. (3.29), ξ-excursions have a typical duration of order ξ/x_0. Therefore $N_e(\xi) \approx \frac{\bar{T}_e(\xi)}{\xi/x_0}$, thus $N_e(\xi)$ is finite for $\xi > 0$. If $\xi = 0$, on the other hand, $N_e(\xi)$ diverges, which illustrates the reason why we chose to take the limit $\xi \to 0$ only in the end.

Consider now the probability that the particle is in *any* $(\xi, \bar{t}')$-excursion such that $\bar{t}' \in [\bar{t}, \bar{t} + \mathrm{d}\bar{t}]$ at the time that we picked. This is equal to

$$\begin{aligned} \mathrm{d}Q_\xi(\bar{t}) &= \sum_{i=1}^{N_e(\xi)} \mathrm{d}q_\xi^i(\bar{t}) \\ &= \frac{N_e(\xi)}{\bar{T}_e(\xi)} \frac{\xi}{\sqrt{4\pi}} \exp\left[-\frac{(\xi - x_0\bar{t})^2}{4\bar{t}}\right] \frac{\mathrm{d}\bar{t}}{\bar{t}^{1/2}}, \end{aligned} \tag{3.31}$$

where the last equality is due to the fact that $\mathrm{d}q_\xi^i(\bar{t})$ does not depend on i. The value of the prefactor $N_e(\xi)/\bar{T}_e(\xi)$ is given by the following fact: the probability that the the particle is in any $(\xi, \bar{t}')$-excursion such that $\bar{t}' \in \mathbb{R}$ at the time we picked is equal to one. Indeed, this probability is nothing but the probability that the particle is in any ξ-excursion at the time we picked. Therefore

$$\begin{aligned} \frac{\bar{T}_e(\xi)}{N_e(\xi)} &= \int_0^{+\infty} \frac{\xi}{\sqrt{4\pi}} \exp\left[-\frac{(\xi - x_0\bar{t})^2}{4\bar{t}}\right] \frac{\mathrm{d}\bar{t}}{\bar{t}^{1/2}} \\ &\underset{\xi\to 0}{\sim} \frac{\xi}{x_0} \exp\left(\frac{x_0\xi}{2}\right). \end{aligned} \tag{3.32}$$

Combining this with Eq. (3.31) yields a well-defined, normalized probability distribution in the $\xi \to 0$ limit

$$\mathrm{d}Q_\xi(\bar{t}) \underset{\xi\to 0}{\to} \mathrm{d}Q_0(\bar{t}) = \frac{x_0}{\sqrt{4\pi}} \exp\left(-\frac{x_0^2\bar{t}}{4}\right) \frac{\mathrm{d}\bar{t}}{\bar{t}^{1/2}} \tag{3.33}$$

Therefore if we pick a time at random among all those where the random walk is in a 0-excursion, the probability that this time belongs to a $(0, \bar{t}')$-excursion with $\bar{t}' \in [\bar{t}, \bar{t} + \mathrm{d}\bar{t}]$ is equal to $\mathrm{d}Q_0(\bar{t})$. Integrating over $\bar{t}$, we find the probability that this time belongs to a $(0, \bar{t} \geqslant \bar{\mathcal{T}})$-excursion:

$$\frac{\bar{T}_e^{\geqslant \bar{\mathcal{T}}}(0)}{\bar{T}_e(0)} = \int_{\bar{\mathcal{T}}}^{+\infty} \mathrm{d}Q_0(\bar{t}) = \mathrm{erfc}\left(\frac{x_0\sqrt{\bar{\mathcal{T}}}}{2}\right), \tag{3.34}$$

where the complementary error function is defined by $\mathrm{erfc}(v) = \frac{2}{\sqrt{\pi}} \int_v^{+\infty} e^{-u^2} \mathrm{d}u$. Note that being in a 0-excursion is equivalent to x being larger than x_0.

We now calculate the average duration and the average square duration of a $(0, \bar{t} \geqslant \bar{\mathcal{T}})$-excursion. Let us first write them for $(\xi > 0, \bar{t} \geqslant \bar{\mathcal{T}})$-excursions:

$$\langle \bar{t}_\xi \rangle_{\bar{t} \geqslant \bar{\mathcal{T}}} = \frac{\int_{\bar{\mathcal{T}}}^{+\infty} \bar{t}\, \mathrm{d}p_\xi^i(\bar{t})}{\int_{\bar{\mathcal{T}}}^{+\infty} \mathrm{d}p_\xi^i(\bar{t})} = \frac{\bar{T}_e^{\geqslant \bar{\mathcal{T}}}(\xi)}{N_e^{\geqslant \bar{\mathcal{T}}}(\xi)}, \tag{3.35}$$

$$\left\langle (\bar{t}_\xi)^2 \right\rangle_{\bar{t} \geqslant \bar{\mathcal{T}}} = \frac{\int_{\bar{\mathcal{T}}}^{+\infty} \bar{t}^2\, \mathrm{d}p_\xi^i(\bar{t})}{\int_{\bar{\mathcal{T}}}^{+\infty} \mathrm{d}p_\xi^i(\bar{t})}. \tag{3.36}$$

Both quantities have a well-defined $\xi \to 0$ limit:

$$\langle \bar{t}_0 \rangle_{\bar{t} \geqslant \bar{\mathcal{T}}} = \frac{2}{x_0^2} \left[\frac{1}{1 - \frac{x_0\sqrt{\bar{\mathcal{T}}}}{2}\sqrt{\pi}\mathrm{erfc}\left(\frac{x_0\sqrt{\bar{\mathcal{T}}}}{2}\right)\exp\left(\frac{x_0^2\bar{\mathcal{T}}}{4}\right)} - 1 \right] = \frac{\bar{T}_e^{\geqslant \bar{\mathcal{T}}}(0)}{N_e^{\geqslant \bar{\mathcal{T}}}(0)}, \quad (3.37a)$$

$$\left\langle (\bar{t}_0)^2 \right\rangle_{\bar{t} \geqslant \bar{\mathcal{T}}} = \frac{4}{x_0^4} \left[\frac{1 + \frac{x_0^2\bar{\mathcal{T}}}{2}}{1 - \frac{x_0\sqrt{\bar{\mathcal{T}}}}{2}\sqrt{\pi}\mathrm{erfc}\left(\frac{x_0\sqrt{\bar{\mathcal{T}}}}{2}\right)\exp\left(\frac{x_0^2\bar{\mathcal{T}}}{4}\right)} - 1 \right]. \quad (3.37b)$$

The quantities calculated here have to do with how the excursion time is distributed between the various possible types of excursions.We now turn to the rest of the random walk and relate the excursion time to the total time $\bar{T}_t$. Since $\bar{T}_t$ is much longer than the thermalization time of the particle, $\bar{T}_e(0)/\bar{T}_t$ is the fraction of the time that the particle spends in $x > x_0$. According to equilibrium statistical mechanics, this is equal to

$$\frac{\bar{T}_e(0)}{\bar{T}_t} = \int_{x_0}^{+\infty} \frac{e^{-\bar{V}(x)}}{\sqrt{2\pi}} \mathrm{d}x = \frac{\mathrm{erfc}\left(\frac{x_0}{\sqrt{2}}\right)}{2} \underset{x_0 \to +\infty}{\sim} \frac{\exp\left(-\frac{x_0^2}{2}\right)}{\sqrt{2\pi}x_0}, \quad (3.38)$$

where we use the low-temperature limit $x_0 \to +\infty$ in the following.

Finally, we turn to the quantity of interest to us: the seeding time of the helix $\bar{t}_{\mathrm{seed}}$. It is convenient to assume that the experimental protocol is the following: the tubule is prepared in $\bar{t} = 0$ and immediately starts fluctuating. The brownian agitation of the membrane quickly thermalizes. At some random time $\bar{t}_d$ between 0 and $\bar{T}_t$, dynamin is injected in the experimental chamber. According to our model, the first dynamin helix forms during the first $(0, \bar{t} \geqslant \bar{\mathcal{T}})$-excursion following $\bar{t}_d$. Let i be such that this excursion is the ith $(0, \bar{t} \geqslant \bar{\mathcal{T}})$-excursion. Note that it is extremely unlikely in the low-temperature limit for dynamin to be injected precisely *during* a $(0, \bar{t} \geqslant \bar{\mathcal{T}})$-excursion. We thus neglect this possibility and denote by $\bar{t}_i^w$ the waiting time between the $(i-1)$th and the ith $(0, \bar{t} \geqslant \bar{\mathcal{T}})$-excursion. Since dynamin can be injected at the beginning just as well as in the end of the waiting period, we have to wait a time $\bar{t}_{\mathrm{seed}} = \bar{t}_i^w/2$ on average before excursion i starts. Let us denote by $\mathrm{d}p_w^j(\bar{t})$ the probability that the jth waiting period has a duration $\bar{t}$. The probability that dynamin is injected during a waiting period of duration $\bar{t}'$ such that $\bar{t}' \in [\bar{t}, \bar{t} + \mathrm{d}\bar{t}]$ therefore reads

$$\mathrm{d}Q_w(\bar{t}) = \frac{\bar{t}\mathrm{d}p_w^j(\bar{t})}{\int_0^{+\infty} \bar{t}\mathrm{d}p_w^j(\bar{t})}. \quad (3.39)$$

The average duration of the waiting period during which dynamin is injected is therefore

$$2\bar{t}_{\mathrm{seed}} = \int_0^{+\infty} \bar{t}\mathrm{d}Q_w(\bar{t}) = \frac{\int_0^{+\infty} \bar{t}^2\mathrm{d}p_w^j(\bar{t})}{\int_0^{+\infty} \bar{t}\mathrm{d}p_w^j(\bar{t})} = \frac{\left\langle (\bar{t}^w)^2 \right\rangle_{\bar{t} \geqslant \bar{\mathcal{T}}}}{\langle \bar{t}^w \rangle_{\bar{t} \geqslant \bar{\mathcal{T}}}}. \quad (3.40)$$

Since the process considered here switches back and forth between $(0, \bar{t} \geqslant \bar{\mathcal{T}})$-excursions and waiting periods between two $(0, \bar{t} \geqslant \bar{\mathcal{T}})$-excursions, the number $N_e^{\geqslant \bar{\mathcal{T}}}(0)$ of $(0, \bar{t} \geqslant \bar{\mathcal{T}})$-excursions is equal to the number of waiting periods[2]. Moreover, the total time spent in

[2]The number of $(0, \bar{t} \geqslant \bar{\mathcal{T}})$-excursions can actually equal to the number of waiting periods plus or minus one. In the $\bar{T}_t \to +\infty$ limit, however, this number is very large and one unit does not matter.

waiting periods is equal to

$$\sum_{i=1}^{N_e^{\geqslant \bar{\mathcal{T}}}(0)} \bar{t}_i^w = \bar{T}_t - \sum_{i=1}^{N_e^{\geqslant \bar{\mathcal{T}}}(0)} \bar{t}_i, \tag{3.41}$$

where $\bar{t}_i$ denotes the duration of excursion i. Dividing by $N_e^{\geqslant \bar{\mathcal{T}}}(0)$ and taking the $\bar{T}_t \to +\infty$ limit, we find

$$\langle \bar{t}^w \rangle_{\bar{t} \geqslant \bar{\mathcal{T}}} = \frac{\bar{T}_t}{N_e^{\geqslant \bar{\mathcal{T}}}(0)} - \langle \bar{t}_0 \rangle_{\bar{t} \geqslant \bar{\mathcal{T}}}. \tag{3.42}$$

Now squaring Eq. (3.41), we find

$$\sum_i (\bar{t}_i^w)^2 + 2 \sum_{i<j} \bar{t}_i^w \bar{t}_j^w = \bar{T}_t^2 - 2\bar{T}_t \sum_i \bar{t}_i - \sum_i (\bar{t}_i)^2 - 2 \sum_{i<j} \bar{t}_i \bar{t}_j. \tag{3.43}$$

We divide this expression by $N_e^{\geqslant \bar{\mathcal{T}}}(0)$ and take the $\bar{T}_t \to +\infty$ limit. Using Eq. (3.42) and noting that $\bar{t}_i^w$, $\bar{t}_j^w$, $\bar{t}_i$, $\bar{t}_j$ with $i \neq j$ are independent variables yields:

$$\left\langle (\bar{t}^w)^2 \right\rangle_{\bar{t} \geqslant \bar{\mathcal{T}}} - \left[\langle \bar{t}^w \rangle_{\bar{t} \geqslant \bar{\mathcal{T}}} \right]^2 = \left\langle (\bar{t}_0)^2 \right\rangle_{\bar{t} \geqslant \bar{\mathcal{T}}} - \left[\langle \bar{t}_0 \rangle_{\bar{t} \geqslant \bar{\mathcal{T}}} \right]^2. \tag{3.44}$$

Combining this with Eq. (3.42) yields the seeding time defined in Eq. (3.40):

$$2\bar{t}_{\text{seed}} = \frac{\left\langle (\bar{t}_0)^2 \right\rangle_{\bar{t} \geqslant \bar{\mathcal{T}}} - 2 \frac{\bar{T}_t}{N_e^{\geqslant \bar{\mathcal{T}}}(0)} \langle \bar{t}_0 \rangle_{\bar{t} \geqslant \bar{\mathcal{T}}} + \left(\frac{\bar{T}_t}{N_e^{\geqslant \bar{\mathcal{T}}}(0)} \right)^2}{\frac{\bar{T}_t}{N_e^{\geqslant \bar{\mathcal{T}}}(0)} - \langle \bar{t}_0 \rangle_{\bar{t} \geqslant \bar{\mathcal{T}}}}. \tag{3.45}$$

Combining Eqs. (3.34), (3.37a) and (3.38), we find that

$$\frac{\bar{T}_t}{N_e^{\geqslant \bar{\mathcal{T}}}(0)} = \frac{\sqrt{2\pi} x_0 \exp\left(\frac{x_0^2}{2} \right)}{\operatorname{erfc}\left(\frac{x_0 \sqrt{\bar{\mathcal{T}}}}{2} \right)} \langle \bar{t}_0 \rangle_{\bar{t} \geqslant \bar{\mathcal{T}}}. \tag{3.46}$$

Finally, using Eqs. (3.37), (3.45) and (3.46) we can calculate a full analytical expression for the seeding time. Since the full form of this expression is rather lengthy and not very informative, here we give only its asymptotic behavior:

$$\bar{t}_{\text{seed}} \underset{x_0 \sqrt{\bar{\mathcal{T}}} \ll 1}{\sim} \frac{1}{\sqrt{2\pi} x_0^3} \exp\left(\frac{x_0^2}{2} \right) \tag{3.47a}$$

$$\underset{x_0 \sqrt{\bar{\mathcal{T}}} \gg 1}{\sim} \frac{\pi x_0^2 \bar{\mathcal{T}}^{3/2}}{2\sqrt{2}} \exp\left[\frac{x_0^2}{2} \left(1 + \frac{\bar{\mathcal{T}}}{2} \right) \right]. \tag{3.47b}$$

We return to normal units to discuss these results. In order to define the tubule-wide seeding time, we note that the seeding time calculated above is the seeding time for one section of tubule of length ℓ. If we consider a tubule of length L, the seeding time is inversely proportional to the number of sections of length ℓ comprised in the tubule,

which is equal to L/ℓ. Using the orders of magnitude $\digamma \approx \left(\sqrt{\sigma^3/\kappa}\right)/\eta \simeq 1/(10\,\mathrm{ns})$, $\ell \approx r_b \approx \sqrt{\kappa/\sigma} \simeq 10\,\mathrm{nm}$ and $k \approx \sigma \simeq 10^{-4}\,\mathrm{N.m^{-1}}$, we have the asymptotic regimes

$$t_{\mathrm{seed}} \underset{\frac{\mathcal{T}}{\eta\sqrt{\kappa/\sigma^3}} \ll \frac{k_BT}{\kappa}}{\approx} \frac{\eta(k_BT)^{3/2}}{\kappa^{1/2}\sigma^2 L} \exp\left[\mathrm{coeff} \times \frac{\kappa}{k_BT}\left(\frac{r_b - r_0}{r_b}\right)^2\right] \tag{3.48a}$$

$$\underset{\frac{k_BT}{\kappa} \ll \frac{\mathcal{T}}{\eta\sqrt{\kappa/\sigma^3}}}{\approx} \frac{\kappa^{5/4}\sigma^{1/4}\mathcal{T}^{3/2}}{\eta^{1/2}k_BTL} \times \exp\left[\left(\frac{\mathrm{coeff} \times \kappa}{k_BT} + \frac{\mathrm{coeff}' \times \mathcal{T}\kappa^{1/2}\sigma^{3/2}}{\eta k_BT}\right)\left(\frac{r_b - r_0}{r_b}\right)^2\right], \tag{3.48b}$$

where "coeff" and "coeff′" stand for unknown numerical coefficients of order one. Since those coefficients are in the exponentials, they have a huge influence on the value of t_{seed}. This and the fact that $\mathcal{T}$ is unknown makes it difficult to give an *a priori* estimate the magnitude of the seeding rate, especially in Eq. (3.48b). We however attempt such an estimate in the small-$\mathcal{T}$ regime of Eq. (3.48a): using $r_b - r_0 \approx r_0 \approx r_b$, the argument of the exponential is $\simeq \mathrm{coeff} \times \kappa/k_BT \simeq 15 \times \mathrm{coeff}$. Choosing $\mathrm{coeff} = 1.5$ in this expression, we find $t_{\mathrm{seed}} \simeq$ s, which is compatible with experimental observations.

Eqs. (3.48) contain a simple prediction which could allow to validate the "stiff dynamin, soft membrane" model and discard the "soft dynamin, stiff membrane" model of Sec. 3.3.1. This prediction is that t_{seed} depends on the viscosity η of the medium surrounding the tube. Note that this viscosity is the viscosity *inside* the tubule. It could be controlled experimentally by forming the vesicles in a buffer containing polymers, for instance. This dependence also allows us to experimentally determine which asymptotic regime corresponds to the experiment at hand. Indeed, the seeding time of Eq. (3.48a) increases with increasing η with an experimentally testable power law, while that of Eq. (3.48b) decreases with increasing η with a more complicated exponential dependence.

Let us now discuss the meaning of these two regimes. In the regime of Eq. (3.48a), $\mathcal{T}$ is smaller than the typical time it takes for a particle described by Eq. (3.28) to settle back down after an upward thermal kick of amplitude k_BT. Therefore once the particle reaches x_0, it will typically remain there for a time longer than $\mathcal{T}$. Thus the seeding rate in this regime is limited mostly by the rate at which the particle visits the vicinity of $x = x_0$, and the expression for t_{seed} is proportional to the first-passage time of the particle in x_0. For long times, Eq. (3.48b) applies. In this regime, $\mathcal{T}$ is long, and typical thermal fluctuations above x_0 relax in times shorter than $\mathcal{T}$. Therefore, once the particle has reached x_0, it still needs a thermal fluctuation of extraordinary amplitude to stay there long enough for helix seeding to occur. This is evidenced by the additional, $\mathcal{T}$-dependent exponential factor in Eq. (3.48b).

Since the main dependence on some of the experimentally tunable parameters of Eqs. (3.48) are multiplied by a large number (of order κ/k_BT) within an exponential, verifying these laws experimentally is particularly challenging as small changes in $(r_b - r_0)$, for instance, could lead to huge changes in the seeding rate. This is reminiscent of the behavior observed in Fig. 3.3(a), where the helix seeding rate soars as soon as $(r_b - r_0)$ goes below a certain value.

The dependence of $t_{\rm seed}$ on the dynamin concentration, on the other hand, could be interesting to investigate. For high c, the encircling time $\mathcal{T}$ should vanish, placing the system in the regime of Eq. (3.48a), where $t_{\rm seed}$ does not depend on $\mathcal{T}$. One should therefore use low dynamin concentrations to study the c-dependence of $\mathcal{T}$. Since the function $\mathcal{T}(c)$ is not known, it is difficult to assess whether dynamin seeding is observable on experimentally realistic time scales in this regime. Note however that the fact that the seeding rate strongly depends on c [compare Figs. 3.2(a) and (c) for instance] therefore indicates that the regime Eq. (3.48b) might be relevant experimentally. If this is the case, then the function $\mathcal{T}(c)$ could be determined by fitting the exponential $\mathcal{T}$-dependence of Eq. (3.48b). Another possible situation is one where the low-c regime itself is not accessible experimentally, but where part of the crossover between Eq. (3.48a) and Eq. (3.48b) can be monitored, for instance by monitoring the modification of the η-dependence of $t_{\rm seed}$. In this case, the σ-dependence of the crossover concentration $c_{\rm cross}$ between the two regimes could be measured. It should then be possible to infer the function $\mathcal{T}(c)$ from the relation $\mathcal{T}(c_{\rm cross}) = \frac{\eta k_B T}{\kappa^{1/2}\sigma^{3/2}}$. Several types of functions $\mathcal{T}(c)$ are imaginable, depending on the process by which a dynamin oligomer encircles the tubule. One possibility is that dynamin dimers are added to the oligomer at a constant rate as long as $r < r_0$. Another possibility would be for the oligomer itself to require a seeding stage before it can grow as described, the rate of which would depend nonlinearly on c. Yet another possibility would be an aggregation process similar to that of Sec. 3.3.1. In any case, it is likely that although challenging, a measurement of the function $\mathcal{T}(c)$ would yield interesting information about the early stages of dynamin assembly.

3.4 Growth kinetics

Following the above discussion of the dynamin polymer, a simple picture of how its growth naturally comes to our mind: new dynamin helices appear either at a constant rate per unit length of bare tubule as in Eqs. (3.21) or (3.48), or at a rate increasing with time, as in the limit used in Eq. (3.20) (in this limit, the number of seeds goes as $N_{n^*} \propto L t^{n^*-1}$). Following this seeding stage, a constant number of dynamin dimers per unit time assembles on each helix extremity. When the helix becomes mechanically continuous, the force exerted by the tube on the bead drops, and polymerization stops when it reaches the value imposed by thermodynamics (Sec. 3.2).

Although this scenario accounts for many experiments quite well, deviations from it are sometimes observed, as described in Sec. 3.4.1. Here we open the way for a more systematic study of these effects, which could yield interesting information about the dynamin-membrane interactions, by analyzing two complementary effects likely to account for at least some of these observations. We name these effects the "antenna" and "bulge" hypotheses and present them in Secs. 3.4.2 and 3.4.3. In Sec. 3.4.4, we discuss the experimental perspectives for the validation of these mechanisms and what information could be extracted from them.

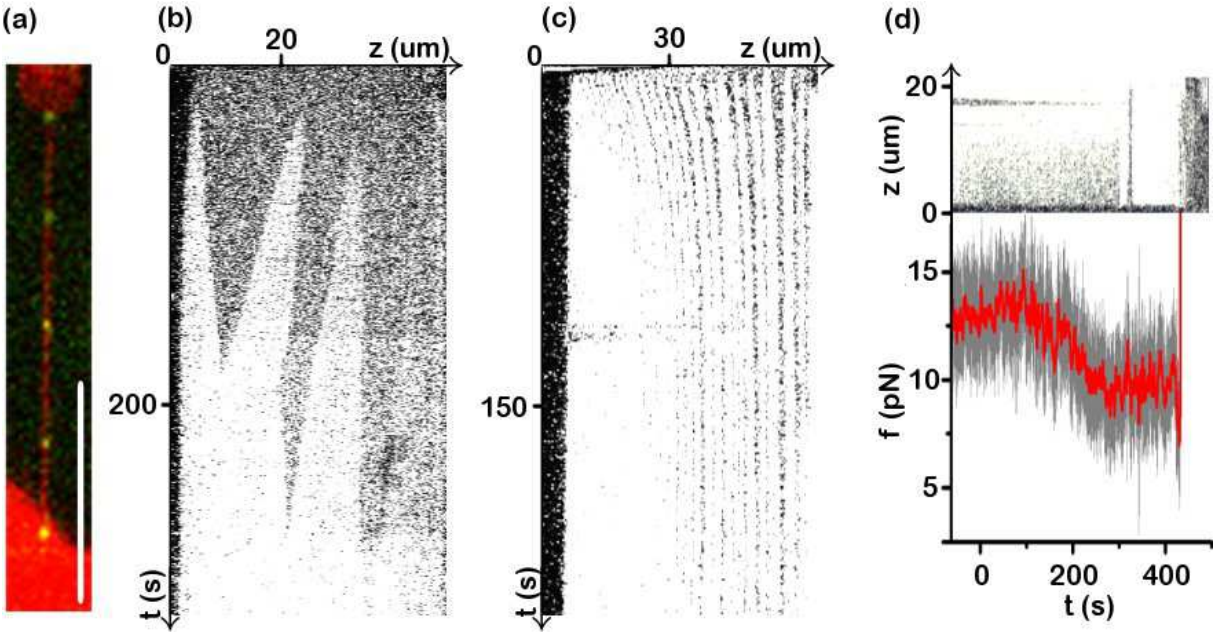

Figure 3.5: Anomalous growth effects in $c = 440\,\mathrm{nM}$ experiments. At this dynamin concentration, growth happens over several minutes. (a) Spatial organization of dynamin seeds. Bar, $10\,\mu\mathrm{m}$. (b) Fast drop in the seeding rate. (c) Early slowing down of polymerization. (d) Force drop at partial coverage.

3.4.1 Anomalous growth effects

The growth process of dynamin can deviate from the scenario sketched above in several ways, which we present here and in Fig. 3.5 (the labeling of the subfigures parallels that of the following items). The parameter regimes in which each of these anomalous growth effects show up are ill-identified as yet. By proposing interpretations for their causes, we hope to guide possible investigations on these matters.

(a) In this micrograph, taken just after the radius was ramped down as in Fig. 3.3(a), the dynamin seeds seem to organize in a periodic array. Such well-defined patterns are not very reproducible, but there often seems to be a characteristic separation length scale between dynamin seeds.

(b) This so-called kymograph represents the integrated fluorescence across the tubule (z coordinate) as a function of time (t). In these coordinates, growing dynamin domains appear as triangles, meaning that they grow with a constant velocity. The tip of the triangles represent seeding events. Three seeding events occur right after dynamin injection, then only growth is observed. This is in conflict with our picture of a constant or increasing seeding rate per unit bare tubule length.

(c) Unlike in the previous kymograph, here helix growth does not proceed at constant velocity but slows down when full coverage of the tubule is approached.

(d) Simultaneous inspection of the force curve presented in Fig. 3.2(b) and the corresponding kymograph reveals that the force starts dropping not when dynamin fully covers the tubule, but slightly earlier.

Each of the two hypotheses presented in the following accounts for three out of those four effects. Depending on the experimental regime, either none, one or both of them can be relevant to the analysis of the experimental data.

3.4.2 Antenna hypothesis

In the model presented here, we take into account the known affinity of unpolymerized dynamin for the membrane [23] and consider the possibility that in order to assemble into a helix, dynamin coming from the solution first has to adsorb on the bare membrane tubule, then diffuse to the extremity of a neighboring helix. This means that we do not consider direct exchange of dynamin between the helix and the solution, although such transitions are possible in principle and could be included in a more elaborate model. In this interpretation, the anomalous growth effects arise from the fact that the helix is not in direct contact with a dynamin reservoir at constant concentration, but with a finite pool of membrane-bound dynamin dimers, which might be depleted by the growth of the helix. This depletion might slow the seeding and growth of dynamin down. Continuing our analogy with first-order phase transitions, this is comparable to the fact that in the absence of a liquid phase, water vapor can exist at a higher pressure than at the coexistence with the liquid (the vapor is then said to be supersaturated). As soon as the liquid phase nucleates, the vapor phase is "depleted" and its pressure drops to the coexistence pressure.

3.4.2.1 Dynamin adsorbed on a bare tubule

Here we consider the bare membrane interval between two sections of helix [Fig. 3.6(a)]. Because we expect the diffusion coefficient of a membrane-bound protein ($\simeq 10^{-13}\,\mathrm{m}^2.\mathrm{s}^{-1}$ [49]) to be much smaller than that of a protein in solution ($\simeq 5\times10^{-11}\,\mathrm{m}^2.\mathrm{s}^{-1}$), we consider the bulk diffusion to be very fast and therefore treat the concentration c of the solution as homogenous. Let us postulate that the polymer growth is much slower than the typical time scale characterizing the exchanges between the solution and the bare sections of the tubule, an assumption that we justify at the end of this section. On the polymer growth time scale, the mass of adsorbed dynamin per unit tubule length ρ satisfies the steady-state equation:

$$\partial_t \rho = 0 = D\partial_z^2 \rho + l_{\mathrm{on}} c - l_{\mathrm{off}} \rho, \tag{3.49}$$

where D is the diffusion coefficient of the protein on the tubule and the reaction rates are defined in Fig. 3.6(a). Imposing that the function $\rho(z)$ is even, we only need to specify the boundary condition at the interface $z = d/2$ with the helix, from which the boundary condition in $z = -d/2$ follows. The dynamin current from the tubule to the helix reads:

$$J(d/2) = -D\partial_z \rho(d/2) = k_{\mathrm{on}} \rho(d/2) - k_{\mathrm{off}}, \tag{3.50}$$

where J denotes the protein current and k_{on}, k_{off} are defined in Fig. 3.6(a). We introduce the dimensionless variables:

$$\tilde{\rho} = \frac{l_{\text{off}}\rho}{l_{\text{on}}c}, \quad \tilde{z} = \frac{z}{\sqrt{D/l_{\text{off}}}}, \quad \tilde{k}_{\text{on}} = \frac{k_{\text{on}}}{\sqrt{Dl_{\text{off}}}}, \quad \tilde{k}_{\text{off}} = \frac{k_{\text{off}}}{l_{\text{on}}c}\sqrt{\frac{l_{\text{off}}}{D}}, \quad \tilde{J} = \frac{J}{l_{\text{on}}c}\sqrt{\frac{l_{\text{off}}}{D}}. \quad (3.51)$$

Here the density unit $l_{\text{on}}c/l_{\text{off}}$ is the equilibrium dynamin density on a bare tubule in contact with the solution only. The actual dynamin concentration on the tubule is actually lower than this value because the helix grows ($\tilde{k}_{\text{on}} > \tilde{k}_{\text{off}}$) and therefore depletes the tubule of dynamin over a characteristic distance equal to the unit length $\sqrt{D/l_{\text{off}}}$. Beyond this distance, the effect of the helix is screened by exchanges of dynamin with the solution, and therefore the tubule does not "see" the helix. In the following, we derive these qualitative features more rigorously. Eqs. (3.49) and (3.50) now read:

$$\partial_{\tilde{z}}^2\tilde{\rho} - \tilde{\rho} - 1 = 0, \quad -\partial_{\tilde{z}}\tilde{\rho}\left(\tilde{d}/2\right) = \tilde{k}_{\text{on}}\tilde{\rho}\left(\tilde{d}/2\right) - \tilde{k}_{\text{off}}. \quad (3.52)$$

The solution reads:

$$\tilde{\rho} = 1 - \frac{\left(\tilde{k}_{\text{on}} - \tilde{k}_{\text{off}}\right)\cosh(\tilde{z})}{\tilde{k}_{\text{on}}\cosh\left(\tilde{d}/2\right) + \sinh\left(\tilde{d}/2\right)} \Rightarrow \tilde{J}\left(\tilde{d}/2\right) = \frac{\tilde{k}_{\text{on}} - \tilde{k}_{\text{off}}}{1 + \tilde{k}_{\text{on}}\coth\left(\tilde{d}/2\right)}. \quad (3.53)$$

Let us consider two limiting cases for these expressions:

1. Case $\tilde{d} \gg 1$ *i.e.* the bare tubule section is large enough (or the diffusion slow enough) for most of the tubule to not "see" the helix. The dynamin concentration is equal to one almost everywhere and quickly falls to $\left(1 + \tilde{k}_{\text{off}}\right) / \left(1 + \tilde{k}_{\text{on}}\right)$ near the helix:
$$\tilde{\rho} = 1 - \frac{\tilde{k}_{\text{on}} - \tilde{k}_{\text{off}}}{1 + \tilde{k}_{\text{on}}}\exp\left[-\left(\tilde{d}/2 - \tilde{z}\right)\right] \quad (\text{for } \tilde{z} > 0)\,. \quad (3.54)$$

2. Case $\tilde{d} \ll 1$ *i.e.* The bare tubule is so short (diffusion is so fast) that the dynamin concentration is homogeneous:
$$\tilde{\rho} = \frac{2\tilde{k}_{\text{off}} + \tilde{d}}{2\tilde{k}_{\text{on}} + \tilde{d}}, \quad (3.55)$$
meaning that the whole tubule "sees" the helix.

3.4.2.2 Helix growth

Having calculated the profile of the adsorbed dynamin dimers on the tube, we are able to calculate the rate at which they join the helix. In other words, we can now calculate the helix growth rate, and predict the dynamics of the experimentally observable variable $d(t)$. The helix growth velocity is proportional to its dynamin intake rate, which is itself equal to the current from the bare tubule to the polymer:

$$\frac{\mathrm{d}}{\mathrm{d}t}\left(\rho_h d/2\right) = -J(d/2), \quad (3.56)$$

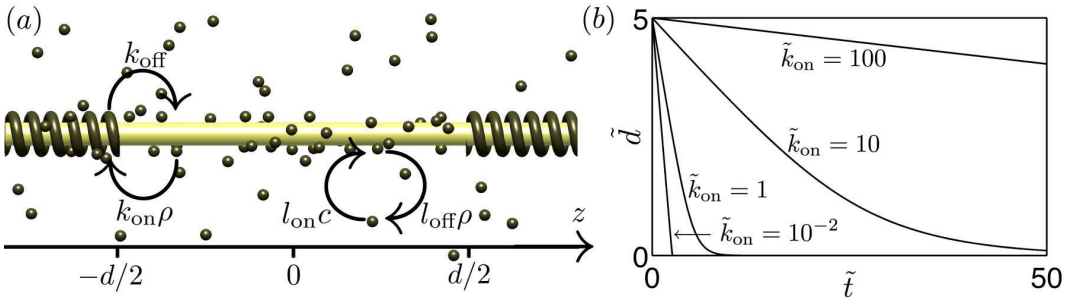

Figure 3.6: Model for the antenna hypothesis. (a) Definition of the reaction rates: dynamin adsorbs on the tubule with a rate $l_{\rm on}c$ per unit tubule length and detaches with $l_{\rm off}\rho$, where ρ is the density of dynamin adsorbed on the tubule. Exchanges with the helix happen only at its extremities $z = \pm d/2$, and the rates for polymerization and depolymerization are $k_{\rm on}\rho(\pm d/2)$ and $k_{\rm off}$, respectively. (b) Growth curves for dynamin helices with $k_{\rm off} = 0$ (consistent with the observation that dynamin hardly depolymerizes over a few minutes even when the dynamin solution is washed away) as a function of $\tilde{k}_{\rm on}$ and starting from a gap of width $\tilde{d} = 5$ between the two helices. For longer tubules, growth proceeds at constant velocity: see Eqs. (3.60a) and (3.60b).

where ρ_h denotes the density of the helix. Let us scale time by the typical helix growth time:

$$\tilde{t} = \left(\frac{k_{\rm on} l_{\rm on} c}{\sqrt{D l_{\rm off}}} - \frac{k_{\rm off}\sqrt{l_{\rm off}}}{\sqrt{D}} \right) \frac{t}{\rho_h} = \frac{\tilde{k}_{\rm on} - \tilde{k}_{\rm off}}{\tilde{\rho}_h} l_{\rm off} t. \tag{3.57}$$

Using Eq. (3.53), this yields the following helix growth equation:

$$\frac{{\rm d}\tilde{d}}{{\rm d}\tilde{t}} = \frac{-2}{1 + \tilde{k}_{\rm on} \coth\left(\tilde{d}/2\right)}, \tag{3.58}$$

which yields

$$\tilde{d}/2 + \tilde{k}_{\rm on} \ln\left[\sinh\left(\tilde{d}/2\right)\right] = {\rm constant} - \tilde{t}. \tag{3.59}$$

This solution is plotted in Fig. 3.6(b). Eq. (3.59) simplifies in the following limiting cases:

$$\tilde{d} \underset{\tilde{k}_{\rm on} \ll 1}{\sim} \tilde{d}\left(\tilde{t} = 0\right) - 2\tilde{t} \tag{3.60a}$$

$$\underset{\substack{\tilde{k}_{\rm on} \gg 1 \\ \tilde{d} \gg 1}}{\sim} \tilde{d}\left(\tilde{t} = 0\right) - \frac{2\tilde{t}}{\tilde{k}_{\rm on}} \tag{3.60b}$$

$$\underset{\substack{\tilde{k}_{\rm on} \gg 1 \\ \tilde{d} \ll 1}}{\sim} 2\sinh\left[\frac{\tilde{d}\left(\tilde{t} = 0\right)}{2}\right] e^{-\tilde{t}/\tilde{k}_{\rm on}}. \tag{3.60c}$$

Qualitatively, in the regime of Eq. (3.60a), chemical equilibrium is always established between the bare tubule and the solution and $\tilde{\rho} = 1$ everywhere [see Eqs. (3.54) and (3.55)

considering $0 \leqslant \tilde{k}_{\text{off}} < \tilde{k}_{\text{on}} \ll 1$]. Therefore the polymerization of dynamin from the bare tubule to the helix is the rate-limiting factor, and proceeds at a constant rate $k_{\text{on}} \frac{l_{\text{on}} c}{l_{\text{off}}} - k_{\text{off}}$, which yields a dimensionless polymerization velocity equal to one [see Eqs. (3.51) and(3.57)]. The factor two in front of $\tilde{t}$ in Eq. (3.60a) is due to the fact that there are two polymerizing helices [one on the left and one on the right: see Fig. 3.6(a)]. This regime is illustrated by the $\tilde{k}_{\text{on}} = 10^{-2}$ curve in Fig. 3.6(b). In the regime of Eq. (3.60b), polymerization is fast ($\tilde{k}_{\text{on}} \gg 1$) and the bare tubule is long ($\tilde{d} \gg 1$). Thus the tubule "sees" the helix only up to a distance ≈ 1 from it, and a large fraction of the dynamin binding in this region of the tubule is funneled to the helix, hence feeding its growth. Therefore each helix grows at a constant velocity, since the size of the region from which dynamin is recruited does not depend on $\tilde{d}$ as long as $\tilde{d} \gg 1$. This regime is illustrated by the $\tilde{d} \gg 1$ part of the $\tilde{k}_{\text{on}} = 10$ curve in Fig. 3.6(b). When $\tilde{k}_{\text{on}} \gg 1$ and $\tilde{d}$ is smaller than one, the system is in the regime of Eq. (3.60c). In this regime the bare tubule is short enough for all of it to see the helices. Therefore a large fraction of the dynamin adsorbing on it ends up polymerizing, and the dynamin intake of the helices is proportional to the length of the tubule. Therefore the rate of shrinkage of the tubule is proportional to its length, meaning that this length decays exponentially as in Eq. (3.60c). This regime is illustrated by the $\tilde{d} \ll 1$ part of the $\tilde{k}_{\text{on}} = 10$ curve in Fig. 3.6(b).

From Eqs. (3.60), it is apparent that helix growth happens on time scales of order (in normal units):

$$\frac{\tilde{\rho}_h \times \max\left(1, \tilde{k}_{\text{on}}\right)}{\left(\tilde{k}_{\text{on}} - \tilde{k}_{\text{off}}\right) l_{\text{off}}} \gtrsim \frac{\tilde{\rho}_h}{l_{\text{off}}}. \tag{3.61}$$

We can now justify our assumption that the growth time scale is much larger than the time scale l_{off}^{-1} over which the bare membrane equilibrates with the dynamin solution. Indeed, experimentally, the fluorescence intensity of dynamin adsorbed on the bare tubule is much weaker than that of polymerized dynamin [see Fig. 3.1(b), for instance]. Therefore, the density of the dynamin helix is much larger than the typical density of adsorbed dynamin. This can be expressed as $\tilde{\rho}_h \gg 1$, from which the validity of our assumption follows.

3.4.2.3 Relation to anomalous growth

The antenna hypothesis might account for three out of four anomalous growth effects presented in Sec. 3.4.1:

(a) The consumption of dynamin by the growth of the helix creates a local depletion of dynamin over a length $\sqrt{D/l_{\text{off}}}$, as visible in Eq. (3.54). Since the seeding rate of dynamin is likely to depend on the local dynamin concentration, this might account for the fact that dynamin seeds seem never to appear in the vicinity of another helix.

(b) In situations where the spacing between dynamin helices is smaller than the screening length $\sqrt{D/l_{\text{off}}}$, the appearance of dynamin helices on the tubule induces a drop in the adsorbed dynamin concentration from $\tilde{\rho} = 1$ to a lower value [Eq. (3.55)—see also the supersaturated vapor discussion at the beginning of this section]. This hinders the seeding of other dynamin helices.

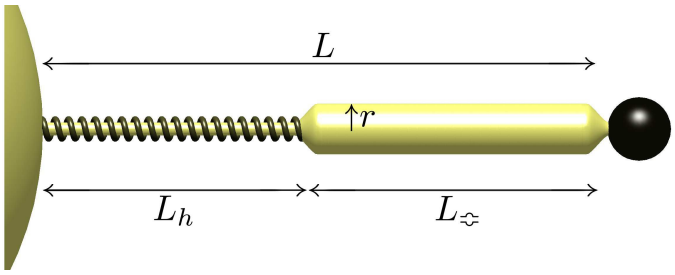

Figure 3.7: Cylindrical membrane bulge isolated from the vesicle by a single helix. In order for the radius of the bulge to relax to r_b, membrane and water have to flow through the helix, which might take a long time.

(c) If an adsorbed dynamin dimer in the vicinity of a helix has a higher chance of polymerizing than of detaching from the tubule (*i.e.* if $\tilde{k}_{\text{on}} \gtrsim 1$), then the growth rate of the helix slows down as the length of bare tubule shrinks [Eq. (3.60c)]. This is due to an antenna effect: polymerization is limited by dynamin intake from the solution, which is itself dependent on the length of bare tubule in contact with the solution. As this length shortens, the growth rate should diminish.

3.4.3 Bulge hypothesis

In this second hypothesis, dynamin polymerizes on a membrane substrate with an initial radius $r_b > r_0$. As the helix grows, the tubule is squeezed down to a radius r_0, and therefore some excess membrane and water accumulate in the bare sections of the tubule. This creates membrane bulges similar to the one depicted in Fig. 3.7, which are isolated from the membrane by the helix. Since the radius of this bulge is larger than prescribed by the equilibrium equation Eq. (3.3), it tends to flatten out and to flow into the vesicle. In this section, we study the bulge relaxation dynamics and show that these effects tend to make the tubule force drop and can be the rate-limiting step of dynamin polymerization.

Let us denote $\varphi = f_h/f_b$ and restrict ourselves to $0 < \varphi < 1$, which is equivalent to being in the "tether polymerization" region of Fig. 3.3(b). In order to keep the following study simple, we restrict our discussion to cylindrical membrane bulges, which we show to be rigorously valid if $\varphi \geqslant \sqrt{3}/2$. We denote the free energy of the bulge by

$$F_{\diamond} = -fL_{\diamond} + \sigma_{\diamond}A_{\diamond} - (P_{\diamond} - P_c)V_{\diamond} + F_{\diamond}^{\text{bending}}, \tag{3.62}$$

where $\sigma_{\diamond}$, $P_{\diamond}$, $L_{\diamond}$, $A_{\diamond}$, $V_{\diamond}$ and $F_{\diamond}^{\text{bending}}$ are the bulge's membrane tension, internal pressure, length, area, volume and bending free energy respectively. Let us define the dimensionless pressure $\Pi = \frac{(P_{\diamond}-P_c)\sqrt{\kappa}}{2\sigma^{3/2}}$ and tension $\varsigma = \sigma_{\diamond}/\sigma$, where $\sigma > 0$ is the tension of the

vesicle. In Appendix A, we prove that the bulge remains cylindrical as long as

$$\begin{aligned} &\varsigma \geqslant 0 \qquad \text{and} \qquad \frac{\Pi}{\varsigma^{3/2}} \leqslant \left(\frac{2}{3}\right)^{3/2} \\ \text{or} \\ &\varsigma < 0 \qquad \text{and} \qquad \frac{\Pi}{(-\varsigma)^{3/2}} \leqslant -2\left(\frac{2}{3}\right)^{3/2}. \end{aligned} \tag{3.63}$$

Qualitatively, the first condition states that if the bulge's tension is positive, then it stabilizes the cylindrical bulge as long as its internal pressure is below a certain threshold. The second condition deals with $\varsigma < 0$ and reveals that a cylindrical bulge can exist even in this case, provided that the pressure inside it is negative enough to compensate for the destabilizing effect of the negative tension. The cylindrical shape imposes

$$A_{\diamond} = 2\pi L_{\diamond} r_b \varrho \tag{3.64a}$$

$$V_{\diamond} = \pi L_{\diamond} r_b^2 \varrho^2 \tag{3.64b}$$

$$F_{\diamond}^{\text{bending}} = \frac{\pi\kappa L_{\diamond}}{r_b}\varrho^{-1}, \tag{3.64c}$$

where $\varrho = r/r_b$ is the scaled bulge radius.

The first dissipative phenomenon at work during bulge relaxation is related to membrane exchanges between the bulge and the vesicle. When these occur, membrane flows through the helix, and energy is dissipated through an effective friction between helix and membrane. In order to calculate an order of magnitude for the corresponding friction coefficient, we propose an oversimplified mechanism inspired by Ref. [23], where it is shown that dynamin inserts into the outer leaflet of the membrane bilayer. In this naive model, we assume that the outer membrane monolayer is attached to the helix and that the energy dissipation comes from the sliding of one monolayer against the other. Experimentally, one measures typical friction coefficients for the relative sliding of lipid monolayers of order $\beta = 10^8\,\mathrm{Pa/(m.s^{-1})}$ [50]. In the following, we show that the time scale associated with this helix-membrane friction is

$$t_m = \frac{\beta L^2 r_b^2}{\kappa \varrho_0} \times \frac{1}{\varphi(1-\varphi^2)} \simeq 3 \times 10^3\,\mathrm{s}, \tag{3.65}$$

where we used $\varrho_0 = r_0/r_b \simeq 0.3$, $L \simeq 10\,\mu\mathrm{m}$ and $\varphi \simeq 0.9$. This order of magnitude is typical of our experiments, which typically happen over tens of minutes. Finally, we define ζ_m, the displacement of the membrane contained inside the helix relative to the dynamin in units of L. Alternatively, ζ_m can be seen as the area of bulge membrane transferred to the vesicle in units of $2\pi L r_0$.

The second dissipative phenomenon is related to water exchange between the inside of the bulge and the vesicle. As shown below, the time scale associated to the Poiseuille flow inside the helix reads

$$t_w = \frac{\eta L^2 r_b}{\kappa \varrho_0^4} \times \frac{32\left[\left(2\varphi - \sqrt{4\varphi^2-3}\right)^5 - \varrho_0\left(2\varphi - \sqrt{4\varphi^2-3}\right)^3\right]}{4\varphi\left(2\varphi - \sqrt{4\varphi^2-3}\right) - 4} \simeq 10^3\,\mathrm{s}, \tag{3.66}$$

where $\eta \simeq 10^{-1}$ Pa.s is the viscosity of water and where the same numerical values as above were used. We define ζ_w, the displacement of the water inside the helix relative to the membrane in units of L. If the membrane is motionless, ζ_w is the volume of water transferred from the inside of the bulge to the vesicle in units of $\pi L r_0^2$. Note that t_w strongly depends on the helix radius ϱ_0.

Membrane and water drainage are of comparable importance ($t_m \simeq t_w$) for the experimentally accessible $\varrho_0 \simeq 0.15$. Because of this, we cannot neglect one mechanism in front of the other, and we discuss both in the following.

On top of the time scales defined in Eqs. (3.65) and (3.66), the dynamics of the system depends on the time scale t_g over which dynamin growth occurs in the absence of membrane bulges. This is typically the type of time scale that we studied in Sec. 3.4.2 in the frame of the antenna hypothesis, or that would come about in a simpler model where dynamin assembles directly from the solution onto the helix. In both cases, t_g is proportional both to L—and so should be much smaller than t_m and t_w for very long tubules—and to c—which makes it experimentally tunable independently of t_m and t_w. We denote the fraction of the tubule covered by the helix by $\zeta_g = L_h/L$. As dynamin grows, it takes membrane and water away from the bulge to form the tube of radius r_0 encircled by the helix. Taking this into account along with the membrane and water flows discussed above (parametrized by ζ_m and ζ_w), we express the conservation of length, area and volume in our system as

$$L_{\circ} = L(1-\zeta_g), \tag{3.67a}$$
$$A_{\circ} = 2\pi L r_b \left[1-\varrho_0(\zeta_g+\zeta_m)\right], \tag{3.67b}$$
$$V_{\circ} = \pi L r_b^2 \left[1-\varrho_0^2(\zeta_g+\zeta_m+\zeta_w)\right]. \tag{3.67c}$$

In Sec. 3.4.3.1, we briefly discuss the case where the bulge-related flows are not relevant for the dynamics. We then turn to more interesting regimes and analyze the two dissipative effects introduced above, separately in Secs. 3.4.3.2 and 3.4.3.3, and then simultaneously in Sec. 3.4.3.4.

3.4.3.1 Case $t_w, t_m \ll t_g$

In the case of rapid membrane and water exchanges, the bulge is always at equilibrium with the vesicle and is therefore well described by Eq. (3.3). The helix therefore "sees" the same bulge of radius r_b throughout its growth. The bulge exerts a constant pulling force f_b on the dynamin-coated part of the tubule, hence the growth of the helix proceeds at constant velocity until the bulge is small enough for it to interact with the bead. When this happens, dynamin growth tends to push the bead away from its initial position in the optical tweezer, which decreases the pulling force felt by the dynamin-coated portion of the tubule. In order to fully describe the dynamics of the tubule in this regime, we would need to introduce a relationship between the force exerted on the polymer and its polymerization velocity. This problem has been extensively studied in the case of actin and microtubules [51, 52, 53, 54, 55, 56]. Here we are not concerned with the details of this process, but only state that dynamin polymerization slows down as the pulling force is reduced, and eventually stalls for $f = f_h$, by definition of f_h (Sec. 3.2.2).

3.4.3.2 Case $t_w \ll t_g \ll t_m$

Here we consider the case where water exchanges between the bulge and the vesicle are instantaneous throughout the growth process. Because of this, the pressure $P_{\wasytherefore}$ inside the bulge is always equal to the pressure P_v inside the vesicle. In the limit where the bare tubule radius is much smaller than that of the vesicle, we can use the approximation $P_v = P_c$ when studying the bulge [see Eq. (3.1)]. We therefore set $P_{\wasytherefore} - P_c = 0$. Since for a membrane tubule without pressure the tension is given by $\sigma_{\wasytherefore} = \kappa/2r^2 > 0$ [see Eq. (3.3)], the criterion Eq. (3.63) is always satisfied under these conditions. On time scales of order t_g or shorter, the helix grows without any membrane exchange between the bulge and the vesicle ($\zeta_m = 0$). Minimization of $F_{\wasytherefore}$ with respect to ϱ using these constraints and Eqs. (3.64) and (3.67) yields

$$\varrho = \frac{1 - \varrho_0 \zeta_g}{1 - \zeta_g} \quad \text{and} \quad \frac{f}{f_b} = \frac{1 - \zeta_g}{1 - \varrho_0 \zeta_g}. \tag{3.68}$$

In this equation, f/f_b is a decreasing function of ζ_g. The helix therefore grows (ζ_g increases) until the force reaches f_h. The growth then stalls. The stall state is characterized by

$$\varrho = \varrho^m = \frac{1}{\varphi} \quad \text{and} \quad \zeta_g = \zeta_g^m = \frac{1 - \varphi}{1 - \varrho_0 \varphi}, \tag{3.69}$$

which defines ϱ^m and ζ_g^m.

After this rapid bulge rearrangement stage, the membrane starts to flow on time scales $t \approx t_m$. The dynamics then proceeds quasi-statically at $f = f_h$, and therefore at constant $\varrho = 1/\varphi$. Let us consider the mechanics of the membrane inside the helix. Applying force balance to a cylindrical membrane element, we find that

$$\frac{\mathrm{d}\sigma}{\mathrm{d}z}(z) = -\sigma_{w\to m} - \sigma_{h\to m}, \tag{3.70}$$

where $\sigma(z)$ is the position-dependent tension of the membrane, and $\sigma_{w\to m}$ and $\sigma_{h\to m}$ are the stresses (forces per unit surface) exerted on the membrane by the water and the helix, respectively. Since we neglect the dissipation due to the water here, we consider that $\sigma_{w\to m} = 0$. On the other hand, the definition of β implies

$$\frac{\sigma_{h\to m}}{\beta} = -L\frac{\mathrm{d}\zeta_m}{\mathrm{d}t}, \tag{3.71}$$

where the right-hand side is the velocity of the membrane flow inside the helix relative to the dynamin. We now impose that $\sigma(z)$ matches the tension of the vesicle in $z = 0$ and that of the bulge in $z = L_h$. Combining the above equations with Eqs. (3.67a) and (3.67b) as well as $\varrho = 1/\varphi$, we find

$$t_m \frac{\mathrm{d}\zeta_g}{\mathrm{d}t} = \frac{1}{2\zeta_g} \quad \Rightarrow \quad \zeta_g = \sqrt{\left(\zeta_g^m\right)^2 + \frac{t}{t_m}}, \tag{3.72}$$

where the time of order t_g needed to reach stall is much smaller than t_m and is therefore neglected in this expression.

3.4.3.3 Case $t_m \ll t_g \ll t_w$

Now we study the case where membrane flow is very fast, which imposes that the tension in the vesicle and bulge are the same ($\varsigma = 1$). On short time scales ($t \lesssim t_g$), there is no flow of water relative to the membrane ($\zeta_w = 0$). Minimizing $F_{\Subset}$ with respect to ϱ using this and Eqs. (3.64) and (3.67), we get

$$\varrho = \frac{\varrho_0}{2} + \sqrt{\left(\frac{\varrho_0}{2}\right)^2 + \frac{1-\varrho_0}{1-\zeta_g}}, \quad \Pi = \frac{\sqrt{2}}{\varrho} - \frac{\sqrt{2}}{\varrho^2} \quad \text{and} \quad \frac{f}{f_b} = \frac{\varrho}{4} + \frac{3}{4\varrho}. \tag{3.73}$$

According to this expression, the cylinder radius is initially given by $\varrho(\zeta_g = 0) = 1$ and then increases as the helix grows (as ζ_g increases). As long as $\varrho \leqslant \sqrt{3}$, f/f_b decreases with ϱ, and Π increases. If $\varphi \geqslant \sqrt{3}/2$, growth stalls before ϱ reaches $\sqrt{3}$, and the stall state of the system is characterized by

$$\varrho = \varrho^w = 2\varphi - \sqrt{4\varphi^2 - 3} \quad \text{and} \quad \zeta_g = \zeta_g^w = 1 - \frac{1-\varrho_0}{(4\varphi - \varrho_0)\left(2\varphi - \sqrt{4\varphi^2-3}\right) - 3}, \tag{3.74}$$

which defines ϱ^w and ζ_g^w. If, on the other hand, $\varphi < \sqrt{3}/2$, ϱ becomes larger than $\sqrt{3}$, which implies that Π increases above the threshold defined by Eq. (3.63) (note that $\varsigma = 1$) The cylinder then loses stability. In the remainder of this section, we only consider cases where $\varphi \geqslant \sqrt{3}/2$.

We now consider the post-stall dynamics of the tubule ($t \approx t_w$), which happens at constant $f = f_h$ and $\varrho = \varrho^w$. Let $P(z)$ be the position-dependent pressure of water inside the helix. Applying force balance to a slice of water encircled by dynamin, we find

$$\frac{\mathrm{d}P}{\mathrm{d}z}(z) = \frac{2}{r_0}\sigma_{m\to w}, \quad \text{where} \quad \sigma_{m\to w} = \frac{4\eta}{r_0} L \frac{\mathrm{d}\zeta_w}{\mathrm{d}t} \tag{3.75}$$

is the stress exerted by the membrane on the water and is given by the requirement that the pressure drop $P(L_h) - P(0) = P_{\Subset} - P_v$ throughout the dynamin-coated tube satisfies the Hagen-Poiseuille equation. Using dimensionless units, the evolution of the system is given by

$$t_w \frac{\mathrm{d}\zeta_g}{\mathrm{d}t} = \frac{1}{2\zeta_g} \quad \Rightarrow \quad \zeta_g = \sqrt{\left(\zeta_g^w\right)^2 + \frac{t}{t_w}}. \tag{3.76}$$

This expression and Eq. (3.72) are of a form known as Washburn's equation [57]. This structural similarity is due to the fact that in both cases, a fluid (membrane or water) is pushed with a constant force (related to the stalled radius ϱ_m or ϱ_w of the bulge) through a capillary (the helix) that grows linearly with the amount of fluid evacuated (since the helix lengthens by the same amount by which the bulge shortens).

3.4.3.4 Case $t_g \ll t_w, t_m$

If both dissipation time scales are relevant for the relaxation of the bulge, then the initial helix growth phase ($t \lesssim t_g$) implicates neither membrane nor water exchanges with the vesicle ($\zeta_m = \zeta_w = 0$). Inserting these constraints into Eqs. (3.64) and (3.67), we find

that unless the uninteresting $\varrho_0 = 1$ case is considered, they imply $\zeta_g = 0$. This means that the helix growth stalls immediately. As in the previous sections, however, the stall of the helix implies a decrease in bulge membrane tension and an increase in bulge pressure. Using Eqs. (3.64), we minimize $F_{\Diamond}$ with respect to ϱ under the stall condition $f = f_h$, which yields equations for ς and Π that remain valid throughout the dynamics of the bulge:

$$\varsigma = \frac{4\varphi}{\varrho} - \frac{3}{\varrho^2} \quad \text{and} \quad \Pi = \frac{4\sqrt{2}\varphi}{\varrho^2} - \frac{4\sqrt{2}}{\varrho^3}. \tag{3.77}$$

These equations are easily shown to imply that the condition Eq. (3.63) is satisfied for all positive ϱs. Therefore the bulge remains cylindrical until its length becomes comparable to its radius.

Now turning to the stalled dynamics, we find the bulge evolution equations by combining Eqs. (3.70), (3.71) and (3.75) with the condition $\sigma_{w\to m} = -\sigma_{m\to w}$:

$$\frac{4\sqrt{2}\beta L^2 r_b^2}{\kappa}\frac{\mathrm{d}\zeta_m}{\mathrm{d}t} = \frac{\varrho_0\Pi - 2\sqrt{2}\varsigma}{\zeta_g}, \tag{3.78a}$$

$$\frac{16\sqrt{2}\eta L^2 r_b}{\kappa\varrho_0^2}\frac{\mathrm{d}\zeta_w}{\mathrm{d}t} = \frac{\Pi}{\zeta_g}. \tag{3.78b}$$

Using the stall condition $f = f_h$ as well as Eqs. (3.64) and (3.67) and minimizing $F_{\Diamond}$ with respect to ϱ yields expressions for ζ_m, ζ_w, ς and Π as functions of ϱ and ζ_g. This leads to the bulge relaxation equations:

$$t_m\frac{\mathrm{d}\varrho}{\mathrm{d}t} = \frac{4\mu^{-1}\varrho_0^4(1-\varphi\varrho) + \varphi\varrho\left[\varrho^3 - 4\varphi\varrho^2 + (3+2\varphi\varrho_0)\varrho - 2\varrho_0\right]}{\varphi(1-\varphi^2)\varrho^3(\varrho-\varrho_0)\zeta_g(1-\zeta_g)} \tag{3.79a}$$

$$t_m\frac{\mathrm{d}\zeta_g}{\mathrm{d}t} = \frac{\mu\varrho^6\zeta_g^2 + 4\varrho_0(1-\varphi\varrho)(2\varrho-\varrho_0)\left[\varrho^3 - 4\varphi\varrho^2 + (3+2\varphi\varrho_0)\varrho - 2\varrho_0\right]}{4\varphi(1-\varphi^2)\varrho^3(1-\varphi\varrho)(\varrho-\varrho_0)^2\zeta_g}, \tag{3.79b}$$

where $\mu = \eta/(\beta r_b) \propto t_w/t_m$. The dynamics described by Eqs. (3.79) is illustrated in Fig. 3.8. It seems rather clear on this figure that the radius saturates at some φ-dependent value. Indeed, if ϱ approaches $1/\varphi$, then $\frac{\mathrm{d}\zeta_g}{\mathrm{d}t}$ diverges while $\frac{\mathrm{d}\varrho}{\mathrm{d}t}$ stays finite. Full coverage is thus reached very quickly, and the radius saturates at the value

$$\varrho^{\text{saturation}} = 1/\varphi. \tag{3.80}$$

3.4.3.5 Relation to anomalous growth

The bulge hypothesis might account for three out of the four anomalous growth effects presented in Sec. 3.4.1:

(b) In all of the above studied cases except that of Sec. 3.4.3.1, we saw that the radius of the bulge initially increases, be it before stall is reached (Secs. 3.4.3.2 and 3.4.3.3), or in the initial stages of growth when two dissipative mechanisms are involved (Sec. 3.4.3.4 and in particular Fig. 3.8). As this happens, nucleation of new helices becomes more and more difficult and the radius of the bare tubule sections (*i.e.* bulges) might even end up exceeding the upper critical radius for nucleation r_+ defined in Eq. (3.7). This would yield a the drop in the helix nucleation rate.

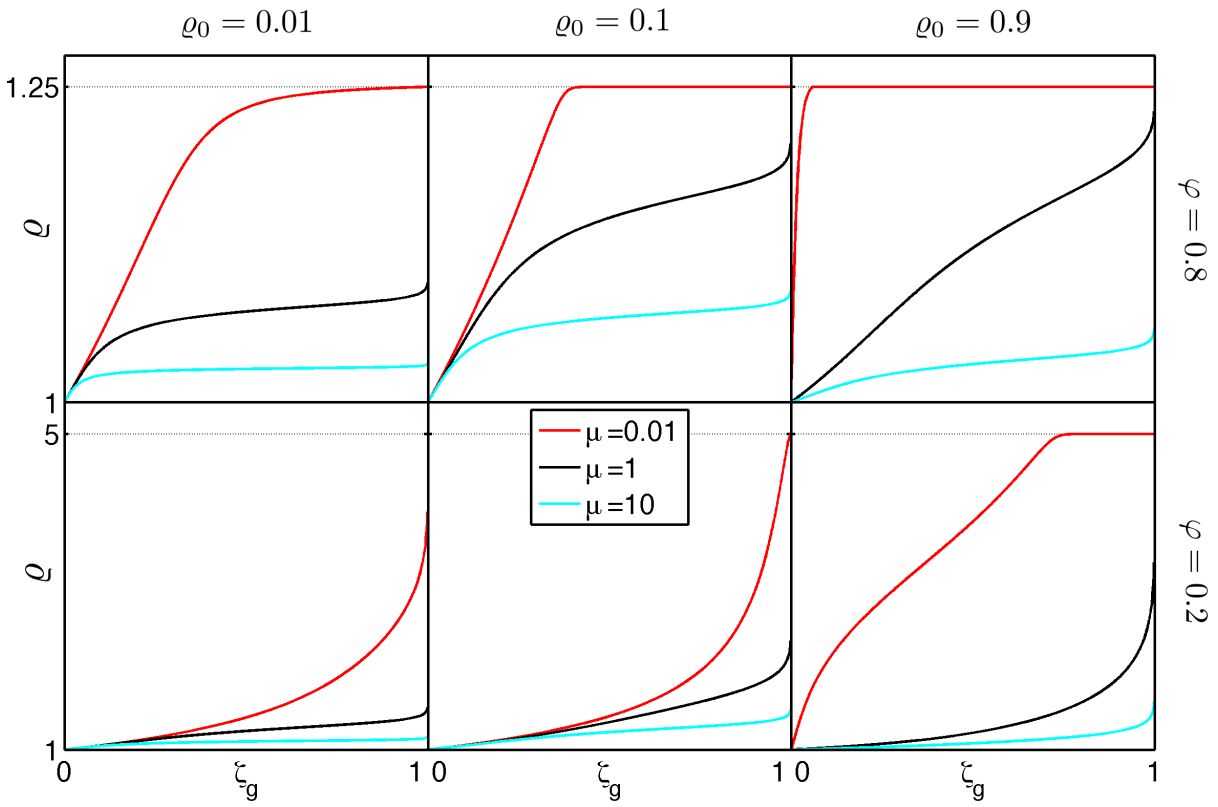

Figure 3.8: Flow lines of the system of equations Eqs. (3.79) describing the evolution of the bulge in the ζ_g, ϱ plane for various values of the parameters ϱ_0, φ and μ. For $\mu \ll 1$, the initial growth involves only water exchanges between the bulge and the vesicle, and Eq. (3.72) describes the dynamics after the radius saturation. Conversely, membrane exchanges dominate short time scales if $\mu \gg 1$, whereas the long time relaxation satisfies Eq. (3.76).

(c) In Secs. 3.4.3.2 and 3.4.3.3, growth happens initially on the fast time scale t_g, then slows down considerably as the stall condition Eq. (3.69) or Eq. (3.74), respectively, is reached. In Sec. 3.4.3.4, many parameter values also yield two distinct phases of growth, as shown in Fig. 3.8. This is in agreement with the experimentally observed slowing down of dynamin growth before full tubule coverage.

(d) As the stall condition is reached in Secs. 3.4.3.2 and 3.4.3.3, the force drops to its value $f = f_h$, which is one of the anomalous growth effects we wish to account for. Note that this happens at the very beginning of growth in the regime described in Sec. 3.4.3.4. This last regime therefore cannot account for the observations of Fig. 3.5(d).

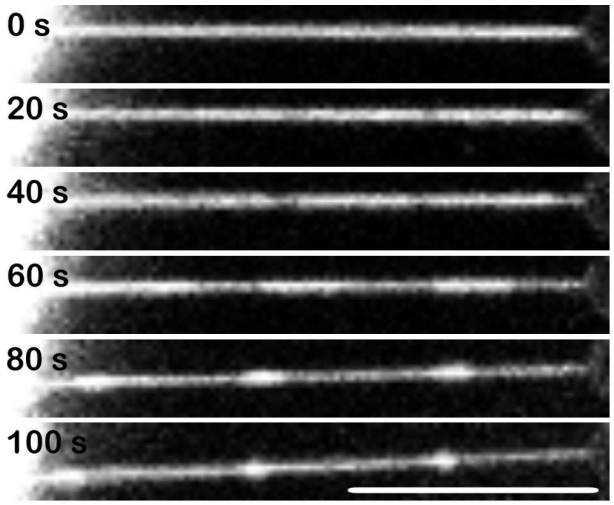

Figure 3.9: Preliminary experimental observation of membrane bulges. The vesicle is on the left, and the bead on the right. For clarity, only the red channel is shown here. Dynamin growth was also monitored in this experiment, and the green regions exactly match the less bright regions of the tubule. Here growth slows down as the bulges form, but the experiment was interrupted before their drainage could be observed. More work is needed to show that the bulges actually cause the slowing down. Bar, 10 μm.

3.4.4 Experimental perspectives

Several experiments could be conducted to validate the mechanisms investigated in Secs. 3.4.2 and 3.4.3. Here we comment on these technical aspects, leaving the discussion of the biological implications for the next section.

As a first approach, both effects discussed here are likely to be directly observable. In the case of the antenna hypothesis, the density of dynamin dimers adsorbed on the tubule could be monitored by increasing the power of the laser used to excite the dynamin-associated fluorophore. The existence of a dynamin depletion in the vicinity of existing helices could then be checked, as could the fact that the associated length scale $\sqrt{D/l_{\rm off}}$ does not depend on dynamin concentration. In the case of the bulge hypothesis, although the tubules used in our experiments are too thin for their radii to be directly resolved by optical wavelengths, they can be inferred from the fluorescence intensity along the tubule. In Fig. 3.9, we present preliminary evidence that bulges indeed occur in our experiments.

After having established the existence of the mechanisms underlying these hypotheses, it still remains to be proved that they are indeed responsible for the anomalous growth effects presented in Sec. 3.4.1. In the following, we summarize a few easily testable predictions that could be used to that effect.

Let us start by a prediction that could be useful to guide these investigations: effects related to the antenna hypothesis are expected to be important when the inter-helix distances are of order $\sqrt{D/l_{\rm off}}$. This length does not depend on the length of the initial tubule, and neither does the typical relaxation time scale given in Eq. (3.57). In the bulge hypothesis, on the contrary, stall (or, in Sec. 3.4.3.4, the transition between two

relaxation regimes) occurs for finite values of ζ_g, and thus when both the bare and covered fractions of the tubule are of order L. Moreover, the time scales involved are of order L^2 [see Eqs. (3.65) and (3.66)]. Therefore, we predict that antenna-related effects are most apparent in short tubules while bulge-related effects dominate the relaxation of long tubules.

Another important parameter influencing the growth of the helix is the initial radius of the tubule. Indeed, while the antenna model depends little on the tubule radius (note that ρ might scale linearly with r_b), the bulge effect disappears completely if $r_b = r_0$. Conversely, while the antenna effect should have little effect of the radius of the bare sections of the tubule, this radius should increase if bulge effects are at work. This experimentally measurable increase is expected to be more pronounced for lower values of f_h (or equivalently of φ), as predicted in Eqs. (3.69), (3.74) and (3.80).

The two hypotheses predict different relaxation dynamics for the gaps between two dynamin helices: exponential for the antenna hypothesis [Eq. (3.60c)], and obeying the Washburn equation for the bulge hypothesis [Eqs. (3.72) and (3.76)]. This could also be tested experimentally.

Finally, we discuss our assumption that the bulge always remains cylindrical. We found that this assumption i always justified in all cases considered, except in Sec. 3.4.3.3. There it is rigorously true only for a large enough f_h, and many practically encountered experimental conditions do not satisfy the conditions $\varphi \in \left[\sqrt{3}/2, 1\right]$. However, even in this case we expect that the growth ends up being stalled by the accumulation of membrane and water. Also, since the resistance of the helix to the membrane and water flows is proportional to its length, it would not be surprising if we recovered a Washburn-type dynamics in this case.

3.5 Biological implications

As its main function is to tubulate and sever the membrane, dynamin has a well-characterized physical influence on lipid bilayers. This chapter demonstrates that the reverse influence also exists, which opens the possibility for the cell to control endocytosis through the characteristics of its membrane.

Here we show that the polymerization of dynamin on a membrane substrate is strongly dependent on the membrane's mechanical properties, such as tension, curvature and bending modulus, as well as on the concentration of the dynamin solution. This is due to a competition between the free energy gain of dynamin upon assembly and the cost of tubulating the membrane. Our results indicate that the dynamin polymer is much more rigid than the membrane. Still, even though the dynamin polymer undergoes little deformation, and is therefore unperturbed by the membrane, in the concentration interval comprised between $c_1 \simeq 280\,\mathrm{nM}$ and $c_2 \simeq 12.6\,\mu\mathrm{M}$, the following two effects take place simultaneously [Fig. 3.3(b)]:

- the curvature of the bare membrane tubule controls dynamin polymerization (this is especially interesting for radii larger than the preferred dynamin radius, which is the biologically relevant regime).

- the dynamin helix squeezes the membrane down and imposes its radius on it.

Interestingly, it is suggested in Ref. [37] that a dynamin concentration of 500 nM could be physiological. This indicates that the regime $c_1 < c < c_2$ could be relevant *in vivo*, and thus that even though polymerized dynamin is not flexible, it could function both as a membrane curvature sensor and a curvature generator, two functions that have sometimes been regarded as separate in previous studies.

There is experimental evidence that the curvature dependence of dynamin polymerization plays a role *in vivo*, for instance in the regulation of the final closure of Clathrin Coated Pits (CCPs). Indeed, treatment of cells with dynasore—a chemical inhibitor of dynamin [58]—results in the widening of their CCP necks to a radius of roughly 20 nm [59], suggesting that this change in curvature could be the reason why dynamin oligomerization is prevented. This effect could also play a role for endophilin and amphiphysin, two proteins that possess a curvature-sensing BAR domain [60]. Although they were not present in the experiments described here, *in vivo* they might be responsible for sensing the curvature of the CCP necks and recruiting dynamin through interactions with its SH3 domain [41].

The influence of membrane tension might also be important in cells. We predict here that for high dynamin concentrations ($c > c_2$), dynamin tubulates only relatively floppy membranes. This supports the idea that recruitment of proteins to the membrane can be controlled by tuning cellular membrane tension, and could participate in the observed up-regulation of endocytosis when plasma membrane tension is reduced [61, 62]

The models of dynamin seeding and growth presented here open equally promising research avenues. The kinetics of dynamin seeding is indeed very relevant for the regulation of endocytosis and might well be its rate-limiting step, hence our interest in determining its mechanism and the time scales involved. The models presented in Sec. 3.3 make concrete predictions that could be used to guide an experimental study of these points.

Although the growth of the dynamin polymer over long lengths is less directly related to the *in vivo* situation of the short necks of clathrin-coated pits, biologically relevant information can also be drawn from it, and we suggest ways to gather it in Sec. 3.4. As an illustration of this relevance, Ref. [13] suggests that the recruitment of dynamin could implicate membrane-mediated elastic interactions between adsorbed dynamin dimers. This model rests on the implicit assumption that dynamin first binds to the membrane, and is then funneled to the CCPs from there. This is very similar to the picture presented in Sec. 3.4.2 in the frame of our antenna hypothesis, and measurement of the rate constants involved would allow to assess the likelihood of the hypothesis proposed in Ref. [13] and maybe to test it experimentally. On the other hand, monitoring the drainage of membrane bulges described in Sec. 3.4.3 would provide us with a direct measurement of the helix-membrane friction coefficient, which we show in the next chapter to be crucial to the dynamics of dynamin's change of conformation.

Chapter 4

Mechanochemical action of dynamin

In this chapter, we turn to the second aspect of the dynamin problem and present a theoretical model for the GTP-induced conformational change of long dynamin-coated membrane tubes accounting for the experimental results presented in Sec. 2.2. We believe that a quantitative description of the tube dynamics can help to understand the mechanisms by which dynamin severs membrane tubules. This is a much-debated question for which several models have been proposed [16]. Since little quantitative information about the microscopic details of the dynamin helix is available, we choose a coarse-grained (hydrodynamic) approach. In this framework, we do not need to speculate about the unknown microscopic details of the non-equilibrium behavior of the tube: its dynamics is characterized by a few phenomenological transport coefficients.

In Sec. 4.1, we introduce the type of assumptions underlying our approach and discuss its level of generality as well as its application to dynamin. In the following three sections, we present the building blocks of our formalism by decreasing order of generality. In Sec. 4.2, we consider only the symmetries of the system and write the most general hydrodynamic theory compatible with these symmetries. We then argue in Sec. 4.3 that one hydrodynamic mode is much slower than the others. This leads to simplified equations describing this mode. In Sec. 4.4, we present two microscopic models of the tube's equilibrium properties aimed at describing two possible experimental situations. This allows us to solve the equations of motion and make predictions about the tube dynamics. In Sec. 4.5, we quantitatively justify some of our assumptions and give a tentative account of the differences in the conformational changes of dynamin reported in Refs. [24, 27, 28, 29, 33] on the one hand and Refs. [34, 35] on the other hand. The validity of our approach is confirmed by experimental results presented in Sec. 4.6. Finally, we discuss the generality of our model, its implications for membrane tubule fission and the experimental possibilities it opens in Sec. 4.7.

4.1 Introduction to the ideas of hydrodynamics

Generalized hydrodynamics is a widespread tool to describe the collective modes of complex systems. A well-known example of a hydrodynamic theory is the Navier-Stokes equation for simple fluids [63]. The generality of the ideas of this field was recognized when more complicated systems, such as liquid crystals or superfluids, were tackled [64, 65, 66].

More recently, they were put to use to describe "active" systems (*i.e.* systems in which energy is continuously injected), be it rods on an vibrating plate [67] or living systems such as bacterial cultures, bird flocks, herds of animals or the cytoskeleton [68, 69, 70].

The point of the hydrodynamic approach is that it generates relatively simple models for systems that can be very intricate at first sight. These simplifications rest on two fundamental assumptions:

① Only the large length and long time scales are consdered. This allows the system to reach local equilibrium.

② The system is weakly perturbed away from a known reference state (*e.g.* thermodynamic equilibrium).

Some further simplifications of the model are drawn from considering

③ the spatial and time-reversal symmetries of the system,

④ other possible general relations describing the system, as discussed further below.

In Sec. 4.1.1 we illustrate these four points in a simplified discussion of an obviously very complicated system: the motion of a population of buffaloes. We then give a preview of their application to dynamin in Sec. 4.1.2. Another good introduction to our methodology is given in Sec. 8.2 of Ref. [71], where a simple hydrodynamic theory is derived following the same steps as in Sec. 4.2.

4.1.1 Buffaloes

Here we consider the spreading of a large herd of buffaloes over vast swaths of grass, with the simplifying assumption that a buffalo does not tend to face any particular direction in the horizontal plane, whatever the direction that its neighbors face[1].

We first present a picture of the behavior considered at the level of a single buffalo (the "microscopic" level). We then derive a hydrodynamic description of the large-scale behavior of the herd. The emphasis is put on how little reference to the microscopic level is needed to do so, and how some of the processes included in it become irrelevant in the hydrodynamic description.

4.1.1.1 Microscopic picture

Consider a buffalo standing on a patch of african grassland. Being hungry, it starts grazing. It takes the buffalo one hour to deplete the patch it is standing on of its grass. The grass then grows back, and completely recovers in three days [Fig. 4.1(a)]. Meanwhile, the buffalo might grow hungry again, and thus move towards greener pastures. We do not need to specify anything about this process, but shall formulate a "fundamental law of buffalo grazing" stating that *on average*, a buffalo moves up the local grass length gradient [Fig. 4.1(b)].

[1] This is the fundamental difference with Ref. [69].

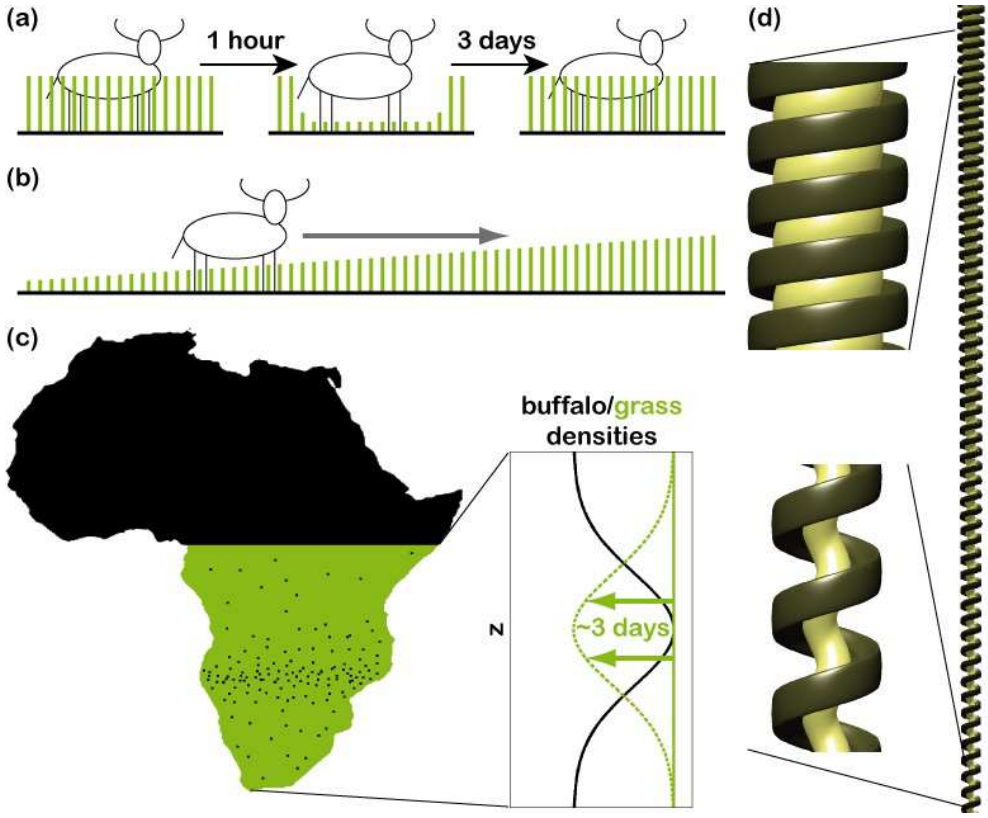

Figure 4.1: Illustration of the basic ideas of generalized hydrodynamics (a) Microscopic rules of buffalo grazing. (b) According to the fundamental law of buffalo grazing, buffaloes tend to move up a grass length gradient—not down. (c) Initial state of the herd spreading process. The equilibration between consumption and re-growth of the grass happens on time scales much shorter than a year (typically 3 days). (d) Long dynamin polymer and close-ups on its local configuration in two different locations.

4.1.1.2 Hydrodynamic description

Even though the above description of buffalo grazing might seem very sketchy, it actually already contains more information than required for us to describe it in hydrodynamic terms. We consider the spreading of an initially localized herd of buffaloes over a one-dimensional Sub-Saharan Africa parametrized by the coordinate z [Fig. 4.1(c)]. We assume that this area is initially covered with a uniform length of grass. Since the distances over which our herd spreads are so large, we need to consider time scales of order no less than say a year. This puts us in the regime described in ①. At this scale, we can consider that the processes described in Fig. 4.1(a) instantaneously leads to a local equilibrium between buffalo density and grass length. This consequence is mentioned in ①.

The time scales we consider are too short for the birth and death of buffaloes to substantially affect the number of individuals in the herd. The density of buffaloes ρ_b (unlike the density of grass) is therefore a conserved quantity, meaning that we can write

the conservation law

$$\partial_t \rho_b = -\nabla J_b, \tag{4.1}$$

where ∇ is the gradient operator (which in our one-dimensional case denotes a differentiation with respect to z) and J_b is the buffalo current. Generically, the current of buffaloes is expected to depend on the local density of grass and its derivatives. Because a local equilibrium is quickly reached, these are in turn imposed by the buffalo density profile. Therefore, there should exist a set of coefficients $\{k_{n,\dots}\}$ such that

$$\begin{aligned} J_b \;=\; & k_0\delta\rho_b + k_1\nabla\delta\rho_b + k_2\nabla^2\delta\rho_b + \cdots \\ & + k_{0,0}\delta\rho_b^2 + k_{0,1}\delta\rho_b\nabla\delta\rho_b + k_{0,2}\delta\rho_b\nabla^2\delta\rho_b + \cdots \\ & + k_{1,1}(\nabla\delta\rho_b)^2 + k_{1,2}\nabla\delta\rho_b\nabla^2\delta\rho_b + \cdots \\ & + \cdots \\ & + k_{0,0,0}\delta\rho_b^3 + k_{0,0,1}\delta\rho_b^2\nabla\delta\rho_b + k_{0,0,2}\delta\rho_b^2\nabla^2\delta\rho_b + \cdots \\ & + \cdots , \end{aligned} \tag{4.2}$$

where $\delta\rho_b$ denotes the deviation of the buffalo density from the reference state, defined as the state where buffaloes are uniformly spread and J_b thus vanishes. Eq. (4.2) is very complicated, but we can simplify it using ②. Indeed, if we assume that the displacement from the reference state is small, terms of order two or more in $\delta\rho_b$ should be negligible compared to the linear terms, and

$$J_b = k_0\delta\rho_b + k_1\nabla\delta\rho_b + k_2\nabla^2\delta\rho_b + \cdots . \tag{4.3}$$

We now make use of the symmetries of the system, as announced in ③. Since nothing in our microscopic description distinguishes the direction of positive zs from the direction of negative zs, one cannot expect that an equation faithfully describes our system unless it is invariant under the $z \to -z$ symmetry operation. In Eq. (4.3), J_b and the odd terms of the right-hand side change sign under z-reversal, unlike the even terms of the right-hand side. Therefore, the coefficients k_n with even n vanish. This is obvious in the case of k_0: imagine that the system is displaced from the reference state by a constant $\delta\rho_b$. According to Eq. (4.3), this should induce a current of amplitude $k_0\delta\rho_b$. But since we assumed that an individual buffalo has no way of telling the difference between north and south, it seems ridiculous that an increase in the population density would drive a northwards (or southwards) average flow of buffaloes. Thus $k_0\delta\rho_b$ must be zero whatever the value of $\delta\rho_b$, hence $k_0 = 0$.

The nth term of Eq. (4.3) contains the operator ∇ to the nth power. Looking at spatial inhomogeneities over length scales comparable to the size of Africa, we estimate that the nth term should be proportional to (size of Africa)$^{-n}$. Since all the other length scales involved in our system (*e.g.* the average inter-buffalo distance) are much smaller than the size of Africa (this is assumption ①), the higher-order terms are negligible in front of the lower-order terms. We can therefore neglect all terms except the lowest-order non-vanishing one:

$$J_b = k_1\nabla\delta\rho_b. \tag{4.4}$$

We have one last condition to exploit. In agreement with ④, we note that the fundamental law of buffalo grazing imposes that $k_1 < 0$. Indeed, this law implies that the

buffaloes tend to move towards areas of lower buffalo density, where grass in more abundant. In thermodynamic systems, the fundamental law of buffalo grazing is replaced by the local Gibbs relation as well as constraints imposed by the second principle of thermodynamics.

Combining Eqs. (4.1) and (4.4), we obtain the equation describing the hydrodynamic relaxation of the buffalo herd:

$$\partial_t \rho_b = |k_1| \nabla^2 \rho_b. \tag{4.5}$$

The dynamics of the herd on long length and time scales is therefore diffusive. This extremely simple behavior contrasts with the plethora of details that one could include in a "realistic" microscopic description of buffalo grazing, from effective repulsive interactions between individuals to the way the nervous system of the animal allows it to detect and react to a grass length gradient. All these effects are relevant to the problem and influence the way the herd spreads over Africa. At our level of description, however, such microscopic details are enclosed in the coefficient k_1 and cannot affect the *form* of Eq. (4.5). Since k_1 depends on very complicated processes, in a hydrodynamic description it should be treated as a phenomenological parameter and be fitted to experimental results rather than calculated *a priori*. Another spectacular feature is that although the local state of the system is characterized by several variables (buffalo density, grass density...), Eq. (4.5) describes the dynamics of the whole system in terms of ρ_b only. The reason why only this variable is relevant on long time scales comes from the fact that it is a *conserved quantity*: in order to restore a uniform buffalo concentration, one should move buffaloes from one side of the system to the other, which takes a very long time if one considers a very large system, as the velocity at which a buffalo moves is finite. This is in strong contrast with the behavior of non-conserved quantities, such as grass density: since the process of grass growth is local, if left alone it takes three days to re-grow over all of Africa, no matter how large the continent. Hence on long time scales, the grass density is slaved to the buffalo density, and can thus be eliminated from the equations describing the system.

4.1.2 Dynamin

Since the dynamin-membrane tubes obtained *in vitro* are much longer ($\sim$ the size of Africa) than the radius and pitch of the helix ($\sim$ the inter-buffalo distance), it is reasonable to describe them using the concepts introduced here. On the time scales considered in this chapter, the dynamin helix is in local equilibrium, but the local equilibrium state is not necessarily the same everywhere along the z-axis [Fig. 4.1(d)]. In the following, we show that the homogenization of the local dynamin conformation is driven by the elasticity of the helix and membrane, and that its hydrodynamically relevant relaxation time scales are fixed by the viscous dissipation in the surrounding water and by a friction between the membrane and the helix. The hydrodynamic approach spares us the risky task of modeling the details of the protein's conformational change. Therefore, our description does not rely on any uncertain microscopic assumption, hence its generality and likely validity.

In this chapter, we show that on long time scales dynamin-membrane tubes have a diffusive dynamics. Two of its relaxational eigenmodes are dominated by the hydrody-

namic drag of the helix in the surrounding aqueous medium. For geometrical reason, the fastest of these eigenmodes is dominated by the longitudinal drag of the tube against water, while the slower one mostly involves rotational hydrodynamic drag. In terms of scaling, we expect the diffusion coefficients D_1 and D_2 corresponding to these modes to involve the viscosity of water $\eta \simeq 10^{-3}\,\mathrm{Pa.s}$, a microscopic length scale of the order of the helix radius $r \approx 10\,\mathrm{nm}$, and the elasticity of the helix, characterized by the coefficient $k_B T \ell_p$, where $\ell_p = 37 \pm 4\,\mu\mathrm{m}$ is the persistence length of the helix [60]. This yields

$$D_{1,2} \approx \frac{k_B T \ell_p}{\eta r^2} \approx 1.5 \times 10^{-6} \mathrm{m}^2.\mathrm{s}^{-1}. \tag{4.6}$$

Considering a tube of length $L \approx 50\,\mu\mathrm{m}$—which is compatible with the experiments of Ref. [36]—we expect those modes to relax on a time scale $\tau_{1,2} \approx L^2/D_{1,2} \approx 1\,\mathrm{ms}$. The third eigenmode involves a different damping process: an effective helix/membrane friction. It therefore involves the membrane viscosity $\eta_{\mathrm{membrane}} \simeq 5 \times 10^{-9}\,\mathrm{kg.s}^{-1}$ [72] rather than η. Since membrane relaxation requires the disentangling of the hydrophobic tails of phospholipids, we expect this eigenmode to relax on time scales longer than τ_1 and τ_2. Indeed, the corresponding diffusion coefficient scales in the following way:

$$D_3 \approx \frac{k_B T \ell_p}{\eta_{\mathrm{membrane}} r} \approx 3 \times 10^{-9}\,\mathrm{m}^2.\mathrm{s}^{-1}, \tag{4.7}$$

which yields $\tau_3 \approx 1\,\mathrm{s}$. This is compatible with the experimentally observed relaxation times of dynamin.

4.2 Hydrodynamic theory

In this section, we derive equations of motion for dynamin-membrane tubes based on the symmetries of the system. As mentioned in Sec. 4.1, we focus on the so-called *hydrodynamic modes*, which are spatially inhomogeneous excitations of the system away from equilibrium with the following properties [65]:

1. the wave vector q and the pulsation $\omega(q)$ characterizing the spatial inhomogeneity of the hydrodynamic mode are such that

$$\lim_{q \to 0} \omega(q) = 0, \tag{4.8}$$

2. the amplitude of these excitations are small enough for us to be able to consider that the system is in a state of local equilibrium everywhere [63].

These two conditions parallel the assumptions ① and ② considered in Sec. 4.1.

The $q \to 0$ limit corresponds to excitations over length scales much larger than the microscopic length scales of the system. Typically, we consider inverse wave vectors of the order of the tube's length: $q^{-1} \approx$ several $10\,\mu\mathrm{m}$. This is indeed much larger than the typical microscopic length: the tube radius $r \approx 10\,\mathrm{nm}$. The hydrodynamic theory thus involves a coarse-graining of the system at the scale of a few tens of nanometers, and so the tube must be treated as a one-dimensional object.

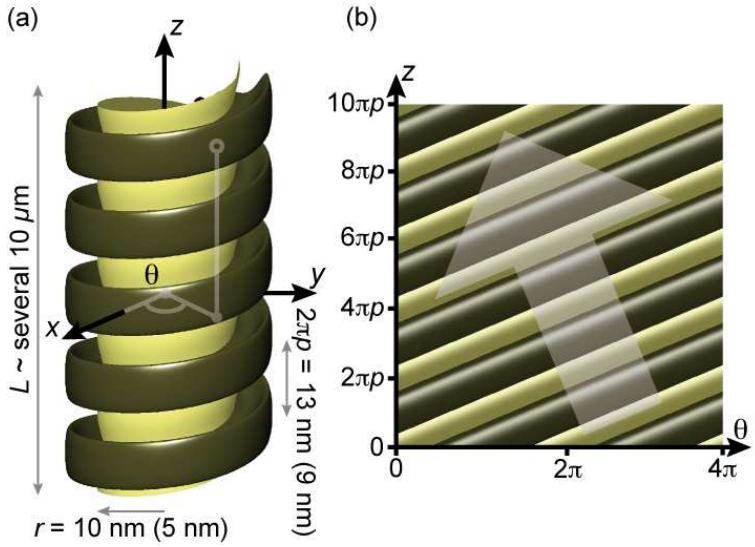

Figure 4.2: Schematics representing the geometry of the tube. (a) The tube comprises two fluids h and m, here pictured in different colors. It is invariant under a rotation around z by an arbitrary angle θ followed by a translation by $p\theta$ along z (we refer to this property as *helical symmetry with pitch* $2\pi p$ in the text). Moreover, the system is assumed to be invariant under a rotation of π around the x-axis (the system is *non-polar*). The latter transformation is equivalent to a reversal of polar coordinates $(\theta, z) \to (-\theta, -z)$. The numerical values measured in Ref. [28] for the radii and pitches in the relaxed (constricted) states are indicated on the figure. (b) Representation of the same helix in the θ, z plane of cylindrical coordinates with periodic boundary conditions on θ. The system clearly has a broken translational symmetry in the direction of the translucent arrow. It is described by a broken-symmetry variable $u_{z\theta}$ obeying Eq. (4.17), which can be understood as a conservation law for the number of stripes visible here. The associated reactive current is $v_h/p - \Omega_h$, the projection of the velocity of the stripes on the direction of the arrow.

Let us now state the hypotheses underlying our hydrodynamic theory. We consider a one-dimensional system comprising two fluids which we refer to as fluids h (representing the helix) and m (the lipid membrane). In agreement with electron microscopy data [27, 28, 29], we assume that the system has a helical symmetry with pitch $2\pi p$ and is non-polar, as shown on Fig. 4.2(a).

In the following, we identify the relevant variables describing this system and derive an expression for its entropy production. Introducing an active term representing the input of free energy in the form of GTP, we write the constitutive (flux/force) equations for the tube. Together with conservation laws, these equations eventually yield the hydrodynamic modes of the system.

4.2.1 Conservation laws and hydrodynamic variables

The first step in building a hydrodynamic theory relies on conservation laws.

We assume that no exchange of membrane or dynamin occur with the aqueous medium

surrounding the tube on the time scale of the conformational change [36]. Therefore, the masses of fluids h and m obey the following conservation equations:

$$\partial_t \rho_h = -\nabla(\rho_h v_h) \tag{4.9a}$$
$$\partial_t \rho_m = -\nabla(\rho_m v_m), \tag{4.9b}$$

where v_h and v_m are the velocities of fluids h and m respectively and ρ_h and ρ_m their mass densities (masses per unit of z length). We now define the mass fraction of h as $\Phi = \rho_h/\rho$, the mass density of the whole tube $\rho = \rho_h + \rho_m$, the linear momentum density of the tube $g = \rho_h v_h + \rho_m v_m = \rho v$ with v the center-of-mass velocity and the diffusion flux of h relative to the center of mass of the tube $J = \rho_h(v_h - v)$. The conservation laws expressed in Eqs. (4.9) can be re-written as

$$\partial_t \rho = -\nabla g \tag{4.10a}$$
$$\partial_t \Phi = -v\nabla\Phi - \rho^{-1}\nabla J, \tag{4.10b}$$

It is shown further below that the inverse relaxation times of ρ and Φ go to zero with vanishing q, meaning that ρ and Φ are indeed hydrodynamic variables.

Let l be the angular momentum density of the tube. The conservation laws for g and l are the force and torque balance equations. There are two contributions to the force (resp. torque) applied to a tube element: first, the divergence of σ (resp. τ), the linear (resp. angular) internal stress of the tube; and second, the external force (resp. torque) due to the coupling of the helix dynamics with the hydrodynamic flow that it induces in the surrounding aqueous medium. For simplicity, we model this "friction against water" as a force and a torque linearly dependent on v_h and on the angular velocity Ω_h of fluid h with proportionality coefficients $\{\gamma_{ij}\}_{i,j=z,\theta}$:

$$\partial_t g = -\nabla\sigma - \gamma_{zz} v_h - \gamma_{z\theta}\Omega_h \tag{4.11a}$$
$$\partial_t l = -\nabla\tau - \gamma_{\theta z} v_h - \gamma_{\theta\theta}\Omega_h. \tag{4.11b}$$

Since $v_h = (g + J/\Phi)/\rho$, we can replace v_h by $g + J/\Phi$ in Eqs. (4.11) after rescaling the friction coefficients in the following way: $\gamma_{zz} \to \rho\gamma_{zz}$ and $\gamma_{\theta z} \to \rho\gamma_{\theta z}$. Since the friction between the two fluids is a local phenomenon (which does not depend on the wave vector q), the quantity $\Omega_h - \Omega_m$ relaxes to zero in a non-hydrodynamic time [that does not respect Eq. (4.8)]. When studying hydrodynamic time scales, we can thus replace Ω_h by Ω_m or equivalently by $\Omega = l/I$ with I the tube's density of moment of inertia. Redefining $\gamma_{z\theta} \to I\gamma_{z\theta}$ and $\gamma_{\theta\theta} \to I\gamma_{\theta\theta}$, we replace Ω_h by l in Eqs. (4.11).

It is now apparent in Eqs. (4.11) that in the presence of friction against water, g and l relax to the solutions of the following equations:

$$\gamma_{zz}\left(g + \frac{J}{\Phi}\right) + \gamma_{z\theta} l = -\nabla\sigma \tag{4.12a}$$
$$\gamma_{\theta z}\left(g + \frac{J}{\Phi}\right) + \gamma_{\theta\theta} l = -\nabla\tau. \tag{4.12b}$$

This relaxation occurs over times of order $1/\gamma_{ij}$. Since the γ_{ij}s do not depend on q, these times are not hydrodynamic times (they do not go to infinity when q vanishes). The

linear and angular momentum densities g and l are therefore not hydrodynamic variables and are given by Eqs. (4.12), which are the force and torque balance equations in the overdamped regime.

The conservation of energy reads:

$$\partial_t \varepsilon + \nabla j^\varepsilon = v \left[-\gamma_{zz} \left(g + \frac{J}{\Phi} \right) - \gamma_{z\theta} l \right] + \Omega \left[-\gamma_{\theta z} \left(g + \frac{J}{\Phi} \right) - \gamma_{\theta\theta} l \right], \tag{4.13}$$

where ε is the energy density and j^ε the current of energy. The right-hand side accounts for energy dissipation by friction.

Although no other conservation law than Eqs. (4.10), (4.12) and (4.13) exist in the system, its hydrodynamic description is still incomplete. Indeed, the system has a broken continuous symmetry similar to that of smectic-A liquid crystal phases [Fig. 4.2(b)]. Just as in the case of liquid crystals [64], we use a strain tensor component $u_{z\theta}$ to describe this symmetry breaking. We define $u_{z\theta}$ in the following way: let $\theta(z,t)$ be the angular displacement of the intersection of the helix with the plane located at altitude z at time t (therefore θ is a eulerian coordinate). The strain is then defined as:

$$u_{z\theta}(z,t) = \frac{\partial \theta}{\partial z}(z,t). \tag{4.14}$$

As any broken-symmetry variable, $u_{z\theta}$ obeys a relation similar to a conservation law. To show this, we first note that in a fully reversible situation

$$\partial_t \theta(z,t) = \Omega_h - \frac{v_h}{p}. \tag{4.15}$$

Differentiating this equation with respect to z, we find

$$\partial_t u_{z\theta} = -\nabla \left(\frac{v_h}{p} - \Omega_h \right), \tag{4.16}$$

where $v_h/p - \Omega_h$ is the reactive current of $u_{z\theta}$ [see also Fig. 4.2(b)]. In the presence of dissipation, one must add a dissipative part X to this current [71], hence

$$\begin{aligned} \partial_t u_{z\theta} &= -\nabla X - \nabla \left(\frac{v_h}{p} - \Omega_h \right) \\ &= -\nabla \left(X + \frac{g + J/\Phi}{\rho p} - \frac{l}{I} \right). \end{aligned} \tag{4.17}$$

4.2.2 Entropy production

As mentioned above, the great simplicity of hydrodynamic theories can be tracked back to the fact that in the long-time limit, one locally describes the state of a potentially very complex system using only a few conserved quantities. Indeed, on time scales going to infinity with the size of the system, all the microscopic (fast) degrees of freedom have relaxed and the system is locally in a state of thermal equilibrium in the thermodynamic ensemble defined by the conserved quantities.

Let us apply this idea to the tube in the general case where friction against water is not necessarily present (*i.e.* the γ_{ij}s can be zero, in which case g and l are hydrodynamic variables). The state of local thermal equilibrium is entirely characterized by the six quantities g, l, ρ, Φ, $u_{z\theta}$ and ε. Equivalently, we can consider a homogeneous tube of length V and study it in the thermodynamic ensemble $(P, \mathfrak{L}, M, \Phi, u_{z\theta}, T, V)$, where $P = Vg$, $\mathfrak{L} = Vl$ and $M = V\rho$ are the total linear momentum, angular momentum and mass of the tube; T denotes temperature. The total differential of the free energy of the tube reads:

$$\mathrm{d}F = v\mathrm{d}P + \Omega\mathrm{d}\mathfrak{L} + \mu\mathrm{d}M + M\mu_e\mathrm{d}\Phi + H\mathrm{d}u_{z\theta} - S\mathrm{d}T - \mathfrak{p}\mathrm{d}V. \tag{4.18}$$

This equation defines the total and exchange chemical potentials μ and μ_e, the reactive stress $h = H/V$ (which can be simply understood as the reactive part of the torque at a given point of the tube), the entropy $S = Vs$ and the equilibrium pressure $\mathfrak{p}$. Note that the velocity v is thermodynamically conjugated to P and the angular velocity Ω to $\mathfrak{L}$. This implicitly assumes that the free energy is the sum of a kinetic energy and a static contribution:

$$F = V\left(\frac{\rho v^2}{2} + \frac{I\Omega^2}{2}\right) + F_s(M, \Phi, u_{z\theta}, T, V), \tag{4.19}$$

where the free energy of the tube in its rest frame can also be written as

$$F_s(M, \Phi, u_{z\theta}, T, V) = V f_s(\rho, \Phi, u_{z\theta}, T). \tag{4.20}$$

Using an extensivity argument, we show the relation

$$\mathfrak{p} = vg + \Omega l + \mu\rho + Ts - \varepsilon \tag{4.21}$$

and prove the local form of the fundamental equilibrium thermodynamic relation:

$$T\mathrm{d}s = -v\mathrm{d}g - \Omega\mathrm{d}l - \mu\mathrm{d}\rho - \rho\mu_e\mathrm{d}\Phi - h\mathrm{d}u_{z\theta} + \mathrm{d}\varepsilon. \tag{4.22}$$

Inserting the conservation equations Eqs. (4.10), (4.11), (4.13) and (4.17) into (4.22) and using (4.21), one finds the following form for the local entropy production of the system [71]:

$$\begin{aligned} T\left[\frac{\partial s}{\partial t} + \nabla\left(vs + \frac{Q}{T}\right)\right] = & - \left(\sigma - \mathfrak{p} - \frac{h}{p}\right)\nabla v - (\tau + h)\nabla\Omega \\ & - J\nabla\mu_e - \left(X + \frac{J}{\rho\Phi p}\right)\nabla h - Q\frac{\nabla T}{T}, \end{aligned} \tag{4.23}$$

where Q is the heat current in the z direction and where higher-order terms in the displacement from equilibrium have been dropped.

4.2.3 Constitutive equations

The right-hand side of Eq. (4.23) is the sum of five terms, each of which is the product of a *flux* and a *force* as displayed in Table 4.1. These fluxes and forces vanish at thermal

Table 4.1: The fluxes, forces and signature of the forces under two symmetry operations: "time symmetry" denotes the time-reversal symmetry and "spatial symmetry" refers to the reversal of the polar coordinates $(\theta, z) \to (-\theta, -z)$ defined in Fig. 4.2(a).

Flux	Force	time symmetry	spatial symmetry
$\sigma - \mathfrak{p} - h/p$	∇v	-	+
$\tau + h$	$\nabla\Omega$	-	+
J	$\nabla\mu_e$	+	-
$X + J/(\rho\Phi p)$	∇h	+	-
Q	$\nabla T/T$	+	-
	$\Delta\mu$	+	+

equilibrium. Also, according to the second law of thermodynamics, entropy production is always positive. Therefore, close to the equilibrium state, the fluxes depend linearly on the forces through a positive definite matrix. In addition to this positivity condition, other constraints exist on the relationships between fluxes and forces:

First, entropy production is invariant under spatial symmetry operations that leave the system unchanged. Therefore, fluxes and forces of opposite signature under the spatial symmetry $(\theta, z) \to (-\theta, -z)$ defined in Fig. 4.2(a) cannot be coupled. This property is a special case of the Curie principle, which states that in an isotropic system, couplings between fluxes and forces of different tensorial characters are forbidden. In this context, the quantities displayed in Table 4.1 that are odd under the transformation $(\theta, z) \to (-\theta, -z)$ are analogous to vectors and those that are even are scalars or second-rank tensors [63].

Time-reversal symmetry imposes another set of constraints. Each flux can be written as the sum of a dissipative part, which has the same time symmetry as the conjugate force, and a reactive part with the opposite symmetry. *Dissipative couplings* occur between fluxes and forces having the same time-reversal symmetry. Conversely, *reactive couplings* relate fluxes and forces of opposite symmetries. According to Onsager's relations, the matrix of dissipative couplings is symmetric and the matrix of reactive couplings antisymmetric [73].

While deriving Eq. (4.23), we have made sure that its right-hand side involves only entropy production terms, and no entropy exchange or energetic effects. Therefore, the fluxes in this equation are dissipative and have a vanishing reactive part. Taking into account the symmetry constraints discussed above, we obtain the following set of constitutive equations:

$$\sigma - \mathfrak{p} - h/p = -\eta_z \nabla v - a\nabla\Omega, \tag{4.24a}$$

$$\tau + h = -a\nabla v - \eta_\theta \nabla\Omega, \tag{4.24b}$$

$$J = -\lambda\nabla\mu_e - b_1\nabla h - b_2\nabla T/T, \tag{4.24c}$$

$$X + J/(\rho\Phi p) = -b_1\nabla\mu_e - \tilde{\lambda}\nabla h - b_3\nabla T/T, \tag{4.24d}$$

$$Q = -b_2\nabla\mu_e - b_3\nabla h - \tilde{\kappa}\nabla T/T. \tag{4.24e}$$

The coefficients in front of the forces are so-called *phenomenological transport coefficients*. They are *a priori* unknown coefficients that depend on the microscopic details of the problem.

4.2.4 Discussion of the phenomenological coefficients

In the spirit of the present chapter, those phenomenological coefficients that are relevant to the relaxation of the system should be determined experimentally. The only way to calculate them *a priori* would be to use a detailed microscopic model, which would require a better knowledge of dynamin than we have. However, in the next few paragraphs, we try to interpret the origin and give typical orders of magnitude of these phenomenological coefficients.

The coefficient $\eta_z > 0$ can be identified as a length $\times$ surface viscosity, where "length" denotes a typical microscopic length of the tube, for instance its inner radius $r \approx 10\,\mathrm{nm}$. Similarly, $\eta_\theta > 0$ is a (length)^3 $\times$ surface viscosity. Assuming that the effective characteristic surface viscosity of the tube is close to that of a lipid bilayer, namely of order $5 \times 10^{-9}\,\mathrm{kg.s^{-1}}$ [74], we estimate that $\eta_z \simeq 10^{-16}\,\mathrm{kg.m.s^{-1}}$ and $\eta_\theta \simeq 10^{-32}\,\mathrm{kg.m^3.s^{-1}}$.

The momentum transfer from translational to rotational degrees of freedom is described by a. This transfer is allowed since the tube is chiral. The amplitude of these effects is constrained by the positivity of the matrix of phenomenological coefficients, which imposes $|a| < \sqrt{\eta_z \eta_\theta}$.

The coefficient $\lambda > 0$ relates a gradient of chemical potential to a diffusion flux. By analogy to Fick's law, we expect it to be proportional to a diffusion coefficient. To better interpret λ, let us set all other phenomenological coefficients to zero. The hydrodynamic dissipation then comes only from the homogenization of the helix mass fraction Φ at fixed mass density ρ, and therefore involves a relative flow between the two fluids h and m. In this scenario, the source of dissipation is obviously the friction between the two fluids. One can therefore interpret λ as the inverse of a helix/membrane friction coefficient. As in the previous chapter, we assimilate helix/membrane friction to a relative sliding of the two lipid monolayers, characterized by the coefficient $\beta = 10^8\,\mathrm{Pa/(m.s^{-1})}$ [50]. Let us consider a motionless isothermal ($\nabla T = 0$) cylinder of membrane of length L surrounded by an undeformed ($h = 0$) helix of dynamin moving at velocity v_h under the influence of a chemical potential gradient difference $\mu_e = L\nabla\mu_e$ between the extremities of the cylinder. The mass flow of helix in such a system is $\rho_h v_h = \rho\Phi v_h$, hence the tube receives a net power $\mathfrak{P} = \mu_e \rho \Phi v_h$ from the reservoirs located at each end of the cylinder. Eq. (4.24c) and $J = \rho v = \rho\Phi(1-\Phi)v_h$ entail $\mathfrak{P}/L = \rho^2\Phi^2(1-\Phi)v_h^2/\lambda$. Assuming that this power is entirely dissipated by the friction between the membrane and the helix implies $\mathfrak{P}/L = 2\pi r \beta v_h^2$ and eventually

$$\lambda = \frac{\Phi^2(1-\Phi)}{2\pi}\frac{\rho^2}{r\beta} \simeq 1.1 \times 10^{-26}\,\mathrm{kg.m^{-1}.s}, \tag{4.25}$$

where the values at equilibrium $\rho_{h0} = \rho_0\Phi_0 \simeq 3.7 \times 10^{-13}\,\mathrm{kg.m^{-1}}$ and $\rho_{m0} = \rho_0(1-\Phi_0) \simeq 3.8 \times 10^{-13}\,\mathrm{kg.m^{-1}}$ are calculated from the molecular mass of dynamin [16] and the number of dynamin monomers per helix turn [28] on the one hand, and from the typical mass per unit area of a lipid bilayer [75] on the other hand. Here Φ_0 denotes the mass fraction of h at equilibrium.

The coefficient $\tilde{\lambda} > 0$ has properties similar to those of λ but only exists if the system has a broken-symmetry variable. If the system under study were a crystal, we would interpret this coefficient as related to the phenomenon of vacancy diffusion, *i.e.*, the displacement of mass without change in the periodic lattice. In our system, unlike in a crystal, there can be two independent diffusion coefficients $\propto \lambda$ and $\propto \tilde{\lambda}$ even if the creation of vacancies (and therefore possibly the breaking of the helix) is forbidden. Indeed, one does not need to create holes in the helix to displace mass without disturbing the periodic lattice of Fig. 4.2(b): this can be done by changing the radius of the helix. As far as orders of magnitude are concerned, we only assume in the following that the transport phenomena associated with $\tilde{\lambda}$ are not much faster than the ones associated with λ.

In the following, we consider the system as isothermal. This condition can be enforced by letting the thermal conductivity $\tilde{\kappa} > 0$ go to infinity, which implies that any thermal gradient relaxes instantaneously. In this $\tilde{\kappa} \to \infty$ limit, we can drop Eq. (4.24e) as well as the last terms of Eqs. (4.24c) and (4.24d).

Finally, b_1, b_2 and b_3 describe couplings between the three diffusion phenomena described above. Such cross-effects give rise for instance to the so-called Soret and Dufour effects. As in the case of a, the positivity of the matrix of phenomenological coefficients sets upper bounds on their values.

4.2.5 Coupling of GTP hydrolysis or binding to the dynamics

We have now developed a complete formalism for the dynamics of a passive, non-polar, diphasic helix submitted to external friction. However, the system considered in this chapter is not passive since nucleotide (*i.e.* GTP or GTP analog in this context) hydrolysis by dynamin or at least binding to dynamin is required for conformational change. In the following, we introduce this external free energy source using arguments similar to those of Ref. [70]: instead of deriving a whole new formalism taking into account the conservation of GTP, GDP and P_i and all the chemical reactions involving them, we model the presence of GTP in the experimental chamber by a spatially homogeneous "chemical force" $\Delta\mu$, where $\Delta\mu$ stands for the free energy provided by the hydrolysis (or, arguably, binding) of one GTP molecule.

From Table 4.1, we see that the spatial symmetry of $\Delta\mu$ only allows it to couple to Eqs. (4.24a) and (4.24b). We also note that time-reversal symmetry imposes that these couplings are reactive. Neglecting thermal diffusion as discussed in Sec. 4.2.4, we obtain a modified set of constitutive equations:

$$\begin{aligned}
\sigma - \mathfrak{p} - h/p &= -\eta_z \nabla v - a \nabla\Omega + \xi_z \Delta\mu, && \text{(4.26a)}\\
\tau + h &= -a \nabla v - \eta_\theta \nabla\Omega + \xi_\theta \Delta\mu, && \text{(4.26b)}\\
J &= -\lambda \nabla\mu_e - b_1 \nabla h, && \text{(4.26c)}\\
X + J/\rho\Phi p &= -b_1 \nabla\mu_e - \tilde{\lambda} \nabla h. && \text{(4.26d)}
\end{aligned}$$

4.2.6 Hydrodynamic modes

The hydrodynamic relaxation modes are studied by linearizing the equations of motion around the state of thermal equilibrium. By definition, all thermodynamic forces vanish

at thermal equilibrium, and in particular $\Delta\mu = 0$. Let $\delta\rho = \rho - \rho_0$ and $\delta\Phi = \Phi - \Phi_0$ be the deviations of the mass density and of the mass fraction of fluid h from this state. Combining the conservation equations of Sec. 4.2.1 with the constitutive equations Eqs. (4.26) yields dynamical equations relating $\delta\rho$, $u_{z\theta}$ and $\delta\Phi$ with g, l and the reactive (equilibrium) forces $\mathfrak{p}$, h and μ_e:

$$\partial_t \begin{pmatrix} \delta\rho \\ u_{z\theta} \\ \delta\Phi \end{pmatrix} = A^r \nabla \begin{pmatrix} g \\ l \end{pmatrix} + A^d \nabla^2 \begin{pmatrix} \mathfrak{p} \\ h \\ \mu_e \end{pmatrix}, \tag{4.27}$$

$$\partial_t \begin{pmatrix} g \\ l \end{pmatrix} = -\gamma \begin{pmatrix} g \\ l \end{pmatrix} + \left[B^r + \gamma \begin{pmatrix} 0 & 0 & \frac{\rho}{\Phi} \\ 0 & 0 & 0 \end{pmatrix} A^d \right] \nabla \begin{pmatrix} \mathfrak{p} \\ h \\ \mu_e \end{pmatrix} + B^d \nabla^2 \begin{pmatrix} g \\ l \end{pmatrix}, \tag{4.28}$$

where the superscripts "r" and "d" denote matrices of reactive and dissipative couplings respectively. These matrices read

$$A^r = \begin{pmatrix} -1 & 0 \\ -\frac{1}{\rho p} & \frac{1}{I} \\ 0 & 0 \end{pmatrix}, \quad A^d = \begin{pmatrix} 0 & 0 & 0 \\ 0 & \tilde{\lambda} & b_1 \\ 0 & \frac{b_1}{\rho} & \frac{\lambda}{\rho} \end{pmatrix}, \quad \gamma = \begin{pmatrix} \gamma_{zz} & \gamma_{z\theta} \\ \gamma_{\theta z} & \gamma_{\theta\theta} \end{pmatrix}, \tag{4.29}$$

$$B^r = \begin{pmatrix} -1 & -\frac{1}{p} & 0 \\ 0 & 1 & 0 \end{pmatrix}, \quad B^d = \begin{pmatrix} \frac{\eta_z}{\rho} & \frac{a}{I} \\ \frac{a}{\rho} & \frac{\eta_\theta}{I} \end{pmatrix}. \tag{4.30}$$

We now consider Eqs. (4.18), (4.19) and (4.20), which describe the equilibrium thermodynamics of the system. They imply that

$$\mathfrak{p} = \rho^2 \left.\frac{\partial\left(f_s/\rho\right)}{\partial\rho}\right|_{\Phi,u_{z\theta}}, \; h = \left.\frac{\partial f_s}{\partial u_{z\theta}}\right|_{\rho,\Phi}, \; \mu_e = \frac{1}{\rho}\left.\frac{\partial f_s}{\partial\Phi}\right|_{\rho,u_{z\theta}}, \tag{4.31}$$

where the temperature T is considered constant. The fields $\mathfrak{p}$, h, μ_e are therefore functions of $\delta\rho$, $u_{z\theta}$, and $\delta\Phi$ only. Close to equilibrium, this dependence can be linearized, and we define the susceptibility matrix χ by:

$$\begin{pmatrix} \mathfrak{p} \\ h \\ \mu_e \end{pmatrix} = \chi \begin{pmatrix} \delta\rho \\ u_{z\theta} \\ \delta\Phi \end{pmatrix} = \chi \boldsymbol{x}. \tag{4.32}$$

Using this definition, we now derive a closed equation for the hydrodynamic variables. From Eq. (4.28), it is obvious that in the presence of friction against water (*i.e.* if γ is positive definite), g and l are irrelevant in the hydrodynamic limit, as shown when going from Eqs. (4.11) to Eqs. (4.12). They can thus be eliminated from the dynamics. In Fourier space and to leading order in the wave vector q, the linearized dynamical equation for $\boldsymbol{x}$ reads

$$i\omega\boldsymbol{x} = -q^2 \left(A^r \gamma^{-1} B^r + \tilde{A}^d \right) \chi \boldsymbol{x}, \tag{4.33}$$

where

$$\tilde{A}^d = \begin{pmatrix} 0 & -\frac{b_1}{\Phi} & -\frac{\lambda}{\Phi} \\ 0 & \tilde{\lambda} - \frac{b_1}{\rho\Phi p} & b_1 - \frac{\lambda}{\rho\Phi p} \\ 0 & \frac{b_1}{\rho} & \frac{\lambda}{\rho} \end{pmatrix}. \tag{4.34}$$

According to Eq. (4.33), the system has three diffusive hydrodynamic modes.

4.3 Very long time dynamics

The results of Section 4.2 allow for a full description of the hydrodynamic behavior of the dynamin-membrane tube. For instance, to predict the relaxation of a helix with some known initial and boundary conditions on the hydrodynamic variables $(\delta\rho, u_{z\theta}, \delta\Phi)$, one should diagonalize the matrix

$$M = \left(A^r \gamma^{-1} B^r + \tilde{A}^d\right) \chi \tag{4.35}$$

and solve three diffusion equations along the directions defined by its eigenvectors. The eigenvalues of M are the diffusion coefficients introduced in Sec. 4.1.2, and we label them in such a way that $D_1 > D_2 > D_3$. Unfortunately, this diagonalization yields very lengthy expressions from which no intuitive picture of the dynamics can be deduced. Nevertheless, we show in this section that all experimentally observable features of the tube's dynamics can be faithfully described by more convenient simplified equations.

The matrix M is the sum of two terms. This reflects the fact that the dynamics of the tube involves two sources of damping: $A^r\gamma^{-1}B^r\chi$ describes the friction against the outer water and $\tilde{A}^d\chi$ is associated with dissipation mechanisms internal to the tube, such as the helix/membrane friction. We now make an estimate of the orders of magnitude of these two effects. Assuming that the friction of the tube against water is that of a rigid rod of radius r_e (defined as the external radius of the dynamin coat) and length L yields[2] [76]

$$\gamma_{zz} \simeq \frac{2\pi\eta\rho^{-1}}{\ln\left(\frac{L}{r_e}\right) - 0.72},\ \gamma_{z\theta} = \gamma_{\theta z} = 0,\ \gamma_{\theta\theta} \simeq \frac{4\pi\eta r_e^2}{I}. \tag{4.36}$$

We evaluate the coefficients of $A^r\gamma^{-1}B^r$ from these expressions. Section 4.2.4 provide a similar estimate of $\tilde{A}^d$ (which is consistent with experiments as shown in Sec. 4.5.3), and the coefficients of $A^r\gamma^{-1}B^r$ are found to be at least four orders of magnitude larger than those of $\tilde{A}^d$. We can therefore diagonalize M perturbatively in $\tilde{A}^d\chi$, a slight generalization of first-order quantum mechanical perturbation theory to non-hermitian matrices [77]. The important point is that the unperturbed matrix $A^r\gamma^{-1}B^r\chi$ has one vanishing eigenvalue $D_3^0 = 0$. Indeed, the definitions of A^r and B^r imply that

$$A^r\gamma^{-1}B^r = \begin{pmatrix} ? & ? & 0 \\ ? & ? & 0 \\ 0 & 0 & 0 \end{pmatrix}, \tag{4.37}$$

where the question marks stand for non-zero coefficients. Clearly, the vector

$$\boldsymbol{x}_3 = \chi^{-1} \begin{pmatrix} 0 \\ 0 \\ 1 \end{pmatrix} \tag{4.38}$$

[2]Note that as far as Eq. (4.41) is concerned, the exact values of the coefficients of γ^{-1} do not matter as long as they are large. Therefore, there would be little point in trying to improve Eq. (4.36), by including hydrodynamic interactions for instance.

is an eigenvector of M associated with D_3^0. To lowest order in $\tilde{A}^d\chi$, D_3 is given by

$$D_3 = \frac{\lambda}{\rho}\frac{\det(\chi)}{\begin{vmatrix} \chi_{1,1} & \chi_{1,2} \\ \chi_{2,1} & \chi_{2,2} \end{vmatrix}}, \tag{4.39}$$

where the denominator of the right-hand side is the (3,3) cofactor of matrix χ, and $\boldsymbol{x}_3$ is the associated eigenvector. Note that D_3, being of order $\tilde{A}^d\chi$, is much smaller than D_1 and D_2.

This slow mode can be interpreted as follows. The orders of magnitude calculations given above show that γ^{-1} is large, meaning that the friction of water against the tube is very weak. Therefore, according to Eqs. (4.12) the tube quickly (although in hydrodynamic times $\propto q^{-2}$) relaxes to a state of constant tension and torque $\nabla\sigma = 0$, $\nabla\tau = 0$. Anticipating on the results of Sec. 4.5.3, we estimate that this regime is reached in a few tens of milliseconds for a tube of $10\,\mu$m. In experimental situations close to that of Ref. [36], this relaxation is much faster even than the injection of GTP in the experimental chamber. Therefore, when interested in observable time scales, one should consider that the two fast modes of Eq. (4.33) are always at equilibrium. Using Eqs. (4.26a), (4.26b), we deduce that $\mathfrak{p}$ and h have the following spatially homogeneous values:

$$\mathfrak{p} = \sigma + \frac{\tau}{p} - \left(\xi_z + \frac{\xi_\theta}{p}\right)\Delta\mu, \tag{4.40a}$$

$$h = -\tau + \xi_\theta\Delta\mu, \tag{4.40b}$$

where σ and τ are independent of z and are fixed by the boundary conditions imposed on the tube. Note that introducing GTP in the system, thus changing the value of $\Delta\mu$, is equivalent to applying a force $-\xi_z\Delta\mu$ and a torque $-\xi_\theta\Delta\mu$ to the tube.

If the two fastest modes are considered at equilibrium, the tube dynamics can be described by the evolution equation of the projection of the state of the system onto the third ("very slow") mode. In our approximation, this projection is $\delta\Phi/\left(\chi^{-1}\right)_{3,3}$. The equations of motion of the system therefore reduce to a single diffusion equation whose diffusion coefficient is the smallest eigenvalue of M:

$$\partial_t\delta\Phi = D_3\nabla^2\delta\Phi. \tag{4.41}$$

4.4 Susceptibility matrices

Although this is already true in the general case of Eq. (4.33), it appears even more clearly in the simplified Eqs. (4.38) and (4.39) that a full understanding of the dynamics requires an expression of the susceptibility matrix χ. Before proposing such expressions, we would like to comment on the nature of the assumptions they imply. Unlike in the previous sections, where only well-controlled approximations based on orders of magnitude and the symmetries of the system are used, the calculation of χ requires an explicit expression for the free energy of the tube. As emphasized in the beginning of this chapter, such a microscopic description is difficult given our limited knowledge of the mechanics of dynamin. Nevertheless, since the models that we develop in this section are equilibrium

models of the tube, all the information about the non-equilibrium behavior of the system is still being captured by the phenomenological coefficients introduced in Section 4.2.3. This means that we do not make any assumptions on the microscopic details of the dissipation mechanisms.

In the following, we first define a microscopic parametrization of the dynamin-membrane tube. Then we propose three equilibrium models of the tube, aimed at describing the experimental situations of Refs. [34, 35] and [24, 27, 28, 29, 33], where different types of lipids were used as templates for dynamin assembly.

4.4.1 Microscopic parametrization

For the sake of simplicity, let us start by idealizing the geometry. We first assume that the membrane is infinitely thin. It is confined to a roughly cylindrical shape by the dynamin helix but small deviations from this shape are allowed in the following. The energy cost of such deformations is fixed by the membrane's stretching and bending moduli k_s and κ. The detailed calculation of the membrane's bending energy in the geometry considered here is presented in Sec. B.1 of the appendix. We furthermore consider the helix as an infinitely thin inextensible elastic rod with spontaneous curvature and torsion, such that its equilibrium shape is a helix of radius $r = r_0$ and pitch $2\pi p = 2\pi\alpha r_0$. Its elasticity is described as that of a classical spring and is parametrized by its curvature and torsional rigidities $k_{\mathfrak{c}}$ and $k_{\mathfrak{t}}$ [78]. All relevant details are presented in Sec. B.2 of the appendix.

The assumption of inextensibility of the rod forming the helix is the most speculative point of this section. As mentioned in chapter 2 electron micrographs of dynamin helices treated with the non-hydrolyzable GTP analog GMPPCP suggest that the number of dynamin subunits per unit of helix length could change upon GTP binding [28, 29]. This is apparent in Fig. 2.3(C-D), where a red line highlights the conformational change that occurs in the middle radial density of the helix upon GMPPCP binding. The fact that this line becomes wavy could correspond to a contraction of each dynamin subunit. We still use the inextensibility assumption for simplicity and by lack of a satisfactory alternative hypothesis.

In the remainder of this chapter and unless otherwise stated, we express all quantities in units of the helix' spontaneous radius r_0, the mass per unit length ρ_0 and the typical force needed to stretch the helix $\mathcal{K} \simeq 2.2 \times 10^{-8}\,\mathrm{N}$ (see Sec. B.3 of the appendix). In these units, we define the deviations of the radius and pitch of the helix from their spontaneous values by $r = 1 + \delta r$ and $p = \alpha(1 + \delta p)$.

Let A be the area per polar head of lipids and A_0 its value at equilibrium. We define the relative deviation of A as $a = \frac{A - A_0}{A_0}$. Eventually, and although the confinement by the protein imposes an overall cylindrical shape on the membrane, we allow it to bend as long as it retains its helical symmetry. We parametrize this deformation by a number u such that the intersection of the membrane with the $x > 0$, $y = 0$ half-plane is the curve (see Fig. 4.3):

$$x = r\{1 + u[\cos(z/p) - 1]\}. \tag{4.42}$$

This approach is similar to that of Ref. [79]. Details are given in Sec B.1 of the appendix.

The elastic properties of the membrane and the helix are such that when assembled together, they tend to deform each other: the equilibrium configuration of the tube is

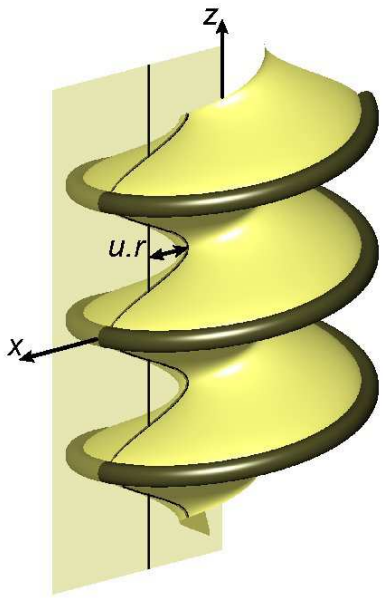

Figure 4.3: Sinusoidal deformations of the membrane out of its cylindrical shape are allowed in our model. The wavy black line materializes the intersection of the membrane with the $x > 0$, $y = 0$ half-plane. The equation of this line is given by Eq. (4.42). Note that it is constrained to touch the helix at each period of the tube.

different from the spontaneous shapes of the helix and membrane taken separately. However, we show in the following that these are small effects in the sense that at equilibrium, $\delta r \simeq \delta p \simeq a \simeq u \simeq 0$ to a good approximation. Therefore, at equilibrium, all the mass of the tube is concentrated at a radius r_0, hence $I = \rho_0 r_0^2 = 1$.

4.4.2 Rigid membrane model

In the experiments of Refs. [34, 35], dynamin is assembled on a mixture of non-hydroxylated fatty-acid galactoceramides, phosphatidylcholine, cholesterol, and PIP_2. The proportions of these lipids are such that even in the absence of dynamin, they spontaneously form nanorods with a diameter comparable to that observed for dynamin-coated tubes. Here we investigate a suggestion made in Ref. [36], namely that these lipid nanorods are very stiff. Consequently, we model them as rigid cylinders ($u = 0$) of fixed radius and area per polar head. The last two conditions are imposed by writing the free energy of the tube as

$$f_s = f_h + \frac{k_\infty}{2}\delta r^2 + \frac{k'_\infty}{2}a^2, \tag{4.43}$$

where f_h is the elastic energy of the helix, as calculated in Sec. B.2 of the appendix. The assumptions $\delta r = 0$, $a = 0$ are enforced by taking the limit $k_\infty, k'_\infty \to \infty$. Using the expression Eq. (B.13) for f_h and in the limit $k_\infty, k'_\infty \to \infty$, we induce no change in the dynamics by replacing Eq. (4.43) by

$$f_s(\delta r, \delta p, a) = \frac{k_\infty}{2}\delta r^2 + \frac{k_{pp}}{2}\delta p^2 + \frac{k'_\infty}{2}a^2. \tag{4.44}$$

Since the rod forming the helix is inextensible, its mass density is proportional to the rod length per unit length of the tube. The membrane's mass density, on the other hand, is proportional to the radius of the membrane cylinder and inversely proportional to the stretching rate of the membrane:

$$\rho_h = \Phi_0 \frac{\alpha\sqrt{r^2+p^2}}{p\sqrt{1+\alpha^2}} \tag{4.45a}$$

$$\rho_m = (1-\Phi_0)\frac{r}{1+a}. \tag{4.45b}$$

Combining these equations, we obtain expressions for $\delta\rho$ and $\delta\Phi$. We also notice that $u_{z\theta} = 1/p - 1/\alpha$, hence the first-order expressions:

$$\delta\rho = \left(1 - \frac{\alpha^2\Phi_0}{1+\alpha^2}\right)\delta r - \frac{\Phi_0\delta p}{1+\alpha^2} - (1-\Phi_0)a \tag{4.46a}$$

$$u_{z\theta} = -\frac{\delta p}{\alpha} \tag{4.46b}$$

$$\delta\Phi = \Phi_0(1-\Phi_0)\left(-\frac{\alpha^2\delta r}{1+\alpha^2} - \frac{\delta p}{1+\alpha^2} + a\right). \tag{4.46c}$$

Combining Eqs. (4.44) and (4.46) yields the function $f_s(\delta\rho, u_{z\theta}, \delta\Phi)$. The susceptibility matrix is essentially the matrix of second derivatives of this function [see Eqs. (4.31) for a more rigorous statement]. Taking the limit $k_\infty, k'_\infty \to \infty$, we finally find:

$$\lim_{\substack{k_\infty\to\infty \\ k'_\infty\to\infty}} \chi_{\mathrm{rm}}^{-1} = \frac{1}{k_{pp}} \begin{pmatrix} \frac{\Phi_0^2}{(1+\alpha^2)^2} & \frac{\Phi_0}{\alpha(1+\alpha^2)} & \frac{\Phi_0^2(1-\Phi_0)}{(1+\alpha^2)^2} \\ \frac{\Phi_0}{\alpha(1+\alpha^2)} & \frac{1}{\alpha^2} & \frac{\Phi_0(1-\Phi_0)}{\alpha(1+\alpha^2)} \\ \frac{\Phi_0^2(1-\Phi_0)}{(1+\alpha^2)^2} & \frac{\Phi_0(1-\Phi_0)}{\alpha(1+\alpha^2)} & \frac{\Phi_0^2(1-\Phi_0)^2}{(1+\alpha^2)^2} \end{pmatrix}. \tag{4.47}$$

4.4.3 Soft membrane models

In many *in vitro* experiments, dynamin is assembled on lipid bilayers containing no cholesterol and which spontaneously form lamellar phases or vesicles in the absence of dynamin [24, 27, 28, 29, 33]. From these two observations, we can presume that they are much softer than the lipids studied above and that their spontaneous curvature is zero or at least negligible compared to the curvature imposed by the dynamin coat ($\simeq 10^8\,\mathrm{m}^{-1}$). For these lipids, the microscopic variables δr, δp, a and u can thus all take non-zero values. The free energy of the tube is therefore the sum of three terms: the spring elastic energy of Eq. (B.13), a simple quadratic membrane stretching energy with stretching constant k_s and the membrane bending energy of Eq. (B.8). To second order:

$$\begin{aligned} f_s = {} & (k_{rr} + 2\pi\kappa)\frac{\delta r^2}{2} + k_{rp}\delta r\,\delta p + k_{pp}\frac{\delta p^2}{2} \\ & + 2\pi k_s\frac{a^2}{2} + \pi\kappa(-\delta r\, u) + k_{uu}\frac{u^2}{2} \\ & + \pi\kappa(-\delta r + u). \end{aligned} \tag{4.48}$$

Minimizing the tube's free energy with respect to δr, δp and u, we find that at equilibrium

$$\delta r_{\mathrm{eq}} \approx \delta p_{\mathrm{eq}} \approx \frac{\kappa}{\mathcal{K} r_0} \simeq 2 \times 10^{-4} \ll 1 \tag{4.49}$$

$$u_{\mathrm{eq}} \approx \frac{\kappa}{k_{uu}} \approx \alpha^4 \simeq 2 \times 10^{-3} \ll 1, \tag{4.50}$$

where we have made use of the fact that k_{rr}, k_{rp}, $k_{pp} \approx k_{\mathfrak{c}}$, $k_{\mathfrak{t}} \approx \mathcal{K}$ in dimensionless units [see Eqs. (B.12)]. We have considered a typical bending modulus $\kappa \simeq 10\, k_B T$ [80] and estimated $\alpha \simeq 0.2$ from Ref. [33]. These orders of magnitude show that the linear terms in f_s are very small and therefore we neglect the last term of Eq. (4.48) in the following. In other words, we use the approximation that at equilibrium the spring assumes its spontaneous radius and pitch $r_{\mathrm{eq}} = 1$, $p_{\mathrm{eq}} = \alpha$ and that the membrane is an unstretched cylinder of radius 1 [since $a_{\mathrm{eq}} = 0$ from Eq. (4.48) and $u_{\mathrm{eq}} = 0$].

As above, we want to express f_s (now a function of the microscopic variables δr, δp, a and u) as a function of the hydrodynamic variables $\delta\rho$, $u_{z\theta}$, $\delta\Phi$. Since there are four microscopic and three hydrodynamic variables, finding a unique relationship between the two sets of variables seems impossible at first sight. However, there exist constraints on the microscopic variables that have not yet been expressed. To understand these constraints, let us calculate two quantities to first order with the help of Eqs. (B.5) and (B.6): the mass density of lipids, which is the ratio of the surface area covered by the lipids to their area per unit mass:

$$\rho_{\mathrm{lipids}} \propto \frac{\mathfrak{s}}{1+a} = 2\pi(1 + \delta r - a - u) \tag{4.51}$$

and the volume of water enclosed by the tube:

$$\mathfrak{v} = \pi(1 + 2\delta r - 2u). \tag{4.52}$$

If all four microscopic variables were independent, ρ_{lipids} and $\mathfrak{v}$ would be independent as well. However, since the membrane tube is filled with water, allowing for a change of $\mathfrak{v}$ at constant ρ_{lipids} implies a flow of the water inside the tube relative to the lipids. We estimate the typical time scale associated to this flow to be that of a Poiseuille flow inside a tube of radius r_0 driven by a pressure difference $\mathcal{K}/r_0^2$ and over a distance $L = 10\,\mu$m:

$$t_{\mathrm{Poiseuille}} = \frac{8\eta(\pi r_0^2 L)}{\pi r_0^4} \frac{L}{\mathcal{K}/r_0^2} \simeq 40\,\mu\mathrm{s}. \tag{4.53}$$

Therefore, on time scales $t \ll t_{\mathrm{Poiseuille}}$, the relative flow of membrane and inner water is insignificant. Consequently, the ratio of mass density of membrane to mass density of inner water $\rho_{\mathrm{lipids}}/(\mathfrak{v}\rho_w)$ has to be a constant. Conversely, on time scales $t \gg t_{\mathrm{Poiseuille}}$, we can consider that the flow of water inside the tube has relaxed, hence ρ_{lipids} and $\mathfrak{v}$ are independent variables. On time scales $t \approx t_{\mathrm{Poiseuille}}$, the situation is more complex and a correct hydrodynamic theory would involve not two, but three different fluids: the helix, the membrane and the inner water. Such a treatment would obviously be quite heavy and relevant only on experimentally unobservable time scales. In the following, we therefore only calculate χ in the two limiting cases $t \ll t_{\mathrm{Poiseuille}}$ and $t \gg t_{\mathrm{Poiseuille}}$.

4.4.3.1 Short time scales: $t \ll t_{\text{Poiseuille}}$

In this limit, no relative flow of membrane and inner water is possible and the ratio $\rho_{\text{lipids}}/(\mathfrak{v}\rho_w)$ is a constant ($\rho_w = 10^3\,\text{kg.m}^{-3}$—the mass per unit volume of water—is considered a constant). Using Eqs. (4.51) and (4.52), this yields to first order:

$$\delta r + a - u = 0. \tag{4.54}$$

On top of this constraint, we can write three equations relating the microscopic variables to the hydrodynamic variables. Since the inner water and membrane cannot flow relative to each other, we treat them as a single fluid, which we label "fluid m", hence $\rho_m = \rho_{\text{lipids}} + \mathfrak{v}\rho_w$. Similarly to Eqs. (4.45) and using Eqs. (4.51), (4.52) and (4.54), we can write to first order:

$$\rho_h = \Phi_0 \frac{\alpha\sqrt{r^2+p^2}}{p\sqrt{1+\alpha^2}} \tag{4.55a}$$

$$\rho_m = (1-\Phi_0)(1+\delta r - a - u). \tag{4.55b}$$

Moreover, one still has $u_{z\theta} = 1/p - 1/\alpha$, hence to first order

$$\begin{aligned}\delta\rho &= \left(1 - \frac{\alpha^2\Phi_0}{1+\alpha^2}\right)\delta r - \frac{\Phi_0\delta p}{1+\alpha^2} \\ &\quad -(1-\Phi_0)a - (1-\Phi_0)u \end{aligned} \tag{4.56a}$$

$$u_{z\theta} = -\frac{\delta p}{\alpha} \tag{4.56b}$$

$$\delta\Phi = \Phi_0(1-\Phi_0)\left(-\frac{\alpha^2\delta r}{1+\alpha^2} - \frac{\delta p}{1+\alpha^2} + a + u\right). \tag{4.56c}$$

Combining these and Eq. (4.54) yields a unique relation between the microscopic and hydrodynamic variables. We express the free energy of Eq. (4.48) as a function of the latter and differentiate it, which yields an expression for $\chi_{\text{sm}}^{t\ll}$. More details are given in Sec. B.4 of the appendix.

4.4.3.2 Long time scales: $t \gg t_{\text{Poiseuille}}$

In this limit, the flow of water inside the tube has already relaxed and therefore ρ_{lipids} and $\mathfrak{v}$ are independent variables. Consistent with the hydrodynamic approach used in this chapter, we consider that the microscopic state of the system has the lowest free energy compatible with the values of the hydrodynamic variables. This yields the following constraint:

$$\left.\frac{\partial f}{\partial u}\right|_{\delta\rho,\, u_{z\theta},\, \delta\Phi} = 0 \quad \Leftrightarrow \quad u = \frac{\pi\kappa}{k_{uu}}\delta r + \frac{2\pi k_s}{k_{uu}}a. \tag{4.57}$$

As above, this constraint yields a unique relationship between the hydrodynamic and microscopic variables. Fluid m now represents only the membrane: $\rho_m = \rho_{\text{lipids}}$. However Eqs. (4.55b) and (4.56) remain valid. As above, $\chi_{\text{sm}}^{t\gg}$ is obtained by combining them with the constraint Eq. (4.57) and the second derivatives of f_s. See Sec. B.4 of the appendix for more details.

4.5 Predicting dynamin's conformational change

In this section we use electron microscopy data to evaluate the active force and torque generated by the tube when supplied with GTP. Using these results, we show that the conformational change of dynamin is expected to depend strongly on whether it is assembled on a soft or rigid membrane tube, which could account for seemingly contradictory experimental results. We then turn to the tube dynamics and make quantitative predictions concerning the conformational change of the tube and the time scales involved. Some of these are compared to experimental data in the next section.

The numerical estimates of this section are based on the typical values $\kappa \simeq 10\, k_B T \simeq 4 \times 10^{-20}\,\mathrm{J}$ [80] and $k_s \simeq 0.25\,\mathrm{N.m^{-1}}$ [75]. $\eta = 9 \times 10^{-4}\,\mathrm{Pa.s}$, and measurements show $r_0 \simeq 10\,\mathrm{nm}$, $\alpha \simeq 0.2$, $r_e \simeq 25\,\mathrm{nm}$ [33] and $\mathcal{K} \simeq 2.2 \times 10^{-8}\,\mathrm{N}$ (see Sec. B.3.4 of the appendix). The water friction and helix elastic constants are calculated from Eqs. (4.36) and (B.12). We also use $\rho_0 \simeq 7.5 \times 10^{-13}\,\mathrm{kg.m^{-1}}$ and $\Phi_0 \simeq 0.5$ (see Sec. 4.2.4).

4.5.1 Determination of the active terms

According to the symmetry arguments developed in Sec. 4.2.5, exposing the tube to GTP yields the same deformation as applying a force $-\xi_z \Delta\mu$ and a torque $-\xi_\theta \Delta\mu$ to it. Making an analogy with a spring submitted to a force and torque, we expect a uniform change of radius and pitch for a dynamin helix incubated with GTP for a very long time. Ignoring fluctuations, this is consistent with experimental data [24, 27, 28, 29, 33, 34, 35].

Let us first turn to Ref. [33], where the nucleotide used is GTP. As discussed is Sec. 4.4.3, this system is described by $\chi_{\mathrm{sm}}^{t\gg}$ on long time scales. In those experiments, the changes of pitch and radius of the dynamin helix are measured to be

$$\Delta r = \lim_{t\to\infty} \delta r \simeq -0.5, \quad \Delta p = \lim_{t\to\infty} \delta p \simeq -0.31, \tag{4.58}$$

which is compatible with the results of Refs. [24, 27, 28, 29]. Here we use our knowledge of $\chi_{\mathrm{sm}}^{t\gg}$, Δr and Δp to deduce the amplitude of the active terms $\xi_z \Delta\mu$ and $\xi_\theta \Delta\mu$, just like the force and torque exerted on a spring can be deduced from its elastic moduli and the amplitude of its deformation.

We consider that no external force or torque are exerted on the tube ($\sigma = 0$, $\tau = 0$) and assume that the tube is connected to a membrane reservoir, which at equilibrium fixes the membrane's chemical potential $\mu_m = \mu - \Phi\mu_e$ throughout the tube, independent of the presence or absence of GTP. Our reference state is a tube in the absence of GTP, which therefore has $\mathfrak{p} = 0$, $h = 0$, $\mu_e = 0$. Eqs. (4.40) yield the values of $\mathfrak{p}$ and h in the presence of GTP. In order to calculate the value of μ_e in this situation, we first write the Gibbs-Duhem relation for the tube:

$$\mathrm{d}\mu = \frac{\mathrm{d}\mathfrak{p}}{\rho} + \mu_e \mathrm{d}\Phi + \frac{h}{\rho}\mathrm{d}u_{z\theta}. \tag{4.59}$$

Since μ_e and h both vanish in the tube's reference state, this equation can be simplified by keeping only the first order terms in the displacement around the reference state:

$$\mathrm{d}\mu = \frac{\mathrm{d}\mathfrak{p}}{\rho_0}. \tag{4.60}$$

The membrane reservoir's chemical potential is defined up to a constant. In the following, we use this indeterminacy to impose $\mu_m = 0$, which yields

$$\mu = \mathfrak{p}, \tag{4.61}$$

where we use the fact that $\rho_0 = 1$ in dimensionless units. To first order, this yields

$$\mu_m = \mathfrak{p} - \Phi_0 \mu_e, \tag{4.62}$$

Since μ_m is independent of the presence or absence of GTP, it must remain equal to zero even in the presence of GTP. Combining Eqs. (4.40) and (4.62), we show that in the presence of GTP

$$\mu_e = -\frac{\xi_z \Delta\mu}{\Phi_0} - \frac{\xi_\theta \Delta\mu}{\alpha \Phi_0}. \tag{4.63}$$

We finally combine Eqs. (4.32), (4.40) and (4.63) to find

$$\begin{pmatrix} \Delta\rho \\ \Delta u_{z\theta} \\ \Delta\Phi \end{pmatrix} = \left(\chi_{\rm sm}^{t\gg}\right)^{-1} \begin{pmatrix} -\xi_z\Delta\mu - \xi_\theta\Delta\mu/\alpha \\ \xi_\theta\Delta\mu \\ -\xi_z\Delta\mu/\Phi_0 - \xi_\theta\Delta\mu/\alpha\Phi_0 \end{pmatrix}. \tag{4.64}$$

Moreover, according to Sec. B.4 of the appendix, the left-hand side of this equation is a known function of Δr, Δp and $\Delta a = \lim_{t\to\infty} a$. We solve Eq. (4.64) in $\xi_z\Delta\mu$, $\xi_\theta\Delta\mu$ and Δa and obtain

$$\xi_z\Delta\mu \simeq -3.5\times10^{-11}\,\mathrm{N}, \quad \xi_\theta\Delta\mu \simeq 2.6\times10^{-17}\,\mathrm{N.m}, \quad \Delta a \simeq -1.6\times10^{-15}. \tag{4.65}$$

4.5.2 Variability of the conformation after GTP hydrolysis

In contrast with the results presented above, Refs. [34, 35] report that the radius of the dynamin helix does not change upon incubation with GTP analogs and that its pitch does not decrease but increases, yielding $\Delta r' \simeq 0$, $\Delta p' \simeq 0.7$ (in the following, the primes denote the deformations associated with these references). Although there are several biochemical differences between these experiments and those reported in Refs. [24, 27, 28, 29, 33], such as the presence or absence of the PRD domain of dynamin and the type of nucleotides used (see Sec. 2.2), we show here that it is possible to account for those apparently contradictory results only by the mechanical properties of the lipids.

We describe the equilibrium properties of the tubes used in these experiments by $\chi_{\rm rm}$, as discussed in Sec. 4.4.2. Assuming that the biochemistry of the tubes considered here is the same as in Refs. [24, 27, 28, 29, 33] implies that the active terms have the values given in Eq. (4.65). Again assuming that μ_m is held constant by a membrane reservoir, we combine Eqs. (4.32) and (4.40) to find

$$\begin{pmatrix} \Delta\rho' \\ \Delta u'_{z\theta} \\ \Delta\Phi' \end{pmatrix} = \left(\chi_{\rm rm}\right)^{-1} \begin{pmatrix} -\xi_z\Delta\mu - \xi_\theta\Delta\mu/\alpha \\ \xi_\theta\Delta\mu \\ -\xi_z\Delta\mu/\Phi_0 - \xi_\theta\Delta\mu/\alpha\Phi_0 \end{pmatrix}. \tag{4.66}$$

It is clear from the assumptions of Sec. 4.4.2 that combining this equation with Eqs. (4.46) and (4.47) yields $\Delta r' = \Delta a' = 0$. More interestingly,

$$\begin{aligned}\Delta p' &= -\alpha u_{z\theta} \\ &= \left[\xi_z + \left(1 - \frac{1+\alpha^2}{\Phi_0}\right)\frac{\xi_\theta}{\alpha}\right]\frac{\Phi_0 \Delta\mu}{(1+\alpha^2)k_{pp}} \\ &= \Delta p + \frac{2(1-\alpha^2)(k_{\mathfrak{c}} - k_{\mathfrak{t}})}{4k_{\mathfrak{c}}\alpha^2 + k_{\mathfrak{t}}(1-\alpha^2)^2}\Delta r. \end{aligned} \tag{4.67}$$

Therefore, we predict that the pitch increases ($\Delta p' > 0$) if and only if

$$\frac{k_{\mathfrak{t}}}{k_{\mathfrak{c}}} > \frac{2(1-\alpha^2)\Delta r + 4\alpha^2 \Delta p}{2(1-\alpha^2)\Delta r - (1-\alpha^2)^2 \Delta p} \simeq 1.5. \tag{4.68}$$

This condition is not satisfied by the cylindrical rod model leading to Eq. (B.12). One should however temper this result by considering the crudeness of this model, the limited applicability of our small deformation formalism to the high nucleotide concentration experiments considered in this section, as well as the rather large uncertainty on several numerical values used here. We therefore consider Eq. (4.67) as a proof of principle that a radius shrinkage on a soft membrane is compatible with a radius increase on a rigid membrane.

4.5.3 Time scales

Turning to the dynamics of the tube as described in Ref. [36], we apply the perturbation scheme of Sec. 4.3 to $\chi_{\rm sm}^{t\gg}$ using the typical numerical values presented throughout this chapter. We furthermore assume that the size and boundary conditions of the system are such that the smallest wave vector allowed is $q_{\rm min} = 1/(30\,\mu{\rm m})$ [81]. Eq. (4.33) implies that the deformations characterized by $q_{\rm min}$ dominate the long-time relaxation of each of the three hydrodynamic modes of the system, yielding three relaxation times $\tau_i = 2\pi/D_i q_{\rm min}^2$, $i = 1, 2, 3$. For simplicity and without loss of generality, we discuss only these deformations in the following. Finally, we assume that one end of the tube is in contact with a membrane reservoir imposing the boundary condition $\mu_m(z = 0) = 0$. The relaxation time scales are found to be well-separated: $\tau_1 \simeq 181\,\mu$s, $\tau_2 \simeq 59\,$ms and $\tau_3 \simeq 4.1\,$s. This retrospectively validates the perturbative approach of Sec. 4.3.

Comparing τ_1 to $t_{\rm Poiseuille}$ [Eq. (4.53)], we find that $\chi_{\rm sm}^{t\gg}$ is probably not a good description of the tube on this time scale and that some intermediate matrix between $\chi_{\rm sm}^{t\ll}$ and $\chi_{\rm sm}^{t\gg}$ should be used. Looking at Fig. 4.4, however, we realize that the dynamics generated by the two matrices are not very different and that using one or the other does not make much difference at our level of description. On the other hand, it is clear that the transformations characterized by τ_2 and τ_3 must be described using $\chi_{\rm sm}^{t\gg}$.

In agreement with Sec. 4.3, τ_1 and τ_2 are smaller than the time needed to inject GTP in the experimental chamber (typically a few tenths of seconds) and are therefore experimentally unobservable: the approximate Eq. (4.41) is sufficient to describe current experiments.

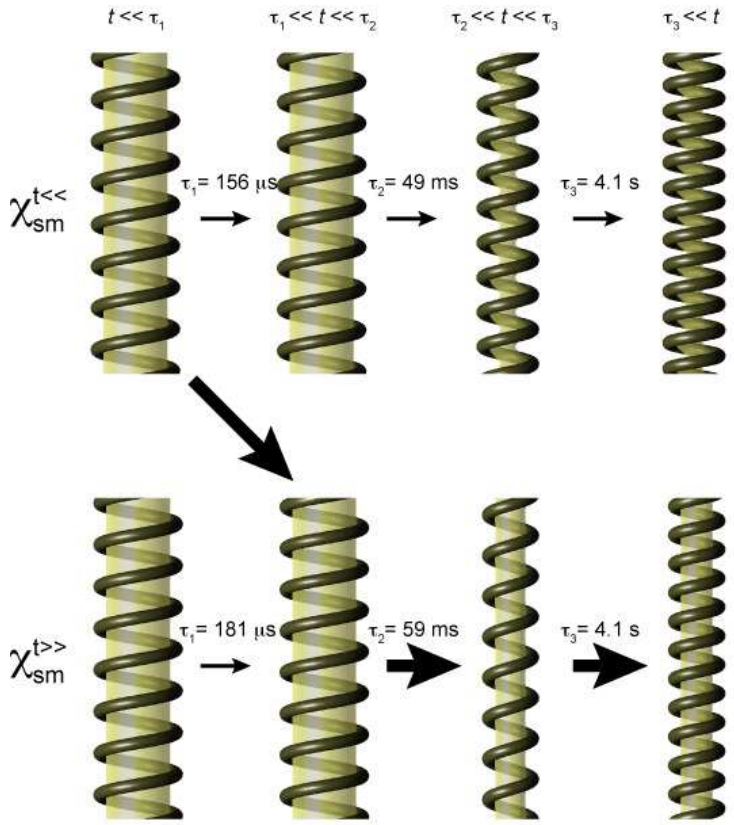

Figure 4.4: Illustration of the dynamics of the tube generated by the susceptibility matrices $\chi_{\rm sm}^{t\ll}$ and $\chi_{\rm sm}^{t\gg}$. Note that to a good approximation, the field of deformation of the tube is independent of z during the lag phases between the relaxation of the chronologically well-separated hydrodynamic modes. The amplitude of the deformations are calculated from Eq. (4.65). The transparency of the membrane illustrate its stretching and is proportional to $1+a$. The thick black arrows represent the expected changes of conformation based on the comparison of the τ_is with $t_{\rm Poiseuille}$ (see text).

4.6 Experimental observation of the hydrodynamic behavior

In this section, we present and discuss recent experimental results obtained by Sandrine Morlot and Aurélien Roux in the group of Patricia Bassereau at Institut Curie that confirm the validity of our hydrodynamic approach.

The basic procedure used in these experiments is described in Ref. [36]. Biotinilated dynamin and streptavidin-coated polystyrene beads (radius $r_{\rm bead} = 130\,{\rm nm}$) are added to a lamellar phase made of a mixture of pure lipids mimicking brain polar lipids and containing 5% PIP_2. This generates long (several tens of micrometers) dynamin-coated membrane tubes with beads attached to them by biotin-streptavidin bonds. When GTP is injected in the experimental chamber, the tubes become more tense and the beads start rotating, revealing the dynamics of the helix' conformational change [Fig. 4.5(a)].

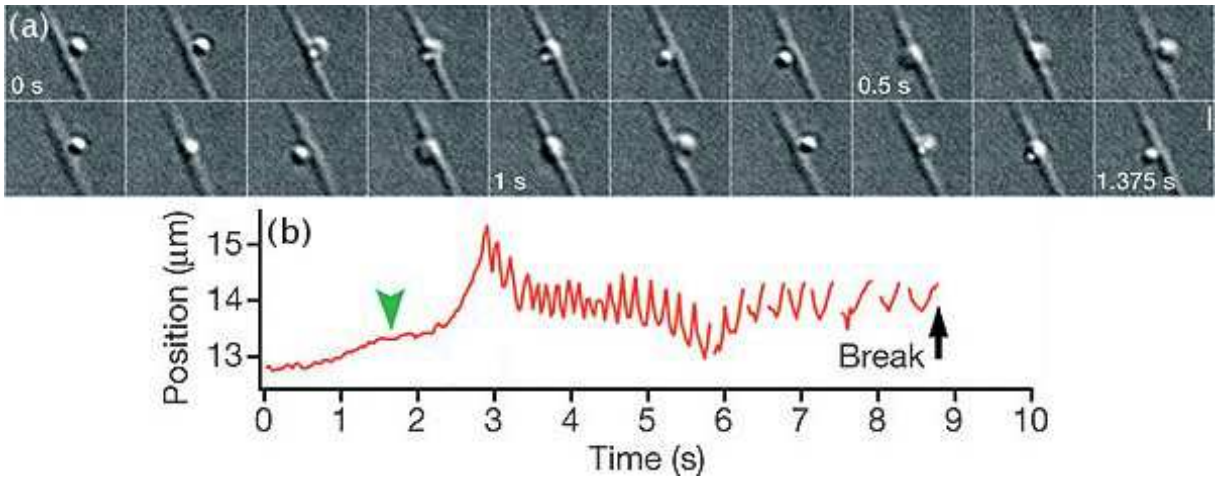

Figure 4.5: Real-time observation of dynamin's conformational change. (a) Rotation of a polystyrene bead bound to the tube observed in differential interference contrast microscopy. Scale bar, 1 μm. (b) Tracking of the bead's position in the direction perpendicular to the tube. The arrowhead denotes the beginning of the injection of a 1000 μM GTP solution into the experimental chamber. After a delay due to the injection procedure, the rotation of the bead is recorded as an oscillation in its position. In this particular experiment, the tube broke before the rotation stopped completely. Figure taken from Ref. [36].

Unless mentioned otherwise, GTP is injected at a concentration 100 μM in all experiments presented here. By using a large quantity of beads, one can label each tube by multiple beads, and thus monitor the strain of the helix both as a function of space and of time.

These experiments are monitored in optical microscopy, which means that their resolution is imposed by the diffraction limit. We thus have access to the dynamics of the tube on length scales of order one micrometer, which is much larger than the typical microscopic length scale of the problem $r \approx 10\,\mathrm{nm}$. Hence we expect any behavior observed by this technique to fall within the domain of applicability of our hydrodynamic formalism. Also, the time resolution of these experiments is typically of the order of 100 ms. Considering the time scales calculated in Sec. 4.5.3, this means that only the longest-lived mode of the tube is observed, and the dynamics should thus be well described by Eq. (4.41).

4.6.1 Exponential relaxation on long time scales

On long time scales, Eq. (4.41) predicts an exponential relaxation of the helix with a longest relaxation time

$$\tau_3 = \frac{1}{D_3 q_{\mathrm{min}}^2} \approx \frac{\rho}{\chi_{\mathrm{sm}} \lambda q_{\mathrm{min}}^2}, \tag{4.69}$$

where the order-of-magnitude equality comes from Eq. (4.39). This is indeed observed experimentally, as seen on Fig. 4.6(a). In this figure, the rotation rate $\mathrm{d}\theta/\mathrm{d}t$ of the bead is plotted against the total amount of rotation θ of the bead since GTP injection.

After a transient stage (due to the non-ideality of the GTP injection procedure and to the relaxation of shorter-lived modes), a linear relationship between $\mathrm{d}\theta/\mathrm{d}t$ and θ is observed (solid line), indeed confirming our prediction of a single exponential relaxation. The slope of the curve is equal to $-1/\tau_3$, and the fit yields $\tau_3 = 3.4\,\mathrm{s}$. This is in good agreement with the value $\tau_3 = 4.1\,\mathrm{s}$ predicted in Sec. 4.5.3 considering the fact that the value $q_{\min} = 1/(30\,\mu\mathrm{m})$ that we use is only an estimate. Also, since we do not know the coefficients of χ_{sm} very accurately, further measurements are required to obtain a precise value of λ. Still, even only an order-of-magnitude agreement between the experimental and *a priori* determined value of τ_3 suggests that both the picture of the long-time dynamics of the tube as dominated by the friction between helix and membrane (Sec. 4.2.4) and our description of χ_{sm} are essentially correct.

By taking into account not only the longest-lived mode of the tube, but also Fourier modes with a shorter wavelength, it is possible to give a good description of the transient, non-exponential regime observed for small values of θ in Fig. 4.6(a). This more complex description involves one more adjustable coefficient compared to the linear fit presented above: the position of the bead on the tube. Assuming that the tube has its $z = 0$ end bound to the experimental chamber $[\theta(z = 0) = 0]$ and the one in $z = L$ free $[\partial_z\theta(z = 0) = 0]$, the best fit to the data is found by placing the bead in $z = 0.62 \times L$.

4.6.2 GTP hydrolysis induces a homogeneous strain

In our formalism, nucleotide addition is equivalent to exerting a force and a torque on the tube. Hence, after relaxation of the transient regime, incubation with GTP should induce a homogeneous strain of the dynamin helix. Therefore, two beads separated by a certain distance should rotate relative to each other a number of times proportional to this distance. Let us consider a tube attached in $z = 0$. Denoting by $\Delta\theta$ the total rotation angle of a bead located at the altitude z between GTP injection and the end of its motion, we expect that

$$\Delta\theta \propto z. \tag{4.70}$$

This proportionality is verified experimentally, as shown in Fig. 4.6(b). In practice, the proportionality coefficient implicit in Eq. (4.70) depends on the tube considered, and we have to scale the two data sets presented in Fig. 4.6(b) in order to collapse them onto the same line. This is not *a priori* expected from the theory, but can easily be accounted for by the limited reproducibility of the experiments. Indeed, experimental parameters such as the composition of the lipid bilayer inside the tube or the concentration of the GTP solution after injection (and therefore dilution) in the experimental chamber are not very well controlled and could vary from experiment to experiment, thus inducing variations in χ_{sm}, $\Delta\mu$ and the dissipative coefficients considered in this chapter.

This result is intimately linked to the assumption of non-polarity of the dynamin helix. Indeed, without it, couplings between the force $\Delta\mu$ and the flux J would have been allowed in Eq. (4.26c). In that case, $\Delta\theta$ would have been not proportional to z only, but a linear combination of z and z^2. Since the points presented in Fig. 4.6(b) are very well aligned, it seems that this coupling is either very weak, or indeed forbidden for symmetry reasons. This suggests that the subunits of the dynamin helix themselves are apolar, as suggested by electron microscopy studies [27, 28, 29].

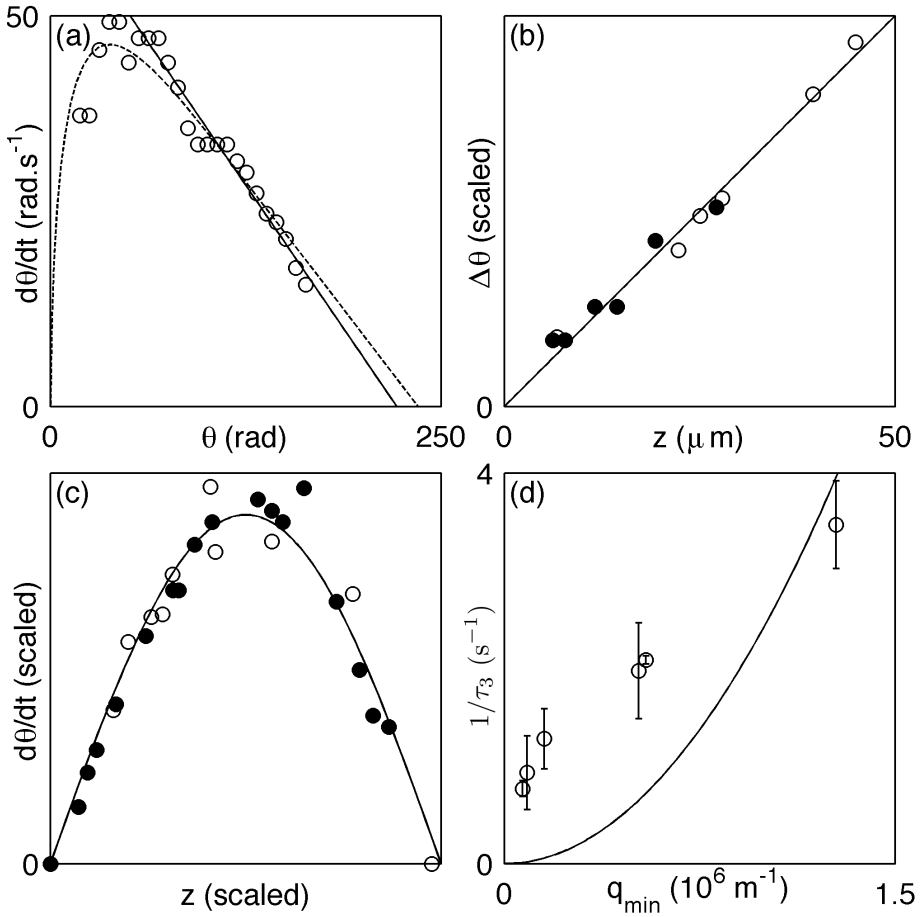

Figure 4.6: Experimental justification of our hydrodynamic approach. (a) Relaxation of the bead visualized in Fig. 4.5 after injection of a 1000 μM solution of GTP. Solid line: fit to an exponential relaxation. Dashed line: all-Fourier-modes fit. Data taken from Ref. [36]. (b) Total amount of rotation between GTP injection and the end of the motion as a function of the coordinate z for two tubes (open and filled circles, respectively) attached at one end only. The data for the two tubes was collapsed by multiplying the $\Delta\theta$s of each tube by an adjustable factor. (c) Long-time angular velocity profile along two tubes (open and close circles, respectively) attached at their two ends. Both the zs and dθ/dts of each tube were multiplied by an adjustable factor. (d) Relaxation time as a function of the smallest wave vector compatible with the boundary conditions on the tube. Unpublished experimental data courtesy of Sandrine Morlot and Aurélien Roux.

4.6.3 The longest-lived mode has a sinusoidal shape

According to Eq. (4.41), the tube's relaxation dynamics is diffusive. This implies that its longest-lived mode should be the broadest sinusoid compatible with the boundary conditions imposed on the tube. Experimentally, one often encounters tubes that are bound to the glass wall of the experimental chamber in two well-identified points. This imposes that the rotation velocity of the helix be zero at those two points. Therefore, we predict that the velocity profile has the sinusoidal shape plotted as a line in Fig. 4.6(c).

In order to verify this prediction, the velocity profile along two such tubes is measured at a given time chosen such that the dynamics is into the single-exponential regime pictured in Fig. 4.6(a). This indicates that the amplitude of the shortest-lived hydrodynamic modes should be negligible. A good agreement with our prediction is observed, as shown in Fig. 4.6(c). In this figure, the coordinate z was scaled to impose that the sinusoid crossed the horizontal axis in the two locations identified as the attachment points between the helix and the glass. The vertical axis also had to be scaled for the same reasons as in Sec. 4.6.2.

4.6.4 Scaling of the relaxation time with the wave vector

According to Eq. (4.69) the dominant relaxation time τ_3 should scale with the inverse square of $q_{\min}$:

$$1/\tau_3 = D_3 q_{\min}^2 \tag{4.71}$$

as the size of the tube (and therefore $q_{\min}$) is varied. Using the experimental protocol described above, tubes of a wide variety of lengths form spontaneously, and one has no control over how and where they attach to the glass. Exploiting data similar to that displayed in Fig. 4.6(c), we estimate that a tube bound to the glass in z satisfies the no-slip boundary condition $\theta(z) = 0$, whereas if it has a free end in z it satisfies a zero-stress boundary condition $\nabla\theta(z) = 0$. Therefore for a tube of length L, the smallest wave vector satisfying the boundary conditions is given by $q_{\min} = \pi/L$ if both its ends are attached and by $q_{\min} = \pi/2L$ if one end is attached and the other is free.

Selecting tubes of various lengths with experimentally apparent boundary conditions yields the results of Fig. 4.6(d). In this figure, each circle corresponds to one tube and the error bars represent the uncertainty over the slope τ_3 stemming from the fit procedure described in Sec. 4.6.1. Note that this is far from being the only source of uncertainty in this system, and that the data presented here is less reliable than the error bars suggest. First of all, as mentioned in Sec. 4.6.2 the variability of the experimental conditions imply that the diffusion coefficient D_3 [which is given by Eq. (4.39)] is likely to vary from experiment to experiment, thus compromising our chances to see the data points of Fig. 4.6(d) align in a parabola as required by Eq. (4.71). Second, one might also consider the possibility that the hydrodynamic drag on the beads attached to the tube might modify its hydrodynamics. However, comparing a typical value for these torques $\tau_{\text{bead}} = 14\pi r_{\text{bead}}^3 \eta\dot{\theta} \simeq 5 \times 10^{-21}\,\text{N.m}$ [82] to our estimate $\xi_\theta \Delta\mu \simeq 1.3 \times 10^{-18}\,\text{N.m}$ of the typical torque driving the dynamics of the tube, we find that this effect should be negligible. It should still be noted that the numerical values used here are only rough estimates deduced from data obtained in a variety of experimental conditions. It would thus be interesting to reconsider this question in the light of forthcoming direct torque measurements. Third, it is apparent in Fig. 4.6(d) that the convexity of the law Eq. (4.71) is not seen in the data points. This might be due to a systematic bias in the evaluation of the lengths of the tubes used in these experiments. Indeed, not all helices formed around the membrane are continuous over tens of micrometers, and longer helices obviously tend to have more breaks than short ones. What appears to be long helices experimentally might thus be several shorter helices, meaning that we underestimate the $q_{\min}$ for the smallest values of $q_{\min}$. This might account for why the data of Fig. 4.6(d) seems to align

in a concave rather than convex curve. More light could be shed on these matters thanks to better-controlled experiments, as discussed in the next section.

Finally, however, it is very clear from Fig. 4.6(d) that the longest relaxation time of the tube strongly depends on its length and is larger for longer tubes. This is experimental evidence that the fundamental assumption of hydrodynamics Eq. (4.8) applies to the experimentally observable relaxation modes of dynamin-coated membrane tubes, and therefore a confirmation of the validity of our theoretical approach.

4.7 Discussion

In this chapter we describe the dynamics of long dynamin-coated membrane tubes typically used in *in vitro*, cell-free experiments. This work is therefore relevant to the biological membrane severing function of dynamin insofar as we assume that the tube breaking mechanisms are similar in those two cases. This last section summarizes and discusses our results in this perspective.

Our formalism describes several previously unaccounted for experimental results. Concerning the statics of dynamin, we suggest an explanation for the variability in the conformational changes obtained by different experimental groups. Moreover, it is reported in Refs. [33, 36] that long tubes incubated with GTP tend to form plectonemic supercoils, which is consistent with our findings. Indeed, in our description, tubes held fixed at both ends and provided with GTP are analogous to rods with persistence length ℓ_p under a torque $\xi_\theta \Delta\mu$ and a compressive force $\xi_z \Delta\mu$. Therefore, creating a circular coil of radius $\mathcal{R}$ has a bending energetic cost of $2\pi k_B T \ell_p/\mathcal{R}$, and a cost associated with working against the force to shorten the tube equal to $2\pi\mathcal{R} \times \xi_z \Delta\mu$. Meanwhile, it allows the helix to give in one turn to the applied torque, thus lowering the system's free energy by a quantity $2\pi\xi_\theta\Delta\mu$. Minimizing the coiled tube's free energy with respect to $\mathcal{R}$, we expect the free energy difference between the coiled and straight configuration to be equal to $2\pi\left(-\xi_\theta\Delta\mu + 2\sqrt{-\xi_z\Delta\mu k_B T\ell_p}\right) \simeq -1.3\times10^{-16}\,\mathrm{J}$. Since this numerical value is negative, we expect tubes to form supercoils with a radius $\mathcal{R} = \sqrt{-k_B T\ell_p/\xi_z\Delta\mu} \simeq 65\,\mathrm{nm}$. This number is consistent with the experimental observation of tightly wound supercoiled tubes [36]. Moving on to the dynamics of the tube, we show that the longest-lived and only experimentally observable internal relaxation phenomenon of the tube is an effective friction mechanism between dynamin helix and lipids. From this we conclude that the internal dynamics of the tube can be approximated by a single diffusion equation.

This very simple form for the tube's dynamics implies robust features that are observed experimentally: first, the relaxation of the tube's dynamics is exponential on long time scales [36]; second, on long time scales, the rotation frequency of the tube has a sinusoidal dependence in z, which is the shape of the slowest eigenmode of the diffusion equation. Finally, the dominant relaxation time of the tube appears to go to infinity as the tube length diverges, which is the signature of a hydrodynamic behavior. All those results are indications that our hydrodynamic approach is valid, meaning that the tubes change conformation in a concerted way, rather than the dynamin depolymerizing upon GTP addition as suggested in Refs. [37, 38].

Because it relies heavily on the symmetries of the system studied, the hydrodynamic

approach also yields some insight into the structure of the dynamin helix. Indeed, we predict that for an apolar polymer, the presence of GTP should be equivalent to applying a force and torque on the tube. Experiments support that conclusion, thus bringing evidence of the non-polarity of the dynamin helix in a very independent way to previously available electron microscopy data [27, 28, 29].

We now discuss the assumptions used to derive our formalism. The most important of these is our use of the large-system limit $L \gg r_0$. The hydrodynamic behavior observed for the tube is only expected in this limit, meaning that this assumption is justified in the *in vitro*, cell-free experiments considered in this work. Unfortunately, dynamin collars observed *in vivo* are much shorter—typically two to three helical repeats [12]. However, we believe that our concepts of friction between helix and membrane and GTP-induced force and torque can be readily transposed to short tubes. One could also be concerned that on small length scales, non-hydrodynamic relaxation phenomena occur on the same time scales as the relaxation phenomena we discuss here and therefore interfere with our picture of the relaxation of the tube. To address this point, we note that according to Ref. [36], breaking long ($\approx \mu$m) tubes takes seconds, which is much longer than any reasonable non-hydrodynamic relaxation time for this system. Equivalently, we can say that the tube does not break in short (non-hydrodynamic) times, from which we conclude that non-hydrodynamic internal relaxation phenomena should not be essential to tube breaking. Therefore, although the *in vivo* situation is undoubtedly more complex than that considered here, we argue that our description of the internal dynamics of the tube is sufficient to study its tube-severing function.

By writing constitutive equations for the tube, we assumed it to be weakly out of equilibrium. Concerning the friction and viscosity-related phenomenological coefficients [those of Eqs. (4.24)], experience shows that this requirement is not very stringent [63], and our constitutive equations are likely to give a good description of the system in most situations. Chemical systems, on the other hand, typically operate far from equilibrium. In this regime, writing the active forces of Sec. 4.2.5 as $\Delta\mu$ does not yield the correct dependence on the GTP concentration. Better results would probably be obtained by using instead $1 - e^{-\Delta\mu/k_BT}$, which is characteristic of molecular motors [83]. Forthcoming experiments involving low levels of GTP are expected to better fall in the domain of applicability of our theory.

Assumptions of small deviations of the tube from its initial state are also used when deriving the susceptibility matrices χ. Again, these are formally correct at small concentrations of GTP. However, given the fact that those matrices involve uncertain microscopic assumptions, we regard them as nothing more than reasonable examples anyway. Therefore, we do not expect them to yield quantitative results. More reliable information about the characteristics of these matrices could be extracted from micromechanical experiments on dynamin-coated tubes. Such experiments are however difficult and might lead to ambiguous results, as exampled in Sec. B.5 of the appendix.

We now turn to dynamin-induced tube breaking models from the literature. We do not discuss the purely biochemical model of dynamin as a regulatory GTPase—which has consistently been regarded as unlikely over the past few years [7, 16, 17]—and rather concentrate on the mechanochemical models. Depending on authors, the critical feature leading to tube breaking by dynamin has alternately been proposed to be a change of

radius [21], of pitch [34], or membrane bending [79]. As can be seen from Sec. 4.4.3, all of these deformations fit very naturally in our theoretical framework. Our formalism moreover takes into account the fact that dynamin's conformational change could stretch the membrane. We would therefore like to attract attention on this fourth type of deformation of the tube, which might play an important role in tube breaking. It should also been kept in mind that external factors, such as the actin cytoskeleton, could play a role in the tube breaking mechanism. Actin has indeed been shown to colocalize with dynamin during clathrin-coated endocytosis events [84], possibly because of cortactin-mediated interactions [85]. Its role could be to maintain the tube under tension [86], an effect that our mechanics-based framework accommodates very easily.

Unlike previous models, the present work does not rely on detailed assumptions about the tube's conformational changes. Instead, we predict them by optimally exploiting the experimental data in the light of thermodynamic considerations, conservation laws and symmetry arguments.

Several models have also been proposed for the coupling of GTP to dynamin activity: GTP hydrolysis could induce a concerted conformational change [35], while some results suggest that the crucial step is the binding of GTP to dynamin [87] and others point to a ratchet-like mechanism for its constriction [88]. Since in our framework the coupling of the energy source to the dynamics is deduced from symmetry considerations only, our theory is equally valid in each of these cases.

In addition to including most features previously discussed in the literature, our formalism yields novel quantitative insight into the mechanism of tube breaking. It would be interesting to further discuss Refs. [79, 86], where it is assumed that lipids cannot flow through the dynamin-coated region of the tube, in parallel with Ref. [89], where this flow is on the contrary considered as instantaneous, in the light of our new knowledge of the helix/membrane friction coefficient λ.

Furthermore, our hydrodynamic point of view could account for some discrepancies between existing models and experiments. Adopting the classification given in Ref. [16] and reproduced in Fig. 4.7, we consider models of the "Molecular Garrote" class—where the reduction of the dynamin radius pinches the membrane tube to its breaking—and of the "Rigid helix/Elastic membrane" class—where the tube breaks because its walls are brought together by a sudden deformation of the helix [Fig. 4.7(a) and (c)]. If taken at face value and applied to a long tube, these local models predict a uniform density of tube breaks, since what is expected to happen at the neck of a clathrin-coated endocytosis vesicle should happen at every point of the long helix. Experimentally, however, no breaking is observed in such tubes unless their ends are firmly attached to a fixed substrate [33]. Moreover, attached tubes are observed to straighten upon GTP injection and then break not at several but at a single point [36]. This sensitivity to distant boundary conditions and spatially inhomogeneous behavior of the tube motivate our description of long-range interactions mediated by tube elasticity and of the z-dependence of the tube deformation, which could account for the existence of a preferred point of breaking.

In the "Molecular Spring" model [34] as well as in Ref. [86], breaking only occurs at the interface between a dynamin-coated and a bare region of the membrane tubule [Fig. 4.7(c)]. We can imagine that in long tubes, such defects in the dynamin coat either appear during polymerization or that the initially homogeneous dynamin coat breaks

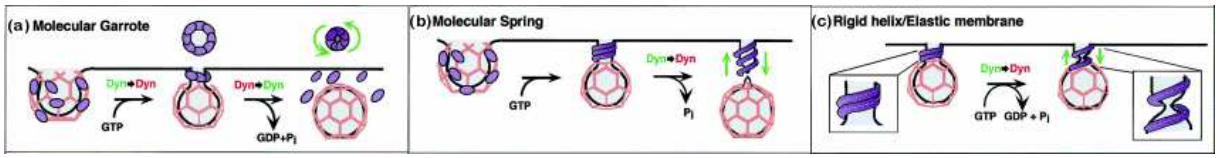

Figure 4.7: Schematics representing the possible modes of membrane tubule breaking by dynamin described in the main text. Figure taken from Ref. [16].

upon GTP injection. It is however very unlikely that the dynamin coats of Ref. [36] have systematically exactly one defect[3], which would account for the fact that they break at most once. Instead, the tube probably often starts with either many or no defects. In the former case, we have to account for the fact that only one of the defects evolves into a full breaking of the tube. In the latter case, we must explain the creation of a defect in the dynamin coat. It is undoubtedly important to consider the space dependence of the stresses in the tube to answer either of these questions. A mechanism of lipid phase separation similar to that of Ref. [45] could also help a defect evolve into a full tube break. Indeed, dynamin is known to strongly bind PIP_2 [90], and could therefore deplete the bare membrane regions in this lipid. Also, depending on the membrane flow through the dynamin-coated regions of the tube and on the dynamics of their conformational change, a bare region might be under more or less stress and therefore break more or less easily.

Further experimental studies are currently under way in the group of Patricia Bassereau and Aurélien Roux in Institut Curie. Their main focus is on monitoring the conformational changes of helices polymerized under the conditions considered in chapter 3. This configuration enables control over and monitoring of the tension of the membrane, the longitudinal force applied to the tube, the tube's length and its boundary conditions. Also, labeling of the tubes by quantum dots should eliminate the uncertainties related to the hydrodynamic drag on the polystyrene beads used in previous experiments. More generally, this setup yields much cleaner data than that presented in Sec. 4.6, and allows for a more thorough discussion of the validity of our hydrodynamic approach, as well as possible deviations from our predictions. Such fine experiments could be used to characterize the precise conditions under which GTP hydrolysis by dynamin induces tube breaking. The formalism developed in this chapter is essential for the interpretation of these experiments. Indeed, the setup described here provides information on the state of the helix mostly at its end points. Therefore in order to know the state of the tube at the point and on the instant of breaking, one needs to be able to interpolate this information to regions not observed directly. This could allow for the formulation of a heuristic criterion for helix breaking—*e.g.* a critical membrane tension, or a critical helix strain—and thus provide a much more solid footing for the microscopic interpretation of the dynamical phenomenon of membrane severing by dynamin than the currently available data.

In conclusion, we developed a complete theoretical framework suited for the analysis of the statics and dynamics of long dynamin-coated membrane tubes. We make several pre-

[3]Indeed, chapter 3 shows that dynamin polymerization typically starts in either zero or a few locations—it is rare for exactly two dynamin seeds to appear on a membrane tubule.

dictions concerning the space and time dependence of forces, torques, membrane tension, membrane stretching and helix deformations. We hope that our theory will facilitate the interpretation of forthcoming experimental results and help generate and quantitatively test novel hypotheses on the biological mode of action of dynamin.

Part II

ESCRT-III

Chapter 5

Membrane buckling induced by curved filaments

5.1 Introduction

Eukaryotic cells are highly compartmentalized, and many of their confining structures are made of lipid bilayers. In order to maintain the exchanges essential for their proper functioning, these cells thus need tools that modulate the membrane's shape and topology. In the first part of this thesis, we focused on one such tool—the dynamin protein—which self-assembles to form tubes in solution [21] and can impose this intrinsic tubular shape on membranes (see chapter 3). In the present chapter, we consider physically more complicated systems where the structure of the protein does not suggest an obvious tubulation mechanism.

In particular, we develop an approach suited for the description of the Endosomal Sorting Complex Required for Transport III (ESCRT-III). The three ESCRT complexes, ESCRT-I, -II and -III, were initially identified for their involvement in protein sorting at the surface of vacuoles, a yeast organelle devoted to the degradation of the cell's waste and the functional equivalent of the mammalian lysosomes. Among all ESCRTs, only ESCRT-III is believed to take part into the mechanical deformation of the vacuolar membrane, a function that we focus on in the present study [91]. This protein complex is known to be implicated in the formation of multivesicular bodies [92, 93, 94], the budding of HIV and other enveloped viruses [95] and cytokinesis [96, 97], three processes which involve deforming the membrane into a bud and/or severing off the resulting membrane protrusion from the inside.

Deep-etch electron micrographs of COS-7 cells overexpressing hSnf-7, one of the constitutive proteins of ESCRT-III, reveal circular arrays of curved hSnf-7 polymers under the plasma membrane [Fig. 5.1(a)] [98]. This is evidence of the known strong affinity of these filaments for the membrane [99] and for each other [100], as well as of their intrinsic curvature. When an ATP-hydrolysis deficient mutant of VPS4—an ATPase involved in the disassembly of ESCRT-III filaments [100, 101]—is present, long membrane-covered tubes of hSnf-7 filaments are observed [Fig. 5.1(b-c)]. Similar structures appear in *in vitro* systems using purified proteins [102]. This suggests that tubes always form *in vivo*, but that in the presence of normal VPS4 alone they are immediately cut off the mem-

brane to form vesicles. Moreover, as shown in Fig. 5.1(d), cells expressing this VPS4 mutant but having only endogenous levels of ESCRT-III proteins show similar features to those observed in Fig. 5.1(c), suggesting that the tubulation mechanism is relevant for the function of normal cells.

In this chapter, we propose that this flat-to-tubular transition is a physical effect and a general feature of systems where curved filaments with attractive interactions bind to a membrane. Fig. 5.2 illustrates this mechanism akin to the buckling of a rod. In Sec. 5.2, we start by presenting our model of membrane/curved polymers interactions. It yields flat arrays of filaments similar to those of Fig. 5.1(a), and the relation between the parameters of the model and their experimentally observed radius is derived in Sec. 5.3. In Sec. 5.4 we study the linear stability of the filament-dressed flat membrane with respect to vertical deformations and calculate a buckling threshold beyond which membrane protrusions should appear. The stability of very tall protrusions is investigated in Sec. 5.5, and it is found that under some experimentally reasonable parameter values the flat configuration can be at the same time linearly stable and less stable than these tall protrusions. Calculating the energy barrier separating the flat configuration from the protruded state requires studying the full nonlinear shape equations for the dressed membrane, which we derive in Sec. 5.6. We solve them numerically in Sec. 5.7. Finally, in Sec. 5.8, we discuss the assumptions underlying our model as well as the biological implications of the results presented here, and propose an experiment to validate our mechanism in the case of ESCRT-III.

5.2 Model

We consider an infinite, initially flat lipid bilayer parametrized by its radial coordinate r. A subdomain $r_i < r < r_e$ of this surface is bound to an array of filaments (Fig. 5.2). The dressed membrane is put into contact with the cytoplasm, which acts as a reservoir of filaments. In the following, we assume that the dressed membrane is very thin and consider only axisymmetric configurations. Note that the tubes shown in Fig. 5.1 probably have a helical structure [101]. Since their pitch is much smaller than their radius, however, this does not affect the conclusions of this work. We write the free energy of the dressed membrane as:

$$\mathcal{F} = \int_{r\in\mathbb{R}^+} \left(\frac{\kappa}{2}c^2 + \sigma\right) \mathrm{d}\mathcal{A} + 2\pi\gamma(r_i + r_e) + \int_{r\in[r_i,r_e]} \left[\frac{k}{2}\left(\frac{1}{r} - \frac{1}{r_0}\right)^2 - \mu\right] \mathrm{d}\mathcal{A}. \qquad (5.1)$$

The first term is the Helfrich free energy of the membrane, with bending modulus κ, local total curvature c and tension σ [Eq. (1.1)]. The second term represents the attractive interactions between filaments, characterized by a line tension γ. We assume that the filaments are closely packed; their surface density is thus constant throughout the array. The last term represents the free energy of the filaments. They have a preferred curvature r_0^{-1}, and due to the cylindrical symmetry their actual curvature is r^{-1}. A Taylor expansion about r_0^{-1} to second order yields the filament stiffness k. Finally, we represent the affinity of the filaments for the membrane by μ, the chemical potential difference between hSnf-7

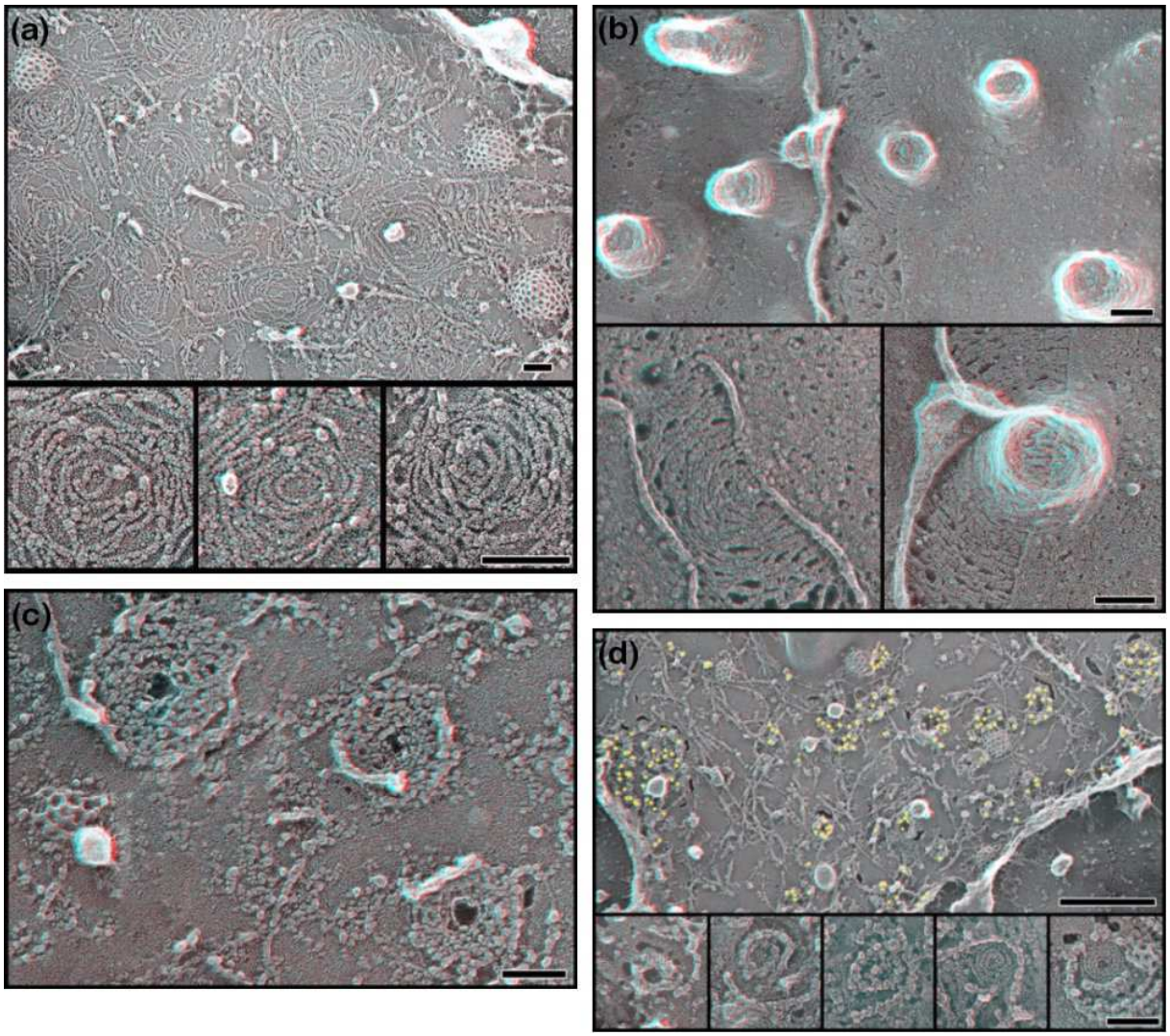

Figure 5.1: 3D stereoscopic micrographs (anaglyphs) of the plasma membrane of COS-7 cells (a) overexpressing hSnf-7 and seen from the inside of the cell. Top panel: low magnification. Bottom panels: high magnification. The hSnf-7 filaments self-organize into circular arrays. (b) overexpressing hSnf-7, expressing the ATP hydrolysis-deficient, GFP-labeled mutant of VPS4 VPS4B(E235Q)-GFP and seen from the outside. Tubular structures stick out of the cell. Much longer tubes are sometimes observed [98]. Spontaneous tears in the membrane can be seen here, revealing the underlying circular hSnf-7 array and how it forms a scaffold supporting the tubular structures. (c) overexpressing hSnf-7, expressing VPS4B(E235Q)-GFP and seen from the inside. The circular hSnf-7 structures are heavily decorated with VPS4B(E235Q)-GFP and have a central hole, presumably corresponding to a tube sticking out of the cell. (d) expressing only endogenous levels of ESCRT-III proteins as well as VPS4B(E235Q)-GFP. Top panel: low magnification. The yellow dots outline 18-nm gold particles immunodecorating VPS4B(E235Q)-GFP. Bottom panels: higher magnification. Circular structures and holes similar to those of (a) and (c) are observed. Bars, 100 nm except for the top panel of (d), 500 nm. All micrographs taken from Ref. [98].

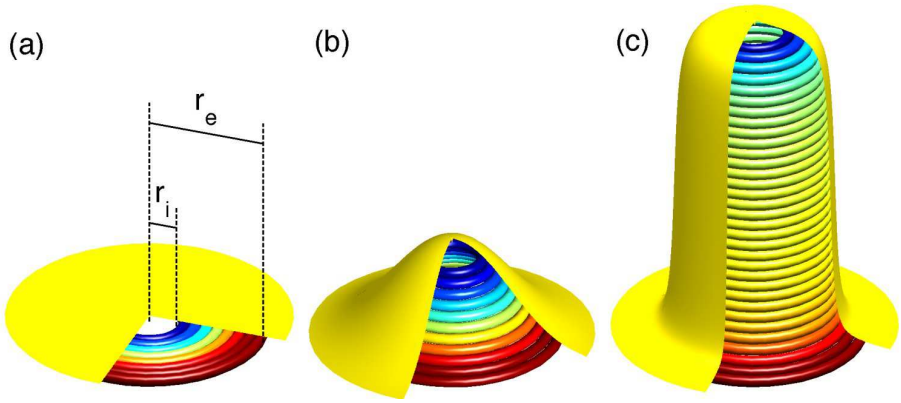

Figure 5.2: Illustration of the proposed buckling mechanism. Overbent filaments are represented in blue, underbent filaments in red and the membrane in yellow. Wedges of the membrane are removed for visualization. (a) Curved filaments with an affinity for each other and the membrane form membrane-bound circular arrays. The tension and bending modulus of the membrane tend to stabilize flat arrays. (b) Buckling, on the other hand, allows the binding of more filaments and the relaxation of those already bound to their preferred (yellow) radius. These stabilizing and destabilizing effects balance at the buckling threshold. (c) The formation of long tubes allows the binding of an arbitrarily large number of filaments close to their preferred radius.

in the cytoplasm and bound to the membrane. Note that μ is expressed as an energy per unit surface area.

In the following, we consider that μ is constant throughout the filament array. One might object that this assumption does not take into account the fact that depending on the radius considered, filaments of different lengths are required to form the circular shapes pictured in Fig. 5.2(a). Then if short filaments were for instance more scarce than long ones, μ would be smaller at the center of the array than at its edges. Going back to Fig. 5.1(a), however, one sees that the circular filaments pictured in Fig. 5.2 are not actually continuous and can be made of several consecutive shorter filaments. It is also possible that the hSnf-7 filaments are "living" polymers and exchange monomers with the cytoplasm. Therefore we consider that filaments of any length are always available, and that their chemical potential per monomer does not depend on their length, hence a uniform μ.

In Eq. (5.1), we also ignore holes in the array resulting from thermal fluctuation, which is correct in the limit of large binding energies. We believe that such fluctuations are unlikely to be essential to the budding of ESCRT-III. Note that the holes visible in Fig. 5.1(a) are most likely due to the treatment of the membrane preliminary to electron microscopy and do not yield any reliable information on the importance of thermal fluctuations.

Finally, it should be noted that even though the filaments we consider are curved, assuming cylindrical symmetry implies that any individual filament always lies in an horizontal plane, even in a buckled configuration [Fig. 5.2(b-c)]. Therefore, they do not

induce an intrinsic curvature in the dressed membrane, which would be an obvious way of giving rise to membrane budding. This is an essential difference between the novel mechanism presented here and previous studies [89, 103, 104]. This is also related to the fact that Eq. (5.1) ignores the up-down asymmetry of the dressed membrane, a simplification discussed in Sec. 5.8.

5.3 Flat arrays of filaments

We first consider the stability of flat arrays of filaments [Fig. 5.2(a)]. In Fig. 5.1(a), it seems that these arrays have a finite, rather well-defined external radius r_e. We attribute this feature to a chemical equilibrium between hSnf-7 in the array and in solution.

Assuming a flat dressed membrane ($c = 0$ and $\mathrm{d}\mathcal{A} = 2\pi r\,\mathrm{d}r$), the free energy reads

$$\mathcal{F} = \frac{k}{2}\ln\left(\frac{r_e}{r_i}\right) + \left(\gamma - \frac{k}{r_0}\right) r_e + \left(\gamma + \frac{k}{r_0}\right) r_i + \left(\frac{k}{2r_0^2} - \mu\right)\frac{r_e^2 - r_i^2}{2}. \tag{5.2}$$

Minimizing this expression with respect to r_e for a flat membrane, one finds that the array has a finite external equilibrium radius only if $k/2r_0^2 > \mu$, *i.e.* only if it is more favorable for a filament to be in solution than bound to the rim of a very large ($r_e \to +\infty$) array. On the other hand, line tension will shrink the array and make r_e vanish unless

$$\gamma < \frac{k}{r_0}\left(1 - \sqrt{1 - \frac{2\mu r_0^2}{k}}\right). \tag{5.3}$$

For our calculations to be consistent with Fig. 5.1(a), one thus needs to make both these assumptions. In that case, we always have $0 < r_i < r_e$ and

$$\frac{r_e}{r_0} = \frac{k - r_0\gamma}{k - 2r_0^2\mu} + \sqrt{\left(\frac{k - r_0\gamma}{k - 2r_0^2\mu}\right)^2 - \frac{k}{k - 2r_0^2\mu}}, \tag{5.4}$$

which we note for later use.

5.4 Linear stability of the flat dressed membrane

We now discuss the buckling of filament-dressed membranes [Fig. 5.2(b)]. Experimentally, it is observed that the typical radius of a hSnf-7 protrusion is much larger than r_i and smaller than r_e [98]. We therefore assume for simplicity that $r_i = 0$ and $r_e \to +\infty$. We describe the dressed membrane by its altitude $z(r)$. In this parametrization, the total curvature and the element area read

$$c = \frac{\frac{\mathrm{d}^2 z}{\mathrm{d}r^2}}{\left[1 + \left(\frac{\mathrm{d}z}{\mathrm{d}r}\right)^2\right]^{3/2}} + \frac{\frac{\mathrm{d}z}{\mathrm{d}r}}{r\left[1 + \left(\frac{\mathrm{d}z}{\mathrm{d}r}\right)^2\right]^{1/2}}, \quad \mathrm{d}\mathcal{A} = \sqrt{1 + \left(\frac{\mathrm{d}z}{\mathrm{d}r}\right)^2}\,\mathrm{d}r. \tag{5.5}$$

The equilibrium states are the solutions of the force balance equation

$$\frac{\delta\mathcal{F}}{\delta z(r)} = 0, \tag{5.6}$$

where $\frac{\delta}{\delta z(r)}$ denotes the functional derivative. The solution must also satisfy the boundary conditions

$$\frac{\mathrm{d}z}{\mathrm{d}r}(0) = 0 \quad \text{and} \quad \frac{\mathrm{d}z}{\mathrm{d}r}(+\infty) = 0. \tag{5.7}$$

Since both $\mathcal{F}$ and the boundary conditions depend only on derivatives of the altitude, $z(r)$ is defined up to an arbitrary additive constant.

As in the case of a buckling rod [105], the buckling threshold is the set of parameters where non-zero solutions of the linearized force balance equation satisfying the boundary conditions exist. Defining the scaled filament stiffness $K = k/\kappa$ and membrane tension $\Sigma = (\sigma - \mu)r_0^2/\kappa + k/(2\kappa)$, this equation reads:

$$z''' + \frac{z''}{R} - \left(\frac{1}{4} - \frac{1 + \sqrt{4 + 2K} + 2\nu}{2R} + \frac{2 + K}{2R^2}\right) z' = 0, \tag{5.8}$$

where the primes denote differentiation with respect to the scaled radius $R = r/u$, and

$$u = \frac{r_0}{2\sqrt{\Sigma}}, \quad \nu = \frac{K}{2\sqrt{\Sigma}} - \sqrt{1 + \frac{K}{2}} - \frac{1}{2}. \tag{5.9}$$

The general solution of Eq. (5.8) reads $z'(R) = c_1 f_1(R) + c_2 f_2(R)$, where c_1 and c_2 are arbitrary constants and

$$\begin{aligned} f_1(R) &= e^{-R/2} R^{\sqrt{1+K/2}} U\left(-\nu, 1 + \sqrt{4 + 2K}, R\right), \\ f_2(R) &= e^{-R/2} R^{\sqrt{1+K/2}} M\left(-\nu, 1 + \sqrt{4 + 2K}, R\right). \end{aligned} \tag{5.10}$$

The confluent hypergeometric functions of the second kind U and M are defined in Ref. [106]. Non-zero solutions of this form satisfying the boundary conditions only exist for certain values of the parameters, thereby defining the buckling threshold. Two parameter regimes must be distinguished:

- For ν not a natural integer ($\nu \notin \mathbb{N}$), we have the following asymptotic behaviors:

$$\begin{aligned} f_1(R) &\underset{R\to 0}{\sim} \frac{\Gamma\left(\sqrt{4 + 2K}\right)}{\Gamma(-\nu)} R^{-\sqrt{1+K/2}}, \\ f_2(R) &\underset{R\to +\infty}{\sim} \frac{\Gamma\left(1 + \sqrt{4 + 2K}\right)}{\Gamma(-\nu)} R^{-1-\nu-\sqrt{1+K/2}} e^{R/2}. \end{aligned} \tag{5.11}$$

  Thus f_1 diverges as $R \to 0$ while Eq. (5.10) implies $f_2(0) = 0$. Hence the boundary condition $z'(0) = 0$ imposes $c_1 = 0$. Similarly, $f_2(R)$ diverges as $R \to +\infty$, thus $z'(+\infty) = 0$ yields $c_2 = 0$. Therefore there is no non-zero solution to the linearized buckling problem.

- For ν natural integer ($\nu = n \in \mathbb{N}$), the singular terms of Eq. (5.11) vanish and f_1 and f_2 are both proportional to the generalized Laguerre polynomials $L_n^{(\alpha)}(R)$ [106]. Hence Eq. (5.8) has a unique solution, up to an arbitrary amplitude $\mathcal{C}$:

$$z_n'(R) = \mathcal{C} e^{-R/2} R^{\sqrt{1+K/2}} L_n^{\left(\sqrt{4+2K}\right)}(R). \tag{5.12}$$

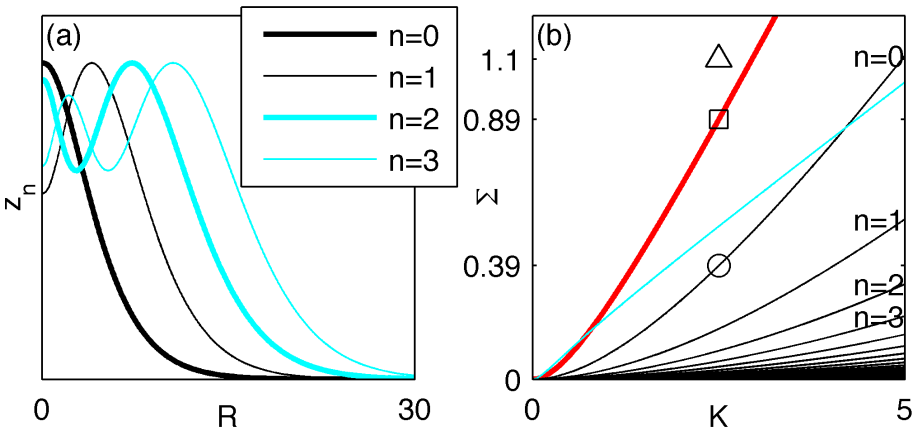

Figure 5.3: Normal modes $z_n(R)$ of the dressed membrane. (a) Spatial structure of the first four normal modes at their respective buckling thresholds for $K = 2.5$. (b) Thin black lines: buckling thresholds as a function of n, K and Σ. Thick red line: stability limit of long, cylindrical dressed membrane tubes. Protrusions are obviously more stable at small Σ, where the destabilizing influence of the filaments overrides the stabilizing effect of the membrane. Therefore the nth normal mode of the flat dressed membrane is linearly unstable for parameter regimes located under the nth thin black line and long tubes exist only under the thick red line. Thin cyan line: parameter regimes compatible with the experimental data of Ref. [98]. Symbols are referred to in the main text.

Since $L_n^{(\alpha)}(R)$ is a polynomial of degree n in R, z_n satisfies the boundary conditions for any n.

Therefore, there is an infinity of buckling thresholds, one per integer $\nu = n$. This is again reminiscent of the buckling rod problem, as each normal mode z_n of the dressed membrane has its own instability threshold. These are illustrated in Fig. 5.3. Physically, the interface is linearly stable if and only if all of its normal modes are stable. Thus in the following we need only consider the most unstable mode $n = 0$.

5.5 Large deformations and metastable regime

We now study strongly deformed dressed membranes [Fig. 5.2(c)]. We first check that our model accounts for the existence of long dressed membrane tubes similar to those observed in Fig. 5.1(b) and in Refs. [98, 101, 102]. For a cylindrical protrusion of radius r_t and length $\ell \gg r_t$ and to dominant order in ℓ/r_t, the rounded tip and base of the tube can be neglected and the free energy reads

$$\mathcal{F} = 2\pi r_t \ell \left[\frac{\kappa}{2r_t^2} + \sigma + \frac{k}{2}\left(\frac{1}{r_t} - \frac{1}{r_0}\right)^2 - \mu \right] + \mathcal{F}_{\text{flat dressed membrane}}. \tag{5.13}$$

Introducing a fictitious vertical point force f pulling the membrane up at $r = 0$, we minimize the free energy $\mathcal{G} = \mathcal{F} - f\ell$ with respect to r_t and ℓ and find

$$r_t = r_0\sqrt{\frac{1+K}{2\Sigma}}, \quad f_t = \frac{2\pi\kappa}{r_0}\left[\sqrt{2(1+K)\Sigma} - K\right]. \tag{5.14}$$

Consider an equilibrium situation in which a long dressed membrane tube is held at a constant length by a force $f = f_t$. The force is then suddenly set to zero. In the case of an upward initial force $f_t > 0$, the tube tends to retract. If $f_t < 0$, on the contrary, ℓ increases and the dressed membrane spontaneously tubulates. This corresponds to the region of Fig. 5.3(b) located under the thick red line. Interestingly, long tubes are always stable when the flat dressed membrane is linearly unstable, but the reverse is not true. Thus there exists a regime, located between the thick red line and the $n = 0$ line of Fig. 5.3(b), where the flat dressed membrane is metastable.

This metastable regime is compatible with biologically reasonable parameter values. Indeed, combining Eqs. (5.4) and (5.14), we find:

$$\Sigma = \frac{2(\kappa r_e r_t)^2 K^2(1+K)}{\left[\kappa r_e^2 + 2(\gamma - \sigma r_e) r_e r_t^2 + \kappa(r_e^2 + r_t^2)K\right]^2}. \tag{5.15}$$

The micrographs presented in Ref. [98], among which those reproduced in Fig. 5.1, consistently indicate that $r_t \simeq 70$ nm and $r_e \simeq 200$ nm. Inserting these values and the estimates $\kappa = 20k_BT$, $\sigma = 10^{-5}$ N.m^{-1} [107] and $\gamma = 1$ pN in Eq. (5.15), we obtain a numerical relation between the scaled tension and filament stiffness characterizing the experiments of Ref. [98]. We plot this condition as a thin cyan line on Fig. 5.3(b). This line traverses both the metastable and unstable regions, making it possible that the experiments of Ref. [98] reflect either regime.

5.6 Full shape equations for the dressed membrane

In the next two sections, we consider the possibility that the flat dressed membranes observed in Fig. 5.1(a) are indeed metastable. In this hypothesis, an important quantity is the energy barrier $\Delta\mathcal{F}$ separating the flat state from the more stable, tubulated state. To compute $\Delta\mathcal{F}$, we need to solve the full nonlinear shape equations of the tube, which we derive here.

Using $Z = z/u$, we define S as the arc length along the dressed membrane in the (R, Z) plane with $R(S = 0) = 0$. We parametrize the dressed membrane by $R(S)$ and the angle $\psi(S)$ defined by

$$\dot{R}(S) = \cos\psi(S), \tag{5.16a}$$
$$\dot{Z}(S) = -\sin\psi(S), \tag{5.16b}$$

where the dot denotes the differentiation with respect to S [Fig. 5.4(a)]. In this parametrization, the free energy of a finite region $0 < R < R_{max}$ of the dressed membrane subjected to a force f reads

$$\frac{\mathcal{G}^{R_{max}}}{2\pi\kappa} = \int_0^{S_{max}} \mathcal{L}\left(\psi, \dot{\psi}, R, \dot{R}, \lambda\right) \mathrm{d}S, \tag{5.17}$$

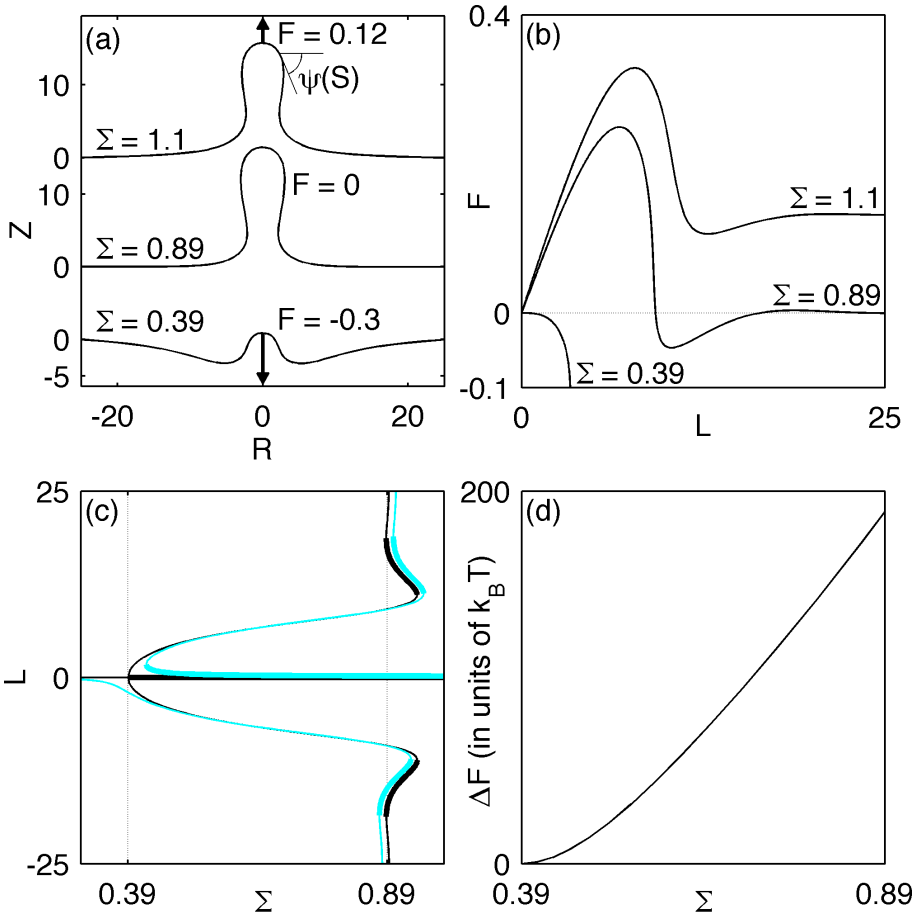

Figure 5.4: Numerically computed mechanical properties of strongly deformed dressed membranes for $K = 2.5$. (a) Parametrization and profiles. (b) Force-extension curves ($L = \ell/u$). (c) Black lines: bifurcation diagram for the $F = 0$ problem. Cyan lines: changes induced by a weak asymmetry of the dressed membrane. In both cases, thick (thin) lines represent stable (unstable) solutions. (d) Activation energy $\Delta\mathcal{F}$ a flat dressed membrane needs to reach the $\ell = +\infty$ buckled solution.

where we introduce the Lagrangian $\mathcal{L}$ defined by:

$$\begin{aligned}\mathcal{L}\left(\psi,\dot{\psi},R,\dot{R},\lambda\right) &= \frac{\dot{\psi}^2 R}{2} + \dot{\psi}\sin\psi + \frac{\sin^2\psi}{2R} - F\sin\psi + \frac{R}{4} + \frac{K}{2R} \\ &\quad +\lambda\left(\dot{R} - \cos\psi\right) - \frac{1+\sqrt{4+2K}+2\nu}{2}. \end{aligned} \tag{5.18}$$

Here $F = fu/(2\pi\kappa)$, S_{max} is defined by $R_{max} = R(S_{max})$ and λ is a Lagrange multiplier imposing the constraint Eq. (5.16a).

Minimizing the free energy of the dressed membrane with respect to $\psi(S)$ and $R(S)$

under the constraint Eq. (5.16a) implies satisfying the Euler-Lagrange equations

$$\begin{aligned}
\frac{\partial \mathcal{L}}{\partial \psi} = \frac{\mathrm{d}}{\mathrm{d}S}\left(\frac{\partial \mathcal{L}}{\partial \dot{\psi}}\right) &\Leftrightarrow \ddot{\psi}R + \dot{\psi}\dot{R} = \frac{\cos\psi\sin\psi}{R} - F\cos\psi + \lambda\sin\psi, \\
\frac{\partial \mathcal{L}}{\partial R} = \frac{\mathrm{d}}{\mathrm{d}S}\left(\frac{\partial \mathcal{L}}{\partial \dot{R}}\right) &\Leftrightarrow \dot{\lambda} = \frac{\dot{\psi}^2}{2} + \frac{1}{4} - \frac{K + \sin^2\psi}{2R^2}, \\
\frac{\partial \mathcal{L}}{\partial \lambda} = \frac{\mathrm{d}}{\mathrm{d}S}\left(\frac{\partial \mathcal{L}}{\partial \dot{\lambda}}\right) &\Leftrightarrow \dot{R} = \cos\psi
\end{aligned} \tag{5.19}$$

for any S. Eliminating λ from these equations, we get the shape equations for the dressed membrane

$$\begin{aligned}
\dddot{\psi} &= -\frac{2\ddot{\psi}\cos\psi}{R} - \frac{\dot{\psi}^3}{2} + \frac{3\dot{\psi}^2\sin\psi}{2R} + \frac{\dot{\psi}}{4} - \frac{1 + \sqrt{4 + 2K} + 2\nu}{2R}\dot{\psi} \\
&\quad + \frac{\dot{\psi}}{2R^2}\left(2 + K - 3\sin^2\psi\right) + \frac{\sin\psi}{4R} + \frac{\sin\psi}{2R^3}\left(\sin^2\psi - 2 - K\right), \\
\dot{R} &= \cos\psi.
\end{aligned} \tag{5.20}$$

We are in presence of one third-order equation and one first-order equation, and therefore need four boundary conditions to have a complete set. The definition of S and the fact that the membrane cannot have a singularity in $S = 0$ impose two of these:

$$R(0) = 0, \quad \psi(0) = 0. \tag{5.21}$$

The other two are found by minimizing $\mathcal{G}^{R_{max}}$ with respect to $\psi_{max} = \psi(S_{max})$ and with respect to S_{max} at fixed R_{max}. These respectively yield the following two conditions:

$$\frac{\partial \mathcal{L}}{\partial \dot{\psi}}(S_{max}) = \dot{\psi}(S_{max})R_{max} + \sin\psi(S_{max}) = 0, \tag{5.22}$$

$$\left(\mathcal{L} - \frac{\partial \mathcal{L}}{\partial \dot{\psi}}\dot{\psi} - \frac{\partial \mathcal{L}}{\partial \dot{R}}\dot{R} - \frac{\partial \mathcal{L}}{\partial \dot{\lambda}}\dot{\lambda}\right)(S_{max}) = 0. \tag{5.23}$$

Since the Lagrangian $\mathcal{L}$ is autonomous (*i.e.* $\partial\mathcal{L}/\partial S = 0$), the Hamiltonian

$$\mathcal{H} = \mathcal{L} - \frac{\partial \mathcal{L}}{\partial \dot{\psi}}\dot{\psi} - \frac{\partial \mathcal{L}}{\partial \dot{R}}\dot{R} - \frac{\partial \mathcal{L}}{\partial \dot{\lambda}}\dot{\lambda}$$

is a constant. Moreover, Eq. (5.23) imposes that this constant is equal to zero. Combining this with Eqs. (5.19) yields a simplified (third-order) system of shape equations for the dressed membrane:

$$\begin{aligned}
\ddot{\psi} &= \left(\frac{1}{4} - \frac{1 + \sqrt{4 + 2K} + 2\nu}{2R} + \frac{\cos^2\psi + 1 + K}{2R^2}\right)\tan\psi \\
&\quad - \frac{\dot{\psi}^2\tan\psi}{2} - \frac{\dot{\psi}\cos\psi}{R} - \frac{F}{R\cos\psi}, \\
\dot{R} &= \cos\psi,
\end{aligned} \tag{5.24}$$

with boundary conditions:

$$\begin{aligned} R(0) &= 0, \\ \psi(0) &= 0, \\ \dot{\psi}(S_{max}) &= -\frac{\sin\psi(S_{max})}{R_{max}}. \end{aligned} \tag{5.25}$$

In the small ψ, infinite R_{max} limit, these equations are identical to those solved in Sec. 5.4. In the absence of protein ($k = 0$, $\mu = 0$), they go to the bare membrane tube shape equations of Refs. [108, 109].

5.7 Numerical computation of the energy barrier

The nonlinear equations derived in the previous section are much too complicated to be solved analytically. In order to calculate $\Delta\mathcal{F}$, we thus resort to numerical methods.

For practical reasons, we define $X = S_{max} - S$ and translate the above system of equations in this new parametrization. We use the following new set of boundary conditions:

$$\begin{aligned} \frac{\mathrm{d}\psi}{\mathrm{d}X}(X=0) &= \frac{\sin\psi(X=0)}{R_{max}}, \\ R(X=0) &= R_{max} \\ \psi = 0 \quad &\text{when} \quad R = 0. \end{aligned} \tag{5.26}$$

Note that the boundary conditions Eqs. (5.26) are expressed in two different locations $X = 0$ and $R = 0$. Such a situation is commonly referred to as a "boundary value" problem and is often tackled with the "shooting method" [110], which we use here. It consists in breaking the boundary value problem down into a (simpler) initial value problem and a root finding problem.

In our case, we start by picking an arbitrary value ψ_0 for the slope of the dressed membrane in $X = 0$ ($R = R_{max}$). We then evolve Eqs. (5.24) using a fourth-order Runge-Kutta routine [110] starting from the initial conditions

$$\psi(X=0) = \psi_0, \quad \frac{\mathrm{d}\psi}{\mathrm{d}X}(X=0) = \frac{\sin\psi_0}{R_{max}}, \quad R(X=0) = R_{max}. \tag{5.27}$$

We stop the routine as soon as R hits zero (actually, when it becomes smaller than some small number), and record the value ψ_c of ψ at this location. For an arbitrary ψ_0, there is no reason to expect that ψ_c is equal to zero as required by our physical problem. Still, the procedure described here defines a function

$$g^F : \psi_0 \mapsto \psi_c, \tag{5.28}$$

where the superscript "F" signals that the function g^F depends on the force. By finding the roots of this function numerically, we find a ψ_0 such that ψ_c vanishes (becomes smaller than some small number), and thus generate a trajectory satisfying the equations of Sec. 5.6.

For the particular equations used here, however, the function g^F usually has many roots, most of them unphysical (typically with a dressed membrane that intersects itself). Since the algorithm used to find the roots of the equation $g^F(\psi_0) = 0$ requires to be initialized by inputting a certain initial value ψ_0^{initial} of ψ_0, it typically converges to the root of g^F that is closest to ψ_0^{initial}. In order to select the physically interesting root, we start from a situation where we know a physically correct solution: a flat membrane under zero force. Note that even though that solution might be *mechanically* unstable under some conditions (see Sec. 5.4), it is always *numerically* stable, meaning that starting a trajectory from $\psi_0 = 0$ always yields $\psi_c = 0$ for reasonably small numerical noise. We then increase the force by a small amount δF. As we do this, the physical ψ_0 also changes, but only by a small amount and it thus remains close to zero. By solving $g^{\delta F}(\psi_0) = 0$ starting from $\psi_0^{\text{initial}} = 0$, we thus converge to the nearby physical ψ_0. By gradually changing F by small increments, we are thus able to follow the physical ψ_0 into strongly deformed regimes.

Let us now discuss the results obtained with this procedure. We use $R_{max} = 25$, which is large enough to be considered quasi-infinite, and tackle only the specific example $K = 2.5$. We however believe that other values of K yield a similar behavior. We first comment on the three regimes presented in Fig. 5.4(a-b). For $\Sigma = 1.1$ [indicated by $\triangle$ in Fig. 5.3(b)], tubes always retract in the absence of an external force, as shown in Fig. 5.4(b). Lowering the surface tension to $\Sigma = 0.89$ ($\square$), we reach the boundary of the metastable region. For $0.39 < \Sigma < 0.89$, a positive force is required to extract short tubes, but long tubes grow spontaneously unless opposed by a negative F. At $\Sigma = 0.39$ ($\bigcirc$) and lower, even short tubes grow spontaneously and can only be maintained at a finite length by a negative force. In Fig. 5.4(b), crossings of the horizontal axis by the force-extension curves denote solutions of the biologically relevant, $F = 0$ problem, the stability of which is indicated by the sign of the curve's slope. Plotting the lengths of these protrusions as a function of Σ, we obtain the diagram Fig. 5.4(c), where we observe that the loss of stability of the $n = 0$ mode studied above yields a subcritical bifurcation. Focusing on the metastable regime ($0.39 < \Sigma < 0.89$), we note that forming an infinitely long tube requires first extruding a short tube from the dressed membrane, which is energetically unfavorable. The associated energy barrier $\Delta\mathcal{F}$ is given by the free energy of the unstable solutions represented by the main thin branch of Fig. 5.4(c). Integrating force-extension curves similar to those of Fig. 5.4(b), we calculate the work required to reach these solutions from the stable, flat state and plot the results on Fig. 5.4(d). Under the effect of thermal fluctuations, an energy barrier of height $\Delta\mathcal{F}$ is crossed at a rate $\tau^{-1}e^{-\Delta\mathcal{F}/k_BT}$, where $\tau \sim$ ns is the characteristic relaxation time scale of the system. When $\Delta\mathcal{F}$ is of the order of a few k_BT, thermal fluctuations are sufficient to ensure the buckling of the dressed membrane within experimentally observable time scales. This is however not the case here, and the large energy barrier makes thermally activated ESCRT-III-mediated budding extremely unlikely in most of the metastable regime.

5.8 Discussion and experimental perspectives

This chapter presents a novel buckling mechanism relevant for a wide range of systems involving interacting membranes and curved filaments. Here we first discuss two approximations made here, then discuss the biological implications of our model and finish by proposing an experiment to validate it.

Throughout this work, we first assume that the interactions between filaments and between filament and membrane are independent of the slope of the dressed membrane (*i.e.* of whether the filaments lie in the same plane or are stacked one upon another). For small slopes, this dependence can be expanded as $\mu(\nabla z) = \mu_0 + \mu_2(\nabla z)^2/2 + \mathcal{O}\left[(\nabla z)^4\right]$ and yields the same linear stability analysis as above provided we redefine $\Sigma = (\sigma - \mu_0 - \mu_2)r_0^2/\kappa + k/(2\kappa)$. Second, we ignore in Eq. (5.1) any terms violating the $z \to -z$ spatial symmetry. These terms are allowed in general since the dressed membrane is not up-down symmetric, and might be responsible for the fact that in ESCRT-III, buckling systematically occurs toward the outside of the cytoplasm [see Ref. [98] and the tubes of Fig. 5.1(b-d)]. Formally, such an asymmetry destroys the bifurcation studied here. If it is weak, however, a stable, almost flat configuration still exists for high tensions and loses stability close to the predicted $\Sigma = 0.39$ threshold, as illustrated in Fig. 5.4(c).

One important focus of the present chapter is the relevance of the proposed buckling mechanism for membrane budding in eukaryotic cells by ESCRT-III. Another model that has been proposed for this phenomenon is the "purse string" model illustrated in Fig. 5.5, over which our mechanism has several advantages. In the purse string model, the deformation of the membrane is induced by the buildup of a flat array of ESCRT-III filaments, and only the membrane is deformed out of the horizontal plane. Unlike our model, it thus fails to account for the scaffold of filaments underlying the tubular structures of Fig. 5.1(b). Furthermore, it is quite obvious that the amount of membrane in a bud is limited to the amount initially circled by the ESCRT-III heteropolymer, thus forbidding the formation of the long tubes of Ref. [98] and Fig. 5.1(b). Finally, the purse string model raises questions regarding the interactions between the membrane and ESCRT-III. In particular, the fact that the cell membrane is liquid would suggest that the forming bud of the top and right panels of Fig. 5.5 should flow back into a flat state. In order to account for it not doing so, one should introduce extra elements in this model, such as a model of the friction between the protein with the membrane. Our buckling mechanism, on the other hand, does not require such detailed—and thus potentially arbitrary—assumptions and its physical consistency is thus easy to establish, as shown in this chapter.

Beyond the simple linear stability criterion associated with any buckling phenomenon, our study predicts the existence of a metastable regime for the flat dressed membrane. It is interesting to consider the possibility that cells function in this regime. Indeed, metastable flat dressed membranes could then coexist with long tubes for extended (*i.e.* experimentally observable) periods of time, and thus account for some observations presented in Ref. [98]. We show in Sec. 5.7 that the height of the free energy barrier separating the flat state from the tubulated state most likely rules out a thermal activation of the buckling of metastable membranes. Therefore, *in vivo*, ESCRT-III-mediated budding either takes place only in (or close to) the regime where the flat dressed membrane is linearly unstable, or is assisted by some unknown active process. A possible process of this kind is actin

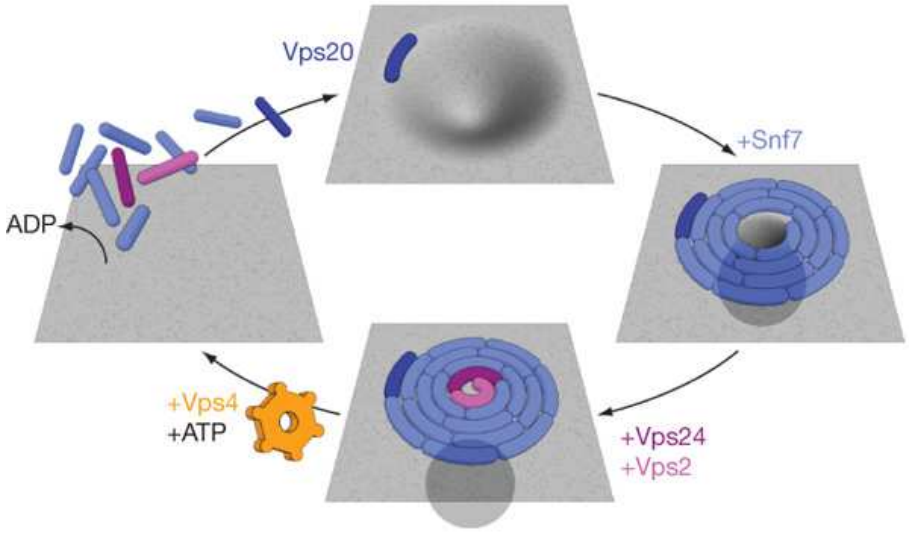

Figure 5.5: In the "purse string" model, the ESCRT-III protein VPS20 initiates an heteropolymer around a region of the membrane that needs to be deformed into a vesicle (*e.g.* a region where some cargo is concentrated—see top panel). The polymer grows by addition of hSnf-7 (here termed Snf7), thus deforming the membrane into a bud (here pictured as a grey sphere below the membrane). VPS24 and VPS2 terminate the polymer and detach the vesicle. Then VPS4 recycles the proteins by disassembling the construct upon ATP hydrolysis. Note that the mechanism proposed in this chapter is only concerned by the first step illustrated here, namely the deformation of the membrane by hSnf-7. Figure adapted from Ref. [102].

polymerization [see chapter 1], which is regulated by the ESCRT-associated protein Alix [111]. If such an active trigger were indeed used *in vivo*, cells might first allow for the formation of complete ESCRT-III arrays, then could activate their rapid budding into potentially large structures by stimulating them at a moment suited for their biological function. Finally, the long tubes observed in some of the micrographs of Ref. [98] do not seem to be length-regulated, in agreement with our predictions for a regime situated under the stability limit of long tubes [thick red line of Fig. 5.3(b)].

We believe that convincing evidence for our description of ESCRT-III budding could be gained by performing a simple *in vitro* experiment where no active processes are present. If the experiment were performed in a cellular environment, such active processes could favor just as well as hinder buckling, thus making the results very difficult to interpret. We propose a biomimetic setup where an aspiration pipette is used to control the tension σ of a giant unilamellar vesicle [112]. This is similar to the setup presented in Fig. 3.1(a) without the optical tweezer. Injecting fluorescent ESCRT-III proteins in the surrounding solution at a known concentration (and therefore at known μ) [102], the formation of tubular structures could be monitored using confocal fluorescence microscopy. By starting at high Σ and then ramping Σ down through σ, one could thus witness the crossing of the linear stability threshold (*i.e.* the metastability limit) through the appearance of long, hSnf-7-rich tubes. This measurement of the buckling threshold and its dependence on

μ could then be compared to our predictions. Finally, when ramping Σ back up from a buckled configuration, we predict that the tubes would only retract when the limit of stability of long tubes is reached, thus giving rise to an as of yet unexpected hysteresis phenomenon.

Part III

Stereocilia

Chapter 6

Shaping of actin bundles by cross-linkers

6.1 Introduction

Maybe the most spectacular feature of our hearing is its exquisite frequency sensitivity. We human beings are able to discriminate sounds with frequencies different by less than 0.2% over a range of three decades [113]. This extraordinary precision finds its root in the physical structure of the auditory system. After entering the ear, sound propagates through the outer and middle ear, pictured in Fig. 6.1(a), with only moderate frequency distortion. It then travels through the inner ear and excites the organ of hearing: the cochlea. Not all regions of the cochlea vibrate in the same way when excited by a given sound, as the stiffness of its so-called basilar membrane is not homogenous. Only the regions tuned to the incoming sound resonate, which is the first stage of the ear's frequency selectivity. On a smaller scale, these vibrations excite cells specialized in the transduction of the mechanical sound stimulus into a nervous signal. These cells are known as "hair cells", after their "hair bundle" [Fig. 6.1(b)], a specialized structure made of rod-like "stereocilia" [Fig. 6.1(c)], which pivot around their ankle upon mechanical stimulation [Fig. 6.1(d)]. The relative motion of the stereocilia causes the opening of ion channels, which induces a depolarization of the membrane that results in the propagation of a nervous signal. In parallel, the influx of ions triggers a sophisticated active feedback machinery that enhances the mechanical resonance of the stereocilia in order to gain better frequency sensitivity [114]. Of crucial importance to this process are the mechanical characteristics of the stereocilia, which are in turn linked to their structure. This role of the form of stereocilia for hearing is evidenced by the fact that their length and shape vary in a very well controlled way both within a single hair bundle and across the whole cochlea.

Stereocilia are primarily made of a hexagonal actin paracrystal enclosed by the cell membrane, as shown in Fig. 6.1(e). Within it, the actin filaments are densely packed, with a lateral spacing of about 10 nm, close to the filament diameter [120]. The filaments are in register, meaning that their helical periods are perfectly aligned in the vertical direction. Their barbed (polymerizing) ends point towards to tip of the stereocilium and their pointed (depolymerizing) ends point towards the cell body. The filaments insert

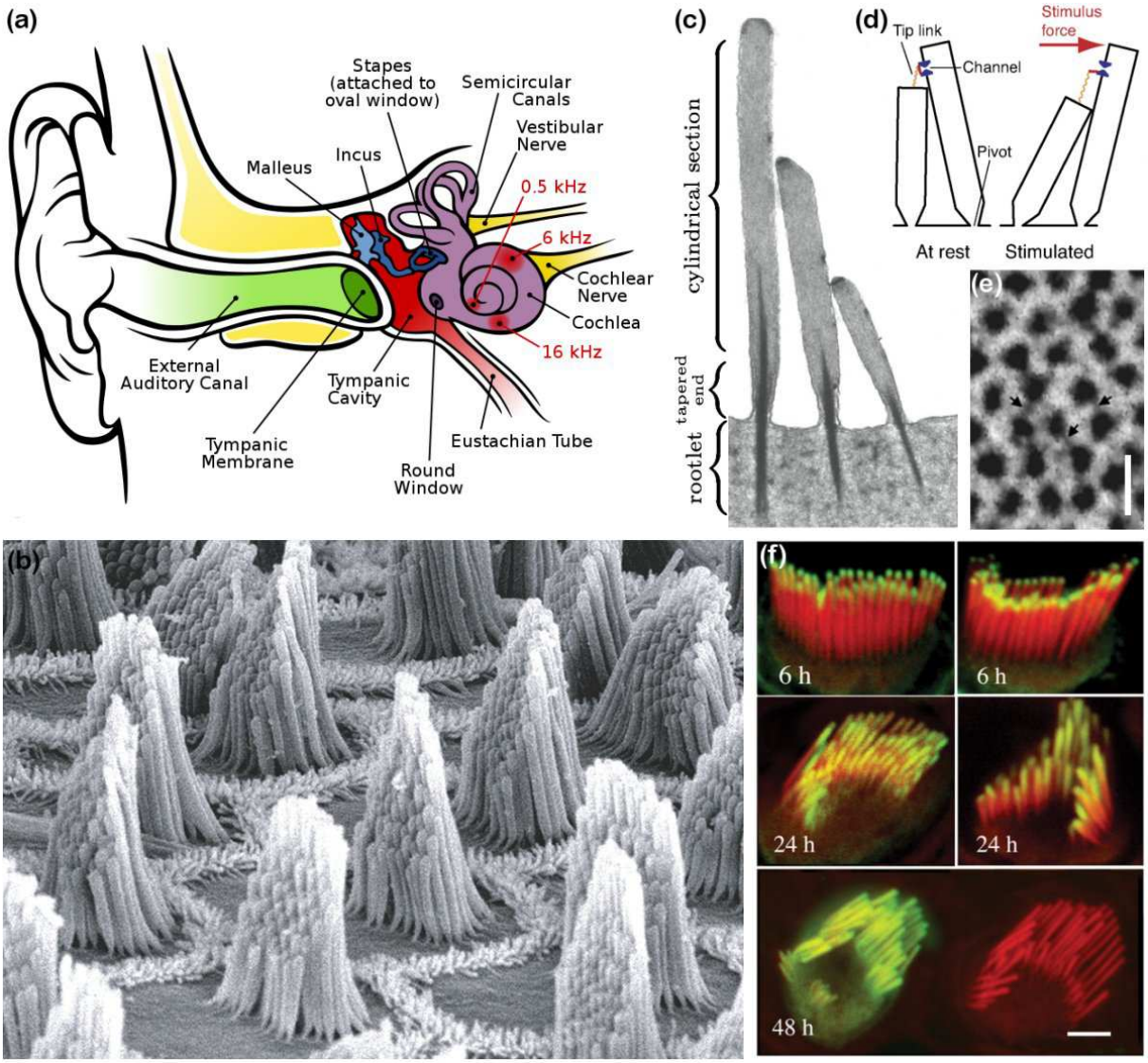

Figure 6.1: Stereocilia and their situation within the ear. (a) Structure of the human ear with indications of the resonant regions of the cochlea for three different stimulus frequencies (red annotations). Green: outer ear; red: middle ear; purple: inner ear. Figure taken from Ref. [115]. (b) Scanning electron micrograph of a chicken's auditory sensory epithelium, located at the core of the cochlea. Individual stereocilia are visible within each hair bundle. Figure taken from Ref. [116]. (c) Transmission electron micrograph through three guinea pig stereocilia. The diameter of the tallest stereocilium is about 250 nm. Figure taken from Ref. [114]. (d) Schematic of the relative motion of stereocilia upon mechanical stimulation. The extension of the spring-like "tip link" induces the opening of an ion channel. Stereocilia pivot around their base, whose elastic properties are therefore very relevant to the tuning of the hair cell [117]. Figure taken from Ref. [116]. (e) Transverse cross-section of a stereocilium, showing the close packing and hexagonal arrangement of the actin filaments (appearing as black circles). Arrows indicate cross-bridges between the actin filaments. Bar, 20 nm. Figure taken from Ref. [118]. (f) Confocal (fluorescence) micrographs of rat hair bundles at various times after transfection with β actin-GFP (green). The non-fluorescent actin (*i.e.* incorporated in the stereocilium before transfection took place) appears red due to treatment with rhodamine/phalloidin. The growth of the green part at the expense of the red is evidence of the actin treadmill. The bottom panel shows a transfected next to a non-transfected cell. Bar, 2.5 μm. Figure taken from Ref. [119].

into the cytoplasm of the underlying hair cell [121], forming a so-called "rootlet" easily visualized in Fig. 6.1(c) because of its dark color upon osmium staining (which probably indicates a dense concentration of proteins). Stereocilia can have over 200 filaments [122] and their length can vary from 1 to 120 μm depending on the animal and on the region of the inner ear considered, meaning that each actin filament within them contains thousands of monomers [123]. Although stereocilia are maintained throughout the life span of an individual, they are dynamic structures that are constantly renewed through actin treadmilling[1]. During this process, actin is continuously incorporated at the tip of the stereocilium and depolymerized at its base [124], as shown in Fig. 6.1(f). Interestingly, the actin treadmilling velocity is proportional to the height of the stereocilium, so that the time necessary to fully renew any rat auditory stereocilium is always 48 h.

Recently, a stereocilium model accounting for this observation has been proposed [125]. In this description, actin is incorporated at the stereocilium tip at a rate dependent on the normal stresses exerted by the membrane on the actin bundle (the more compressed the bundle, the more difficult the incorporation of new actin monomers). These stresses are determined by the radius of the stereocilium, which is itself fixed by an unspecified biological mechanism (possibly the activity of the numerous regulatory proteins found at the stereocilium tip [118, 126, 127, 128]). The treadmilling velocity does not explicitly depend on the height of the stereocilium, and is not limited by the actin supply to the tip, consistent with the experimental observation that actin overexpression does not influence the treadmilling velocity [119]. The central feature imposing the length of the stereocilium in Ref. [125] is that the depolymerization of the actin filaments happens independently of polymerization or of any mechanical influence of the surroundings. Instead, the depolymerization time of an actin filament is fixed by some "internal clock", which (if set to 48 h) allows the authors to recover the proportionality between stereocilium length and treadmilling velocity. Ref. [125] proposes two possible origins for this characteristic time inherent to the actin: first, it considers the stochastic dynamics of an actin filament polymerizing at a rate k_p at one end, and depolymerizing at $k_d > k_p$ at the other. The inverse depolymerization rate $1/k_d$ is the first of the two time scales. In the limit of long stereocilia, this dynamics can be mapped onto the biased diffusion of a particle and yields an exponential distribution of the filament size with a characteristic length scale $\ell_{p/d} = \frac{k_d+k_p}{2(k_d-k_p)} \times$ monomer size. Second, the authors consider the dynamics of a hypothetical actin pointed end capping protein that would prevent filament depolymerization and detach at a rate k_u, which yields the second characteristic time scale, $1/k_u$. Through this mechanism, a capped filament would extend on average by $\ell_u = \frac{k_p}{k_u} \times$ monomer size before uncapping occurs. If those two length scales are matched very precisely, the authors recover reasonable elongated stereocilia shapes.

Here we argue that although it is essentially adequate to describe the shape of stereocilia, the formalism of Ref. [125] misidentifies the internal clock at work in the actin bundle. A first indication of this flaw is that obtaining acceptable shapes within this framework requires a fine tuning of $\ell_{p/d}$ to ℓ_u. If the shape of the stereocilium were indeed very dependent on the tuning of two such parameters *in vivo*, this would mean that it would be very sensitive to an accidental change of either of them. Therefore, this model

[1] See chapter 1 for a definition of treadmilling.

does not yield robust stereocilia, which is in contradiction with experiments indicating that the shape of stereocilia is very well defined. As far as stereocilium shapes are concerned, those calculated from this model have a tapered profile for reasonable values of the parameters as expected from the electron micrographs of Fig. 6.1(c). Indeed, the authors point out that their description yields shapes similar to those represented in Fig. 6C of Ref. [119]. Unfortunately, the stereocilium represented in this figure is from a deaf shaker 2J mutant rat, and the model fails to account for healthy profiles. In the present chapter, we propose another origin for the characteristic depolymerization time based on an experimentally well-characterized protein, that Ref. [125] incorrectly suggests could be modeled as an actin pointed-end capping protein. This protein is espin, a cross-linker of actin filaments.

It was already noticed in the early days of the study of the structure of stereocilia that the actin filaments they contain are not simply in contact, but are connected by cross-bridges [121] such as the ones indicated by arrows in Fig. 6.1(e). It was later discovered that these cross-bridges are in fact two actin cross-linking proteins, fimbrin [129] and espin [130]. The cross-bridges are arranged periodically with a period 12.5 nm along the actin filaments. This indicates that they could be responsible for the filaments being in register, due to the fact that they can bind only if correctly aligned with the periodicity of the actin helix [131]. In this chapter we focus on espin, as it is thought to provide sturdier cross-linking than fimbrin. Indeed, unlike fimbrin it binds actin in a Ca^{2+}-resistant way [132], which is crucial as the mechanism of hearing implies calcium ions penetrating into the stereocilium [122]. Also, its binding affinity for actin is 10-100 fold higher than that of other actin cross-linkers [133]. Note however that our theoretical study applies equally to any kind of actin cross-linker, and is a first step towards the study of situations where several different types of cross-linkers are simultaneously involved.

Although the tertiary structure of espin has not yet been resolved, it is known to be an anisotropic protein with a Stokes radius of 3.4 nm [134]. It exists under various isoforms with masses ranging from 25 to 110 kDa [132], all having two or three F-actin binding sites and one G-actin binding site. *In vitro*, espin bundles actin filaments within a large range of concentrations, yielding an average inter-filament spacing of 12.6 nm [135]. If targeted to a specific cellular location, it causes the *de novo* assembly of large actin bundles (both the G-actin and two F-actin binding sites are required for this) [136]. When transfected into CL4 cells, they cause an average 6-fold elongation of microvilli, a type of stereocilia-related protrusions presented in Fig. 1.2(c) [137]. One likely cause of this elongation is the experimentally observed slowing down of actin depolymerization upon cross-linking by espin [138]. Also, cross-linkers are known to slow down the disassembly of actin bundles during the disassembly of the *Drosophila* bristle [Fig. 1.2(c)] [139]. Note that such an actin depolymerization inhibitor seems to be necessary to account for actin dynamics in stereocilia, as the actin depolymerization rate there ($\simeq 0.004$-$0.04\,s^{-1}$ [119]) is much smaller than that of F-actin *in vitro* ($\simeq 1\,s^{-1}$ [140]). The idea that espin cross-linking has an influence on the lifetime of stereociliary filaments is supported by the fact that it is incorporated at its tip and treadmills down simultaneously with actin [119]. Its role is probably at least as crucial as that of actin for the length control of stereocilia. Indeed, espin—but not actin—overexpression induces their lengthening and a mutation resulting in espin underexpression causes their shortening [126]. Even under normal *in*

vivo conditions, the variability in the length of stereocilia throughout the cochlea as well as within a single hair bundle is correlated with the espin expression level [138]. During development, espin expression levels correlate with stereociliary elongation and maturation in chicken [141], and so does the sequence in which various espin isoforms are expressed as a function of the location of the stereocilium in the inner ear [142]. Finally, two recessive and four dominant mutations of espin are responsible for deafness in human [132]. Out of the four dominant ones, three induce less microvilli lengthening than wild type espin when transfected into CL4 cells [137].

In this chapter, we focus on the role of espin in stereocilia. It should be noted that it also plays a role in several other actin bundle-based protrusions such as the microvilli of hair cells[2], vomeronasal organ sensory neurons, solitary chemoreceptor cells, taste cells, and Merkel cells [143]. Actin turnover in microvilli and in the related filopodia [Fig. 1.2(c)] is however very quick and their shapes are rather ill-defined, which is why we choose to study stereocilia [123]. Note also that espin could regulate actin polymerization and depolymerization by other mechanisms besides cross-linking [122].

In Sec. 6.2, we present a model for the coupled dynamics of espin cross-linking and actin depolymerization, thus proposing an "internal clock" devoid of the drawbacks of the ones proposed in Ref. [125]. Solving the simple case where espin is incorporated into the actin bundle only at the tip of stereocilia, we show in Sec. 6.3 that our model yields robust stereocilia shapes with only one adjustable parameter and accounts for experimental results not previously discussed in the theoretical literature. We show the modifications induced by espin reattachment during the course of treadmilling by discussing a simplified situation involving only one filament. In Sec. 6.4, we treat this single-filament case far away from the polymerizing end of the filament and in Sec. 6.5 we deal with the filament's stationary profile. Sec. 6.6 then focuses on the lateral correlations that espin reattachment induces in a multi-filament bundle, and we discuss our results in Sec. 6.7.

6.2 Model for the actin and cross-linker dynamics

Consistent with the experimental data presented in the previous section, here we consider the coupling of the actin bundle's polymerization dynamics to that of espin.

In our model, presented in Fig. 6.2(a), maximally cross-linked actin is continuously produced at a location $\ell = 0$ at an externally imposed treadmilling velocity v. The polymerization dynamics of the actin bundle is thus assumed to be deterministic. In practice, this polymerization is highly regulated by several proteins comprised in the electron-dense "tip complex" located at the stereocilium tip [Appearing darker in Fig. 6.1(c)—see also Refs. [118, 126, 127, 128]]. Here we do not speculate about the fluctuations induced by this complicated and still poorly understood dynamics, but note that since the filaments across the bundle are cross-linked, they move together at a velocity equal to the average polymerization rate of the filaments. This velocity is almost constant: indeed, considering as a first approximation that the fluctuations in the polymerization rates of different filaments are independent, we conclude from the central limit theorem that the amplitude

[2]The microvilli of hair cells are much shorter than their stereocilia. Some are visible in Fig. 6.1(b), where they coincide with the boundary between different cells.

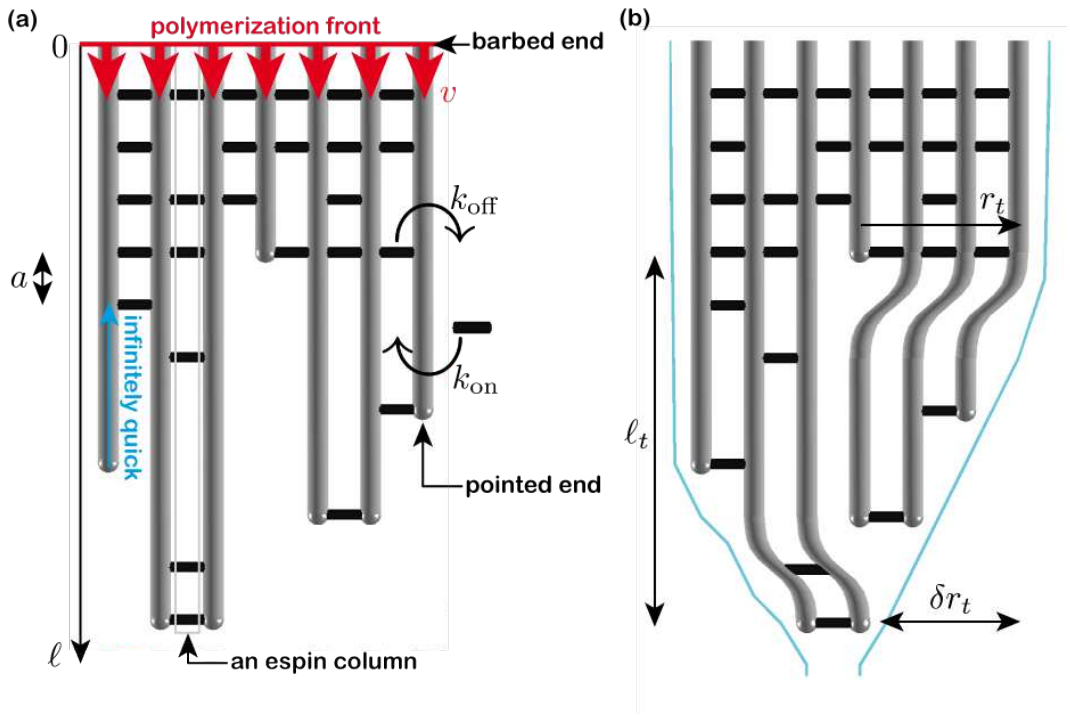

Figure 6.2: Illustration of our model. (a) Cross-linked actin is produced in $\ell = 0$ and treadmills down with a velocity v. Meanwhile, espins are exchanged with the surrounding solution with rates k_{on} and k_{off}. An actin filament not held by a cross-linker at its pointed end immediately depolymerizes to the next espin. (b) Membrane tension tends to make the radius of the protrusion shrink, and thus pushes the filaments together into a tapered shape. We respectively denote by r_t, $r_t - \delta r_t$ and ℓ_t the largest radius, smallest radius and length of the tapered end. The membrane is represented in cyan.

of the fluctuations in the treadmilling velocity of the whole bundle are proportional to $N^{-1/2}$, where N is the number of filaments in the bundle. In the limit of large bundles, we are thus justified in neglecting these fluctuations.

As the actin moves down, espin is exchanged with the surrounding medium. This represents the attachment/detachment dynamics of the cross-linker as well as its possible degradation. Considering that the typical time for the depolymerization dynamics is $\simeq$ 1000 s (the time required to depolymerize one helical period of the actin filament according to Ref. [119]) and assuming a diffusion constant of $60\,\mu\text{m}^2.\text{s}^{-1}$ (estimated from the Stokes radius of espin [134]), we estimate that the unbound espin concentration is homogeneous over length scales of order at least $250\,\mu$m, *i.e.* larger than the size of the stereocilium. We thus consider that the espin attachment and detachment rates k_{on} and k_{off} are constant throughout the stereocilium. Note that this reasoning would not hold if espin were actively localized in some regions of the stereocilia, or if the diffusion of espin were slowed down considerably, for instance by crowding effects. It is however not known how much the actin bundle slows the diffusion of espin down, and we assume throughout this chapter that this effect is not sufficient to induce significant espin density gradients.

The opposite hypothesis is considered in Ref. [144], which we further discuss in Sec. 6.7. A similar discussion applies to the supply of actin to the tip of the stereocilium, which we consider to always be sufficient to maintain the treadmilling velocity v. Finally, espin attachment at the altitude ℓ is only possible between two neighboring filaments of length equal to or larger than ℓ (indeed, espin obviously cannot reattach if there are no actin filaments).

We consider as a simplifying hypothesis that actin filaments can only depolymerize from their pointed ends. In agreement with the experimental results presented in the previous section, we assume that espin prevents the depolymerization of the actin filaments it cross-links. We furthermore assume that actin depolymerization happens on much shorter time scales ($\simeq 1\,\mathrm{s}$) than the espin attachment dynamics (the bundle treadmilling time is $\simeq 48\,\mathrm{h}$). Hence on the time scales relevant for the morphogenesis of stereocilia, actin filaments depolymerize instantaneously up to the next point where they are cross-linked, and are then stalled until the cross-linker detaches, which it does with a rate k_{off}. We denote by a the spacing between two actin cross-linkers. A filament cannot depolymerize further than $\ell = 0$—this means that we consider that a filament of vanishing length does not disappear, but is immediately re-nucleated by the tip complex so that the total number N of filaments is conserved.

From the model described here, we expect the lower end of the actin bundle to have a very irregular shape due to the stochastic character of the espin detachment and subsequent actin depolymerization [as in Fig. 6.2(a) for example]. At first sight, this does not seem consistent with the smooth tapered end observed experimentally [Fig. 6.1(c)]. The two behaviors are however compatible if one takes into account the influence of the membrane. Using the results of Sec. 3.1, we note that since the radius of the stereocilium ($\simeq 200\,\mathrm{nm}$) is larger than the natural membrane tether radius $\left[(\kappa/2\sigma)^{1/2} \simeq \text{a few tens of nm}\right]$, the dominant influence of the membrane is that of its tension σ, which tends to shrink the tube and therefore push the irregularly distributed filaments together, as illustrated in Fig. 6.2(b). In doing so, the membrane lowers its surface tension energy by an amount $\approx \sigma \ell_t \delta r_t$, and a number ≈ 100 of actin filaments are bent with a radius of curvature $\approx \ell_t^2/\delta r_t$ over a length $\approx \ell_t$, hence a cost $\approx 100 k_B T \ell_p \times \ell_t \times (\delta r_t/\ell_t^2)^2$ in bending energy, where ℓ_p is the persistence length of actin and the other lengths are defined in Fig. 6.2(b). Using $\sigma \simeq 10^{-5}\,\mathrm{N.m^{-1}}$, $\ell_t \simeq 10\,\mu\mathrm{m}$, $\delta r_t \simeq 100\,\mathrm{nm}$ and $\ell_p \simeq 10\,\mu\mathrm{m}$, we find that the tension energy gain $\approx 10^{-17}\,\mathrm{J}$ upon pushing the filaments into a tapered shape exceeds the filament bending energy cost $\approx 4 \times 10^{-23}\,\mathrm{J}$ by far, thus validating our picture. Indeed, experimentally, actin filaments are observed to be packed together throughout the stereocilium [121]. Because of this packing mechanism, actin filaments that are not neighbors in $\ell = 0$ might come into contact. Here we neglect the possibility that such accidental neighbors become cross-linked by espin. Therefore, we take into account the spatial structure of the bundle in the horizontal direction only through the notion of nearest neighbor in the initial ($\ell = 0$) paracrystal.

Since espin is in principle able to bind the membrane [132] and it has been shown experimentally that cross-linkers-mediated contact with the membrane stabilizes actin bundles during *Drosophila* bristle disassembly [139], the membrane surrounding the actin bundle might to some extent be able to stabilize an actin filament through cross-linking in a similar way that a neighboring filament does. The question of the influence of the

lateral boundary conditions on the stereocilium shape is further discussed in Sec. 6.6.4.

In the remainder of this chapter, we express lengths in units of the distance a between espin sites and times in units of the average lifetime k_{off}^{-1} of a cross-linker unless otherwise specified. We denote the dimensionless polymerization velocity $v/(ak_{\text{off}})$ simply by v, and define $k = k_{\text{on}}/k_{\text{off}}$.

6.3 Stereocilium shape without espin reattachment

In this section we solve the model presented above in the case where espin is incorporated in the actin bundle only at the stereocilium tip, meaning that $k = 0$. In this situation, the problem simplifies considerably as the probability of presence of an espin cross-linker at any potential espin cross-linking site is independent of the dynamics of the surrounding actin filaments and of the other cross-linkers. Indeed, the site located at a distance ℓ from the polymerization front is occupied if and only if an espin has been incorporated when this site was located at the polymerization front and has then survived detachment for a time ℓ/v. Since the detachment process is analogous to a radioactive decay-like stochastic process with rate 1, the site in question is occupied with probability

$$P_{\text{on}}(\ell) = P_0 e^{-\ell/v}, \tag{6.1}$$

where $P_{\text{on}}(0) = P_0$ is the probability with which an espin cross-linker is incorporated at $\ell = 0$. For a maximally cross-linked bundle, $P_0 = 1$. Now considering not one espin site, but a full espin column [see definition in Fig. 6.2(a)], we ask for the probability that the last espin of the column is located at an distance ℓ or smaller from the polymerization front. This probability is given by the infinite product

$$P_c^{\leqslant}(\ell) = [1 - P_{\text{on}}(\ell+1)] \times [1 - P_{\text{on}}(\ell+2)] \times [1 - P_{\text{on}}(\ell+3)] \times \ldots, \tag{6.2}$$

where $\ell \leqslant 0$. Now turning to the actin filaments, we see that an actin filament has a length smaller or equal to ℓ if and only if all neighboring espin columns have their last espin in ℓ or above. Denoting by n the number of neighbors of an actin filament [$n = 6$ in stereocilia—see Fig. 6.1(e); $n = 2$ in Fig. 6.2(a)], the probability for a filament to have a length smaller or equal to ℓ in the absence of espin reattachment reads

$$P_f^{\leqslant}(\ell) = P_c^{\leqslant}(\ell)^n = \prod_{i=1}^{+\infty} \left[1 - P_0 e^{-(\ell+i)/v}\right]^n. \tag{6.3}$$

Indeed, the filament is shorter than ℓ if and only if none of the neighboring espin columns contain any cross-linker below ℓ.

We now discuss this result and compare it to experimental data. For more clarity, we temporarily go back to non-scaled units. Qualitatively, $P_f^{\leqslant}(\ell)$ is equal to zero for small ℓs, and to one for large ℓs. If a large number of filaments are present, the number of filaments of length larger than ℓ is proportional to $P_f^{>}(\ell) = 1 - P_f^{\leqslant}(\ell)$. According to the discussion of Sec. 6.2, the section $\pi[r(\ell)]^2$ of the stereocilium is proportional to the number of filaments longer than ℓ, so that

$$r(\ell) = r(0)\sqrt{1 - P_f^{\leqslant}(\ell)}. \tag{6.4}$$

Here we do not specify the physical processes fixing $r(0)$, the radius at the polymerizing end of the actin bundle. For relatively short-lived actin-based protrusion, $r(0)$ could be fixed by dynamical effects operating during the initial actin bundling phase [145]. In stereocilia, mechanical regulation within the tip complex might lead to its continuous regulation [125]. Since the length of the stereocilia ($\simeq 5\,\mu$m) is much larger than that the distance between two cross-linking sites ($\simeq 10\,$nm), we can use the continuum limit of Eq. (6.3):

$$P_f^{\leqslant}(\ell) \underset{v/(ak_{\rm off})\gg 1}{\sim} \exp\left[-e^{-(\ell-\ell_s)k_{\rm off}/v}\right], \tag{6.5}$$

where

$$\ell_s = \frac{v}{k_{\rm off}} \ln\left(\frac{nvP_0}{ak_{\rm off}}\right). \tag{6.6}$$

Equivalently, the probability density for the filament end to be in ℓ reads

$$P_f(\ell) \underset{v/(ak_{\rm off})\gg 1}{\sim} \frac{k_{\rm off}}{v} \exp\left[-\frac{(\ell-\ell_s)k_{\rm off}}{v} - e^{-(\ell-\ell_s)k_{\rm off}/v}\right]. \tag{6.7}$$

Note that in the discrete case, this probability density is related to the cumulative probability $P_f^{\leqslant}$ by

$$P_f^{\leqslant}(\ell) = \sum_{\ell' \leqslant \ell} P_f(\ell'). \tag{6.8}$$

Therefore, in the continuum limit

$$P_f(\ell) = -\frac{{\rm d}P_f^{\leqslant}}{{\rm d}\ell}(\ell). \tag{6.9}$$

A more rigorous definition of what we mean by "continuum limit" is given in Sec. 6.5.3. For small values of ℓ, this equation yields a cylindrical profile with a characteristic length ℓ_s given by Eq. (6.6). The cylinder then tapers over a length $v/k_{\rm off}$. These predictions are plotted and compared to experimentally observed stereocilia shapes in Fig. 6.3. Several parameters involved in our theoretical shapes are well known experimentally. Up to six espins can bind to each helical period of the actin filament, which yields $a/n = (37/6)\,\mu$m [131]. The actin of the part of the stereocilium that sticks out of the cell is completely renewed by treadmilling in $48\,{\rm h} = \ell_s/v$ [119], which imposes a different value of v depending on the length of the stereocilium. In agreement with electron microscopy studies, we assume that the actin bundle is heavily cross-linked by espin, so that $P_0 = 1$. This leaves only one free parameter $k_{\rm off}$. Since the three stereocilia of Fig. 6.3 belong to the same cell, we furthermore impose that they are all described by the same value of $k_{\rm off}$. Taking $k_{\rm off} = 0.14\,{\rm h}^{-1}$ yields a good fit for all three stereocilia.

More quantitative experimental results are also accounted for by our model. As mentioned earlier, Ref. [119] indicates that the treadmilling velocity of a stereocilium is proportional to its length. One might thus be worried that Eq. (6.6) predicts a nonlinear relationship between those two quantities. The non-linearity is however weak as it is due to a logarithm, and we show in Fig. 6.4(a) that the velocity-length relationship predicted there is compatible with experimental observations. Here the value of $k_{\rm off}$ is the same as the one determined in Fig. 6.3, meaning that no adjustable parameter is used in

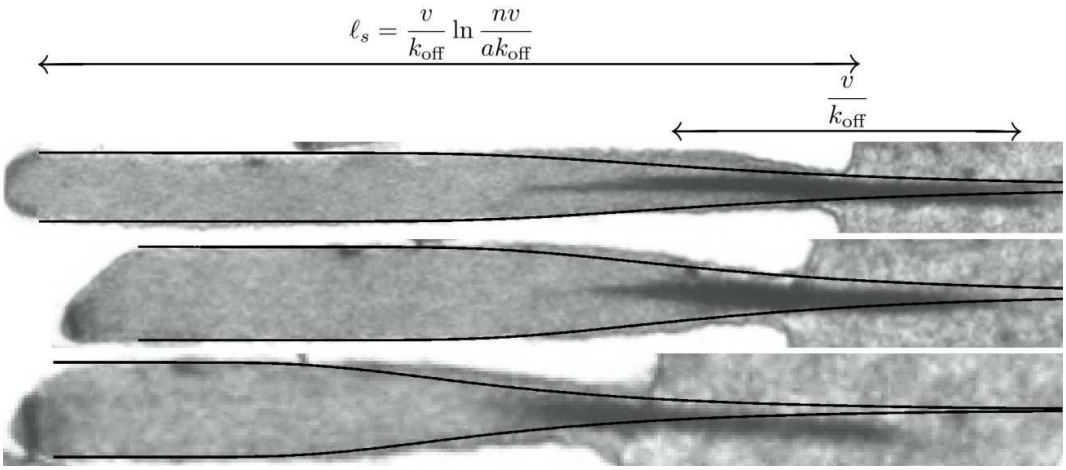

Figure 6.3: Comparison between our predictions [Eq. (6.4)—plotted as thick black lines], and the micrographs of healthy, wild-type guinea pig stereocilia presented in Fig. 6.1(c) and taken from Ref. [114]. The stereocilia are presented in decreasing order of size and with different magnifications. The left ends of the lines indicate the reference $\ell = 0$ corresponding to the position of the polymerization front.

Fig. 6.4(a). In Fig. 6.4(b), we compare the experimentally measured [128] density profile of one specific type of espin, espin 1, along three stereocilia belonging to the same vestibular hair cell[3] to an exponential, as the espin density is expected to be proportional to the probability $P_{\rm on}$ defined in Eq. (6.1). The decay length of the experimental curves increases with stereocilium length (and therefore treadmilling velocity) as predicted by this equation. Consequently, three different stereocilia of the same cell are again well described by using one common value of $k_{\rm off}$. Note however that although espin 1 does bind actin, its main role could be the regulation of actin polymerization, while other espins might be responsible for most of the cross-linking [146]. Another interesting result is presented in Ref. [138]. In this study, CL4 cells were transfected with espin, which caused the elongation of the cells' microvilli. The average elongation was measured and correlated to the level of expression of espin. Assuming that espin is incorporated at the tip of the protrusion at a rate proportional to its level of expression c_e, we can consider that P_0 is proportional to c_e. Following this, Eq. (6.6) yields a prediction for the dependence of ℓ_s on c_e, which we show in Fig. 6.4(c). We used two new adjustable parameters, as these experiments deal with a different cell type and different protrusions the the ones presented above (in particular, the renewal time of microvilli is much shorter than that of stereocilia). The best fit is found for $v/k_{\rm off} = 1.5\,\mu$m. The value of the other parameter, $\mathrm{d}\left(\frac{nvP_0}{ak_{\rm off}}\right)/\mathrm{d}c_e$ does not contain any exploitable information as only relative values of c_e are known experimentally.

Overall, we find that the simple case where espin does not reattach to actin yields good agreement with experimental data, while relying on only one adjustable parameter. Note also that the stereocilium length given by Eq. (6.6) has a smooth dependence on

[3]The actin bundle renewal time in vestibular hair cells is 72 h [119].

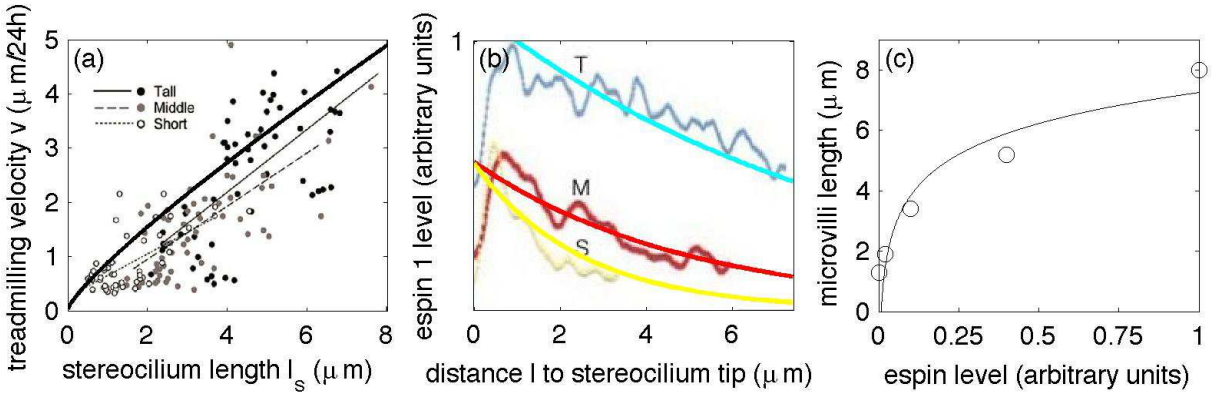

Figure 6.4: Dependence of the protrusion length on various parameters predicted by Eq. (6.6) and determined from experiments. (a) Measured treadmilling velocity versus length in the stereocilia of the rat cochlea. In mammals, cochlear stereocilia are arranged into three rows of graded height, as illustrated in Fig. 6.1(c). Experimental data for each of these rows (denoted by "tall", "middle" and "short" in the figure) are indicated by different symbols, and the best linear fits for each subgroup are given as thin lines. The thick line is the plot of Eq. (6.6), using the same value $k_{\mathrm{off}} = 0.14\,\mathrm{h}^{-1}$ as in Fig. 6.3. Experimental data taken from Ref. [119]. (b) Espin 1 density as a function of ℓ in the vestibular stereocilia of guinea pigs. The three curves correspond to three stereocilia of the same hair cell with different lengths (T $\simeq 35\,\mu$m, M $\simeq 20\,\mu$m, S $\simeq 10\,\mu$m). Agreement with Eq. (6.1) is found for $k_{\mathrm{off}} = 0.35\,\mathrm{h}^{-1}$, which is of the same order of magnitude as the value deduced from the fit of Fig. 6.3. Experimental data taken from Ref. [128]. (c) Dependence of the length of microvilli of CL4 cells on the espin overexpression level. Experimental data taken from Ref. [138].

both $\frac{v}{k_{\mathrm{off}}}$ and $\frac{nvP_0}{ak_{\mathrm{off}}}$, as illustrated by Fig. 6.4(a) and (c). This makes the stereocilium robust with respect to perturbations of the cellular conditions, which is expected for such a well-regulated structure.

6.4 Single-filament dynamics with reattachment

Although the results presented above give a good description of the shape of experimentally observed stereocilia, it is interesting to study the effects of espin reattachment on our model. We might indeed have to take this effect into account in more detailed studies of stereocilia or when interested in other types of cellular protrusions. In actual stereocilia, cross-linkers detaching from the actin filaments might diffuse for a while, and then reattach somewhere else in the actin bundle. If diffusion is considered fast in the sense of Sec. 6.2, this is equivalent to putting the filament in contact with a reservoir of cross-linkers, represented by the attachment rate k. In this configuration, the espin dynamics influences actin depolymerization in the same way as above, but the reverse becomes also true, as espin can only reattach at a given site only if this site is surrounded by two actin

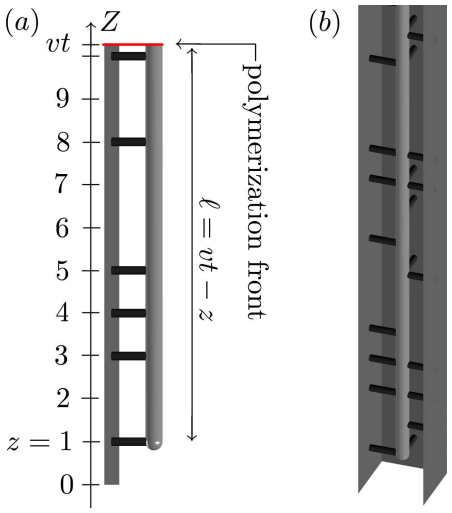

Figure 6.5: Schematics of the single-filament problem. (a) Single filament bound to a single wall and the coordinate system used in Sec. 6.4. (b) Single filament bound to $n = 3$ walls.

filaments. In contrast to the previous section, the actin is not slaved to the espin anymore, which makes the problem more complicated.

In the present section, we consider only the simplified case of a single filament cross-linked to a wall, as shown in Fig. 6.5(a). In Sec. 6.4.1, we write a master equation for the stochastic dynamics of this problem. The espin variables can be eliminated from this equation, as shown in Sec. 6.4.2. Far away from the polymerization front, a chemical equilibrium between bound and unbound espins is reached and the problem can be solved exactly, which we do in Sec. 6.4.3.

6.4.1 Master equation

Unlike in the previous section, here we consider the altitude in the reference frame of the filament, not of the polymerization front. We assume that the polymerization front is at altitude zero at time $t = 0$. Since it moves with a velocity v in the reference frame of the filament, it is at altitude vt at time t. Thus the altitude $z = vt - \ell$ of the pointed end of the filament is an integer smaller or equal to the altitude vt of the polymerization front [Fig. 6.5(a)]. We denote by $\{e_i = 0 \text{ or } 1\}$ the variables representing the state of the potential espin-binding sites, with $e_i = 0$ ($e_i = 1$) denoting an empty (occupied) site at position i.

Let Z be an integer smaller than vt and $\{E_i\}$ a set of numbers equal to either 0 or 1. The master equation describes the evolution of

$$\mathcal{P}\left[\{e_i = E_i\}_{i\in\mathcal{E}(Z,t)}, z = Z; t\right], \tag{6.10}$$

i.e. of the probability that the filament altitude z is equal to the integer Z and the espin variables e_i are equal to the E_is at time t. Note that the probability of Eq. (6.10) is a

function of the E_is with indices such that

$$i \in \mathcal{E}(Z,t), \tag{6.11}$$

where $\mathcal{E}(Z,t)$ is the set of active espin sites at time t for a filament with its pointed end in Z. The condition Eq. (6.11) means that i is an integer satisfying the two following conditions:

- $i \geqslant Z+1$. Indeed, all espins lower than the tip of the filament ($i < Z$) have to be off, as there is no actin filament for them to attach to. On the other hand, the espin in $i = Z$ must be on, otherwise the filament end cannot be in $z = Z$ (it would immediately depolymerize) and the probability of Eq. (6.10) vanishes. As a consequence of this, we consider that the detachment of the espin in z and the instantaneous depolymerization of the filament to the next occupied espin site are one and the same event.

- $i \leqslant vt$, as we do not consider what happens above the polymerization front. In the following, we consider a situation analogous to the case $P_0 = 1$ of the previous section, meaning that any espin at altitude $i = vt$ has a probability one of being on. Its subsequent evolution is described by the master equation.

Following this, the master equation for the probability of Eq. (6.10) is concerned only with espin detachment/attachment events.

If $Z \leqslant vt - 1$, the master equation reads

$$\partial_t \mathcal{P}\left[\{e_i = E_i\}_{i\in\mathcal{E}(Z,t)}, z = Z; t\right] = -\mathcal{P}\left[\{e_i = E_i\}_{i\in\mathcal{E}(Z,t)}, z = Z; t\right] + \mathcal{K}^b + \mathcal{K}^u + \mathcal{D}. \tag{6.12}$$

The first term of the right-hand side of this equation is the probability current away from the $(\{E_i\}, Z)$ state due to the detachment of the espin holding the filament's pointed end at the altitude Z, which induces a depolymerization event. The term $\mathcal{K}^b$ is the probability current due to espin binding events. It reads

$$\begin{aligned}\mathcal{K}^b \;=\; & k \sum_{j\in\mathcal{E}_1(\{E_i\},Z,t)} \mathcal{P}\left[\{\ldots, e_{j-1} = E_{j-1}, e_j = 0, e_{j+1} = E_{j+1}, \ldots\}_{i\in\mathcal{E}(Z,t)}, z = Z; t\right] \\ & -k \sum_{j\in\mathcal{E}_0(\{E_i\},Z,t)} \mathcal{P}\left[\{\ldots, e_{j-1} = E_{j-1}, e_j = 0, e_{j+1} = E_{j+1}, \ldots\}_{i\in\mathcal{E}(Z,t)}, z = Z; t\right],\end{aligned}$$

where $\mathcal{E}_0\left[\{E_i\}_{i\in\mathcal{E}(Z,t)}, Z, t\right]$ and $\mathcal{E}_1\left[\{E_i\}_{i\in\mathcal{E}(Z,t)}, Z, t\right]$ are the complementary subsets of $\mathcal{E}(Z,t)$ containing all indices j such that $E_j = 0$ and $E_j = 1$, respectively. Both terms of $\mathcal{K}^b$ implicate the probabilities of states with the espin site j unoccupied, meaning that an espin is susceptible to bind in j. The first term represent binding events to sites such that $E_j = 1$ and therefore represents a probability influx to the $(\{E_i\}, Z)$ state. The second term, on the other hand, represents events where an espin binds to a site j such that $E_j = 0$ and thus represents a probability flux away from the $(\{E_i\}, Z)$ state. The term $\mathcal{K}^u$ is the probability current due to espin unbinding events that do not induce any

depolymerization (*i.e.* occurring at altitude $Z+1$ or higher). It reads

$$\begin{aligned}\mathcal{K}^u &= \sum_{j\in\mathcal{E}_0(\{E_i\},Z,t)} \mathcal{P}\left[\{\ldots,e_{j-1}=E_{j-1},e_j=1,e_{j+1}=E_{j+1},\ldots\}_{i\in\mathcal{E}(Z,t)},z=Z;t\right]\\ &\quad-\sum_{j\in\mathcal{E}_1(\{E_i\},Z,t)} \mathcal{P}\left[\{\ldots,e_{j-1}=E_{j-1},e_j=1,e_{j+1}=E_{j+1},\ldots\}_{i\in\mathcal{E}(Z,t)},z=Z;t\right],\end{aligned}$$

which has a similar interpretation to $\mathcal{K}^b$. The term $\mathcal{D}$ stands for the probability current to the $(\{E_i\},Z)$ state due to depolymerization events. It reads

$$\mathcal{D}=\sum_{Z'=-\infty}^{Z-1}\mathcal{P}\left[\{e_{Z'+1}=0,\ldots,e_{Z-1}=0,e_Z=1,e_{Z+1}=E_{Z+1},\ldots\}_{i\in\mathcal{E}(Z',t)},z=Z';t\right],$$

meaning that the depolymerization of a filament with its pointed end located at the altitude Z' results in an increase of the probability of the $(\{E_i\},Z)$ state if and only if all espins between Z' and Z are off (*i.e.* the filament immediately depolymerizes to the position Z) and the espin is Z is on (*i.e.* depolymerization stops in Z).

We now turn to the boundary condition at the polymerization front, *i.e.* to the master equation for $vt-1<Z\leqslant vt$. At this location, none of the three first terms of the right-hand side of Eq. (6.12) exist. Indeed, the filament is not allowed to depolymerize further than the polymerization front and there are no espin sites undergoing attachment/detachment events except for the one in Z. Denoting by $\lfloor x\rfloor$ the integral part (or floor) of any real number x, the master equation for the site closest to the polymerization front reads

$$\partial_t\mathcal{P}\left[\{e_i=E_i\}_{i\in\mathcal{E}(\lfloor vt\rfloor,t)},z=\lfloor vt\rfloor;t\right]=\partial_t\mathcal{P}\left[z=\lfloor vt\rfloor;t\right]=\mathcal{D}'. \tag{6.13}$$

In this equation, the first equality reflects the fact that there are no active espin sites above $z=\lfloor vt\rfloor$—otherwise said $\mathcal{E}(\lfloor vt\rfloor,t)=\emptyset$. The term $\mathcal{D}'$ is a modified depolymerization current taking into account the fact that filaments cannot depolymerize beyond the polymerization front:

$$\begin{aligned}\mathcal{D}' &= \sum_{Z'=-\infty}^{\lfloor vt\rfloor-1}\mathcal{P}\left[\left\{e_{Z'+1}=0,\ldots,e_{\lfloor vt\rfloor-1}=0\right\}_{i\in\mathcal{E}(Z',t)},z=Z';t\right]\\ &= \sum_{Z'=-\infty}^{\lfloor vt\rfloor-1}\mathcal{P}\left[\left\{e_{Z'+1}=0,\ldots,e_{\lfloor vt\rfloor-1}=0,e_{\lfloor vt\rfloor}=0\right\}_{i\in\mathcal{E}(Z',t)},z=Z';t\right]\\ &\qquad+\mathcal{P}\left[\left\{e_{Z'+1}=0,\ldots,e_{\lfloor vt\rfloor-1}=0,e_{\lfloor vt\rfloor}=1\right\}_{i\in\mathcal{E}(Z',t)},z=Z';t\right].\end{aligned}$$

This probability has exactly the same interpretation as $\mathcal{D}$, except that depolymerization cannot continue beyond $Z=\lfloor vt\rfloor$ and stops there whatever the state of the espin site *i.e.* whatever the value of $e_{\lfloor vt\rfloor}$.

The master equation is now completely specified, but the initial state of the system is not. In the following, we consider situations where the system is prepared at $t=0$

in a superposition of states where the position $Z_0 \leqslant 0$ of its tip is well-defined, and the probabilities for the espin sites between Z_0+1 and 0 to be occupied are arbitrary, although independent from one another. Here we denote the initial probability for the espin site in i to be on by $\frac{k+\delta_0(i)}{1+k}$, where the $\{\delta_0(i)\}_{i\in\{Z_0+1\,..\,-1\}}$ are arbitrary numbers to be specified depending on the particular problem at hand and $\delta_0(0) = 1$, meaning that the espin site located at the polymerization front is occupied. Here the notation $\{i\,..\,j\}$ with $(i,j) \in \mathbb{N}^2$ stands for the integer interval comprising i, j and all integers in between. Leaving the filament dynamics aside for an instant, it is fairly obvious that the probability for an espin site to be occupied when at equilibrium with the espin reservoir is $\frac{k}{1+k}$. Therefore $\delta_0(i)$ represents the deviation of the state of site i away from equilibrium. Following this discussion, the initial state is given by

$$\begin{aligned}&\mathcal{P}\left[\{e_i = E_i\}_{i\in\mathcal{E}(Z,t)}, z = Z; t = 0\right]\\ &\quad= \left[\prod_{j\in\mathcal{E}_0(\{E_i\},Z,0)} \frac{1-\delta_0(j)}{1+k}\right]\left[\prod_{j\in\mathcal{E}_1(\{E_i\},Z,0)} \frac{k+\delta_0(j)}{1+k}\right]\delta_{Z,Z_0},\end{aligned} \tag{6.14}$$

where the symbol δ_{Z,Z_0} denotes the Kronecker delta.

6.4.2 Simplifying espin out of the master equation

The problem specified in the previous section is at first sight a very complicated one, since it deals with a system whose state is specified by a large number of variables: the filament end position z, and $\lfloor vt - z\rfloor$ additional espin variables. In this section, we show that if an initial condition of the form of Eq. (6.14) is used, this dynamics simplifies considerably and it is possible to write an effective master equation in a closed form for the filament height probability

$$P(Z,t) = \sum_{\{E_i=0,1\}_{i\in\mathcal{E}(Z,t)}} \mathcal{P}\left[\{e_j = E_j\}_{j\in\mathcal{E}(Z,t)}, z = Z; t\right], \tag{6.15}$$

where the sum is over all possible values of the espin variables.

In order to prove this, we introduce the quantity

$$\begin{aligned}&\mathcal{Q}\left[\{E_i\}_{i\in\mathcal{E}(Z,t)}, Z; t\right]\\ &\quad= \left[\prod_{j\in\mathcal{E}_0(\{E_i\},Z,t)} \frac{1-\delta(j,t)}{1+k}\right]\left[\prod_{j\in\mathcal{E}_1(\{E_i\},Z,t)} \frac{k+\delta(j,t)}{1+k}\right]P(Z,t),\end{aligned} \tag{6.16}$$

with $\delta(i,t) = \delta_0(i)e^{-(1+k)t}$. Here the $\{\delta_0(i)\}_{i\in\{Z_0+1\,..\,0\}}$ are the same as the numbers defined in Eq. (6.14). The $\{\delta_0(i)\}_{i\in\mathbb{N}^*}$, on the other hand, are new constants, the value of which we discuss in the following. The factor $e^{-(1+k)t}$ by which the $\delta_0(i)$s are multiplied reflect the exponential relaxation of the espin sites towards a chemical equilibrium with the espin reservoir. Here we show that $\mathcal{Q}$ is a solution of the master equation provided that the $\{\delta_0(i)\}_{i\in\mathbb{N}}$ are chosen properly and that $P(Z,t)$ obeys a system of equations to be specified.

There are two boundary conditions to be considered on top of Eq. (6.12). The first one concerns the espin variables and stipulates that if vt is an integer, the probability that the espin site located at the altitude $i = vt$ is equal to one. This condition reads

$$\mathcal{P}(e_i = 1; t = i/v) = \sum_{\{E_j=0,1\}_{j<i}} \sum_{Z=-\infty}^{i} \mathcal{P}\left[\{e_l = E_l\}_{l\in\mathcal{E}(Z,t)}, z = Z; t = i/v\right] = 1. \quad (6.17)$$

Using Eq. (6.16) and the normalization condition

$$\sum_{Z\leqslant vt} P(Z,t) = 1, \quad (6.18)$$

we find that $\mathcal{Q}$ satisfies Eq. (6.17) if and only if

$$\forall i \in \mathbb{N} \quad \delta(i, i/v) = 1 \quad \Leftrightarrow \quad \forall i \in \mathbb{N} \quad \delta_0(i) = e^{(1+k)i/v}. \quad (6.19)$$

In the following, we use this condition as the definition of the $\{\delta_0(i)\}_{i\in\mathbb{N}}$. This implies

$$\forall i \in \mathbb{N} \quad \forall t \in \mathbb{R}^+ \quad \delta(i,t) = \exp\left[-(1+k)\left(t - \frac{i}{v}\right)\right]. \quad (6.20)$$

The second boundary condition is Eq. (6.13), which $\mathcal{Q}$ satisfies if and only if

$$\partial_t P(\lfloor vt \rfloor, t) = \sum_{Z'=-\infty}^{\lfloor vt\rfloor-1} \left[\prod_{i=Z'+1}^{\lfloor vt\rfloor-1} \frac{1-\delta(i,t)}{1+k}\right] P(Z',t). \quad (6.21)$$

We now consider the initial condition. It is obvious that $\mathcal{Q}$ satisfies Eq. (6.14) at $t = 0$ if and only if

$$P(Z, t = 0) = \delta_{Z,Z_0}. \quad (6.22)$$

Finally, we consider the master equation Eq. (6.12) for a generic filament length $Z \leqslant vt - 1$. Inserting $\mathcal{Q}$ into Eq. (6.12), we find that the time derivatives of the two products in $\mathcal{Q}$ simplify with $\mathcal{K}^b$ and $\mathcal{K}^u$. We are thus left with the condition

$$\forall Z \in \{Z_0 .. \lfloor vt-1 \rfloor\} \quad \partial_t P(Z,t) = -P(Z,t) + \frac{k+\delta(Z,t)}{1+k} \sum_{Z'=-\infty}^{Z-1} \left[\prod_{i=Z'+1}^{Z-1} \frac{1-\delta(i,t)}{1+k}\right] P(Z',t). \quad (6.23)$$

The interpretation of this equation is fairly straightforward. The first term of its right-hand side is the probability current away from the (Z) state (*i.e.* the state where the pointed end of the filament is in Z). The rate of escaping this state is 1, which is the detachment rate of the espin holding the filament in Z. The second term represents the probability influx to the (Z) state. This influx is due to filaments depolymerizing from any altitude $Z' < Z$ to the altitude Z, which is reflected by the sum over Z'. Just like a filament in Z, a filament in Z' has a rate 1 of depolymerizing, which is the off rate of the espin located at altitude Z'. Whether it is going to depolymerize all the way to the altitude Z depends on the state of the espins located between Z' and Z. Let us consider a

filament with its pointed end in Z' that starts depolymerizing. It contributes to $\partial_t P(Z,t)$ under two conditions. First, all espins between Z' and Z have to be off, which happens with probability

$$\frac{1-\delta(Z'+1,t)}{1+k} \times \frac{1-\delta(Z'+2,t)}{1+k} \times \ldots \times \frac{1-\delta(Z-1,t)}{1+k}. \tag{6.24}$$

Second, the espin in Z has to be on, which happens with probability $\frac{k+\delta(Z,t)}{1+k}$. Assuming that the espins above the pointed end of the filament behave independently from each other—which we show in the next paragraph—we just have to multiply these probabilities to account for the form of Eq. (6.23).

Let us now prove more rigorously that $P(Z,t)$ is indeed the probability of finding the pointed end of the filament in Z at time t. The problem defined in Sec. 6.4.1 has a unique solution. On the other hand, the function $\mathcal{Q}$ defined in Eqs. (6.16) and (6.20) is a solution of this problem if and only if $P(Z,t)$ satisfies the system constituted of Eqs. (6.21), (6.22) and (6.23). Therefore, $\mathcal{Q}$ is *the* unique solution of the problem defined in Sec. 6.4.1 if and only if the system Eqs. (6.21), (6.22) and (6.23) has a solution that is normalized to one. This is true because of the following three reasons: this system is linear; $P(Z,t=0)$ is normalized to one; and Eqs. (6.21) and (6.23) conserve probability. Thus we proved that $\mathcal{Q}$ always exists, and is therefore the unique solution of the problem studied here.

In conclusion, solving the master equation of the one-filament problem is equivalent to solving the system of equations Eqs. (6.21), (6.22) and (6.23). In Sec. C.1 of the appendix, we show that the distribution given in Eq. (6.3) is the stationary solution of the special case $k=0$. In Secs. 6.4.3 and 6.5, we focus on deriving solutions valid for $k \neq 0$.

Before moving on to this study, however, we pause to reflect on the meaning of Eq. (6.16). Using this equation, we find the conditional probability for the ith espin to be on assuming the filament tip is in Z ($i \in \{Z+1\,..\,\lfloor vt \rfloor\}$):

$$\mathcal{P}(e_i = 1 | z = Z; t) = \frac{\mathcal{P}(e_i = 1, z = Z; t)}{P(Z,t)} = \frac{k+\delta(i,t)}{1+k}, \tag{6.25}$$

meaning that the state of the espin site in i is independent of the altitude z of the filament's pointed end as long as $z < i$. This is the key to the simple form of $\mathcal{Q}$: in the process described here, all espins above the altitude of the filament's pointed end attach and detach independently from each other and from the filament dynamics. On the other hand, if the filament end is assumed to be at altitude Z, then the espin in Z is on with probability one, meaning that it is completely correlated with the filament, although uncorrelated with the other espins. Although this fact might seem obvious at first sight, one should note that this is only true in the special case considered here where the depolymerization rate of the filament is infinite. In the generic situation where depolymerization happens on a time scale comparable to that of the espin dynamics, the correlations between filaments and espin are not confined to the very last espin site anymore, but penetrate into the following sites. This situation is studied numerically in Ref. [147], and we propose that the case of large but finite depolymerization rates could be tackled by a perturbation scheme around the analytical results presented here.

6.4.3 Exact solution at chemical equilibrium

According to Eq. (6.25), the probability for the espin site located at altitude $i > z$ to be occupied is equal to $\frac{k+\delta(i,t)}{1+k}$. This allows us to extend our interpretation of $\delta_0(i)$ to $\delta(i,t)$, which we can now interpret as the deviation of the espin density at site i from the steady-state density $\frac{k}{1+k}$ corresponding to a situation where site i is in equilibrium with the espin reservoir. Depending on the value of i, this imbalance can have two distinct origins. For $i \in \{Z_0 + 1 \,..\, -1\}$, it originates in the arbitrarily chosen initial state of the espin site, which is reflected by our choice of the $\{\delta_0(i)\}_{i\in\{Z_0+1\,..\,-1\}}$. For $i \geqslant 0$, it comes from the fact that espin sites are always occupied at the polymerization front (they are incorporated into the actin bundle with probability one). With time, however, espin sites lose the memory of their initial conditions, and relax back to an equilibrium with the espin reservoir. This is reflected by the fact that for $i < 0$, $\delta(i,t) = \delta_0(i)e^{-(1+k)t}$ relaxes to zero at large times and that for $i \geqslant 0$, $\delta(i,t)$ vanishes far away from the polymerization front [*i.e.* for $vt - z \gg v/(1+k)$—see Eq. (6.20)].

In this section, we tackle the effective dynamics of the filament's pointed end in a situation where all espins are in chemical equilibrium with the bulk, which is valid for long times and far away from the polymerization front. Let us define Q by

$$P(Z,t) = \frac{Q(Z,t)e^{-t}}{(1+k)^{Z_0-Z}}. \tag{6.26}$$

Here the boundary condition Eq. (6.21) need not be considered as the polymerization front is assumed to be far away. Thus we only need to solve the system constituted by Eqs. (6.22) and (6.23), which now read

$$Q_e(Z,t=0) = \delta_{Z,Z_0} \tag{6.27a}$$

$$\partial_t Q_e(Z,t) = k \sum_{Z'=-\infty}^{Z-1} Q_e(Z',t), \tag{6.27b}$$

where the index e denotes the fact that the espins are at equilibrium with the reservoir. We solve this system in Sec. C.2 of the appendix and find

$$P_e(Z_0,t) = e^{-t} \tag{6.28a}$$

$$P_e(Z,t) = \frac{e^{-t}}{(1+k)^{Z_0-Z}} \sum_{i=1}^{Z-Z_0} \frac{(Z-Z_0-1)!}{(i-1)!(Z-Z_0-i)!}\frac{(kt)^i}{i!}, \tag{6.28b}$$

where it is understood in Eq. (6.28b) that $Z > Z_0$ [note that $P(Z,t) = 0$ for $Z < Z_0$].

Eq. (6.28) describes the depolymerization dynamics of the filament. Since Eq. (6.27b) is invariant by both time and space translations, we expect that depolymerization takes place at a constant average velocity. Also, since depolymerization is a stochastic process, the initially peaked altitude distribution Eq. (6.27a) broadens as time increases. These features are indeed observed of Fig. 6.6(a), where we plot the probability distribution P_e derived here. From an analytical point of view, the dynamics of the filament's pointed end is expected to be diffusive on long length and time scales. We show this by considering the $t \to +\infty$ limit, where Stirling's approximation can be applied to the factorials of

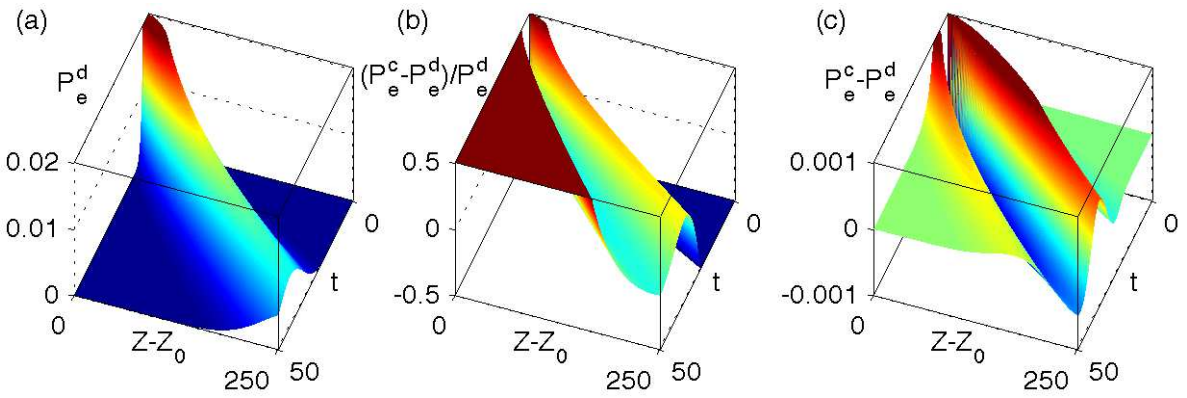

Figure 6.6: Probability distribution for the depolymerization of a filament cross-linked by espins at equilibrium with a reservoir characterized by $k = 0.2$. Here we denote by P_e^d the exact discrete solution given in Eqs. (6.28) and by P_e^c the continuum approximation Eq. (6.29). (a) Discrete solution plotted as a function of time and space. (b) Relative error $(P_e^c - P_e^d)/P_e^d$. Large values of the relative error are observed in regions where the probability is very small (*i.e.* in unimportant regions). (c) Absolute error $P_e^c - P_e^d$, where these seemingly large errors do not appear.

Eq. (6.28) and the discrete sum can be replaced by an integral. Expanding the resulting expression to lowest order in $1/t$ in the scaling region defined by $\langle Z - Z_0 \rangle (t) = \mathcal{O}(t)$ and $\langle [(Z - Z_0) - \langle Z - Z_0 \rangle]^2 \rangle (t) = \mathcal{O}(t)$ yields a gaussian integral, which we compute to find

$$P_e(Z,t) \underset{t\to+\infty}{\propto} \exp\left\{ -\frac{k^2}{2(1+k)(2+k)t} \left[Z - Z_0 - \frac{(1+k)t}{k} \right]^2 \right\}, \tag{6.29}$$

which is characteristic of a biased diffusion with diffusion coefficient $D_d = \frac{(1+k)(2+k)}{2k^2}$ and average depolymerization velocity $v_d = \frac{1+k}{k}$. Interestingly enough, this depolymerization velocity can be recovered from the following very simple argument: consider a filament cross-linked to the wall at its pointed end. Since the cross-link detaches with a rate 1, the average waiting time for the filament to unpin is $\tau = 1$. Once the filament is released, it quickly depolymerizes to the next cross-linker, and then becomes pinned again. Since the espins are at equilibrium with the reservoir, the average cross-linker density is $\rho = \frac{k}{1+k}$, meaning that the filament depolymerizes over an average distance $d = 1/\rho$ before becoming pinned again. Therefore, the average depolymerization velocity of the filament is $v_d = d/\tau = \frac{1+k}{k}$.

The asymptotic expression Eq. (6.29) is in good agreement with the full solution for long times, as shown in Fig. 6.6(b-c).

6.5 Long stationary filament with reattachment

Here we continue studying the single-filament master equation derived in the previous section. Although the study of Sec. 6.4.3 yields an exact analytical solution, it is unlikely

to be of interest in the case of stereocilia. Indeed, as mentioned above, stereocilia are maintained in hair cells over extended periods of time, and should therefore be described as stationary solutions of our master equation. In the following, we show that this implies that we cannot ignore the interactions between the depolymerizing end of the filament and the polymerization front anymore. In order to tackle this extra level of complexity, we restrict ourselves to long filaments (*i.e.* much longer than the spacing between two cross-linking sites).

In Sec. 6.5.1 we discuss the qualitative features of the stationary state considered here and show that it cannot be mapped onto a Fokker-Planck equation in the continuum limit. Some elements of this discussion allow us to extend the master equation derived in the previous section to cases where a single filament is bound to several walls, which we do in Sec. 6.5.2. In Sec. 6.5.3, we derive an appropriate continuum limit for this generalized master equation. The stationary solution of this problem is given in Sec. 6.5.4.

6.5.1 Discussion of the stationary state

Starting from the situation considered in Sec. 6.4.3, we can distinguish between two regimes:

If the depolymerization velocity is smaller than the polymerization velocity ($v_d < v$), then the pointed end of the filament never catches up on the polymerization front, and Eqs. (6.28) are a good approximation of its dynamics. In this case, the filament length—which is equal to the distance between polymerization front and pointed end—grows indefinitely at velocity $v - v_d$ and the filament has no stationary state. In order to favor this regime, one should cross-link the actin as heavily as possible, so as to slow depolymerization down as much as possible. It is worth noting, however, that v_d cannot be smaller than 1, which corresponds to a maximally cross-linked situation (*i.e.* to jumps of size 1 at a rate 1). Therefore, if $v < 1$, the regime described here can never be reached.

If, on the other hand, the depolymerization velocity is larger than the polymerization velocity ($v_d > v$), the pointed end moves closer and closer to the polymerization front. Thus the length of the filament is bounded in this regime. We hereafter call the threshold $v = v_d$ the *growth transition*. As it comes closer to the polymerization front, the pointed end of the filament penetrates into regions where the cross-links have not yet lost the memory of their incorporation into the bundle, and are therefore more dense than at equilibrium. More specifically, their average density is given by Eq. (6.25) and reads

$$\rho(\ell) = \frac{k + e^{-\frac{1+k}{v}\ell}}{1+k}, \tag{6.30}$$

where $\ell = vt - z$ is the length of the filament. Using the same argument as in the previous section, the depolymerization velocity of a filament of length ℓ is equal to $1/\rho(\ell)$. A stationary filament length is obtained when this velocity matches the polymerization velocity. This approximative reasoning yields a value of the stationary length ℓ_s:

$$v = \frac{1}{\rho(\ell_s)} \quad \Leftrightarrow \quad \ell_s = \frac{v}{1+k} \ln \left[\frac{1}{(1+k)\left(\frac{1}{v} - \frac{1}{v_d}\right)} \right], \tag{6.31}$$

where $v_d = \frac{1+k}{k}$. Eq. (6.31) matches Eq. (6.6) for $k = 0$, $P_0 = 1$ and $n = 1$. *In vivo*, stereocilia are much longer than the spacing between two cross-linkers, meaning that we are interested in the regime $\ell_s \gg 1$. There are two ways to enter this regime. One is for the logarithm in Eq. (6.31) to be very large, which can only be achieved if $\frac{1}{v} - \frac{1}{v_d}$ is very small. This happens when the polymerization and equilibrium depolymerization velocities are very well matched. As discussed in Sec. 6.1, this is not reasonable from a biological point of view. Indeed, stereocilia shapes relying on fine tuning are not robust as we demand. Therefore, we discard this first way of obtaining $\ell_s \gg 1$ and turn to the second one, which is $\frac{v}{1+k} \gg 1$. In this case, since $v < v_d$

$$1 \ll \frac{v}{1+k} < \frac{v_d}{1+k} = \frac{1}{k} \quad \Rightarrow \quad k \ll 1. \tag{6.32}$$

This result has two interesting consequences for our study, which we discuss in the remainder of this section.

First, Eq. (6.32) implies that we do not need to consider the depolymerization problem in all its generality, but only the small-k, large-v case, which is simpler. Let

$$\alpha = kv. \tag{6.33}$$

Multiplying Eq. (6.32) by k, we note that below the growth transition

$$0 \leqslant \alpha < 1. \tag{6.34}$$

Therefore, in the $v \to +\infty$ limit the growth transition occurs for $\alpha = 1$ (or equivalently $v = v_d = \frac{1+k}{k}$, which is its definition). The interesting regimes to consider are therefore those where α is finite, and in the following we take the $v \to +\infty$ limit at finite α.

Second, it was mentioned in Sec. 6.3 that the $v \to +\infty$ limit means that the stereocilium shape is smooth, and therefore that it can be treated in some continuum limit. Sec. 6.4.3 demonstrates that on large length scales, the behavior of the pointed end of the depolymerizing filament can be assimilated to a particle diffusing in a locally homogeneous environment. It is tempting to extrapolate this result to the regions where espins are not in equilibrium with the reservoir. Doing so is actually a very common continuum approximation for one-dimensional stochastic processes, and is equivalent to approximating the master equation of Sec. 6.4.1 by a Fokker-Planck equation (*i.e.* a diffusion equation with position-dependent drift and diffusion coefficient) [47]. From the considerations of the present section, we however see that such an approximation is not valid. In order to understand this, we remind ourselves that there are *two* conditions of applicability of the Fokker-Planck approximation. The first one is that the scale over which the environment is inhomogeneous (in this case, the decay length $\frac{v}{1+k}$ of the espin density) must be much larger than the distance between two sites. This is the case as $\frac{v}{1+k} \gg 1$. But there is also a second one, which states that the size of the particle's jumps must be much smaller than the scale over which the environment is inhomogeneous. In our case, the jump size is the typical length d over which the filament depolymerizes in a single depolymerization event. Comparing it to $\frac{v}{1+k}$ and using Eqs. (6.31) and (6.32), we find

$$\frac{d(\ell_s)}{v/(1+k)} = \frac{1+k}{v\rho(\ell_s)} = 1 + k \simeq 1. \tag{6.35}$$

Thus the jumps size is of the order of the length of the whole filament, and the Fokker-Planck approximation does not apply.

6.5.2 Master equation with several walls for large v

Here we extend Eq. (6.23) to the case where the filament is bound not to one, but to n walls, a situation pictured in Fig. 6.5(b). We do this in the limit $v \to +\infty$ with $\alpha = kv$ fixed, as discussed in the previous section.

Building from our experience of stereocilia shapes acquired in the $k = 0$ case (Sec. 6.3) and noting that we are studying the case $P_0 = 1$, we are able to speculate that the upper section of the stereocilium is cylindrical over a length $v \ln v$, followed by a transition region (corresponding to the tapered region of the stereocilium) with a size of order v, which is the non-trivial part. In this region, $z \approx v \ln v \Rightarrow \delta(z,t) \approx e^{-(v \ln v)/v} \approx v^{-1}$. This implies that the probability for an espin site located in the transition region to be occupied is of order $\frac{k+e^{-\ln v}}{1+k} = \mathcal{O}(v^{-1})$. In other words, espins are scarce in the transition region.

Let us consider a filament with its pointed end at the altitude z belonging to the transition region and in contact with several walls, as illustrated in Fig. 6.5(b). The probability for at least one of the n espin sites located at altitude z to be occupied is equal to one, otherwise the filament would not be there. Because espins are scarce in the transition region, the probability to have two or more sites occupied in Z is smaller than that of having only one by a factor $\approx v^{-1}$. To lowest order in v^{-1}, we can therefore consider that the pointed end of the filament is held at the altitude z by exactly one espin.

Under this assumption, we can derive a master equation similar to Eq. (6.23) using the same arguments as in Sec. 6.4.2. Here we present a qualitative justification for its form. Let $P(Z,t)$ be the probability that the pointed end of the filament is held in Z by any one of the espin sites located at this altitude. Like previously, the filament depolymerizes from this site with a rate 1. This means that the first term of Eq. (6.23) is unchanged. If a filament is initially located in $Z' < Z$, it goes to Z upon detachment of the espin holding it in Z' on two conditions. First, all espin sites between Z' and Z need to be empty, which happens with probability

$$\left[\frac{1-\delta(Z'+1,t)}{1+k}\right]^n \times \left[\frac{1-\delta(Z'+2,t)}{1+k}\right]^n \times \ldots \times \left[\frac{1-\delta(Z-1,t)}{1+k}\right]^n . \tag{6.36}$$

Second, at least one out of n espin sites in Z has to be occupied. This happens with probability

$$1 - \left[\frac{1-\delta(Z,t)}{1+k}\right]^n . \tag{6.37}$$

Following these arguments, the master equation for a filament bound to n walls for $v \gg 1$ and in the transition region reads:

$$\partial_t P(Z,t) = -P(Z,t) + \left\{1 - \left[\frac{1-\delta(Z,t)}{1+k}\right]^n\right\} \sum_{Z'=-\infty}^{Z-1} \left\{\prod_{i=Z'+1}^{Z-1} \left[\frac{1-\delta(i,t)}{1+k}\right]^n\right\} P(Z',t). \tag{6.38}$$

Note that the approach of this section is valid only in the transition region, which is very far away ($\approx v \ln v$) from the polymerization front in the $v \to +\infty$ limit. Therefore the

boundary condition Eq. (6.21) is irrelevant here. In the $v \to +\infty$ limit, $\delta(Z,t) \approx \delta(i,t) \approx k \approx v^{-1}$. Using the same level of approximation that we used when reasoning on the scarcity of espins, we expand the master equation to lowest order in v^{-1}:

$$\partial_t P(Z,t) = -P(Z,t) + n\left[k + \delta(Z,t)\right] \sum_{Z'=-\infty}^{Z-1} \left\{ \prod_{i=Z'+1}^{Z-1} \left[1 - n\delta(i,t) - nk\right] \right\} P(Z',t). \quad (6.39)$$

6.5.3 Continuum limit for the master equation

According to the arguments of Sec. 6.5.1, the limit $v \to +\infty$ with $\alpha = kv$ fixed can also be understood as the continuum limit for the master equation Eq. (6.39). This means that we are studying a situation where the typical decay length of the espin probability of presence is much larger than the distance between two cross-linkers, *i.e.* $v \gg 1$. In the stationary regime, the filament tip probability distribution depends only on the coordinate $\ell = vt - Z$. We define the coordinate ξ by

$$\ell = vt - Z = v \ln v + v\xi. \quad (6.40)$$

Since we are considering the transition region of the filament, *i.e.* a region of size $\approx v$ located at $\ell \approx v \ln v$, we consider only the region where ξ is of order 1. In the $v \to +\infty$ limit, we should thus be able to derive a v-independent shape equation for the transition region as a function of ξ. We therefore write the stationary filament length probability distribution as $P(\xi) = P(Z,t)$. According to Eq. (6.40), $\partial_t P(Z,t) = \mathrm{d}P(\xi)/\mathrm{d}\xi$, and the prefactor of the last term of Eq. (6.39) has the following asymptotic behavior

$$n\left[k + \delta(Z,t)\right] \underset{v\to+\infty}{\sim} nv\left(\alpha + e^{-\xi}\right). \quad (6.41)$$

Meanwhile, the sum behaves as

$$\sum_{Z'=-\infty}^{Z-1} \underset{v\to+\infty}{\sim} \int_{\xi}^{+\infty} \frac{\mathrm{d}\xi'}{v}. \quad (6.42)$$

We also note that the product of Eq. (6.39) has a finite limit:

$$\begin{aligned}
\prod_{i=Z'+1}^{Z-1} \left[1 - n\delta(i,t) - nk\right] &= \exp\left\{ \sum_{i=Z'+1}^{Z-1} \ln\left[1 - ne^{-(1+\alpha/v)(t-i/v)} - \frac{n\alpha}{v}\right] \right\} \\
&= \exp\left\{ \int_{v\xi}^{v\xi'} \left[\ln\left(1 - \frac{ne^{-y/v}}{v} - \frac{n\alpha}{v}\right) + \mathcal{O}(v^{-2}) \right] \mathrm{d}y + \mathcal{O}(v^{-1}) \right\} \\
&= \frac{\exp\left(n\alpha\xi - ne^{-\xi}\right)}{\exp\left(n\alpha\xi' - ne^{-\xi'}\right)} \left[1 + \mathcal{O}(v^{-1})\right], \quad (6.43)
\end{aligned}$$

where $vt - Z' = v\ln v + v\xi'$. Finally, we are able to write the $v \to +\infty$ continuum limit of the master equation Eq. (6.39):

$$\frac{\mathrm{d}P}{\mathrm{d}\xi}(\xi) = -P(\xi) + n\left(\alpha + e^{-\xi}\right) \exp\left(n\alpha\xi - ne^{-\xi}\right) \int_{\xi}^{+\infty} \frac{P(\xi')}{\exp\left(n\alpha\xi' - ne^{-\xi'}\right)} \mathrm{d}\xi'. \quad (6.44)$$

6.5.4 Continuum solution for the stationary state

In this section we fully solve Eq. (6.44), and show that it has a unique normalized solution. We define the function $f(\xi)$ by

$$P(\xi) = f(\xi) \times \exp\left[-(1-n\alpha)\xi - ne^{-\xi}\right]. \tag{6.45}$$

We divide Eq. (6.44) by $n\left(\alpha + e^{-\xi}\right)\exp\left(n\alpha\xi - ne^{-\xi}\right)$, differentiate with respect to ξ and make the change of variable $x = e^{-\xi}$. This yields

$$x(x+\alpha)f''(x) - \left[x - 2(x+\alpha) + n(x+\alpha)^2\right]f'(x) = 0. \tag{6.46}$$

This second order linear differential equation has two linearly independent solutions, one of which is obviously a constant. Integration of the fraction $f''(x)/f'(x)$ yields the second one. This finally yields

$$P(x) = c_1 x^{1-n\alpha}e^{-nx} + c_2\left[-\alpha + x^{1-n\alpha}e^{-nx}\int^x \left(u^{n\alpha-1}e^{nu}\right)\mathrm{d}u\right], \tag{6.47}$$

where c_1 and c_2 are arbitrary constants to be determined. Note that choosing the lower bound in this equation is equivalent to modifying the value of c_1.

Since $\ell \geqslant 0$, the variable ξ is defined on the interval $\xi \in [-\ln v, +\infty[$. As $\ln v \to +\infty$ in the limit considered here, the normalization condition for the probability distribution reads:

$$\int_{-\infty}^{+\infty} P(\xi)\,\mathrm{d}\xi = 1. \tag{6.48}$$

Meanwhile, Eq. (6.47) implies

$$P(\xi) \underset{\xi\to+\infty}{\to} -\alpha c_2, \tag{6.49}$$

meaning that the normalization condition Eq. (6.48) can only be fulfilled if $\alpha = 0$ or $c_2 = 0$. If $\alpha = 0$ then

$$P(\xi) = \exp\left(-\xi - ne^{-\xi}\right)\left[c_1 + c_2\int^{e^{-\xi}} \frac{e^{-nu}}{u}\mathrm{d}u\right]. \tag{6.50}$$

The asymptotic behavior of the integral in this expression is given by

$$\int^x \frac{e^{-nu}}{u}\mathrm{d}u \underset{x\to+\infty}{\sim} \frac{e^{-nx}}{nx}. \tag{6.51}$$

Therefore if $\alpha = 0$ the probability density function has the following finite limit

$$P(\xi) \underset{\xi\to-\infty}{\to} \frac{c_2}{n}, \tag{6.52}$$

which prevents normalization unless $c_2 = 0$. Therefore c_2 always vanishes whatever the value of α.

Determining c_1 from the normalization condition Eq. (6.48), the filament length distribution reads

$$P(\xi) = \frac{n^{1-n\alpha}}{\Gamma(1-n\alpha)} \exp\left[-(1-n\alpha)\xi - ne^{-\xi}\right], \tag{6.53}$$

where

$$\Gamma(b) = \int_0^{+\infty} \left(u^{b-1}e^{-u}\right) \mathrm{d}u \tag{6.54}$$

is the Gamma function. Qualitatively, the filament profiles described by Eq. (6.53) are quite similar to those obtained in the absence of espin reattachment and discussed in Sec. 6.3. Indeed, $P(\xi)$ decays extremely quickly (superexponentially) for negative ξs, while it decays as $e^{-(1-n\alpha)\xi}$ for $\xi \to +\infty$. By comparison, the distribution of Eq. (6.7) decays as $e^{-\xi}$.

Eq. (6.4) relates the radius of the stereocilium to the probability that the filament is shorter than ξ. It is therefore interesting to write the cumulative probability distribution:

$$P^{\leqslant}(\xi) = \frac{\Gamma\left(1-n\alpha, ne^{-\xi}\right)}{\Gamma\left(1-n\alpha\right)}, \tag{6.55}$$

where the incomplete Gamma function is defined as

$$\Gamma(b,x) = \int_x^{+\infty} \left(u^{b-1}e^{-u}\right) \mathrm{d}u. \tag{6.56}$$

Plots representing $P^{\leqslant}$ as a function of ℓ are presented as red lines in Fig. 6.10. The average filament length is given by

$$\langle\xi\rangle = \ln n - \psi(1-n\alpha) \quad \Leftrightarrow \quad \langle\ell\rangle = v\ln(nv) - v\psi(1-nkv), \tag{6.57}$$

where the digamma function and its behavior in 0 and 1 are given by

$$\psi(z) = \frac{\mathrm{d}\left[\ln\Gamma(z)\right]}{\mathrm{d}z} \tag{6.58a}$$

$$\underset{z\to 0^+}{=} -\frac{1}{z} - \gamma + \mathcal{O}(z) \tag{6.58b}$$

$$\underset{z\to 1}{\to} -\gamma, \tag{6.58c}$$

where $\gamma \simeq 0.577216$ is the Euler constant. Similarly to the situation of Sec. 6.3, the transition region is at a distance $v\ln(nv)$ away from the polymerization front. Note that for $k = 0 \Leftrightarrow \alpha = 0$, Eq. (6.55) goes to the distribution given in Eq. (6.5).

Differences with the $k = 0$ case are observed when considering the width of the transition region, which is equal to $-v\psi(1-nkv)$. According to Eq. (6.58b) this width diverges as

$$\langle\ell\rangle \underset{k\to k_c^-}{\sim} \frac{v}{1-nkv} \propto \frac{1}{|k-k_c|} \tag{6.59}$$

when k approaches the critical value

$$k_c = \frac{1}{nv}. \tag{6.60}$$

Therefore, for a large enough espin reattachment rate, a stationary filament profile ceases to exist. This is the n-walls generalization of the growth transition discussed in Sec. 6.5.1. Indeed, for $k \geqslant k_c$, espin slows the depolymerization down so much that the pointed end can never catch up on the polymerization front.

6.6 Coupling between filaments

Here we use numerical simulations—which we describe in Sec. 6.6.1—to study the effect of espin reattachment in the biologically relevant situation of a stereocilium composed of several filaments. Unlike in the previous sections, filaments are now bound to each other and not to walls. Their espin environment thus depends on their altitude and on the state of their neighbors. It is therefore unclear what form the growth transition introduced in Sec. 6.5.1 takes. We study this question in Sec. 6.6.2, and find a new critical value of k corresponding to an effective number of neighbors $n^{\text{eff}} = 2.5$. This anomalous behavior arises for the following reasons: in the $k = 0$, multi-filament case, the stochastic dynamics of each actin cross-linker is completely independent of the rest of the system, as shown in Sec. 6.3. The actin filaments are slaved to the espins, and their dynamics is very simple. Therefore, correlations between the lengths of actin filaments are limited to nearest neighbors, since only filaments with a common actin cross-linker are coupled. In the case studied in Secs. 6.4 and 6.5 (a single filament with espin reattachment), on the other hand, the length of the filament influences the espin sites, as it determines whether a cross-linker can reattach or not. In the situation considered in the present section, we expect filaments to be correlated over relatively long distances, as similar mutual correlations between filaments and espins mean that the state of a filament can now influence the neighboring espin column, which influences the next filament, and so on. In Sec. 6.6.3, we show that these correlations do indeed extend beyond the nearest neighbors, but present an argument suggesting that they are not sufficient to yield a self-affine interface. Finally, in Sec. 6.6.4 we compare the stereocilium shapes obtained from numerical simulations to those derived from a one-filament calculation.

6.6.1 Numerical simulations

In order to implement the stereocilium dynamics as described in Sec. 6.2, we design a Monte-Carlo simulation based on the Gillespie algorithm [148]. We simulate a square array of $L \times L$ filaments and denote the coordinates of a filament in the horizontal plane by (X, Y). Each filament (X, Y) is connected to each of its four neighbors $(X \pm 1, Y)$, $(X, Y \pm 1)$ by an espin column.

The altitude of the pointed end of filament (X, Y) is initially $Z_0(X, Y) = 0$, and is subsequently allowed to take any positive integer value smaller than vt, where t is the time elapsed since the beginning of the simulation. For each couple of neighboring filaments $\{(X, Y), (X + 1, Y)\}$ (or any other possible combination) and for each integer altitude i such that

$$\max[z(X, Y), z(X + 1, Y)] \leqslant i \leqslant vt, \tag{6.61}$$

there is an espin site $[(X, Y), (X+1, Y), i]$, which can be either occupied or empty. Espins

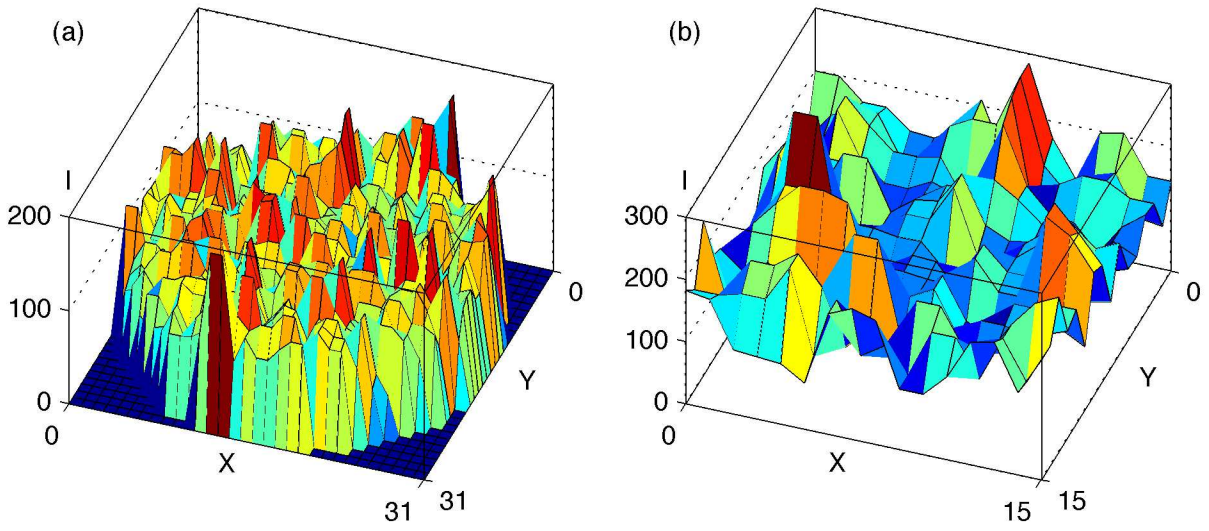

Figure 6.7: Profiles of two filament bundles obtained from the simulations described in the main text. The vertical axis represents the length $\ell = vt - z$ of the filaments, and was shrunk for easier visualization. In actual biological situations, we expect the longest filaments to be brought together by the membrane as illustrated in Fig. 6.2(b). (a) 32×32 bundle with a circular support and $k = 0$. (b) 16×16 bundle with periodic boundary conditions and $k = 0.015$—which we shown below to be a substantial reattachment rate, although below the growth transition. Both bundles are in their stationary state.

are incorporated with probability $P_0 = 1$ in $i = vt$. A filament with its pointed end in $z(X, Y)$ cannot depolymerize if there is an espin in at least one of the four following espin sites: $[(X, Y), (X \pm 1, Y), z(X, Y)]$, $[(X, Y), (X, Y \pm 1), z(X, Y)]$. Unlike in the model presented in Sec. 6.2, if all those four sites are empty, the filament does not depolymerize instantaneously but does so with a finite rate k_d. In practice we set k_d to a very large value ($10^5 \times k_{\text{off}}$ or larger), therefore the simulation should yield the same results as the model presented in Sec. 6.2.

In the following we focus on long stereocilia, for which we expect the continuum approach introduced in Sec. 6.5 to apply. This approach is valid for $v \gg 1$. Since simulating long bundles is time-consuming, we use $v = 20$ throughout this section, which represents a good compromise.

Two types of boundary conditions are used in our simulations. The first one is a periodic array of filaments, which is convenient when numerical simulations are used to investigate the $L \to +\infty$ limit. The second one is a circular array, where we impose that all filaments whose coordinates do not satisfy $(X - L/2)^2 + (Y - L/2)^2 < (L/2)^2$ are maximally depolymerized, and therefore that their pointed ends are always in $z = vt$. This allows us to simulate actual stereocilia more realistically. Example profiles from the simulations are shown in Fig. 6.7.

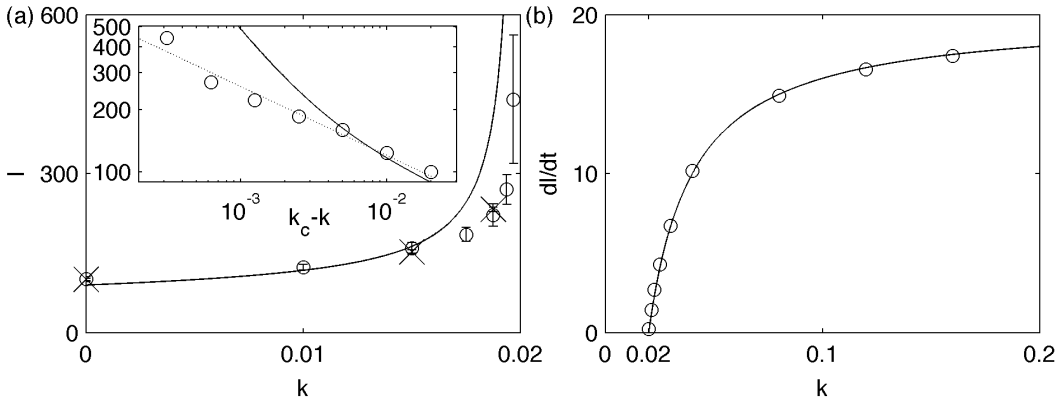

Figure 6.8: Growth transition for multi-filament bundles with reattachment. (a) Average length as a function of k below the transition and comparison with Eq. (6.57) for $n = 2.5$ (line). Open circles: 8×8 periodic arrays. Crosses: 16×16 periodic arrays, showing that the lengths do not depend much on L. Error bars represent the height fluctuations in the steady state. Inset: log-log representation of the same $\langle \ell \rangle$ data from 8×8 arrays as a function of the distance $k_c - k$ to the growth transition threshold. Solid line: Eq. (6.57) as in the main figure. Dotted line: power law fit as in Eqs. (6.62) and (6.63). (b) Growth velocity of the bundle as a function of k above the growth transition for 8×8 periodic arrays (open circles) and comparison to the generalization of the one-filament theory given in Eqs. (6.64) and (6.65) for $n = 2.5$ (line).

6.6.2 Couplings modify the growth transition

In order to investigate whether multi-filament bundles have a growth transition, we simulate several 8×8 periodic filament bundles for various value of the espin reattachment rate k.

We first focus on the values of k where stationary stereocilium profiles exist and monitor the average filament length, as shown in Fig. 6.8(a). At $k = k_c = 0.02$, the average filament length diverges, showing that coupled filaments do undergo a growth transition. This value of k_c matches the threshold of Eq. (6.60) if n is set to $n^{\text{eff}} = 2.5$. This effective n can be viewed as the average number of neighbors available for each filament to cross-link at each given instant, *i.e.* of neighbors longer than the filament. This view of the multi-filament growth transition is however only approximate. In Fig. 6.8(a), we fit a power law to the divergence of the stereocilium length and show that

$$\langle \ell \rangle \underset{k \to k_c^-}{\propto} \frac{1}{|k - k_c|^{\beta}} \tag{6.62}$$

with a multi-filament divergence exponent

$$\beta \simeq 0.33, \tag{6.63}$$

which is different from the exponent $\beta_1 = 1$ characterizing the divergence in the single filament case [Eq. (6.59)].

Now considering values of k above the growth transition puts us in the phase where the stereocilium grows indefinitely and at constant velocity. In Fig. 6.8(b), we plot the stereocilium's growth velocity as a function of k. As k is reduced, the pointed ends of the filaments depolymerize more and more quickly and catch up to the polymerization front for $k_c = 0.02$, which is consistent with the threshold determined in Fig. 6.8(a). At steady state, the stereocilium lengthening velocity is the difference between its polymerization velocity and its depolymerization velocity far from the polymerization front:

$$\frac{\mathrm{d}\ell}{\mathrm{d}t} = v - v_d. \tag{6.64}$$

This growth velocity vanishes at the growth transition. While v is imposed in our simulations, v_d depends on k and n. We can calculate its value for a single filament bound to n walls by generalizing the discussion given at the end of Sec. 6.4.3. Far away from the polymerization front, the probability for an espin to be on is $\frac{k}{1+k}$. In the cases considered here $k \ll 1$, meaning that espins are scarce far from the polymerization front. Otherwise said, the probability for a filament to be bound to several cross-linkers at one given altitude is negligible. This puts us exactly in the situation considered in Sec. 6.4.3: the filament is bound to cross-linkers with an average density ρ, and cannot be bound to more than one cross-linker at any given altitude. Compared to the discussion of Sec. 6.4.3, the density of the cross-linkers in the case considered here is n times larger, since there are n walls instead of one. To lowest order in k, this yields

$$v_d = \frac{1}{nk}. \tag{6.65}$$

This single-filament result is compared to the multi-filament simulations in Fig. 6.8(b) using $n = n^{\mathrm{eff}}$, and the two are found to be in very good agreement. Note that we expect the function $v_d(k)$ to diverge in 0 but be a smooth function of k for $k > 0$. In particular, $v_d(k)$ has no reason to have a singularity in $k = k_c$: indeed, k_c is defined by $v_d(k_c) = v$, and v_d does not depend on v. Thus $k = k_c$ is a generic point of the function $v_d(k)$. Therefore at the transition the following generic crossing scenario applies whether or not the filaments are coupled:

$$\frac{\mathrm{d}\ell}{\mathrm{d}t}(k) \underset{k \to k_c^+}{\propto} (k - k_c). \tag{6.66}$$

6.6.3 Correlations between filaments and interface width

The results of the previous section show that the behavior of coupled filaments below the growth transition is rather different from that of a single filament bound to several walls, even if the number of walls is chosen to represent an effective number of longer neighbors. That such discrepancies exist is not very surprising, as the dynamics of coupled filaments are interdependent, which cannot be represented by static walls. In the present section, we study these correlations further.

Let us define the two-dimensional interface width function of the bundle as

$$w(X, Y) = \sqrt{\left\langle [\ell(X, Y) - \ell(0, 0)]^2 \right\rangle}. \tag{6.67}$$

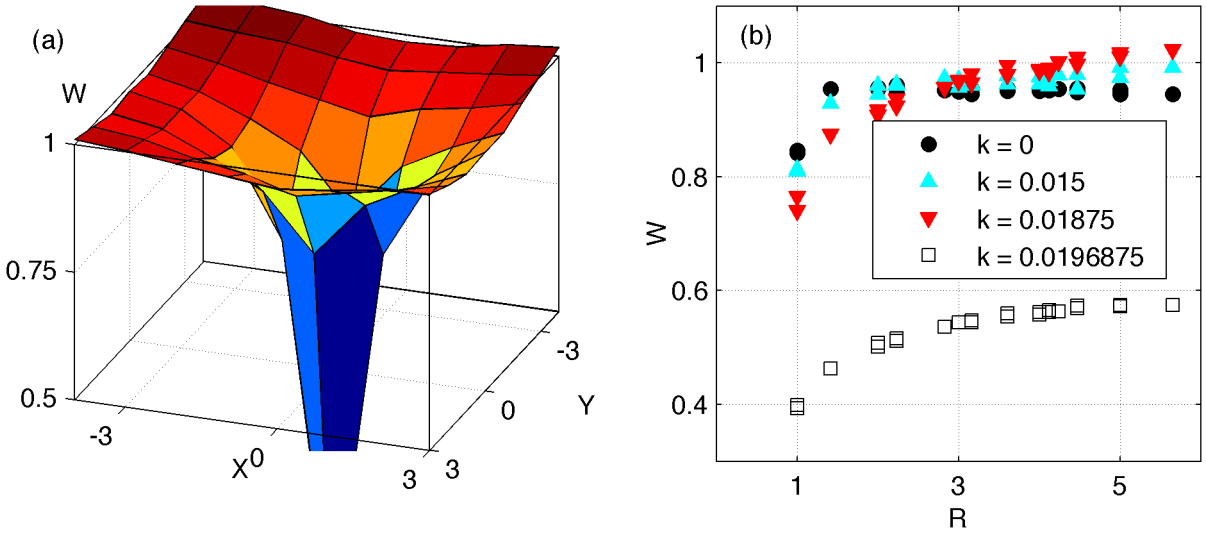

Figure 6.9: Normalized width functions $W(X,Y)$ for periodic filament bundles, as defined in Eq. (6.68). (a) Two-dimensional normalized width function for a 8×8 periodic bundle with $k = 0.01875$. (b) Normalized width function plotted as a function of the distance R for 8×8 periodic bundles and for various values of k. The width function vanishes for $R = 0$ (not shown) by definition. For $k = 0$, the width is different from its asymptotic value only for $R = 1$, meaning that only nearest neighbors are correlated. For $k = 0.0196875$, the width of the interface never reaches 1 because correlations extend over the whole bundle, thus calling for simulations with a larger L.

This function reflects the amount of correlations between the heights of the filaments located in $(0,0)$ and in (X,Y). It is equal to 0 in the limit where the filaments are infinitely correlated, or if $X = Y = 0$. If the interface as a whole has a finite width $\sqrt{\langle \ell^2 \rangle - \langle \ell \rangle^2}$, then $w(X,Y)/\sqrt{2}$ goes to this value in the limit where the filaments are completely uncorrelated. Finally, $w(X,Y) > \sqrt{2}\sqrt{\langle \ell^2 \rangle - \langle \ell \rangle^2}$ represents a situation where the filaments are anticorrelated.

In Fig. 6.9(a), we present the normalized width function of a weakly cross-linked 32×32 filament bundle, which we define as

$$W(X,Y) = \frac{1}{\sqrt{2}} \frac{w(X,Y)}{\sqrt{\langle \ell^2 \rangle - \langle \ell \rangle^2}}. \tag{6.68}$$

The closer to one $W(X,Y)$ is, the less correlated the filaments are. Here the averages are over all the filaments of the bundle and over $\simeq 100$ time points of the bundle dynamics. The time between two time points is chosen to be larger than the time over which the length of the filaments are correlated. In other words, our time points can be considered as independent samples. We also make sure that all time points are taken after the bundle reaches its stationary state.

In Fig. 6.9(b), we collapse the data of this plot into a function of $R = \sqrt{X^2 + Y^2}$ and compare it with similar ones obtained for other values of k. We observe that the correlations between filaments decay as R increases. The precise functional form of this

decay (*e.g.* is it exponential for large R?) is difficult to assess from the data presented here, although a more thorough study could yield more information. Another related question is whether there is a well-defined correlation length associated with this decay, and how it behaves at the growth transition. For instance, one might venture that the correlation length could diverge as $k \to k_c^-$, similarly to what happens in second-order phase transitions. In the following we give a few scaling comments on the morphology of the interface, which allows us to return to these questions at the end of the present section.

It is well known that out-of-equilibrium surface growth problems similar to the one studied here can lead to rough interfaces. During the past two decades, extensive efforts have gone into characterizing this roughness in terms of the self-affine geometry of the interface [149, 150]. In terms of the width function defined here, the self-affinity property means that when R is large, $w(R)$ grows as a well-defined power law

$$w(R) \underset{R\to+\infty}{\propto} R^{\zeta}, \tag{6.69}$$

which defines the roughness exponent $\zeta > 0$. Determining ζ—among other exponents—allows to define universality classes among out-of-equilibrium growth processes. Another type of behavior that can be characterized using the function $w(R)$ is the roughening transition of crystals [151]. This transition proceed as follows. Consider a periodically pinned interface, for instance the surface of a crystal (where the crystal layers are discrete and therefore the height of the interface can only take discrete values). For low temperatures, $w(R)$ goes to a constant for $R \to +\infty$, and the crystal is said to be facetted. As the temperature is increased above the so-called roughening temperature (which can be lower than the melting temperature of the crystal), the interface becomes "rough", meaning that its width diverges as

$$w(R) \underset{R\to+\infty}{\propto} \ln R. \tag{6.70}$$

Here we discuss whether laws of the type of Eqs. (6.69) or (6.70) could apply to our stereocilium model for $k < k_c$. At first sight, the interface defined by the lengths of the filaments as a function of X and Y has similarities with both types of models, as it is both out-of-equilibrium and as its altitude can take only discrete values determined by the periodic arrangement of the cross-linkers in the vertical direction. We note however that two phenomena limit the divergence of the interface width expressed in Eqs. (6.69) and (6.70). First, the finite size of the bundle means that R cannot be larger than L. Second, even for $L \to +\infty$ the interfaces presented here have a finite width of order $\sqrt{\langle \ell^2 \rangle - \langle \ell \rangle^2}$. Indeed, the polymerization front traps them in the $\ell > 0$ half-space, and long filaments always tend to depolymerize if $k < k_c$, which keeps their lengths finite, although they might fluctuate to large values. The only way for us to apply the concepts presented in Eqs. (6.69) and (6.70) to stationary stereocilia is therefore to consider systems where L and $\sqrt{\langle \ell^2 \rangle - \langle \ell \rangle^2}$ are large (*i.e.* large bundles with k close to k_c) and study the shape of the interface in the domain where $1 \ll R \ll L$ and $1 \ll w(R) \ll \sqrt{\langle \ell^2 \rangle - \langle \ell \rangle^2}$. In other words, we are wondering whether we can make a statement about width functions of the type of those presented in Fig. 6.9(b) in the intermediate region where $(\langle \ell^2 \rangle - \langle \ell \rangle^2)^{-1/2} \ll W(R) \ll 1$. Here we prove by contradiction that no such region exists. Assume that there

is a typical R scale, which we denote by R_0, that has the properties

$$1 \ll R_0 \ll L \quad \text{and} \quad 1 \ll w(R_0) \ll \sqrt{\langle \ell^2 \rangle - \langle \ell \rangle^2}. \tag{6.71}$$

Moreover, we expect $w(R)$ to be an increasing function of R, as neighboring filaments should have more strongly correlated lengths than filaments far apart. Let (X, Y) and $(X+1, Y)$ be two neighboring filaments with initially very similar heights $z(X, Y) \simeq z(X+1, Y)$. Now consider that (X, Y) undergoes a depolymerization event. We saw in Eq. (6.35) that the typical depolymerization length is $\langle \ell \rangle$, meaning that after the depolymerization event $z(X+1, Y) - z(X, Y) \approx \langle \ell \rangle$. This kind of event is very common in our system, which implies that since $w(1) \approx z(X+1, Y) - z(X, Y)$, we typically have $w(1) \approx \langle \ell \rangle$. Since $w(R)$ is an increasing function of R, we have $w(R_0) \gtrsim \langle \ell \rangle$. From the previous sections we expect that $\langle \ell \rangle$ should be of order $v \ln v$ and $\sqrt{\langle \ell^2 \rangle - \langle \ell \rangle^2}$ of order v. Thus in the continuum limit $v \to +\infty$ considered here $\sqrt{\langle \ell^2 \rangle - \langle \ell \rangle^2} < \langle \ell \rangle$. Therefore, we finally find that $w(R_0) > \sqrt{\langle \ell^2 \rangle - \langle \ell \rangle^2}$, which is in contradiction with Eq. (6.71).

In conclusion, in long stationary bundles of coupled filaments the interface reaches its maximum width $\sqrt{\langle \ell^2 \rangle - \langle \ell \rangle^2}$ over distances of order a few filaments, which means that it is impossible to define a mesoscopic scale where properties of the type described in Eqs. (6.69) and (6.70) could be observed. This accounts for the very spiky appearance of the profiles presented in Fig. 6.7. This also means that the width functions presented in Fig. 6.9(b) decay to a value very close to one on short length scales [$R = \mathcal{O}(1)$]. This argument seems to indicate that correlations between the filaments are smeared out by the large depolymerization jump sizes on length scales much smaller than the size of the system. It is therefore not obvious whether correlations could span the whole system, although Fig. 6.9(b) does seem to indicate that the typical correlation range grows as the growth transition is approached.

6.6.4 Multi-filament stereocilium profiles

In this last section we return to the question of the shape of stereocilia. In Fig. 6.10, we compare the shapes obtained from the simulations with theoretical expectations from the single-filament theory. For each value of k, the theoretical curve Eq. (6.55) is plotted using the effective number of neighbors $n^{\text{eff}} = 2.5$ defined in Sec. 6.6.2. As k is increased, the description of the bundle by the single-filament theory becomes worse and worse, as expected from Fig. 6.8(a).

Another theoretical result our simulations should be compared with is Eq. (6.55) using the actual number of neighbors $n = 4$. Note however that this is only possible for k smaller than 0.0125, which is the growth transition threshold for $n = 4$. Consistent with this, we plot the $n = 4$ theoretical curve only in Fig. 6.10(a), where $k = 0$. Excellent agreement with the numerical simulations is found. This is expected, as when espins are not allowed to reattach Eq. (6.55) is identical to Eq. (6.5), which is the exact solution of the multi-filament problem for $k = 0$.

In Fig. 6.10(b), we illustrate the dependence of the bundle shape on the number of filaments included in the simulations. No change in the shape is observed when multiplying the number of filaments by four, but the amplitude of the fluctuations is reduced. This

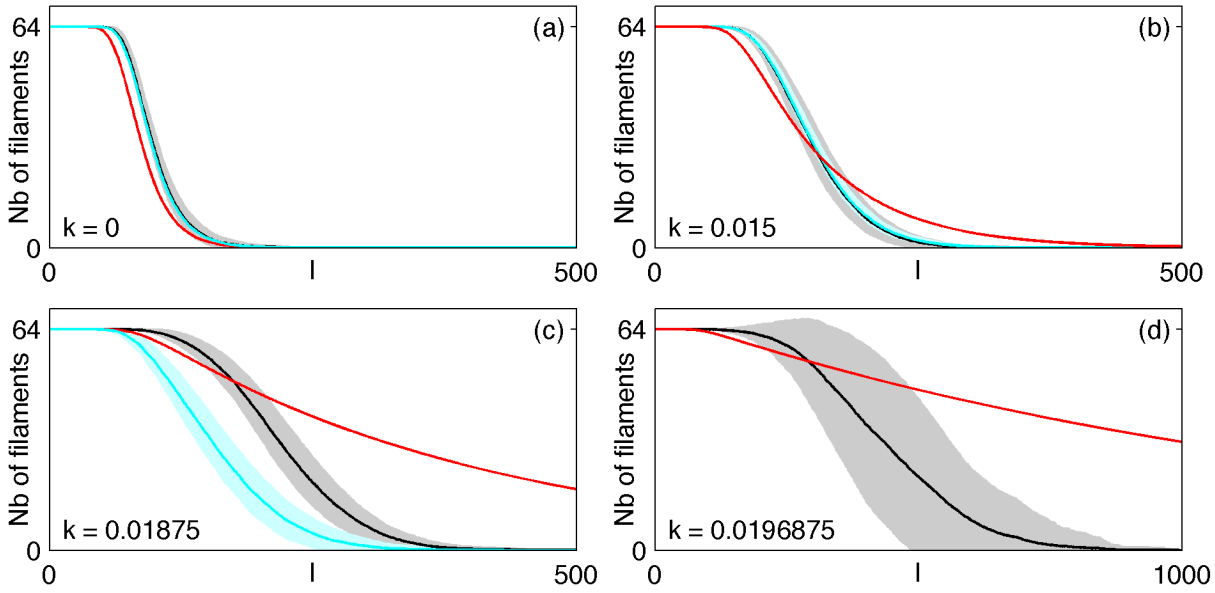

Figure 6.10: Profiles of multi-filament bundles for various values of k. Red lines represent $P^{>} = 1 - P^{\leqslant}$, with $P^{\leqslant}$ given by the single-filament theory Eq. (6.55) scaled to the number of filaments in the bundle with $n = 2.5$. Black lines represent the average number of filaments longer than ℓ for numerical 8×8 bundles. The gray area represents the standard deviation of the steady-state fluctuations around this average. The cyan lines have different meanings depending on the figure considered: (a) $n = 4$ single filament theory; (b) Average number of filaments longer than ℓ and fluctuations for a 16×16 bundle—data normalized to match the black line in $\ell = 0$; (c) Average number of filaments longer than ℓ and fluctuations for a circular bundle (32 filaments—data normalized to match the black line in $\ell = 0$). Note the dilated ℓ scale in (d).

suggests that in this regime at least, the average profile given by our $L = 8$ simulations is a good assessment of the $L \to +\infty$ limit.

In Fig. 6.10(c), we illustrate the dependence of the bundle shape on the boundary conditions of the bundle. It is found that the circular bundle [see illustration in Fig. 6.7(a)] is markedly shorter than the one with periodic boundary conditions. This is due to the fact that its outer filaments tend to depolymerize more quickly, as they have less neighbors. In the parameter regime presented here, this is sufficient to significantly reduce the average length of the bundle. This effect becomes negligible for small k and large L, *i.e.* if the filaments are correlated over a length much shorter than the radius of the bundle.

Finally, in Fig. 6.10(d) we note that as the growth transition is approached, the amplitude of the bundle's fluctuations increases dramatically. This is due to the fact that as the depolymerization velocity becomes very close to the polymerization velocity, the filament are more and more loosely confined to a finite length. Similarly to what happens for *e.g.* a brownian particle in a harmonic potential, a looser confinement means fluctuations of a larger amplitude.

6.7 Discussion

This chapter presents a simple physical model for the morphogenesis of stereocilia, whose very well-regulated shapes are crucial for the frequency selectivity of hearing in a wide range of animals. Our model is to be understood in the framework of Ref. [125], where the shape of stereocilia is attributed to an "internal clock" of the actin bundle. Here we propose that the "internal clock" is provided by the stochastic attachment-detachment dynamics of the well-characterized protein espin, or some other actin cross-linker. Many other known proteins, and probably unknown ones as well, play a role in the shaping of stereocilia. However most of them are localized in a precise region of the stereocilium—*e.g.* its tip—and therefore might not have access to any information about the overall length of the stereocilium, which would mean that they cannot be involved in its regulation. For this reason, we believe that the shape and size of stereocilia can be described by taking into account the dynamics of only a few crucial proteins, namely actin cross-linkers.

Although the emphasis of this chapter is on stereocilia, the simplicity of our model makes it general enough to describe several other biological length-regulation processes. The most obvious of these are of course other cellular protrusions, such as filopodia, microvilli and *Drosophila* bristles, where actin filaments are also coupled by cross-linkers. In addition, our approach is relevant to single-filament problems where each monomer stochastically switches between two states, which have different properties with respect to depolymerization. An example is the depolymerization of a single actin filament, where each monomer can be associated to either ATP or ADP as mentioned in chapter 1, and where the two states have different depolymerization rates [140]. Similarly, the tubulin monomers constituting microtubules—another type of cytoskeletal filament—can be associated to GTP or GDP. If the end of the filament is GTP-associated, it is stable and the microtubule grows. If it is GDP-associated, very fast depolymerization ensues. GTP-associated regions might however exist further down the microtubule, and stop the microtubule depolymerization, similarly to what espin does for actin in our model [152]. Conversely, some microtubule-associated proteins make the filament more susceptible to depolymerization, which could also be described with our approach [153].

We solve our model analytically in three simplified situations, and study it numerically in the general case. First, we tackle the situation where espins do not reattach to actin below the polymerization front. This problem is simple and we calculate the exact probability distribution for the lengths of coupled filaments. We then turn to the dynamics of a single filament in the case where espin is allowed to reattach. We completely solve this problem far away from the polymerization front. Close to the polymerization front, we calculate its steady-state solution in a suitably defined continuum limit. This analytical study reveals that finite-length filaments cease to exist above a critical value of the espin reattachment rate, and we term this change of behavior the "growth transition" of the system. We then go on to numerically study this transition in a multi-filament system. We find that when approaching the transition from above, the bundle dynamics is well described by a mean-field approach consisting in approximating the environment of each filament by a constant effective number of longer neighbors. When approaching the transition from the finite-length phase, on the other hand, the bundle length has a power law divergence as expected from the mean-field theory, but with an anomalous ex-

ponent. Numerical evidence points towards an increase of the correlation length between the filaments near the transition, but we argue that the bundle surface is unlikely to have so strong correlations as to become self-affine close to the critical reattachment rate.

On the biological side, stereocilia models have been proposed in the literature that yield good agreement with electron micrographs of stereocilia. The approach of Ref. [125] was described in the introduction of this chapter and forms the basis of the proposal made here. It however raises three serious concerns, which do not arise in our description: First, this reference depends partly on a hypothetical actin pointed end capping protein, whereas we only assume well-identified proteins; Second, it reproduces the shape of the stereocilia of deaf shaker 2J mutants, and we account for those of healthy animals; Third, its stereocilia shapes, unlike ours, rely on the fine tuning of some parameters, which is not consistent with the biological robustness of the well-controlled stereocilia shapes. Another quite different model was proposed in Ref. [144]. It is based on the fact that actin-polymerizing and actin-depolymerizing proteins could be actively localized at the stereocilium base, *e.g.* by molecular motors. Should the stereocilium accidentally elongate, actin-polymerizing proteins would become more scarce at its tip, thus polymerization would slow down and the stereocilium would shrinks back to its steady-state shape. Actin-depolymerizing proteins localized at its base drive the narrowing of the actin bundle there. This model offers an interesting insight into the possible roles of the experimentally well-documented active transport within the stereocilium. It is however difficult to assess its validity quantitatively as it hypothesizes several experimentally uncharacterized protein-protein interactions, and has an accordingly large number of adjustable parameters. Another problem is that localization in stereocilia has been experimentally observed to take place over length scales significantly shorter than the stereocilium (roughly $1\,\mu$m versus $10\,\mu$m). If this is the case, the actin-polymerizing proteins concentration at the tip depends only very weakly on the length of the stereocilium. Therefore for the stereocilium length to be well-controlled, the actin polymerization velocity must be very sensitive to the concentration of these proteins, which makes the length of the stereocilium extremely sensitive *e.g.* on the efficiency of the localization process. As in the previous model, this seems incompatible with the expected robustness of this structure. Finally, although this model accounts for the shape of reptile and bird stereocilia, it does not predict the existence of the rootlet, which is observed in mammals.

The model presented in this chapter is in qualitative agreement with several experiments showing the importance of espin in stereocilium length regulation. Our theoretical study allows us to predict that the reattachment rate of espin to actin must be much smaller then its detachment rate ($k \approx v^{-1} \ll 1$), or the actin bundle does not reach a stationary profile. This is consistent with the observation made in Ref. [119] that espin in the stereocilium seems to treadmill along with actin—in other word, that espin is essentially incorporated at the tip of the stereocilium and not so much exchanged with the solution in the bulk of the actin bundle. More quantitatively, we are able to reproduce the shape of several stereocilia within the same hair bundle with only one common fit parameter. In these fits we use $k = 0$. The reason for this is that the espin reattachment rate must be small enough for the system to be far from the growth transition. Indeed, close to the transition the stereocilium length strongly depends on k [Fig. 6.8(a)], and the stereocilium is not robust as we require. If on the contrary k is substantially smaller

than k_c, then the length of the bundle only weakly depends on k, and our choice to use $k = 0$ does not have much influence on the stereocilium's shape. We also account for the apparent proportionality between stereocilium length and turnover time. Finally, our approach faithfully captures the quantitatively measured relationship between microvillus length and espin expression.

Although our model yields biologically satisfactory stereociliary shapes by taking into account only espin exchanges between the actin bundle and a homogeneous espin reservoir, other related phenomena might play an important role in the shaping of actin-based cellular protrusions, and these effects deserve further investigations. First, it could be interesting to consider the case where the cross-linker does not diffuse instantaneously throughout the actin bundle. Indeed, in stereocilia its escape is hindered by the surrounding dense actin paracrystal, which might trap espin in the middle of the stereocilium and make its reattachment rate larger there than in the periphery. This might induce more elongated shapes than the ones calculated here. In other actin-based protrusion, this effect is even more likely to play a role as the actin turnover time is smaller, meaning that diffusion is comparatively slower. Second, we mentioned in the introduction that more than one type of actin cross-linkers are involved in several instances of actin-based protrusions. This effect might also significantly affect the shapes calculated here. Finally, in microvilli and filopodia the time scales involved in actin turnover could be small enough for the actin depolymerization dynamics to happen on the same time scales as the cross-linker dynamics. A first approach to this problem could be to perform a perturbation analysis of the results presented above by making the actin depolymerization rate is very large, rather than infinite as was done in this chapter.

Even within the framework of the model presented here, several questions remain open. The coupling of the dynamics of depolymerizing filaments, in particular, yields dramatic effects that are still poorly understood. In this chapter, we presented these effect by comparing the coupled filaments case with a single-filament system bound to an effective number of walls. As observed in Fig. 6.8, this description yields very good results above the growth transition, which we have yet to justify. It should also be checked whether this effective number of neighbors depends on v. Below the transition, our approach is significantly less successful, and a first step in improving it could be a better mean-field approach where the effective number of neighbors of each filament could be a function of its length and/or be determined self-consistently rather than fitted to numerical results. The range of the length correlations between filaments is another topic deserving attention, and is likely to be highly relevant to those questions. In particular, we would like to understand how this range behaves at the growth transition. Finally, the fact that the filament length diverges at this transition with a power law very different from that predicted by mean-field theory suggests that interesting non-trivial collective effects remain to be studied in this system.

Chapter 7

Conclusion

The present thesis deals with membrane-based tubular structures found in cells. Throughout the life of the cell, matter is sorted within its cytoplasm and exchanged with the outside. Membrane tubes appear very generically during such trafficking events. Our study focuses on three significantly different systems.

The first of these systems is dynamin, a protein specialized in polymerizing around short membrane tubes, and then severing them. In close connection with experiments, we show that the physical properties of the membrane, its curvature in particular, control the recruitment of dynamin to the membrane and could be important players for the regulation of endocytosis *in vivo*. We then pave the way for a more detailed understanding of this regulation by proposing two hypotheses about the mechanism of helix seeding, representing two limiting cases: First we consider the case where dynamin oligomers are much softer than the membrane and initially accommodate a high curvature; then we study the case where the membrane is much softer than dynamin oligomers and has to fluctuate down to a small radius for a helix to form. We propose experimental tests to discriminate between these two hypotheses. We also find that current helix growth experiments might involve non-trivial effects due to dynamin binding and diffusion, as well as interesting membrane and water flow patterns. Analyzing them could reveal novel information about dynamin-membrane interactions.

Once polymerized, dynamin changes conformation upon GTP hydrolysis and may or may not rupture the membrane depending on its mechanical environment. Again combining theory and experiments, we show that this conformational change is concerted, meaning that a long dynamin helix changes shape as one continuous body, *i.e.* does not break immediately. We uncover the forces at work during this process and show that the energy released by GTP hydrolysis—which drives the conformational change—is mainly used to squeeze the membrane out of the region encircled by dynamin. We develop a versatile theoretical formalism to analyze the mechanics of this composite process involving a mixture of twisting, elongation and constriction, and demonstrate its relevance by unifying seemingly contradictory experimental results through simple mechanical arguments.

Further developments of our approach to dynamin are closely tied to experimental progress. Regarding polymerization, we show here that several equally reasonable hypotheses about dynamin's seeding rate and growth kinetics can only be discerned experimentally. As far as its conformational change is concerned, any purely theoretical

approach is fated to rely on somewhat arbitrary assumptions. In this perspective, our hydrodynamic formalism has the advantage of enclosing all the unknown details of the system in a few well-identified phenomenological coefficients. We are currently designing a joint theoretical and experimental approach to monitor the rupture of dynamin-coated tubes under well-controlled mechanical conditions. Our approach is to first characterize the external conditions inducing tube breaking experimentally, and then infer the local state of the membrane at the breaking point from theoretical arguments. This method should enable us to formulate a heuristic criterion for membrane severing, which could then be used to guide more detailed microscopic modeling of the membrane's rupture. Another interesting direction where experiments could be a driving force is the study of the supercoiling of dynamin-coated tubes. More precise measurements of the conditions under which supercoils form could motivate a covariant version of the formalism presented in chapter 4, which would describe the coupling between flows of conserved quantities and the geometry of the tube. This in turn would help characterize the mechanics of dynamin in a detailed manner.

In vivo, several proteins assist dynamin in its severing action, although the experimental data discussed in chapter 4 shows that they are not absolutely necessary to get membrane fission. For instance, amphiphysin co-polymerizes with dynamin and facilitates its recruitment and that of clathrin to liposomes [41]. Endophilin might have a similar role [154]. Finally, actin colocalizes with dynamin shortly before vesicle detachment, which suggests that it is also involved in dynamin-mediated endocytosis [84]. It is probably not possible to obtain a complete picture of the action of dynamin without a better understanding of these interactions, and possibly of other relevant ones.

More generally, studying dynamin's conformational change could yield a broader perspective on membrane breaking in cells. It is interesting to note for instance that vesicle formation by clathrin on the one hand and by COPI and COPII on the other implicate very similar protein-membrane configurations [see Fig. 1.1(c)]. However, the former uses dynamin to sever the membrane neck it generates, while the latter does not. From an evolutionary perspective, the fact that the cell has come up with two very different solutions to a seemingly unique membrane-severing problem is intriguing. By understanding those mechanisms, we might uncover significant functional differences between these two pathways and therefore gain a deeper insight into intracellular traffic.

In a second part, we theoretically demonstrate a novel mechanism for membrane deformation by curved filaments. This mechanism is based on a buckling-like instability that naturally arises as soon as such filaments adhere to the membrane and to each other. A simple model yields a phase diagram with three regions: one where flat filament-dressed membranes are stable, one where they are unstable and immediately form long membrane tubes, and a metastable region. Metastable flat dressed membranes could be an interesting means of quickly generating long membrane tubes following a gentle push provided by some active cell machinery.

We propose that this buckling mechanism could account for membrane budding events mediated by the protein complex ESCRT-III, which induces long dressed membrane tubes under certain experimental conditions. This complex is known to deform the membrane at the very end of cell division, during virus release by the cell and in the early stages of the recycling of phospholipids and integral membrane proteins. We propose an experimental

test to validate our hypothesis. Other biological instances of this type of behavior might also exist, and it could be interesting to identify them.

In a third part, we propose a general mechanism for the shaping of actin-based cellular protrusions. We focus more specifically on stereocilia, a key element of the auditory system whose proper shape and size regulation is crucial to hearing. Our model puts forward the regulation of actin depolymerization by the well-characterized cross-linker espin as a robust way to control the structure of stereocilia. We find a good agreement with experimental shapes using only one adjustable parameter. We also account for the experimentally observed relationships between protrusion length and actin treadmilling velocity in stereocilia on the one hand, and between protrusion length and espin expression level in the related microvilli on the other.

This biological problem leads us to formulate a physically interesting interface growth model which, to the best of our knowledge, was never studied before. We are able to solve it exactly in the simple case where espins only detach from the actin filaments. We also solve the single-filament problem in the general case, which might prove useful to study several other biopolymer problems. Turning to the full, multi-filament growth process in the presence of espin reattachment, we find that it is quite different from the smooth, translation-invariant interfaces previously studied in the light of their self-affine properties. Our interface undergoes a "growth transition" during which it loses its stationary profile. Numerical results indicate that correlations between filaments yield strong modifications of the single-filament theory close to this transition, which requires further theoretical investigations.

Although studying the depolymerization dynamics of the stereocilium and its length control mechanism theoretically yields interesting insights, biological investigations are likely to be the most productive approach to some other crucial features. This is probably the case of the dynamics of the actin polymerization front, where many regulatory proteins play a role. These might impose the radius of the filament's tip, which is undetermined in our approach.

On a broader level, the dynamics of the cell's cytoskeleton implicates many out-of-equilibrium surface growth processes. Besides tube-like protrusions, one could quote the dynamics of the cell cortex, a layer of actin underlying the plasma membrane. Cortical actin undergoes polymerization and depolymerization as well as transient cross-linking, similarly to the system studied in chapter 6. On top of that, its dynamics involves actin filament branching and barbed end capping, as well as binding molecular motors that make it contractile. Another similarly complicated system is the lamellipodium, a thin sheet of actin that some cell types (*e.g.* keratocytes) extend in front of them while moving, for instance towards a chemical attractant. The precise interplay between all the sources of activity in these processes is not well understood. The study of chapter 6 could be a first step towards the formulation of criteria that would allow one to identify the dominant mechanisms underlying each of these growing interfaces by analyzing their shape and dynamics. Indeed, our study of stereocilia suggests that each possible growth model is characterized by a few features (*e.g.* a length divergence exponent, or a self-similar interface) that do not depend on the microscopic parameters of the system studied (*e.g.* the cross-linker reattachment rate). By identifying those features and recognizing them in actual cellular systems, we should be able to use them as signatures of the underlying

interface-shaping phenomena, and therefore show which mechanism dominates which type of interface.

Throughout this thesis, biological systems are approached with a twofold focus. First, we attempt to ground our theoretical considerations in experimental observations, and propose experiments whenever possible. Second, we make an effort towards generality and formulate the simplest possible models compatible with the symmetries and the essential features of the systems studied. By doing this, we keep the number of adjustable parameters in our models to a minimum and formulate conclusions that are valid for a range of systems rather than in just one particular case. We believe that this is a fruitful approach when studying biology, as the detailed parameters of the problems it involves are rarely well known *in vitro*, let alone *in vivo*. Because of this, we are hopeful that the work contained in this thesis could be relevant for many cellular mechanisms.

Appendices

Appendix A

Stability of a membrane tubule

Here we consider the stability of an initially cylindrical membrane tubule of volume V, area A, and fixed length L much larger than its radius. We write its free energy as

$$F = -PV + \sigma A + \int \frac{\kappa c^2}{2} \mathrm{d}A, \tag{A.1}$$

where P is the pressure difference between the inside and the outside of the tubule, σ is the tension of the membrane, $\kappa > 0$ its bending modulus and c the local total curvature. The integral runs over the surface of the membrane. If $P = 0$, the tubule has a cylindrical shape imposed by the balance between the tension, which tends to shrink the tubule, and the bending modulus, which tends to increase its radius. This situation is discussed in Sec. 3.1. Let us now consider an increase in P, which also tends to make the tubule swell up. As P increases, the radius of the tubule also increases, its bending energy tends to zero and the swelling effect due to the bending modulus becomes negligible compared that due to the pressure. When this is the case, the tubule becomes similar to a soap bubble of fixed length, as its local shape is imposed by the balance between pressure and surface tension only—the competition between the two defines the Laplace radius $r_l = 2\sigma/P$, which is the radius of a spherical soap bubble. Soap bubbles rarely have a cylindrical shape. Therefore, we expect that there should be a transition between a cylindrical regime where the bending modulus dominates and a more complicated one where pressure does. In this appendix, we show that cylindrical tubules are linearly unstable unless the following condition is satisfied:

$$\begin{aligned} &\sigma \geqslant 0 \qquad \text{and} \qquad \frac{P\sqrt{\kappa}}{\sqrt{\sigma^3}} \leqslant \left(\frac{2}{3}\right)^{3/2} \\ &\text{or} \\ &\sigma < 0 \qquad \text{and} \qquad \frac{P\sqrt{\kappa}}{\sqrt{-\sigma^3}} \leqslant -2\left(\frac{2}{3}\right)^{3/2}. \end{aligned} \tag{A.2}$$

While the $\sigma \geqslant 0$ condition corresponds to the qualitative picture discussed above, if $\sigma < 0$ the tubule is not stable for $P = 0$. Indeed, in this case both its tension and bending modulus have a swelling effect and nothing stabilizes the radius of the tubule. What the above $\sigma < 0$ condition tells us is that these swelling effects can be stabilized by a negative

internal pressure of the tubule. Note that the ratio $P\sqrt{\kappa/\sigma^3}$ appearing in Eq. (A.2) is proportional to the ratio r_b/r_l between the bare tubule radius defined in Eq. (3.3) and the Laplace radius.

This appendix focuses on the local stability a cylindrical tubule in the ensemble where P, σ and L are fixed. Since we are dealing with a thermodynamic system, our results remain valid when P and σ are determined self-consistently to satisfy volume and area conservation, and when the force conjugate to L is imposed, as in Sec. 3.4.3. In Sec. A.1, we calculate the radius of the cylinder. In Sec. A.2, we derive a formalism allowing for the study of perturbations away from the cylindrical shape. In Sec. A.3, we consider the stability of the cylinder under an arbitrary infinitesimal perturbation. Finally, in Sec. A.4 , we regroup these results and derive Eq. (A.2).

A.1 Cylindrical configuration

Here we assume that the tubule has a cylindrical shape. Neglecting the ends of the cylinder and denoting its radius by r, we write $V = \pi L r^2$ and $A = 2\pi L r$. This yields the free energy

$$F = -P\pi L r^2 + \sigma 2\pi L r + \frac{\kappa\pi L}{r}. \tag{A.3}$$

We differentiate F with respect to r to obtain the radial force balance equation, then multiply by r^2, which yields:

$$f(r) = -1 \quad \text{with} \quad f(r) = \frac{2P}{\kappa} r^3 - \frac{2\sigma}{\kappa} r^2. \tag{A.4}$$

Here we show that depending on the values of P and σ, Eq. (A.4) has at most one stable solution, which we denote by r^*. Four cases must be distinguished:

- If $P > 0$ and $\sigma \geqslant 0$, $f(r)$ decreases from $f(0) = 0$ to $f(2\sigma/3P) = -8\sigma^3/(27\kappa P^2)$, then increases to $f(+\infty) = +\infty$. If $f(2\sigma/3P)$ is larger than -1, Eq. (A.4) has no solution. If $f(2\sigma/3P)$ is smaller than -1, it has two solutions. The one with the smallest radius is stable under a small change of r, and the one with the largest radius is unstable. Therefore in the cases where r^* exists, $r^* \leqslant 2\sigma/3P$.

- If $P > 0$ and $\sigma < 0$, $f(r)$ is always positive for $r > 0$, thus Eq. (A.4) has no solution.

- If $P < 0$ and $\sigma \geqslant 0$, $f(r)$ decreases from $f(0) = 0$ to $f(+\infty) = -\infty$. Thus Eq. (A.4) has one solution, which is stable under a change of r.

- If $P < 0$ and $\sigma < 0$, $f(r)$ increases from $f(0) = 0$ to $f(2\sigma/3P) = 8\sigma^3/(27\kappa P^2)$, then decreases to $f(+\infty) = -\infty$. This yields one solution, which stable under a change of r. In this case, $r^* > 2\sigma/3P$.

The case $P = 0$ is not included here, as it is treated in Sec. 3.1. Eq. (A.4) therefore has a solution in the two following cases

$$\begin{array}{lll} \sigma \geqslant 0 & \text{and} & \dfrac{P\sqrt{\kappa}}{\sqrt{\sigma^3}} \leqslant \left(\dfrac{2}{3}\right)^{3/2} \\ \text{or} & & \\ \sigma < 0 & \text{and} & P < 0. \end{array} \tag{A.5}$$

In the following, we ask whether these cylindrical solutions are stable not only under a uniform change of r, but under any perturbation. In the remainder of this appendix, we consider only the cases where a stable solution of Eq. (A.4) exists. We express all lengths in units of r^* and all energies in units of κ. In these units, Eq. (A.4) reads:

$$\sigma = P + \frac{1}{2}. \tag{A.6}$$

A.2 Energetic cost of perturbations

Here we consider a cylinder satisfying Eq. (A.4). The z-axis is defined as the axis of symmetry of the cylinder, and x, y are two directions such that (x, y, z) is an orthogonal coordinate system. If ϕ is the angle in the (x, y) plane and the tubule is weakly deformed from its cylindrical shape, we can write its radius as

$$r(\phi, z) = 1 + \delta(\phi, z), \tag{A.7}$$

with $\delta \ll 1$. In the following, we calculate the free energy of the tubule using some notions of differential geometry introduced *e.g.* in Ref. [155]. The position vector on the tubule is $\mathbf{r} = [1 + \delta(\phi, z)]\,\mathbf{e}_r + z\mathbf{e}_z$, where $\mathbf{e}_X$ is the unit vector in the direction X. The tangent and normal vectors read

$$\mathbf{t}_\phi = \partial_\phi \mathbf{r} = \partial_\phi \delta\, \mathbf{e}_r + (1+\delta)\mathbf{e}_\phi \tag{A.8a}$$

$$\mathbf{t}_z = \partial_z \mathbf{r} = \partial_z \delta\, \mathbf{e}_r + \mathbf{e}_z \tag{A.8b}$$

$$\begin{aligned} \mathbf{n} &= \frac{\mathbf{t}_z \times \mathbf{t}_\phi}{\sqrt{(\mathbf{t}_z \times \mathbf{t}_\phi)^2}} \\ &= -\left[1 - \frac{(\partial_\phi \delta)^2 + (\partial_z \delta)^2}{2}\right] \mathbf{e}_r + \partial_\phi \delta (1-\delta)\mathbf{e}_\phi + \partial_z \delta\, \mathbf{e}_z + \mathcal{O}\left(\delta^3\right). \end{aligned} \tag{A.8c}$$

In order to write F as a function of δ, we express the volume and surface elements

$$\mathrm{d}V = (1+\delta)\,\mathrm{d}\phi\,\mathrm{d}z \tag{A.9a}$$

$$\begin{aligned} \mathrm{d}A &= \sqrt{(\mathbf{t}_z \times \mathbf{t}_\phi)^2}\,\mathrm{d}\phi\,\mathrm{d}z \\ &= \left[1 + \delta + \frac{(\partial_\phi \delta)^2 + (\partial_z \delta)^2}{2} + \mathcal{O}\left(\delta^3\right)\right] \mathrm{d}\phi\,\mathrm{d}z. \end{aligned} \tag{A.9b}$$

The metric on the surface of the tubule reads

$$
\begin{aligned}
g^{\phi\phi} &= 1 - 2\delta + 3\delta^2 - (\partial_\phi \delta)^2 + \mathcal{O}\left(\delta^3\right) && \text{(A.10a)}\\
g^{\phi z} &= -\partial_\phi \delta \times \partial_z \delta + \mathcal{O}\left(\delta^3\right) && \text{(A.10b)}\\
g^{z\phi} &= g^{\phi z} && \text{(A.10c)}\\
g^{zz} &= 1 - (\partial_z \delta)^2 + \mathcal{O}\left(\delta^3\right). && \text{(A.10d)}
\end{aligned}
$$

The extrinsic curvature tensor $\mathcal{K}_{ij} = -\mathbf{n} \cdot (\partial_i \mathbf{t}_j)$ is given by

$$
\begin{aligned}
\mathcal{K}_{\phi\phi} &= -1 - \delta + \partial_\phi^2 \delta - \frac{3}{2}(\partial_\phi \delta)^2 + \frac{1}{2}(\partial_z \delta)^2 + \mathcal{O}\left(\delta^3\right) && \text{(A.11a)}\\
\mathcal{K}_{\phi z} &= \partial_\phi \partial_z \delta - \partial_\phi \delta \times \partial_z \delta + \mathcal{O}\left(\delta^3\right) && \text{(A.11b)}\\
\mathcal{K}_{z\phi} &= \mathcal{K}_{\phi z} && \text{(A.11c)}\\
\mathcal{K}_{zz} &= \partial_z^2 \delta + \mathcal{O}\left(\delta^3\right). && \text{(A.11d)}
\end{aligned}
$$

The total curvature c is obtained by contracting this tensor by the metric (*i.e.* c is the trace of this tensor). Using summation over repeated indices:

$$
\begin{aligned}
c &= g^{ij}\mathcal{K}_{ij}\\
&= -1 + \delta + \partial_\phi^2 \delta + \partial_z^2 \delta - 2\delta \times \partial_\phi^2 \delta - \delta^2 - \frac{1}{2}(\partial_\phi \delta)^2 + \frac{1}{2}(\partial_z \delta)^2 + \mathcal{O}\left(\delta^3\right). \qquad \text{(A.12)}
\end{aligned}
$$

Finally, inserting Eqs. (A.9) and (A.12) into Eq. (A.1) and using Eq. (A.6) to eliminate σ, the free energy of the tubule to second order in δ reads

$$
\begin{aligned}
F = \frac{1}{2}\int_{-L/2}^{L/2} \mathrm{d}z \int_{-\pi}^{\pi} \mathrm{d}\phi \Big[&- 2\left(\partial_\phi^2 \delta + \partial_z^2 \delta\right) + (1-P)\delta^2\\
&+ (P-2)(\partial_\phi \delta)^2 + P(\partial_z \delta)^2 + \left(\partial_\phi^2 \delta + \partial_z^2 \delta\right)^2 \Big]. \qquad \text{(A.13)}
\end{aligned}
$$

A.3 Linear stability

In this section, we consider a tubule with periodic boundary conditions in $z = \pm L/2$. We decompose the perturbation of the radius introduced in Eq. (A.7) into Fourier modes:

$$
\delta(\phi, z) = \sum_{m,n=-\infty}^{+\infty} \hat{\delta}_{m,n} e^{\imath(m\phi + nqz)}, \qquad \text{(A.14)}
$$

where $q = 2\pi/L$ goes to 0 as L goes to infinity, which is the case considered here (the tubule is much longer than its radius). In this limit, qn can take a value arbitrarily close to any real number and can therefore be treated as a continuous variable. The free energy Eq. (A.13) can be rewritten as

$$
F = \sum_{m,n=-\infty}^{+\infty} \frac{K_{mn}}{2} \left|\hat{\delta}_{m,n}\right|^2, \qquad \text{(A.15)}
$$

where we note that the terms linear in δ in Eq. (A.13) have a zero integral over the surface of the tubule. The cylinder is stable under any small perturbation if and only if the elastic constants K_{mn} associated with the Fourier modes (m, n) are all positive. They read

$$K_{mn} = \frac{(2\pi)^2}{q}\left\{(1-P) + (P-2)m^2 + P(qn)^2 + [m^2 + (qn)^2]^2\right\}, \tag{A.16}$$

The modes $m = \pm 1$, $n = 0$ corresponds to a translation of the tubule and therefore have a zero energy associated to them. This expression is identical to the expression given in Ref. [156] for $P = 0$. As expected from this reference, the modes with $m = \pm 1$ and fixed n become infinitely soft in the $L \to +\infty$ limit. In the following, we study the sign of K_{mn}, distinguishing three cases depending on the value of P.

A.3.1 Case $P < -2$

If $P < -2$, the cylinder is unstable. We show this by considering the $m = \pm 1$ modes. Their elastic constants factorize into

$$K_{\pm 1n} = \frac{(2\pi)^2}{q}(qn)^2\left[(qn)^2 - (-P-2)\right]. \tag{A.17}$$

Therefore all $m = \pm 1$ modes such that $0 < qn < \sqrt{-P-2}$ are unstable. There always are such modes, since $P < -2 \Rightarrow \sqrt{-P-2} \in \mathbb{R}$ and since qn can be arbitrarily small in the $L \to +\infty$ limit.

A.3.2 Case $-2 \leqslant P \leqslant 1$

The cylinder is linearly stable in this case. We prove this by first showing that the $m = 0$ modes are not unstable, and then proving the same thing for $|m| \geqslant 1$.

- For $m = 0$, the elastic constant reads

$$K_{0n} = \frac{(2\pi)^2}{q}\left[(qn)^4 + P(qn)^2 + 1 - P\right]. \tag{A.18}$$

  Considering this expression as a quadratic polynomial in $(qn)^2$, we find that its discriminant is $\Delta = (P+2)^2 - 8$. For $P < 2\left(\sqrt{2}-1\right)$, Δ is negative and K_{0n} is always positive. For $2\left(\sqrt{2}-1\right) \leqslant P \leqslant 1$, K_{0n} is negative in the range

$$\frac{-P-\sqrt{\Delta}}{2} < (qn)^2 < \frac{-P+\sqrt{\Delta}}{2}. \tag{A.19}$$

  However, $P \leqslant 1$ implies $-P + \sqrt{\Delta} \leqslant 0$, therefore K_{0n} is never negative since $(qn)^2$ is always positive. Therefore the $m = 0$ modes are stable in the range of pressures considered here.

- For $|m| \geqslant 1$, we see that K_{mn} is an increasing function of $(qn)^2$ by rewriting Eq. (A.16) in the following form:

$$K_{mn} = \frac{(2\pi)^2}{q}\left[(qn)^4 + (2m^2+P)(qn)^2 + (m^2-1)(m^2-1-P)\right]. \tag{A.20}$$

  Therefore proving that K_{m0} is positive for $|m| \geqslant 1$ is sufficient to prove that all $|m| \geqslant 1$ modes are stable. This is obviously the case since $|m| \geqslant 1$ implies both $m^2 - 1 \geqslant 0$ and $m^2 - 1 - P \geqslant 0$ in the range of pressures considered here.

A.3.3 Case $1 < P$

If $P > 1$, then $K_{00} = 1 - P < 0$ and the $m = 0$, $n = 0$ mode is unstable. Therefore the cylinder is unstable.

A.4 Non-scaled units

Going back to normal units, we put reformulate the stability criteria of Sec. A.3 as

$$\begin{aligned} \frac{P(r^*)^3}{\kappa} &\geqslant -2 \\ \text{and} & \\ \frac{P(r^*)^3}{\kappa} &\leqslant 1, \end{aligned} \tag{A.21}$$

where it is assumed that r^* is well-defined and positive, *i.e.* that the criterion Eq. (A.5) is fulfilled.

Let us first consider the first inequality of Eq. (A.21). If $P \geqslant 0$, it is automatically satisfied. If $P < 0$, then it is equivalent to

$$\begin{aligned} & (r^*)^3 \leqslant \frac{2\kappa}{|P|} \\ \Leftrightarrow\quad & f(r^*) \geqslant f\left[\left(\frac{2\kappa}{|P|}\right)^{1/3}\right] \\ \Leftrightarrow\quad & -1 \geqslant -4 - \frac{2^{5/3}\sigma}{\kappa^{1/3}|P|^{2/3}} \\ \Leftrightarrow\quad & \begin{cases} & \sigma \geqslant 0 \\ \text{or} & \\ & \sigma < 0 \quad \text{and} \quad P\sqrt{-\kappa/\sigma^3} \leqslant -2^{5/2}3^{-3/2} \end{cases}. \end{aligned} \tag{A.22}$$

Thus the first inequality of Eq. (A.21) can be reformulated as

$$\begin{aligned} & \sigma \geqslant 0 \\ \text{or} & \\ & \sigma < 0 \quad \text{and} \quad \frac{P\sqrt{\kappa}}{\sqrt{-\sigma^3}} \notin \left]-2\left(\frac{2}{3}\right)^{3/2}, 0\right[. \end{aligned} \tag{A.23}$$

The second inequality of Eq. (A.21) is automatically satisfied if $P < 0$. If $P \geqslant 0$ then $\sigma \geqslant 0$ (otherwise r^* would not exist) and the inequality is equivalent to

$$\begin{aligned}
&(r^*)^3 \leqslant \frac{\kappa}{P} \\
&\quad\Leftrightarrow\quad \left(\frac{\kappa}{P}\right)^{1/3} \leqslant \frac{2\sigma}{3P} \quad \text{and} \quad f(r^*) \geqslant f\left[\left(\frac{\kappa}{P}\right)^{1/3}\right] \\
&\quad\Leftrightarrow\quad \frac{P\sqrt{\kappa}}{\sqrt{\sigma^3}} \leqslant \left(\frac{2}{3}\right)^{3/2} \quad \text{and} \quad -1 \leqslant 2 - \frac{2\sigma}{\kappa^{1/3}P^{2/3}}.
\end{aligned} \tag{A.24}$$

Thus the second inequality of Eq. (A.21) can be reformulated as

$$\frac{P\sqrt{\kappa}}{\sqrt{\sigma^3}} \leqslant \left(\frac{2}{3}\right)^{3/2}. \tag{A.25}$$

Finally, we put together all the conditions derived in this appendix and require that Eqs. (A.5), (A.23) and (A.25) are all satisfied simultaneously. This yields the criterion Eq. (A.2). Therefore if we conduct an experiment with an initially cylindrical membrane tubule, make sure that it always satisfies Eq. (A.2) and assume that it is only subjected to small fluctuations of its shape, then this tubule always remains cylindrical. Note that the criterion Eq. (A.2) does not make a difference between a linearly stable and a marginally stable tubule. This subtlety only concerns singular values of the parameters and therefore is not relevant for the usage of the present appendix made in Sec. 3.4.3.

Appendix B

Dynamin mechanics

B.1 Membrane geometry and bending energy

The calculations of this section are inspired by those of Ref. [79]. Here we calculate the bending energy of an infinitely thin membrane with no spontaneous curvature surrounded by a helical scaffold of radius r and pitch $2\pi p$. We assume that this scaffold imposes two constraints on the membrane: first, the membrane has the same helical symmetry as the scaffold; and second, the membrane is attached to the scaffold and must therefore touch it at every point. Under these constraints, the membrane radius as a function of the angle $\theta \in [-\infty, \infty]$ of cylindrical coordinates and the elevation $\zeta \in [0, 2\pi p]$ from the scaffold reads (see Fig. B.1):

$$r_m(\theta, \zeta) = r[1 + \epsilon(\zeta)], \tag{B.1}$$

where $\epsilon(0) = \epsilon(2\pi p) = 0$. It can be shown that in the $\epsilon \ll 1$ regime, approximating ϵ by its first Fourier component changes all results presented in chapter 4 by less than 1%. We therefore use this approximation throughout:

$$r_m(\theta, \zeta) = r\{1 + u[\cos(\zeta/p) - 1]\}. \tag{B.2}$$

The bending free energy of the membrane is given by Eq. (1.1) and reads

$$F_m = \iint \left(\frac{\kappa}{2} c^2\right) \mathrm{d}\mathfrak{S}, \tag{B.3}$$

where c is the total curvature of the membrane and κ its bending modulus. The integration runs over the surface of the membrane. For the configurations considered in chapter 4, the dependence of κ on the area per polar head of lipids can be neglected [157]. We now calculate F_m as a function of r, p and ϵ using differential geometry [155]. To second order in ϵ, the surface element of the membrane reads

$$\mathrm{d}\mathfrak{S} = \left[1 + \epsilon + \frac{1}{2}\left(1 + \frac{p^2}{r^2}\right) r^2 (\partial_\zeta \epsilon)^2\right] r \, \mathrm{d}\theta \, \mathrm{d}\zeta. \tag{B.4}$$

Integrating this surface element and using Eq. (B.2), we calculate $\mathfrak{s}$, the membrane area per unit of z-length of the tube to first order in u:

$$\mathfrak{s} = 2\pi r \, (1 - u) \, . \tag{B.5}$$

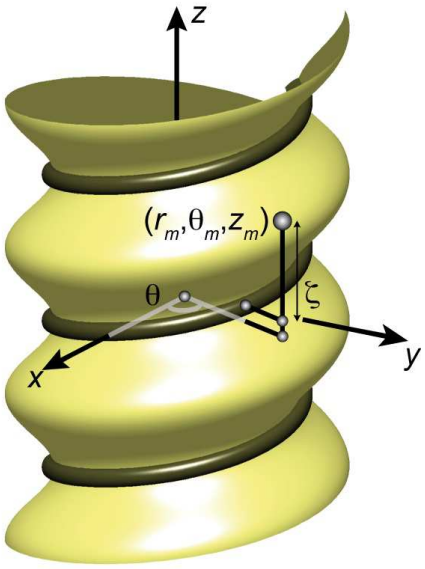

Figure B.1: Parametrization of a surface confined by a helical scaffold. Any point whose cylindrical coordinates (r_m, θ_m, z_m) can be written as $r_m = r\,[1 + \epsilon(\zeta)]$, $\theta_m = \theta$, $z_m = p\theta + \zeta$ with $\theta \in [-\infty, \infty]$, $\zeta \in [0, 2\pi p]$ belongs to the membrane.

Similarly, to first order in u the volume enclosed by the membrane by unit of z-length is

$$\mathfrak{v} = \pi r^2 \,(1 - 2u)\,. \tag{B.6}$$

To second order in ϵ, The total curvature of the membrane reads

$$c = -\frac{1}{r}(1-\epsilon) + \left(1 + \frac{p^2}{r^2}\right) r(\partial_\zeta^2 \epsilon) - \frac{\epsilon^2}{r} - 2\frac{p^2}{r}\epsilon(\partial_\zeta^2\epsilon) + \frac{1}{2}\left(1 - \frac{p^2}{r^2}\right) r(\partial_\zeta \epsilon)^2. \tag{B.7}$$

Performing the integration of Eq. (B.3) using Eqs. (B.2), (B.4) and (B.7), we find the membrane's bending energy per unit of z-length

$$\begin{aligned} f_m &= \frac{\pi\kappa}{r}\left[1 + u + \left(\frac{3}{2} + \frac{3\alpha^{-2}}{2} + \alpha^{-4}\right)\frac{u^2}{2}\right] \\ &= \frac{1}{r}\left[\pi\kappa(1+u) + k_{uu}\frac{u^2}{2}\right]. \end{aligned} \tag{B.8}$$

This last equality defines k_{uu}.

B.2 Elastic properties of the helix

We describe the elasticity of the dynamin helix as that of a simple rod with constant spontaneous curvature and torsion [78]. Its elastic energy therefore reads

$$F_h = \int \left\{ \frac{k_{\mathfrak{c}}}{2}[\mathfrak{c}(\ell)-\mathfrak{c}_0]^2 + \frac{k_{\mathfrak{t}}}{2}[\mathfrak{t}(\ell)-\mathfrak{t}_0]^2 \right\} \mathrm{d}\ell \tag{B.9}$$

$$= \int \left\{ \frac{\sqrt{r^2+p^2}}{p} \left[\frac{k_{\mathfrak{c}}}{2} \left(\frac{r}{r^2+p^2} - \frac{r_0}{r_0^2+(\alpha r_0)^2} \right)^2 + \frac{k_{\mathfrak{t}}}{2} \left(\frac{p}{r^2+p^2} - \frac{\alpha r_0}{r_0^2+(\alpha r_0)^2} \right)^2 \right] \right\} \mathrm{d}z, \tag{B.10}$$

where the first integral is calculated over the arc length of the rod and the second one over the z-coordinate (see Fig. 4.2(a)). In the second expression we replace the curvature $\mathfrak{c}(\ell)$ and torsion $\mathfrak{t}(\ell)$ by their values for a spring of radius r and pitch $2\pi p$. We also choose the spontaneous curvature $\mathfrak{c}_0$ and torsion $\mathfrak{t}_0$ such that the ground state of the rod is a helical spring of radius r_0 and pitch $2\pi\alpha r_0$.

The dynamin helix binds to the membrane through a specific domain, the PH domain. Let $\mathbf{u}(\ell)$ be the unitary vector field defined on the helix that always points in the direction of the PH domain. Since the PH domain always faces the membrane, $\mathbf{u}(\ell)$ always faces the inside of the helix. Hence $\mathbf{u}(\ell) = \mathbf{N}(\ell)$, the normal to the helix. Consequently, according to Ref. [158], the twist density of the helix is exactly equal to its torsion, which allows us to write F_h as a function of $\mathfrak{c}(\ell)$ and $\mathfrak{t}(\ell)$ only.

B.2.1 Curvature and torsion coefficients of a rod.

In order to calculate the curvature and torsion moduli of the rod, we consider it as a rod of cross-section $\pi\left(\frac{r_e-r_0}{2}\right)^2$, where r_e is the outer radius of the dynamin coat. We first define the typical force needed to deform the helix

$$\mathcal{K} = \frac{\pi E \left(\frac{r_e-r_0}{2}\right)^4}{r_0^2}, \tag{B.11}$$

where E is the Young modulus of the rod. Assuming that the Poisson ratio of the rod is $1/2$, its curvature and torsion elastic moduli read [105]

$$k_{\mathfrak{c}} = \frac{\pi E \left(\frac{r_e-r_0}{2}\right)^4}{4} = \frac{1}{4} \tag{B.12a}$$

$$k_{\mathfrak{t}} = \frac{\pi E \left(\frac{r_e-r_0}{2}\right)^4}{6} = \frac{1}{6}, \tag{B.12b}$$

where the equalities on the right are valid if all quantities are expressed in units of r_0, ρ_0, $\mathcal{K}$. We use these scaled units in the rest of this section.

B.2.2 Elastic energy of a rectilinear spring

Writing $r = 1 + \delta r$ and $p = \alpha(1 + \delta p)$, the integrand of Eq. (B.10) (*i.e.* the elastic energy per unit z-length) reads to second order in δr, δp

$$\begin{aligned} f_h &= \frac{\alpha}{(1+\alpha^2)^{7/2}} \times \left\{ \left[\alpha^{-2}(1-\alpha^2)^2 k_{\mathfrak{c}} + 4k_{\mathfrak{t}}\right] \frac{\delta r^2}{2} \right. \\ &\quad \left. +2\left(1-\alpha^2\right)(k_{\mathfrak{c}} - k_{\mathfrak{t}})\delta r \delta p + \left[4\alpha^2 k_{\mathfrak{c}} + (1-\alpha^2)^2 k_{\mathfrak{t}}\right] \frac{\delta p^2}{2} \right\} \\ &= k_{rr}\frac{\delta r^2}{2} + k_{rp}\delta r\, \delta p + k_{pp}\frac{\delta p^2}{2}. \end{aligned} \tag{B.13}$$

This equality defines k_{rr}, k_{rp} and k_{pp}.

B.3 Helix persistence length

B.3.1 Definition of the persistence length

We now consider the possibility for the central axis of the helix to bend with a radius of curvature $\mathcal{R} \gg r, p$ (Fig. B.2). For simplicity, we assume in this section that r, the radius of both the deformed membrane and the helix, is uniform. Therefore the membrane has a toroidal shape (*i.e.* deformations of the type of those studied in Sec. B.1 are not considered). Since the tube is bent, the pitch on the inside of the tube and on the outside are different and we let p denote the *average* pitch of the helix. The persistence length of the tube can be defined by expanding its elastic energy in powers of $\mathcal{R}^{-1}$:

$$F(\mathcal{R}) - F(\mathcal{R} = +\infty) = k_B T \int_0^L \frac{\ell_p}{2\mathcal{R}^2}\, \mathrm{d}(\mathcal{R}\phi), \tag{B.14}$$

where $\mathcal{R}\phi$ is equal to the coordinate z defined in Fig. 4.2 in the limit $\mathcal{R} \to +\infty$. There are two contributions to F: the free energies F_m and F_h of the membrane and helix. Since we are considering a more complicated geometry than in the two previous sections, we need to use the general expressions Eqs. (B.3) and (B.9) for these two quantities. All our calculations are be made to the lowest non-trivial order in $\iota = r/\mathcal{R}$.

B.3.2 Membrane energy

At any point of the torus, the two radii of curvature of the membrane are equal to r and $\cos\theta/\mathcal{R} + \mathcal{O}(\iota)$. Here θ is the angle in the $\mathcal{R}$, $\mathcal{Z}$ plane, which is the same as the definition given in Fig. 4.2 in the limit $\mathcal{R} \to +\infty$. Integrating over θ, one uses Eq. (B.3) to find the free energy of the membrane per unit of tube length:

$$\frac{F_m}{2\pi\mathcal{R}} = \frac{\pi\kappa}{r}\left(1 + \frac{\iota^2}{2}\right). \tag{B.15}$$

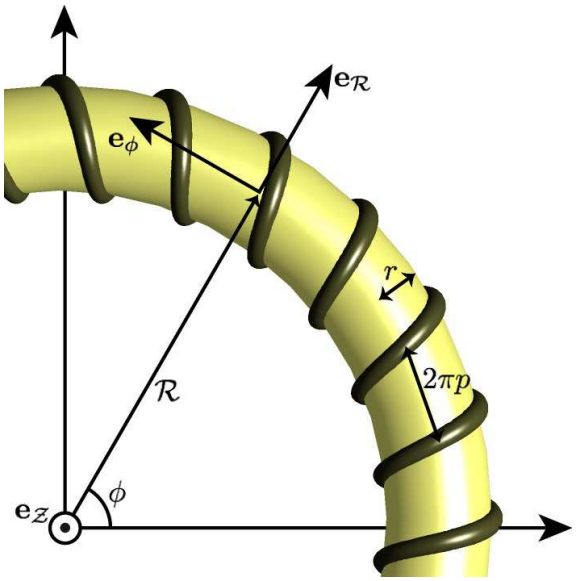

Figure B.2: Parametrization of the helix and membrane in a torus configuration. The unit vectors in the $\mathcal{R}$, ϕ and $\mathcal{Z}$ directions are denoted $\mathbf{e}_\mathcal{R}$, $\mathbf{e}_\phi$ and $\mathbf{e}_\mathcal{Z}$ respectively.

B.3.3 Helix energy

Although we use the simplifying assumption that the helix is always on the surface of a perfect torus (*i.e.* has a constant radius), it is always possible for the pitch of the helix to vary as a function of θ in order to minimize the elastic energy. Here we calculate this effect to lowest order in ι. We treat θ and ϕ as functions of the arc length ℓ along the helix and define the scaled variable:

$$\bar{\ell} = \frac{\ell}{r\sqrt{1+(p/r)^2}}. \tag{B.16}$$

Let us begin by expressing the coordinates θ and ϕ as functions of $\bar{\ell}$. The definition Eq. (B.16) is such that when $\mathcal{R} = +\infty$, we have $\theta = \bar{\ell}$. To first order, we describe the modulation of the helix' pitch by a function $h\left(\bar{\ell}\right)$ defined by

$$\theta = \bar{\ell} + \iota h\left(\bar{\ell}\right). \tag{B.17}$$

Since the lowest energy state of the helix on the torus is obviously periodic, h must be a 2π-periodic function of θ, and thus of $\bar{\ell}$ to lowest order in ι. We can thus expand h as a Fourier series:

$$h\left(\bar{\ell}\right) = \sum_{n=1}^{+\infty} a_n \sin n\bar{\ell}, \tag{B.18}$$

where we left all even terms out because they do not respect the $(\theta, \phi) \to (-\theta, -\phi)$ symmetry of the problem (Figs. 4.2 and B.2). Let us now write

$$\phi = \iota A. \tag{B.19}$$

This defines the variable A which is of the same order as θ and $\bar{\ell}$. The position vector of the point of the helix with coordinate θ reads

$$\mathbf{r} = (\mathcal{R} + r\cos\theta)\mathbf{e}_{\mathcal{R}} + r\sin\theta\,\mathbf{e}_{\mathcal{Z}}, \tag{B.20}$$

where $\mathbf{e}_{\mathcal{R}}$ and $\mathbf{e}_{\mathcal{Z}}$ are defined in Fig. B.2. Differentiating this relation, we find

$$\mathrm{d}\ell^2 = (\mathcal{R} + r\cos\theta)^2\mathrm{d}\phi^2 + r^2\mathrm{d}\theta^2. \tag{B.21}$$

Combining this with Eqs. (B.16), (B.17) and (B.19) yields

$$A = \frac{p}{r}\left\{\bar{\ell} - \iota\left[\frac{h}{(p/r)^2} + \sin\bar{\ell}\right]\right\} + \mathcal{O}(\iota^2). \tag{B.22}$$

We now combine Eqs. (B.17), (B.20) and (B.22) to express $\mathbf{f} = \mathbf{r}/\mathcal{R}$ as a function of $\bar{\ell}$ and calculate the curvature $\mathfrak{c}\left(\bar{\ell}\right)$ and torsion $\mathfrak{t}\left(\bar{\ell}\right)$ of the helix, which are defined by

$$\mathbf{t} = \frac{\partial\mathbf{r}}{\partial\ell} = \frac{\partial_{\bar{\ell}}\mathbf{f}}{\sqrt{1+(p/r)^2}}\iota^{-1} \tag{B.23}$$

$$\mathfrak{c}\left(\bar{\ell}\right)\mathbf{n} = \frac{\partial\mathbf{t}}{\partial\ell} = \frac{\partial^2_{\bar{\ell}}\mathbf{f}}{r[1+(p/r)^2]}\iota^{-1} \tag{B.24}$$

$$\mathfrak{c}\left(\bar{\ell}\right)\mathbf{b} = \mathbf{t}\times\mathfrak{c}\left(\bar{\ell}\right)\mathbf{n} = \frac{\partial_{\bar{\ell}}\mathbf{f}\times\partial^2_{\bar{\ell}}\mathbf{f}}{r[1+(p/r)^2]^{3/2}}\iota^{-2} \tag{B.25}$$

$$\mathfrak{t}\left(\bar{\ell}\right)\mathbf{n} = -\frac{\partial\mathbf{b}}{\partial\ell} = \frac{\mathbf{b}\cdot\partial_{\bar{\ell}}\left[\mathfrak{c}\left(\bar{\ell}\right)\mathbf{n}\right]}{r\sqrt{1+(p/r)^2}}. \tag{B.26}$$

Here the vectors $\mathbf{t}$, $\mathbf{n}$ et $\mathbf{b}$ are called the tangent, normal and binormal to the helix [158]. This yields:

$$\mathfrak{c}\left(\bar{\ell}\right) = \frac{1+\iota\left[(p/r)^2\cos\bar{\ell} + 2h'\right]}{r[1+(p/r)^2]} + \mathcal{O}\left(\frac{\iota^2}{r}\right), \tag{B.27}$$

$$\mathfrak{t}\left(\bar{\ell}\right) = -\frac{p}{r^2}\times\frac{1-\iota\left\{\left[(r/p)^2+1\right]h''' + \left[(r/p)^2-1\right]h' + \left[(p/r)^2+2\right]\cos\bar{\ell}\right\}}{1+(p/r)^2} + \mathcal{O}\left(\frac{\iota^2}{r}\right), \tag{B.28}$$

where the primes denote the differentiation with respect to $\bar{\ell}$. The following notations make the ι-expansion explicit:

$$\mathfrak{c}\left(\bar{\ell}\right) = \mathfrak{c}_0 + \bar{\mathfrak{c}} + \iota\mathfrak{c}_1\left(\bar{\ell}\right) + \mathcal{O}\left(\frac{\iota^2}{r}\right), \tag{B.29}$$

$$\mathfrak{t}\left(\bar{\ell}\right) = \mathfrak{t}_0 + \bar{\mathfrak{t}} + \iota\mathfrak{t}_1\left(\bar{\ell}\right) + \mathcal{O}\left(\frac{\iota^2}{r}\right), \tag{B.30}$$

where $\mathfrak{c}_0$, $\mathfrak{t}_0$ are the quantities introduced in Sec. B.2 and $\bar{\mathfrak{c}}$, $\bar{\mathfrak{t}}$ characterize homogeneous deviations of order δr, δp from these values (therefore $\bar{\mathfrak{c}} \ll 1/r$, $\bar{\mathfrak{t}} \ll 1/r$). The free energy Eq. (B.9) of the helix thus has the following ι-expansion:

$$\begin{aligned} F_h = \int\Bigg[&\left(\frac{k_{\mathfrak{t}}}{2}\bar{\mathfrak{t}}^2 + \frac{k_{\mathfrak{c}}}{2}\bar{\mathfrak{c}}^2\right) + \iota\left(k_{\mathfrak{t}}\mathfrak{t}_1\bar{\mathfrak{t}} + k_{\mathfrak{c}}\mathfrak{c}_1\bar{\mathfrak{c}}\right) + \iota^2\left(\frac{k_{\mathfrak{t}}}{2}\mathfrak{t}_1^2 + \frac{k_{\mathfrak{c}}}{2}\mathfrak{c}_1^2\right) \\ &+\mathcal{O}\left(\frac{k_{\mathfrak{c}}\bar{\mathfrak{c}}\iota^2}{r}\right) + \mathcal{O}\left(\frac{k_{\mathfrak{c}}\bar{\mathfrak{t}}\iota^2}{r}\right) + \mathcal{O}\left(\frac{k_{\mathfrak{c},\mathfrak{t}}\iota^3}{r^2}\right)\Bigg]\mathrm{d}\ell. \end{aligned}$$

By noting that $\mathfrak{c}_1$ and $\mathfrak{t}_1$ are linear in h and that h and its derivatives average to zero over a turn of the helix, we find that F_h decomposes into the sum of two terms:

$$F_h = \int \left[\frac{k_\mathfrak{t}}{2}\bar{\mathfrak{t}}^2 + \frac{k_\mathfrak{c}}{2}\bar{\mathfrak{c}}^2\right] \mathrm{d}\ell + \iota^2 \int \left[\frac{k_\mathfrak{t}}{2}\mathfrak{t}_1^2 + \frac{k_\mathfrak{c}}{2}\mathfrak{c}_1^2 + \mathcal{O}\left(\iota^2\frac{k_\mathfrak{t}}{r^2}, \iota^2\frac{k_\mathfrak{c}}{r^2}\right) + \mathcal{O}\left(\frac{k_\mathfrak{t}\bar{\mathfrak{t}}}{r}, \frac{k_\mathfrak{c}\bar{\mathfrak{c}}}{r}\right)\right] \mathrm{d}\ell. \tag{B.31}$$

The first term of this sum is exactly the free energy calculated in Eq. (B.10). It is independent of h and represents the energy cost of changing the radius and average pitch of the helix. To lowest order in $\bar{\mathfrak{c}}$, $\bar{\mathfrak{t}}$, we can replace r, p in the second term by their equilibrium values r_0, αr_0. In order to find the free energy cost of a bend in the tube, one must find the minimum of F_h with respect to h. It is reached when

$$a_1 = \frac{\alpha^2}{2}\frac{(2+\alpha^2)k_\mathfrak{t} - k_\mathfrak{c}}{\alpha^2 k_\mathfrak{t} + k_\mathfrak{c}} \quad \text{and} \quad a_{n\geqslant 2} = 0. \tag{B.32}$$

Injecting this into F_h and using Eqs. (B.12), (B.14), (B.15) and (B.18) yields the persistence length of the tube:

$$\ell_p = \frac{2\alpha\sqrt{1+\alpha^2}}{k_B T}\frac{k_\mathfrak{t} k_\mathfrak{c}}{\alpha^2 k_\mathfrak{t} + k_\mathfrak{c}} + \frac{\pi r \kappa}{k_B T} = \frac{\mathcal{K}\alpha\sqrt{1+\alpha^2}}{k_B T(3+2\alpha^2)} + \frac{\pi r\kappa}{k_B T}. \tag{B.33}$$

B.3.4 Experimental determination of $\mathcal{K}$

In Ref. [60], the persistence length of a tube of brain polar lipids and PIP_2 coated with rat brain dynamin is measured to be $\ell_p = 37 \pm 4\,\mu\mathrm{m}$. Since $\pi r\kappa/k_B T \simeq 300\,\mathrm{nm}$, the contribution of the membrane to the elastic energy is negligible[1] and Eq. (B.33) yields

$$\mathcal{K} = \frac{3+2\alpha^2}{\alpha\sqrt{1+\alpha^2}}\frac{k_B T \ell_p}{r_0^2} \simeq 2.2 \times 10^{-8}\,\mathrm{N}. \tag{B.34}$$

Using Eq. (B.11), we estimate $E \simeq 220\,\mathrm{MPa}$, a value of the same order of magnitude as the typical Young modulus of proteins $E = 2\,\mathrm{GPa}$ [159].

B.4 Soft membrane susceptibility matrices

For clarity's sake, we regroup some expressions associated with the models of Sec. 4.4.3 here. In both limits discussed in Sec. 4.4.3 (short and long time), one combines the relations Eqs. (4.56) between the three hydrodynamic and four microscopic variables with a constraint [Eqs. (4.54) and (4.57) respectively] to find a unique linear relation between the hydrodynamic and microscopic variables, which we write:

$$\begin{pmatrix} \delta\rho \\ u_{z\theta} \\ \delta\Phi \end{pmatrix} = Q_{\mathrm{sm}} \begin{pmatrix} \delta r \\ \delta p \\ a \end{pmatrix}. \tag{B.35}$$

[1] Note that since the contribution of the membrane to the persistence length is negligible, allowing the membrane to depart from its torus shape in the model of Sec. B.3.3 would not change our results much.

In a unit system such that $\rho_0 = 1$, Eqs. (4.31) and (4.32) imply that χ is the matrix of second derivatives of the free energy of Eq. (4.48) as a function of $(\delta\rho, u_{z\theta}, \delta\Phi)$. Hence

$$\chi_{\rm sm} = \left[(Q_{\rm sm})^{-1}\right]^T K_{\rm sm} \left(Q_{\rm sm}\right)^{-1}. \tag{B.36}$$

Here $K_{\rm sm}$ is the matrix of second derivatives of the free energy of Eq. (4.48) as a function of $(\delta r, \delta p, a)$, where the dependence in u is eliminated using the constraints Eq. (4.54) or Eq. (4.57) The expressions for the matrices implicated in this formula depend on the time scale considered. They read

$$K_{\rm sm}^{t\ll} = \begin{pmatrix} k_{rr}+k_{uu} & k_{rp} & k_{uu}-\pi\kappa \\ k_{rp} & k_{pp} & 0 \\ k_{uu}-\pi\kappa & 0 & 2\pi k_s + k_{uu} \end{pmatrix}, \tag{B.37}$$

$$Q_{\rm sm}^{t\ll} = \begin{pmatrix} \frac{\Phi_0}{1+\alpha^2} & -\frac{\Phi_0}{1+\alpha^2} & -2(1-\Phi_0) \\ 0 & -\frac{1}{\alpha} & 0 \\ \frac{\Phi_0(1-\Phi_0)}{1+\alpha^2} & -\frac{\Phi_0(1-\Phi_0)}{1+\alpha^2} & 2\Phi_0(1-\Phi_0) \end{pmatrix}, \tag{B.38}$$

$$K_{\rm sm}^{t\gg} = \begin{pmatrix} k_{rr} - 2\pi\kappa + \frac{(\pi\kappa)^2}{k_{uu}} & k_{rp} & 0 \\ k_{rp} & k_{pp} & 0 \\ 0 & 0 & 2\pi k_s\left(1+\frac{2\pi k_s}{k_{uu}}\right) \end{pmatrix}, \tag{B.39}$$

$$Q_{\rm sm}^{t\gg} = \begin{pmatrix} 1-\frac{\alpha^2\Phi_0}{1+\alpha^2} - \frac{\pi\kappa(1-\Phi_0)}{k_{uu}} & -\frac{\Phi_0}{1+\alpha^2} & -(1-\Phi_0)\left(1+\frac{2\pi k_s}{k_{uu}}\right) \\ 0 & -\frac{1}{\alpha} & 0 \\ \Phi_0(1-\Phi_0)\left(-\frac{\alpha^2}{1+\alpha^2}+\frac{\pi\kappa}{k_{uu}}\right) & -\frac{\Phi_0(1-\Phi_0)}{1+\alpha^2} & \Phi_0(1-\Phi_0)\left(1+\frac{2\pi k_s}{k_{uu}}\right) \end{pmatrix}. \tag{B.40}$$

Neither $\chi_{\rm sm}^{t\ll}$ nor $\chi_{\rm sm}^{t\gg}$ have compact explicit expressions.

B.5 Comment on dynamin compressibility experiments

As emphasized in chapter 4, the change of conformation of dynamin is related to its mechanical properties, which we analyze throughout the present appendix. In this section, we discuss a micromechanical experiment aimed at providing a direct measurement of these properties, and express a concern that it might unfortunately not yield much information about the dynamin helix. We use the notations of chapter 3 throughout this section.

The setup used here is that of Fig. 3.1, except that the pipette is not held fixed relative to the bead, but is successively brought closer to and further form it at constant velocity, as shown in Fig. B.3(a-b). The force on the bead is monitored throughout the experiment. When the vesicle and bead are further apart than the equilibrium length of the dynamin helix, the force plateaus at the value f_b defined in Eq. (3.3). When they are taken too close together, the helix buckles and the force vanishes. Between those two regimes, however, the force depends linearly on the displacement δL of the pipette:

$$f = K\delta L. \tag{B.41}$$

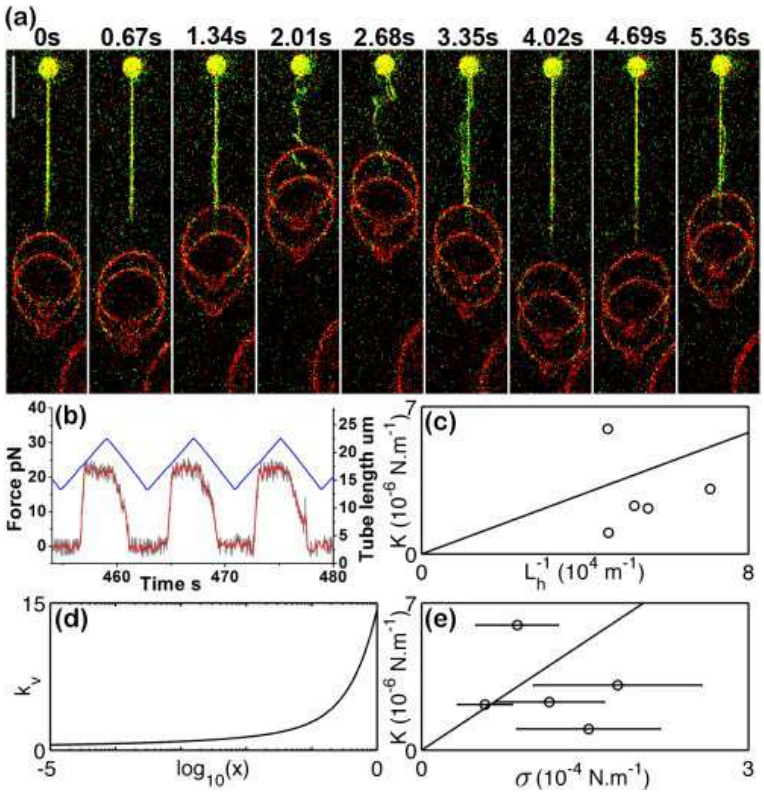

Figure B.3: Dynamin compression experiment. (a) Sequence of images showing the triangular-wave displacement of the pipette/vesicle and the resulting compression of the dynamin-coated tube. Note the phases during which the helix covers only part of the tubule and those during which it buckles. Scale bar, $10\,\mu$m. (b) Force (red) and displacement (blue) curves corresponding to this experiment. The slopes in the phase where the force depends linearly on the displacement yield the spring constant K. (c) Experimental test of the relationship $K = k_h/L_h$. The fit yields $k_h = 7.2 \times 10^{-11}\,$N. (d) Illustration of the weak dependence of k_v [as given in Eq. (B.50)] on x in the experimentally relevant regime (note the logarithmic scale in the horizontal axis). (e) Experimental test of the relationship $K = k_v\sigma$. The values of σ were inferred from bare tubule force measurements through the relation $\sigma = \frac{1}{2\kappa}\left(\frac{f_b}{2\pi}\right)^2$ and the error bars reflect the experimental uncertainty on κ. The fit yields $k_v = 3.4 \times 10^{-2}$. All experimental data courtesy of Aurélien Roux.

A possible interpretation of this result is that as the pipette and bead are brought closer to each other, the helix is compressed, so that the spring constant $K = K_h$ would reflect the compressibility of the dynamin helix. In this case, one would expect that $K_h = k_h/L_h$, where L_h is the length of the helix, and k_h is an intrinsic rigidity of dynamin.

Dimensionally[2],

$$k_h \simeq \mathcal{K} \simeq 2.2 \times 10^{-8}\,\mathrm{N}. \tag{B.42}$$

We confront these predictions with data from five experiments in Fig. B.3(c). Two difficulties arise: first, the experimental data does not reflect the proportionality between K and L_h^{-1}; second, the value of k_h is smaller than the expected value by more than two orders of magnitude.

Here we propose another interpretation of these results. As the pipette and the bead are brought closer to each other, it is not only a spring of rigidity K_h corresponding to the helix that is compressed, but two springs K_h and K_v put in series, where K_v corresponds to the vesicle. Thus

$$\frac{1}{K} = \frac{1}{K_h} + \frac{1}{K_v}, \tag{B.43}$$

and if the vesicle is much softer than the helix, it dominates the compressibility of the whole.

In the following we calculate a theoretical expression for the spring constant K_v of the vesicle. Setting L_h to a constant and approximating the initial shape of the vesicle to a sphere, we can assimilate δL to the variation of the distance between the poles of the sphere. For small displacement, we can describe the surface of the vesicle in terms of the spherical harmonics $Y_{l,m}$. Restricting ourselves to axisymmetric configurations and denoting by Ω the solid angle on the sphere, we write the local radius as

$$r_v(\Omega) = r_v^0 \left[1 + \sum_{l=0}^{+\infty} u_l Y_{l,0}(\Omega) \right], \tag{B.44}$$

where r_v^0 is the same as the radius r_v defined in Sec. 3.1 and the u_ls are real numbers much smaller than one. Let σ be the tension of the membrane. The free energy of the vesicle, not including the membrane cylinder that is sucked into the pipette, reads (up to a constant):

$$F_v = -(P_v - P_c)\delta V + \sigma \delta A - f \delta L + \delta E_{\mathrm{bending}}. \tag{B.45}$$

Indeed, for this system, the membrane cylinder sucked into the pipette acts as a reservoir of membrane at tension σ and a reservoir of water at pressure P_v. Moreover, in order to expand, the vesicle has to work against the pressure P_c in the chamber. To second order in u_l, the deviations of volume, surface area, height and bending energy away from the

[2]It would in principle be possible to derive a precise relation between k_h and $\mathcal{K}$ in the framework of Sec. B.2. However, this would require a few uncertain assumptions, *e.g.* about whether or not some amount of unwinding of the helix is allowed on the timescales considered, and would thus end up yielding no more than a reasonable order of magnitude for k_h.

spherical shape are given by [160]

$$\frac{\delta V}{(r_v^0)^3} = \sqrt{4\pi}u_0 + u_0^2 + \sum_{l=1}^{+\infty} u_l^2, \tag{B.46a}$$

$$\frac{\delta A}{(r_v^0)^2} = 4\sqrt{\pi}u_0 + u_0^2 + \sum_{l=1}^{+\infty} u_l^2 \left[1 + \frac{l(l+1)}{2}\right], \tag{B.46b}$$

$$\frac{\delta L}{r_v^0} = \sum_{l=0}^{+\infty} u_l \sqrt{\frac{2l+1}{\pi}}, \tag{B.46c}$$

$$\frac{\delta E_{\text{bending}}}{\kappa} = \sum_{l=0}^{+\infty} u_l^2 \frac{(l-1)l(l+1)(l+2)}{2}. \tag{B.46d}$$

We now make the assumptions that the membrane is inextensible, and the water incompressible. Therefore the only way for the vesicle to change its volume or surface area is to flow into the pipette. Since the pipette forces the membrane to assume a cylindrical shape of radius r_p, those changes must satisfy the constraint

$$\delta V = \frac{r_p}{2}\delta A. \tag{B.47}$$

It is worth noting that the left-hand side of this equation is of order $(r_v^0)^3$ while the right-hand side is of order $r_p(r_v^0)^2$. In the simplifying limit where the pipette is much smaller than the vesicle($r_p \ll r_v^0$), we can thus write

$$\delta V = \mathcal{O}\left[r_p(r_v^0)^2\right] \Rightarrow u_0 = -\frac{1}{\sqrt{4\pi}} \sum_{l=1}^{+\infty} u_l^2 + \mathcal{O}\left[(u_{l>0})^3\right] + \mathcal{O}\left(\frac{r_p}{r_v^0}\right). \tag{B.48}$$

Using Eq. (3.1), the first term in the free energy of Eq. (B.45) can be written $\frac{2\sigma}{r_v^0}\delta V = \frac{r_p}{r_v^0}\sigma\delta A \ll \sigma\delta A$ and is thus negligible compared to the second term. The volume variation δV can thus be set to zero everywhere. Minimizing F_v under this constraint, we find that for $l > 0$

$$u_{2l} = \frac{\sqrt{4l+1}}{2\sqrt{\pi}(l+1)(2l-1)\left[1 + \frac{2\kappa l(2l+1)}{\sigma(r_v^0)^2}\right]} \frac{f}{\sigma r_v^0} \quad \text{and} \quad u_{2l+1} = 0. \tag{B.49}$$

Therefore

$$k_v = \frac{K_v}{\sigma} = \frac{f}{\sigma\delta L} = \left\{\sum_{l=1}^{+\infty} \frac{4l+1}{2\pi(l+1)(2l-1)\left[1 + 2xl(2l+1)\right]}\right\}^{-1}, \tag{B.50}$$

where $x = \kappa/\sigma(r_v^0)^2$. Note that if $\kappa = 0$, the sum in this expression diverges, yielding a vanishing spring constant. This is related to the fact that the fluctuations of a membrane with a zero bending modulus diverge at small wavelength. Putting $\kappa \neq 0$ thus has a similar effect to introducing an ultraviolet cutoff at wave vector $\sqrt{\sigma/\kappa}$. Since the divergence is logarithmic, however, k_v depends only weakly on the exact value of the cutoff parameter

x, as shown in Fig. B.3(d), and can therefore be treated as a constant of order unity for all relevant parameter regimes.

We compare the predictions of this second interpretation with experiments in Fig. B.3(e). Again, the precision is not sufficient to detect the linear dependence of K_v on σ, and the measured dimensionless spring constant is significantly smaller than the value $k_v \simeq 2.3$ expected from the theory for an experimentally reasonable $x = 6 \times 10^{-2}$.

In conclusion, evaluations of the expected spring constants of the helix and the vesicle suggest that they are both too rigid to account for the experimental measurements presented here. One possible explanation would be for them to be in series with an even weaker spring, for instance a very floppy membrane bulge of the type studied in Sec. 3.4.3. It could also be that the dynamin helix is much softer than the approximate Eq. (B.42) suggests. Such a claim should however be supported by further experimental verifications, *e.g.* of the relation $K_h \propto L_h^{-1}$.

Appendix C

Solutions of the discrete filament profile equation

C.1 Steady state, no reattachment

Here we show that the probability distribution of Eq. (6.3) is a stationary solution of the problem specified by Eqs. (6.21) and (6.23) for $n = 1$ (single filament case), $k = 0$ (no espin reattachment) and $P_0 = 1$ (all espin sites are occupied at the polymerization front). Note that the initial condition Eq. (6.22) need not be considered as it is irrelevant in the stationary state. In the coordinate system defined in Fig. 6.5, Eq. (6.3) yields the following probability for the altitude of the filament's pointed end to be at altitude Z or larger

$$P_f^{\geqslant}(Z,t) = \prod_{i=1}^{+\infty} \left[1 - e^{-\left(t - \frac{Z}{v} + \frac{i}{v}\right)}\right] = \sum_{Z'=Z}^{\lfloor vt \rfloor} P_f(Z',t). \tag{C.1}$$

In Sec. C.1.1 we show that this probability distribution satisfies the bulk master equation Eq. (6.23), then in Sec. C.1.2 we show that it satisfies the boundary condition Eq. (6.21).

C.1.1 Bulk equation: satisfying Eq. (6.23)

According to Eq. (C.1), the probability for the filament's pointed end to be exactly in $Z < \lfloor vt \rfloor$ reads

$$P_f(Z,t) = P_f^{\geqslant}(Z,t) - P_f^{\geqslant}(Z+1,t) = e^{-(t-Z/v)} P_f^{\geqslant}(Z,t). \tag{C.2}$$

The left-hand side of Eq. (6.23) is the time derivative of $P_f(Z,t)$, which reads:

$$\partial_t P_f(Z,t) = P_f(Z,t) \left\{ -1 + \sum_{i=1}^{+\infty} \frac{\exp\left[-\left(t - \frac{Z}{v} + \frac{i}{v}\right)\right]}{1 - \exp\left[-\left(t - \frac{Z}{v} + \frac{i}{v}\right)\right]} \right\}. \tag{C.3}$$

The product in Eq. (6.23) can be expressed in terms of $P_f^{\geqslant}(Z,t)$. The right-hand side

of this equation thus reads

$$\begin{aligned}
&-P_f(Z,t) + e^{-(t-Z/v)} \sum_{Z'=-\infty}^{Z-1} \left\{ \prod_{i=Z'+1}^{Z-1} \left[1 - e^{-(t-i/v)}\right] \right\} P_f(Z',t) \\
&= -P_f(Z,t) + e^{-(t-Z/v)} \sum_{Z'=-\infty}^{Z-1} \frac{\prod_{i=-\infty}^{Z-1} \left[1 - e^{-(t-i/v)}\right]}{\prod_{i=-\infty}^{Z'} \left[1 - e^{-(t-i/v)}\right]} P_f(Z',t) \\
&= -P_f(Z,t) + e^{-(t-Z/v)} \sum_{Z'=-\infty}^{Z-1} \frac{P_f^{\geqslant}(Z,t)}{P_f^{\geqslant}(Z'+1,t)} P_f(Z',t) \\
&= -P_f(Z,t) + P_f(Z,t) \sum_{Z'=-\infty}^{Z-1} \frac{\exp\left[-\left(t - \frac{Z'}{v}\right)\right]}{1 - \exp\left[-\left(t - \frac{Z'}{v}\right)\right]}.
\end{aligned} \tag{C.4}$$

This expression is equal to that of Eq. (C.3), thus proving that the probability distribution of Eq. (6.3) is a stationary solution of Eq. (6.23).

C.1.2 Boundary condition: satisfying Eq. (6.21)

According to Eq. (C.1), the probability for the filament's pointed end to be exactly in $z = \lfloor vt \rfloor$ is

$$P_f(\lfloor vt \rfloor, t) = P_f^{\geqslant}(\lfloor vt \rfloor, t) = \prod_{i=1}^{+\infty} \left[1 - e^{-\left(t - \frac{\lfloor vt \rfloor}{v} + \frac{i}{v}\right)}\right], \tag{C.5}$$

where the first equality is due to the fact that the filament's pointed end cannot be any higher than $\lfloor vt \rfloor$.

The left-hand side of Eq. (6.21) reads:

$$\partial_t P_f(\lfloor vt \rfloor, t) = P_f(\lfloor vt \rfloor, t) \sum_{i=1}^{+\infty} \frac{\exp\left[-\left(t - \frac{\lfloor vt \rfloor}{v} + \frac{i}{v}\right)\right]}{1 - \exp\left[-\left(t - \frac{\lfloor vt \rfloor}{v} + \frac{i}{v}\right)\right]}. \tag{C.6}$$

Using Eqs. (C.2) and (C.5) we can express the right-hand side of Eq. (6.21) in a similar way to what was done in Eq. (C.4):

$$\begin{aligned}
&\sum_{Z'=-\infty}^{\lfloor vt \rfloor - 1} \left\{ \prod_{i=Z'+1}^{\lfloor vt \rfloor - 1} \left[1 - e^{-(t-i/v)}\right] \right\} P_f(Z',t) \\
&= \sum_{Z'=-\infty}^{\lfloor vt \rfloor - 1} \frac{P_f^{\geqslant}(\lfloor vt \rfloor, t)}{P_f^{\geqslant}(Z'+1,t)} P_f(Z',t) \\
&= P_f(\lfloor vt \rfloor, t) \sum_{Z'=-\infty}^{\lfloor vt \rfloor - 1} \frac{\exp\left[-\left(t - \frac{Z'}{v}\right)\right]}{1 - \exp\left[-\left(t - \frac{Z'}{v}\right)\right]}.
\end{aligned} \tag{C.7}$$

This expression is equal to that of Eq. (C.6), thus proving that the probability distribution of Eq. (6.3) is a stationary solution of the system of equations Eqs. (6.21) and (6.23), and therefore of the full problem formulated in Sec. 6.4.2.

C.2 Far away from the polymerization front

Here we prove Eq. (6.28). In Sec. C.2.1 we establish a preliminary result necessary for our demonstration, then we conclude in Sec. C.2.2.

C.2.1 Preliminary result

Let $(A, i) \in \mathbb{N}^{*2}$ with $i < A$. Here we prove the relationship

$$\sum_{j=1}^{A-i} \frac{i(A-j-1)!}{(A-j-i)!} = \frac{(A-1)!}{(A-i-1)!} \tag{C.8}$$

by recursion over A.

C.2.1.1 Base case

Let $A = i + 1$. In this case, Eq. (C.8) reads

$$\sum_{j=1}^{1} \frac{i(i+1-j-1)!}{(i+1-j-i)!} = \frac{(i+1-1)!}{(i+1-i-1)!}, \tag{C.9}$$

which is true as both sides of the equation are equal to $i!$.

C.2.1.2 Recursion

Assuming that the relationship Eq. (C.8) is true for A, we establish it for $A + 1$. Incrementing A by one unit, the left-hand side of Eq. (C.8) reads

$$\sum_{j=1}^{A+1-i} \frac{i(A-j)!}{(A+1-j-i)!} = \sum_{j'=0}^{A-i} \frac{i(A-j'-1)!}{(A-j'-i)!} = \frac{i(A-1)!}{(A-i)!} + \sum_{j'=1}^{A-i} \frac{i(A-j'-1)!}{(A-j'-i)!}, \tag{C.10}$$

where we made the change of dummy variable $j' = j-1$. The right-hand side of Eq. (C.8), on the other hand, reads

$$\frac{A!}{(A-i)!} = i\frac{(A-1)!}{(A-i)!} + (A-i)\frac{(A-1)!}{(A-i)!} = \frac{i(A-1)!}{(A-i)!} + \frac{(A-1)!}{(A-i-1)!}. \tag{C.11}$$

Using the recursion hypothesis shows that the last terms of Eqs. (C.10) and (C.11) are equal, thus establishing Eq. (C.8) for all As.

C.2.2 Full solution

Eqs. (6.28) is equivalent to

$$Q_e(Z_0, t) = 1 \tag{C.12a}$$

$$Q_e(Z, t) = \sum_{i=1}^{Z-Z_0} \frac{(Z-Z_0-1)!}{(i-1)!(Z-Z_0-i)!} \frac{(kt)^i}{i!}, \tag{C.12b}$$

which obviously satisfy Eqs. (6.27) for $Z = Z_0$, as well as for $t = 0$. Injecting Eq. (C.12b) in Eq. (6.27b), redefining $i \to i + 1$ in the left-hand side and permuting sums in the right-hand side with $i = Z - Z'$, we find that the probability distribution of Eqs. (6.28) is a solution of Eqs. (6.27) if and only if

$$k + k \sum_{i=1}^{Z-Z_0-1} \frac{(kt)^i}{(i!)^2} \frac{(Z - Z_0 - 1)!}{(Z - Z_0 - i - 1)!} = k \sum_{i=1}^{Z-Z_0-1} \frac{(kt)^i}{(i!)^2} \sum_{j=1}^{Z-Z_0-i} \frac{i(Z - Z_0 - j - 1)!}{(Z - Z_0 - j - i)!} + k. \tag{C.13}$$

This equality is proved by using Eq. (C.8) with $A = Z - Z_0$.

Appendix D

Non tube-related articles

Although the work on the shape of tubes in eukaryotic cells described in the main text of the present volume is the main focus of this thesis, it also involves contributions to several unrelated projects. In this appendix we present one article and one manuscript scheduled for publication stemming from these collaborations, corresponding to items 3. and 6. of the publication list presented in page 2.

ATP-dependent mechanics of red blood cells

Timo Betz[1], Martin Lenz, Jean-François Joanny, and Cécile Sykes

Centre de Recherche, Institut Curie, Unités Mixte de Recherche 168, F-75248 Paris, France

Edited by Thomas D. Pollard, Yale University, New Haven, CT, and approved July 20, 2009 (received for review April 28, 2009)

Red blood cells are amazingly deformable structures able to recover their initial shape even after large deformations as when passing through tight blood capillaries. The reason for this exceptional property is found in the composition of the membrane and the membrane-cytoskeleton interaction. We investigate the mechanics and the dynamics of RBCs by a unique noninvasive technique, using weak optical tweezers to measure membrane fluctuation amplitudes with μs temporal and sub nm spatial resolution. This enhanced edge detection method allows to span over >4 orders of magnitude in frequency. Hence, we can simultaneously measure red blood cell membrane mechanical properties such as bending modulus $\kappa = 2.8 \pm 0.3 \times 10^{-19}$J $= 67.6 \pm 7.2\ k_BT$, tension $\sigma = 6.5 \pm 2.1 \times 10^{-7}$N/m, and an effective viscosity $\eta_{eff} = 81 \pm 3.7 \times 10^{-3}$ Pa s that suggests unknown dissipative processes. We furthermore show that cell mechanics highly depends on the membrane-spectrin interaction mediated by the phosphorylation of the interconnection protein 4.1R. Inhibition and activation of this phosphorylation significantly affects tension and effective viscosity. Our results show that on short time scales (slower than 100 ms) the membrane fluctuates as in thermodynamic equilibrium. At time scales longer than 100 ms, the equilibrium description breaks down and fluctuation amplitudes are higher by 40% than predicted by the membrane equilibrium theory. Possible explanations for this discrepancy are influences of the spectrin that is not included in the membrane theory or nonequilibrium fluctuations that can be accounted for by defining a nonthermal effective energy of up to $E_{eff} = 1.4 \pm 0.1\ k_BT$, that corresponds to an actively increased effective temperature.

erythrocyte | membrane fluctuations | nonequilibrium | optical tweezer | spectrin

The extraordinary deformability of RBCs is vital for their proper function, as it enables the cells to be elongated by more than twice their size when passing through μm-sized capillaries. The elastic properties of RBCs are dominated by the interaction between the cell membrane and the underlying cytoskeleton, mainly consisting of spectrin, a long heterodimer that aligns tail to tail forming a 200-nm-long tetramer. Each spectrin filament interconnects to up to 5 other spectrins and is bound to the cell membrane via a protein complex consisting of protein 4.1R, actin, and glycophorin C (1). The plasma membrane fluctuations are related to RBCs' mechanical properties that have been extensively studied over the past three decades (2–6). It is well known that fluctuations of the membrane depend on its bending rigidity κ and its membrane tension σ (7). Furthermore, RBCs gain their elasticity from the elastic shear modulus of the cytoskeletal spectrin network (8, 9). Recent theoretical analysis (10) suggest that the spectrin cytoskeleton acts as a steric barrier restricting membrane undulations toward the network.

Experiments by Tuvia and coworkers showed an ATP dependent effect by monitoring the static fluctuation amplitude of RBCs under normal and ATP-depletion conditions (11). In these measurements, the fluctuation amplitude (the root mean square displacement; *rmsd*), was found to decrease substantially under ATP depletion. This was interpreted as a sign for activity-dependent fluctuations. However, a recent report did not confirm this decrease (6), arguing that the fluctuations are purely thermally driven. Additionally to the fluctuation decrease under ATP depletion, Tuvia et al. found a fluctuation decrease upon increase of the external medium viscosity, in disagreement with thermodynamics, which predicts that all equilibrium quantities are independent of transport coefficients such as the viscosity. This suggested an active, energy-consuming process, depending on phosphorylation of the 4.1R protein or erythrocyte myosin motors. Subsequent theoretical studies argue that the viscosity dependence of static fluctuations could be explained by the ATP-dependent phosphorylation of the 4.1R protein (12), which controls the spectrin-membrane connection (1). This phosphorylation is catalyzed by protein kinase C (PKC) (13), which disassembles the 4.1R/spectrin/actin trimer, thus leading to a decreased overall stability of the RBC membrane.

Previous measurements to determine membrane fluctuations suffer from the restricted time resolution of camera acquisition (6), or can only detect relative and uncalibrated fluctuation amplitudes (5, 11). To overcome both limitations we used a unique approach to monitor the time-dependent fluctuation of the RBC membrane at a single point with sub nm spatial and μs time resolution (14). Our measurements are in excellent agreement with the theory of fluctuating membranes at frequencies >10Hz and enable us to simultaneously measure the membrane bending modulus κ, the tension σ, and an effective viscosity η_{eff} of RBCs, thereby showing that the external viscosity has no effect on the time averaged fluctuation amplitudes.

Results

Interferometric Fluctuation Detection. The method used to measure RBC membrane fluctuations is an extension of well-known interferometric particle detection using optical tweezers (15). However, the laser is operated at minuscule powers ($\approx$50 μW) at the sample, too small to create a trapping potential. In the experiments, a volume of 15 μL of a RBC suspension was sealed between two coverslips, and cells were allowed to weakly attach on the substrate for 30 min. Only discocyte-shaped RBCs with diameters varying from 6 to 8 μm were used. Weak attachment of the RBCs to the coverslip was checked by reflection interference contrast microscopy (RICM) (*SI Appendix* and Fig. S1). The infra-red (λ = 1064 nm) laser was positioned at the edge of the cell, and a calibration curve (line scan) was acquired by moving the RBC through the laser with a step size of 4 nm using a piezoelectric stage and recording the signal with a quadrant photodiode (QPD) at the condenser's back focal plane as shown in Fig. 1. The method is based on a difference in refractive index, thus detecting the plasma membrane at the interface between the cell and the medium. Each data point of the calibration curve represents an average of 500 recordings taken at a sampling rate of 100 kHz. The acquired calibration curve shows a linear regime, which was used to convert between QPD voltage and edge position in nm by determining the slope. To record the fluctuations, the edge of the RBC was positioned at the

Author contributions: T.B. and C.S. designed research; T.B. performed research; T.B., M.L., and J.-F.J. analyzed data; and T.B. and C.S. wrote the paper.

The authors declare no conflict of interest.

This article is a PNAS Direct Submission.

[1]To whom correspondence should be addressed. E-mail: timo.betz@curie.fr.

This article contains supporting information online at www.pnas.org/cgi/content/full/0904614106/DCSupplemental.

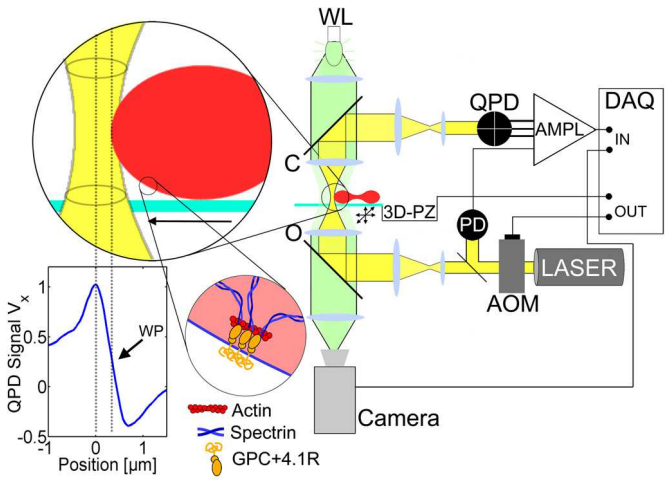

Fig. 1. Schematics of the setup used to detect the RBC edge fluctuations. Infra-red (λ = 1064 nm) laser light is emitted from a fiber laser and intensity-controlled using an acousto-optical modulator (AOM). Five percent of the light is projected on a photodiode (PD) as intensity reference. A 10× telescope increases the beam diameter to 14 mm. The beam is coupled in the optical path of an inverted microscope using a dichroic mirror and focused on the sample by a water-immersion objective (O). At the sample the light is partially scattered off the cell edge. Scattered and unscattered light are collected by a water-immersion condenser (C) and imaged on a QPD. Before digitalization (DAQ), the data are amplified and filtered using custom made low-noise hardware (AMPL). Round *Inset* 1 shows a detailed view of the experiment. Part of the laser interacts with the cell by light scattering, which is monitored by the QPD. A calibration curve is recorded by moving the RBC through the laser focus using a 3D piezoelectric stage (3D-PZ) and determining a linear regime as shown in the plot. The center of this linear regime is used as the working point (WP) of the experiment. A camera images the position of the cell using white light (WL). Round *Inset* 2 sketches the interaction between the membrane and the spectrin network, which is maintained by the protein 4.1 forming a trimer with spectrin and a short actin filament.

center of the linear regime (called the working point WP, Fig. 1). To measure the membrane fluctuations, the QPD voltage was recorded in 10 subsequent measurements of 10 seconds each and converted to nm using the previously determined linear slope of the calibration curve. After each recording, the line scan was repeated to ensure that the cell's properties and position did not change during the experiment. From each time series, the power spectral density (PSD) was calculated (see *SI Appendix*) and filtered using log binning. For further evaluation of the data, the mean PSD of the 10 recordings was used. To ensure that the laser did not interfere with the measurements, we recorded the PSD as a function of the applied power and found no dependence for laser powers smaller than 1 mW (see Fig. S1), thus confirming that the used power of 50 μW does not influence the measurement.

Mechanics of Normal RBCs. The PSD in Fig. 2 represents mean and standard error (n = 210) of 21 normal RBCs. A theoretical description of the PSD has been established previously (16) (*SI Appendix*, *Calculations*). In the limit of a flat membrane the PSD decays at high frequencies with a theoretical predicted power law of $PSD_{HF} \propto f^{-5/3}$, illustrated by the dashed line in Fig. 2. At low frequency the curve levels off because of the finite size of the RBC and membrane tension. The theoretical description (*SI Appendix*, *Calculations*) provides an excellent fit in both regimes (Fig. 2) ($r^2 = 1-\Sigma\ (PSD_{exp}-PSD_{model})^2/\Sigma\ PSD_{model}^2 = 0.98$), which allows us to measure the RBCs mechanical properties of bending rigidity $\kappa^{dy} = 2.8 \pm 0.3 \times 10^{-19}$J, surface tension $\sigma = 6.5 \pm 2.1 \times 10^{-7}$N/m, and effective viscosity $\eta^{eff} = 81 \pm 3.7 \times 10^{-3}$Pa s (Table 1). The used fit function has three independent parameters, each changing the curve in a characteristic way,

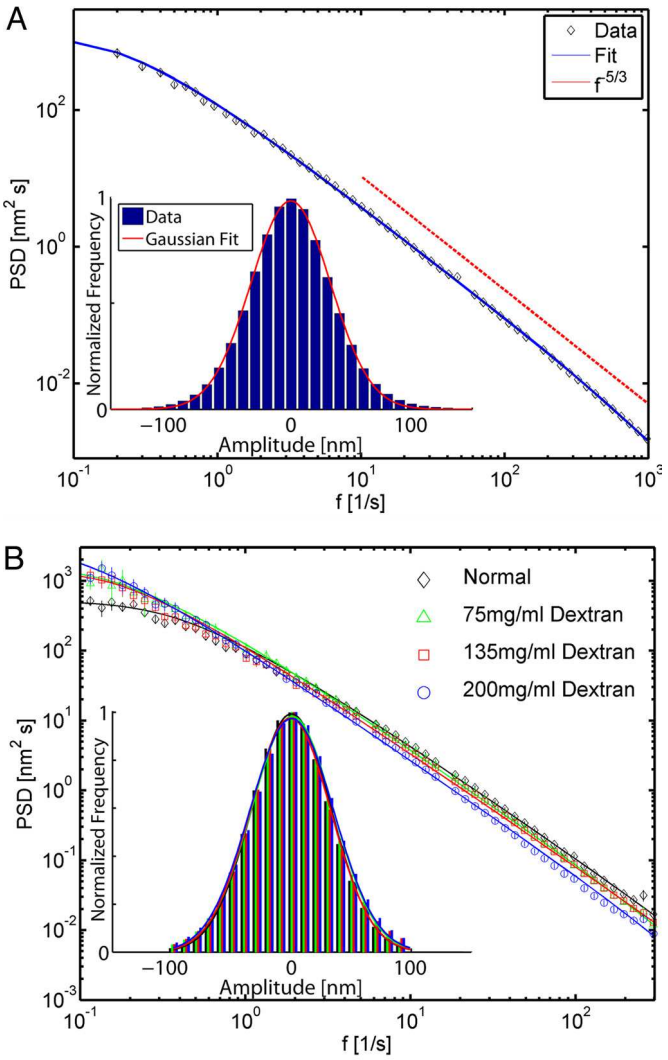

Fig. 2. Fluctuation spectra of normal RBC under various medium viscosities. (*A*) Mean PSD of 21 normal RBCs. The presented error (at the center of the diamond data) is the standard error for the 210 individual PSDs. The fit provides an excellent explanation for the data over four decades. The theoretical slope of (-5/3) is shown presented as an eye-guide (dashed line). (*Inset*) Static fluctuations histogram of a normal RBC. (*B*) PSD of RBCs immersed in media of increasing viscosities, and the corresponding fluctuation histogram in the *Inset*. Although the PSD differ significantly, the fluctuation histogram remains almost independent of the viscosity.

which ensures that all parameters can be determined simultaneously. The bending modulus and the tension are both consistent with literature values that have been measured with other methods (3–6).

Furthermore, for a consistency check, we determined the mechanics of hypertonic swollen cells (see Fig. S2) and found an increase in tension and a decrease in viscosity as expected (6). Previous work estimated κ by measuring the *rmsd* of edge fluctuations (4, 6), which is equivalent to the standard deviation of the Gaussian distributed histogram of the fluctuation amplitude (Fig. 2, *Insets*). For normal RBCs we find a *rmsd* value of $\Delta h = 33.0 \pm 1.3$ nm, consistent with literature (4, 14, 17). The *rmsd* is a static measurement that averages the fluctuation amplitudes over time and is independent of the viscosity in equilibrium systems. Its measurement enables us to crosscheck our results in two ways. First, we can show the consistency of the measured *rmsd* with the theoretical static fluctuation amplitude

Table 1. Collection of mechanical parameters of RBCs under various conditions, compared with previous findings by Evans et al. (6) and Strey et al. (4)

	Normal	ATP-depl.	PKC
$rmsd_{ex}$ [nm]	33.0 ± 1.3	22.3 ± 0.6	36.7 ± 2.8
$rmsd_{th}$ [nm]	36.3 ± 12	24.0 ± 9.0	47.2 ± 13
κ^{stat}_{SPS} [10^{-19}J]	2.8 ± 0.2	6.1 ± 0.3	2.3 ± 0.4
κ^{dyn} [10^{-19}J]	2.8 ± 0.3	3.9 ± 0.3	2.6 ± 0.2
σ [10^{-7} N/m]	6.5 ± 2.1	19 ± 1	2.7 ± 1.1
η_{eff} [10^{-3}Pa s]	81 ± 3.7	118 ± 11.8	57 ± 2.4
$rmsd_{Evans}$ [nm]	23.6 ± 0.6	22.8 ± 1.0	—
$rmsd_{Strey}$ [nm]	30.0 ± 5	—	—

$rmsd_{th}$ = 36 ± 11 nm, which is calculated using the mechanical parameters determined from the dynamic measurements (Table 1). Additionally, in the literature the *rmsd* has been used to determine the bending stiffness by assuming a tensionless limit and accounting for the shear modulus on the first fluctuation mode. Strey, Peterson, and Sackmann (SPS) established an approximation to calculate a bending modulus from the *rmsd* (4): $\kappa^{stat}{}_{SPS} = (6 \times 10^{-6}) k_B T R^2/(\Delta h_{l=1})^2 = 2.8 \pm 0.2 \times 10^{-19}$J, where R denotes the cell radius, and k_B the Boltzmann constant. This approximative static bending modulus is an alternative method, and in the case of normal RBCs it agrees well with the dynamic bending modulus obtained from the PSD (see Table 1). We furthermore checked the dependence of the fluctuation on the viscosity of the external medium. We increased the medium viscosity by the addition of 75 mg/mL ($\eta_{75} = 2.4 \pm 0.1 \times 10^{-3}$Pa s), 135 mg/ml ($\eta_{135} = 4.4 \pm 0.2 \times 10^{-3}$Pa s), and 200 mg/mL ($\eta_{200} = 10.9 \pm 0.9 \times 10^{-3}$Pa s) of Dextran 41000. In all cases fluctuation histograms were well Gaussian distributed, but did not depend on the external viscosity (Fig. 2*B*), as expected from equilibrium statistical mechanics. Furthermore, we used the PSD of RBC immersed in solvents of different viscosities to determine the effective viscosity as a function of external viscosity. The resulting dependence (*SI Appendix* and Fig. S3) can be well fitted with a linear function $\eta_{eff} = a \times \eta_{ext} + b$, yielding fit parameters of $a = 8.3 \pm 2.3$ and $b = 53 \pm 11 \times 10^{-3} Pa\ s$.

PSD of ATP-Depleted Cells. To investigate the effect of ATP on membrane mechanics, we removed ATP from the RBCs by applying an ATP depletion medium for 3 h and then measured the resulting PSD. As presented in Fig. 3*A* (green, $n = 200$, fit quality: $r^2 = 0.85$) the fluctuation amplitude was significantly smaller than for the normal RBCs over the full frequency spectrum, showing a strong dependence of the membrane fluctuations on ATP. We measured a slightly increased bending rigidity, and dynamic measurements showed that the effective viscosity was also increased by ≈50% (Table 1). The effect of ATP-depletion was additionally reflected in the static measurement of the *rmsd*, which was strongly decreased compared with normal cells (Table 1). Interestingly, removing ATP led to a strong increase of tension, which explains the discrepancy between the dynamic bending modulus presented in this work and the static bending modulus which assumes a vanishing tension (4) (Table 1).

PSD of PKC-Activated Cells. The fluctuation decrease in ATP-depleted cells might be because of an inhibition of the phosphorylation of the 4.1R protein, which connects the spectrin to the membrane in its unphosphorylated state (13). To investigate the influence of this connection we activated PKC, an enzyme that had been shown to phosphorylate 4.1R, thus resulting in an increased dissociation of the spectrin network and unbinding of spectrin from the membrane (13). The resulting PSD of 21 PKC activated cells is

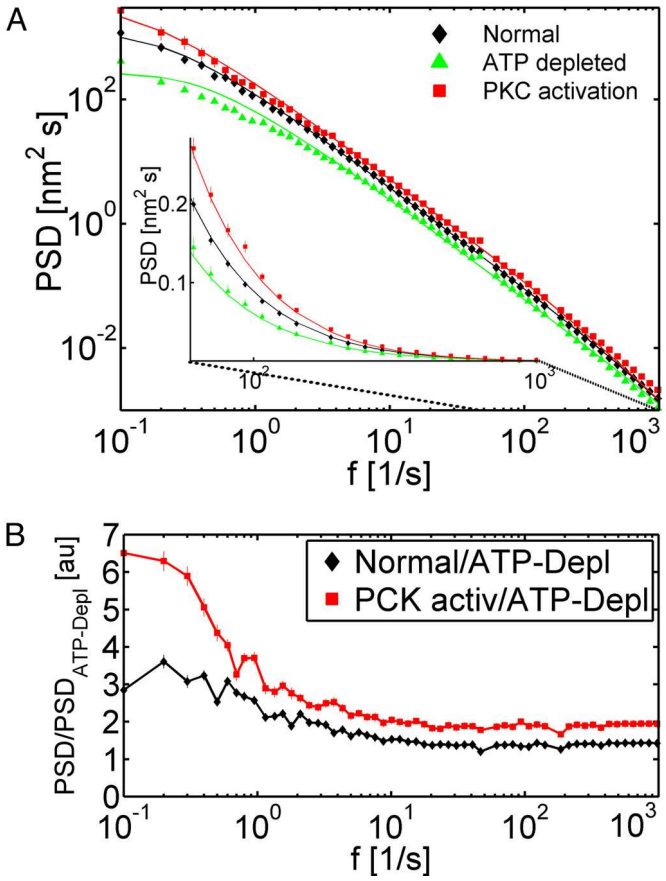

Fig. 3. Absolute and normalized fluctuation spectra. (*A*) Mean PSD of 21 normal RBCs ($n = 210$, black) and 20 ATP-depleted ($n = 200$, green) and 21 PKC-activated ($n = 210$, red). The solid lines show the fit. (*Inset*) Semilog plot of the same data for the marked frequency range showing that the ATP-depleted cells have the smallest amplitude. (*B*) Semi logarithmic representation of the fluctuation amplitudes normalized by the ATP-depleted PSD, which can be considered to be a purely thermally driven system because of the lack of the energy source ATP.

presented in Fig. 3*A* (red, $n = 210$, fit quality: $r^2 = 0.97$). Fluctuations increased over the accessible frequency range compared with the normal RBCs. The analysis of the data yields static and dynamic bending rigidities consistent with the bending rigidity measured on normal RBCs (Table 1). However, our results showed that overactivation of PKC decreases membrane tension by ≈50% and resulted in a slight decrease of the effective viscosity (Table 1). DMSO control experiments showed no difference with the normal cells. Additionally, we checked the effect of cells treated with the actin depolymerizing drug latrunculin A (*SI Appendix* and Fig. S4). The data are similar to the PKC activated cells (*SI Appendix* and Fig. S5), however, our controls show that F-actin in RBCs was not affected by latrunculin A (*SI Appendix* and Fig. S6), which indicates that there is no actin dynamics in RBCs. Our experiments suggest a yet unknown effect of LA on the cytoskeleton membrane interaction.

Relative Fluctuation Amplitudes. To investigate the effect of non-thermal contributions, we normalized the fluctuations of normal and PKC-activated cells by the PSD of ATP-depleted cells (Fig. 3*B*). A striking result of this normalization arose at frequencies >10Hz, where all relative amplitudes level off to plateaus. Here, the fluctuations for PKC-activated cells level to a value of approximately twice the fluctuation of ATP-depleted cells, and the amplitude of normal cells was ≈30% higher than in ATP-

depleted cells. However, <10 Hz we found relative amplitudes peaking at 6.5 ± 0.3 (PKC-activated) and 3.6 ± 0.2 (normal cells), all in arbitrary units.

Discussion

The presented results allow us to investigate membrane dynamics with millisecond time and sub nm spatial resolution, using a standard optical tweezers setup equipped with a QPD. In contrast to previous fluctuation analysis which mostly used video microscopy, our method provides great advantages in terms of spatial and temporal resolution, which is not restricted by camera properties and image analysis. In contrast, the presented method is easy to implement, only limited by fundamental signal to noise ratio and does not require complex image analysis. Using the theory of membrane fluctuations, we can extract the mechanical parameters of RBCs under various conditions. The high reproducibility of the experiments and the data quality also allow us to explore the limitations of the applied equilibrium model.

RBC Viscosity. As presented in Table 1, we discover surprisingly high values for the effective viscosity ($\approx 100 \times 10^{-3}$ Pa s) compared with literature values for RBC viscosity, which was reported to be approximately $\eta_{RBC} \approx 10 \times 10^{-3}$ Pa s (18). Such an increase of the effective viscosity at the membrane was predicted to be a confinement effect caused by close association of the spectrin to the membrane, providing a steric obstacle for the fluid flow (19). Hence, our measurements confirm these predictions. To gain further insight into the effective viscosity, we varied the external viscosity as presented in the results section: The effective viscosity depends linearly on the external viscosity, with a slope of $a = 8.3 \pm 2.3$ (*SI Appendix* and Fig. S3). This phenomenological dependence can be used to extract a RBC viscosity of $\eta_{RBC} = 6.4 \pm 1.9$ Pa s (see *SI Appendix*), which is consistent with previously reported values (18).

Comparison with the Literature. Our results confirm previous reports by Tuvia et al. (11) of decreased static fluctuation amplitudes under ATP-depletion conditions that were put into question recently by Evans et al. (6) (see Table 1). Because the *rmsd* presents the integral over the PSD, it is dominated by the low frequency domain. The low frequency part depends on tension, whereas the high frequency part is dominated by the bending modulus. This allows us to give a mechanical reason for the fluctuation decrease in ATP-depleted cell, which is more pronounced in the low frequency part (see Fig. 3). We identify an increase in tension as reason for these decreased fluctuations, as discussed in the next paragraph (see also Table 1). It should be mentioned that our measurements of the *rmsd* is consistent with several previous reports (4, 14, 17), but not with Evans et al. A possible explanation for the difference is the duration of drug application. Evans et al. reported having applied the ATP-depletion medium for 1 h. Although we can measure already a slight decrease in the rmsd after 1 h, we found that the rmsd stabilized to a lower value only after 3 h (see Fig. S7 and Fig. S8).

Besides the effect of ATP-depletion Tuvia et al. (11) also report a decreased static fluctuation amplitude if the external viscosity is increased. However, our measurements do not confirm this (Fig. 2*B*), as we see no dependence of the static fluctuation amplitudes for external viscosities in the range of $1-10 \times 10^{-3}$ Pa s. This lack of viscosity dependence has been predicted to happen if the characteristic time of membrane relaxation on length scales of the spectrin-membrane connections (≈0.1 − 1 ms) is faster than the timescale of activity (≈100 ms) (12), as observed in this work. Furthermore, we tested recent theoretical considerations predicting an additional spring like interaction between the spectrin cytoskeleton and the membrane (10). Including the respective term in our fit function hardly altered the other fit parameters, which remained essentially constant (*SI Appendix* and Table S1). Hence, our data can be well explained without these additional terms.

ATP-Depletion Effects. Our measurements can give insight into the longstanding question why ATP depletion has such a strong effect on RBC fluctuation histograms. We can identify a partial mechanical reason for these reduced membrane fluctuations because we measure an increase in membrane bending modulus and surface tension, which decreases the *rmsd* of the measured histograms. We can explain these findings by a stronger association between the spectrin and the membrane, as ATP depletion prevents the phosphorylation of the 4.1R protein. In its unphosphorylated state, the 4.1R protein strongly couples the spectrin to the membrane, which has important implications for membrane fluctuations. As the persistence length of spectrin is short compared with its contour length and end-to-end distance, the spectrin should be considered to be an entropic spring under tension even in the relaxed state of the RBCs (12, 20). Hence, the measured tension in normal and ATP-depleted cells might be mostly because of the underlying spectrin cytoskeleton. As the presented measurements cannot distinguish between membrane and spectrin tension, we suspect that we effectively detect spectrin tension, which is in turn related to an effective shear modulus (9). The fact that the shear modulus of the spectrin network might show up as an additional tension was recently proposed theoretically by Auth et al. (10). We furthermore attribute the increased effective viscosity in the ATP-depleted cells to the same stronger spectrin-membrane interaction. As suggested, the effective viscosity might be dominated by a yet unknown mechanism, and the continuous association and dissociation of the spectrin under shear could be a molecular reason for an additional dissipative process.

Decreasing the Spectrin-Membrane Interaction. In contrast to ATP depletion, PKC activation is believed to weaken the spectrin-membrane interaction, as PKC phosphorylates the 4.1R protein (13), thereby dissolving the binding complex. This detachment of the spectrin from the membrane can account for the measured decrease in tension, whereas the bending modulus remains almost unaffected. Furthermore, the decrease of the effective viscosity is consistent with the idea that an additional and dominating dissipative process depends on the spectrin-membrane interaction. In fact, after the model proposed by Gov et al. (12) for the nonequilibrium energy production via the phosphorylation of the 4.1R protein, activation of PKC should not only detach the membrane from the spectrin but also increase the amount of chemical energy used to drive the membrane fluctuations. Because PKC activation implies higher energy consumption, the increase in fluctuations at small frequencies might be because of active ATP-dependent energy injection.

Limitations of the Equilibrium Membrane Description. Let us analyze the higher relative fluctuation amplitudes in the low frequency regime as shown in (Fig. 3*B*). The low frequency part of the spectrum is dominated by tension, which varies considerably between the different conditions (Table 1). Because we have used a passive membrane theory, the ratio:

$$\frac{E_{\mathrm{eff}}(f)}{k_{\mathrm{B}}T} = \frac{PSD_{\mathrm{N,P}}}{PSD_{\mathrm{ATP\text{-}D}}} \times \frac{g^{\mathrm{ATP\text{-}D}}(\sigma, \kappa, \eta; f)}{g^{N,P}(\sigma, \kappa, \eta; f)} \qquad [1]$$

is equal to one if $E_{\mathrm{eff}} = k_{\mathrm{B}}T$, which we expect for a purely passive system. Here, the membrane mechanics is completely described by the g function (defined in *SI Appendix Calculations*, N: Normal, P:PKC), which depends on the mechanical parameters (κ, σ, η) and the frequency f. Experimentally, this ratio equals

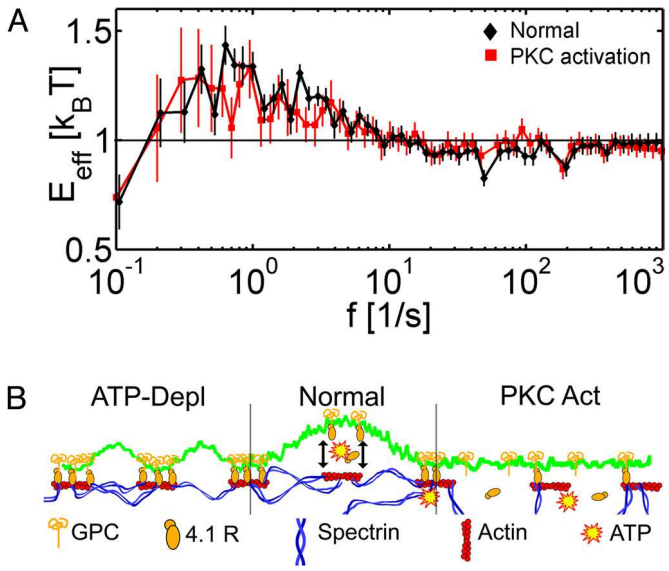

Fig. 4. Effective energy and membrane model. (*A*) Frequency-dependent energy for the various cells. At high frequencies, the fluctuations are driven by thermal activation shown by the value of 1 k_BT, whereas for low frequencies the maximal effective energy is, $E_N^{max} = 1.43 \pm 0.09\ k_BT$ for normal cells and $E_P^{max} = 1.32 \pm 0.08\ k_BT$ for the PKC-activated cells. (*B*) Model to explain the measured mechanical differences (17). The fluctuations depend on the membrane properties and on the integrity of the underlying spectrin cytoskeleton, connected to the membrane by actin, glycophorin C (GPC), and protein 4.1R. In normal cells, a continuous de-and reattachment of the spectrin results in a certain net tension. ATP depletion increases the spectrin-membrane connection and the integrity of the spectrin network, leading to an increased tension. In contrast, disrupting the spectrin-membrane interaction by PKC activation weakens the spectrin network and hence decreases the measured tension.

one for the high frequency domain (f >10Hz) in all RBC conditions. Hence, in this regime the passive equilibrium membrane theory seems to be a correct description. However, we observe for the low frequency part a deviation from one, leaving up to 40% of the fluctuations unaccounted for (Fig. 4*A*). This discrepancy can be potentially explained in two ways. First, at low frequency the simple membrane description of the complex RBC membrane yielding the function g might break down. Hence, it would be necessary to extend the model, for example to composite membrane systems explicitly including the spectrin. A second possible explanation is the breakdown of the equilibrium description, leading to a frequency-dependent effective energy $E_{eff}(f)$ that becomes important at frequencies <10Hz. This energy term corresponds to a frequency-dependent "effective temperature" $T_{eff}(f) = E_{eff}(f)/k_B$. At high frequencies (>10Hz) $T_{eff} \approx 300K$, whereas at low frequencies $T_{eff} > 300K$, indicating that the system behaves as if its temperature was increased. Such frequency dependence resembles the results of recent experiments on the nonequilibrium behavior of cytoskeleton-motor systems (21) and the oscillation of hair cells (22), where at high frequency equilibrium thermodynamics dominates whereas at frequencies <10Hz, the nonequilibrium effects become apparent.

Our finding is of great importance for the theoretical description of RBCs, because our results define a regime in which it is reasonable to apply standard thermodynamics of a single membrane, and one where either out-of-equilibrium phenomena must be taken into account or an extended description of the composite membrane has to be developed. In previous experiments on RBCs such observations were experimentally inaccessible, because their detection requires the knowledge of the full mechanics and access to high-frequency fluctuations, which is generally restricted by the camera acquisition rate of usually 25Hz. However, it should be noted that the current analysis only shows that a passive membrane model does not explain the behavior at low frequencies, and further experiments are required to prove whether this is because of an active process or requires a more complex description of the composite membrane.

Model. A possible model accounting for the data are sketched in Fig. 4*B* (17). Note that the presented data reflect the fluctuation of the membrane but does not give direct information about the cytoskeleton, which consists of the floppy spectrin network. This model is based on theoretical suggestions by Gov et al. (12, 23). We attribute the physical origin of the drug dependence to the dissociation of the spectrin-membrane connection. In the context of the 4.1R/spectrin binding, this means that depleting the ATP pool forces the 4.1R protein to be in the unphosphorylated state, which favors the 4.1R/spectrin/actin binding (13, 24). If bound to the membrane, the spectrin cytoskeleton acts like a network of entropic springs, thus imposing a tension that partially compresses the membrane (Fig. 4*B*) (23). Upon phosphorylation of the 4.1R the spectrin-membrane connection is released and the compressed membrane can relax. The schematics can explain the measured tensions by changes in the spectrin network integrity and variations in the spectrin-membrane interactions, thus leading to modified shear of the spectrin network upon membrane fluctuations. The tension of the spectrin network depends strongly on the network integrity and its association with the membrane. It was already predicted theoretically that at the percolation transition a strong change in tension should be observed (12, 23), which our measurements confirm when modifying the spectrin network by PKC activation or ATP depletion. Increasing the spectrin-membrane connection for ATP-depleted cells leads to an increase in tension, whereas weakening the connection alters the network integrity and hence results in a decrease of tension in PKC-activated cells. As the membrane bending modulus is unaffected by the drugs used, the proposed model predicts that the membrane bending modulus stays constant, as confirmed in our measurements. An additional consequence of the presented model is a nonlinear response to strong deformations caused by a breakdown of the spectrin cytoskeleton at large strains, previously proposed by several authors (25, 26).

The continuous phosphorylation and dephosphorylation of the 4.1R protein is believed to inject mechanical energy in the system. The time scales involved in this binding/unbinding have not yet been determined, but our results indicate that this cycling is slower than 100 ms. In the case of PKC-activation the phosphorylation is favored, however, the cyclic binding/unbinding is not affected, hence energy injection is not perturbed and we measure approximately the same effective energy. The suggested additional dissipative process because of the spectrin-membrane binding might also explain the found increase of effective viscosity in ATP-depleted cells, and its decrease in PKC-activated cells.

Conclusion

In this article we report on a unique, efficient, and fast measurement to detect RBC viscosity, membrane tension, and membrane bending modulus. We confirm theoretical predictions for membrane fluctuations over a wide range of frequencies. The application of ATP-depletion medium and PKC-activation drugs clearly confirms the ATP-dependence of the membrane fluctuations and suggests that the fluctuations might be partially nonthermal in the low frequency domain (f <10Hz) or that an alternative more complex composite membrane model should be developed for this regime. At high frequencies the system is well described by an equilibrium single membrane theory. Depending on the applied drug, we detect changes in

tension, which we attribute to the coupling of the membrane to the tense spectrin cytoskeleton. The changes in tension might have a role in unfolding the spectrin to expose hidden binding sites in the spectrin which could act as mechanosensors (27). The presented results are also important in the context of other cell organelles, because the spectrin network can be found to be attached to most cell membrane systems, like Golgi membranes, lysosomal membranes, and intracellular vesicles in cerebella neurons, as well as on the plasma membrane (28). Based on previous work by Gov et al. (12), we suggest a model in which the effective energy is provided by a continuous phosphorylation/dephosphorylation of the 4.1R protein, which also alters the spectrin network. The current data does not allow us to decide whether RBC fluctuations are active processes or should be described by a more refined membrane-spectrin interaction. It is also possible that both explanations are required for a full understanding of the RBCs fluctuations.

Materials and Methods

Preparation of RBCs. Human RBCs were freshly prepared before each experiment by finger pricking of a healthy donor. Twenty microliters of blood were diluted in 250 μL of a PBS solution containing 130 mM NaCl, 20 mM K/Na phosphate buffer, 10 mM glucose, and 1 mg/mL BSA. RBCs were washed twice in the described PBS buffer by centrifugation (2 min, 200 g) and aspiration of the supernatant. Cells were diluted 1:12 in the final experimental buffers. Before the experiment was started, the slight attachment of the cells was checked by RICM microscopy. If not stated otherwise, all materials were purchased at Sigma–Aldrich, France.

Drug Application. We tested RBCs under ATP depletion, PKC activation and LA. ATP depletion was performed by incubating the cells for 3 h at 37 °C in a PBS solution deficient, of Glucose containing 6 mM iodoacetamide and 10 mM inosine, as described previously (11). We found that only 1 h incubation under this condition was not sufficient to significantly reduce the fluctuation amplitudes. Cells were stored in the ATP depletion medium during the experiments. PKC activation was achieved as described previously (13). Briefly, cells were incubate for 30 min at 37 °C with 0.02 μM calyculin A solved in DMSO (0.2% final concentration) and subsequently for 90 min at 37 °C with 2 μM phorbol 12-myristate 13-acetate (PMA). LA was applied at a concentration of 20 μM LA for 30 min at 37 °C. In the control experiment 0.4% DMSO was applied for 1 h at 37 °C.

Experimental Setup. To measure the fluctuation amplitude of the RBCs edge, we use a technique recently described (14), and summarized in Fig. 1. Laser light from a 1 Watt Ytterbium fiber laser (YLM-1–1064-LP, IPG Photonics, Germany) with a wavelength of 1064 nm is collimated and subsequently intensity controlled by a acousto optical modulator (MT80-A1,5–1064 nm, AA Opto Electronic, France), to reduce the power to 50μW at the sample. Up to laser powers of 1mW, no effect of trapping the RBC was observed (*SI Appendix* and Fig. S1). A 10× telescope increases the diameter of the beam to 14 mm before it is introduced in the beam path of the microscope with an dichroic mirror. The laser is focused in the sample by a 60× water objective (UPLSAPO 60XW/IR, NA 1.2). To control the focus and the imaging position the samples are mounted on a 3D piezoelectric stage (Tritor 102 SG, Piezosystem-Jena, Germany). The scattered light is collected by a long distance water-immersion objective (U LUMPL FL 60XW/IR NA 0.9), and projected on a InGaAs QPD (G6849, Hamamatsu, France) by imaging the back focal aperture of the collecting objective on the QPD. The signal was preamplified and finally amplified and anti-alias filtered by a custom made amplification and filtering electronics (Oeffner Electronics, Germany). The signal was digitized at 100 kHz with a 16 bit AD converter card (PCIE-6259, National Instruments, France), and analyzed using LabView (National Instruments) and Matlab (Mathworks, France).

If operated with higher laser power (5 mW), the setup can also be used as an optical tweezer. By trapping 1 μm beads and recording the PSD of the bead's position we determined the friction coefficient, which is proportional to the medium viscosity (29). For the different media prepared with Dextran 41000 concentrations of 75 mg/mL, 135 mg/mL, and 200 mg/mL we measured the viscosities to be $2.4 \pm 0.1 \times 10^{-3}$Pa s, $4.4 \pm 0.2 \times 10^{-3}$Pa s, and $10.9 \pm 0.9 \times 10^{-3}$ Pa s, respectively.

ACKNOWLEDGMENTS. We thank S. Safran, N. Gov, and T. Auth for helpful discussion. This work was supported by the Human Frontier Science Program and a grant of the French Agence Nationale de la Recherche-Physique et Chimie du Vivant. T.B. was supported by a fellowship within the Postdoc Program of the German Academic Exchange Service (DAAD) and by a long-term European Molecular Biology Organization (EMBO) fellowship.

1. Bennett V, Baines AJ (2001) Spectrin and ankyrin-based pathways: Metazoan inventions for integrating cells into tissues. *Physiol Rev* 81:1353–1392.
2. Brochard F, Lennon JF (1975) Frequency spectrum of the flicker phenomenon in erythrocytes. *Journal de Physique* 36:1035–1047.
3. Evans EA (1983) Bending elastic modulus of red blood cell membrane derived from buckling instability in micropipet aspiration tests. *Biophys J* 43:27–30.
4. Strey H, Peterson M, Sackmann E (1995) Measurement of erythrocyte membrane elasticity by flicker eigenmode decomposition. *Biophys J* 69:478–488.
5. Popescu G, et al. (2006) Optical measurement of cell membrane tension. *Phys Rev Lett* 97:218101.
6. Evans J, Gratzer W, Mohandas N, Parker K, Sleep J (2008) Fluctuations of the red blood cell membrane: Relation to mechanical properties and lack of atp dependence. *Biophys J* 94:4134–4144.
7. Helfrich W (1973) Elastic properties of lipid bilayers: Theory and possible experiments. *Z Naturforsch C* 28:693–703.
8. Discher DE, Mohandas N, Evans EA (1994) Molecular maps of red cell deformation: Hidden elasticity and in situ connectivity. *Science* 266:1032–1035.
9. Mohandas N, Evans E (1994) Mechanical properties of the red cell membrane in relation to molecular structure and genetic defects. *Annu Rev Biophys Biomol Struct* 23:787–818.
10. Auth T, Safran SA, Gov NS (2007) Fluctuations of coupled fluid and solid membranes with application to red blood cells. *Phys Rev E Stat Nonlin Soft Matter Phys* 76:051910.
11. Tuvia S, et al. (1997) Cell membrane fluctuations are regulated by medium macroviscosity: Evidence for a metabolic driving force. *Proc Natl Acad Sci USA* 94:5045–5049.
12. Gov NS, Safran SA (2005) Red blood cell membrane fluctuations and shape controlled by atp-induced cytoskeletal defects. *Biophys J* 88:1859–1874.
13. Manno S, Takakuwa Y, Mohandas N (2005) Modulation of erythrocyte membrane mechanical function by protein 4.1 phosphorylation. *J Biol Chem* 280:7581–7587.
14. Gogler M, Betz T, Kas JA (2007) Simultaneous manipulation and detection of living cell membrane dynamics. *Opt Lett* 32:1893–1895.
15. Neuman KC, Block SM (2004) Optical trapping. *Rev Sci Instrum* 75:2787–2809.
16. Milner ST, Safran SA (1987) Dynamical fluctuations of droplet microemulsions and vesicles. *Phys Rev A* 36:4371–4379.
17. Lee JC, Discher DE (2001) Deformation-enhanced fluctuations in the red cell skeleton with theoretical relations to elasticity, connectivity, and spectrin unfolding. *Biophys J* 81:3178–3192.
18. Cokelet GR, Meiselman HJ (1968) Rheological comparison of hemoglobin solutions and erythrocyte suspensions. *Science* 162:275–277.
19. Gov N, Zilman AG, Safran S (2004) Hydrodynamics of confined membranes. *Phys Rev E Stat Nonlin Soft Matter Phys* 70:011104.
20. Fournier JB, Lacoste D, Raphael E (2004) Fluctuation spectrum of fluid membranes coupled to an elastic meshwork: Jump of the effective surface tension at the mesh size. *Phys Rev Lett* 92:018102.
21. Mizuno D, Tardin C, Schmidt CF, Mackintosh FC (2007) Nonequilibrium mechanics of active cytoskeletal networks. *Science* 315:370–373.
22. Martin P, Hudspeth AJ, Julicher F (2001) Comparison of a hair bundle's spontaneous oscillations with its response to mechanical stimulation reveals the underlying active process. *Proc Natl Acad Sci USA* 98:14380–14385.
23. Gov N, Safran SA (2004) Pinning of fluid membranes by periodic harmonic potentials. *Phys Rev E Stat Nonlin Soft Matter Phys* 69:011101.
24. Ohanian V, et al. (1984) Analysis of the ternary interaction of the red cell membrane skeletal proteins spectrin, actin, and 4.1. *Biochemistry* 23:4416–4420.
25. Li J, Lykotrafitis G, Dao M, Suresh S (2007) Cytoskeletal dynamics of human erythrocyte. *Proc Natl Acad Sci USA* 104:4937–4942.
26. Gov NS (2007) Active elastic network: Cytoskeleton of the red blood cell. *Phys Rev E Stat Nonlin Soft Matter Phys* 75:011921.
27. Johnson CP, Tang HY, Carag C, Speicher DW, Discher DE (2007) Forced unfolding of proteins within cells. *Science* 317:663–666.
28. Stankewich MC, et al. (1998) A widely expressed betaiii spectrin associated with golgi and cytoplasmic vesicles. *Proc Natl Acad Sci USA* 95:14158–14163.
29. Tolic-Norrelykke SF, et al. (2006) Calibration of optical tweezers with positional detection in the back focal plane. *Rev Sci Instrum* 77:103101–103111.

Supporting Information

Betz et al. 10.1073/pnas.0904614106

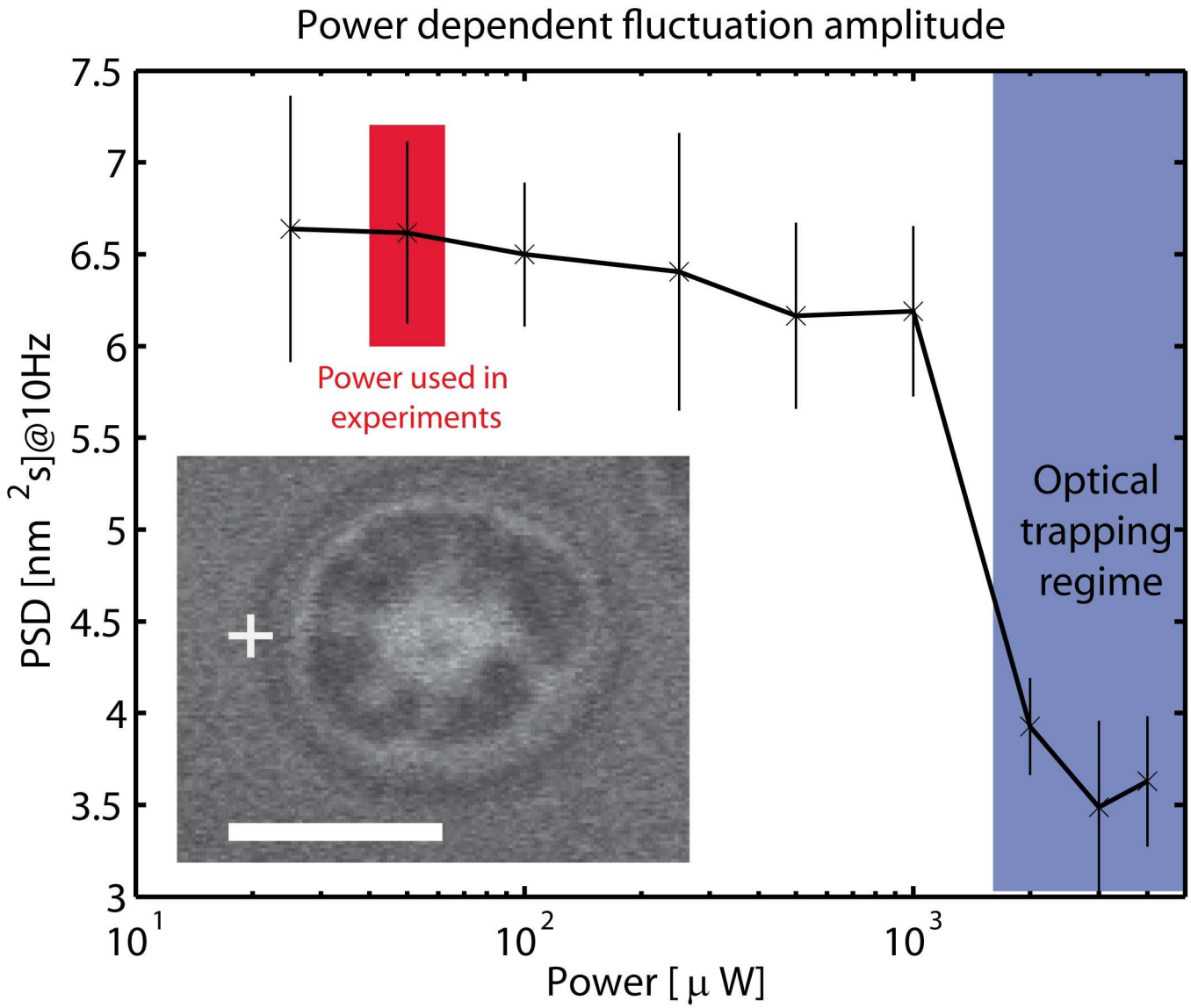

Fig. S1. PSD at 10 Hz as a function of the laser power. Up to 1 mW, the variation in the PSD is within the error, and is hence not significant. At ≈1 mW, the pulling force of the laser becomes important, which is reflected in the plot as a strong decrease of the signal, because of the increase of membrane tension whereas pulling of the RBC. (*Inset*) RICM image of a RBC showing a slight attachment, without a change of the biconcave shape. (Scale bar, 5 μm.)

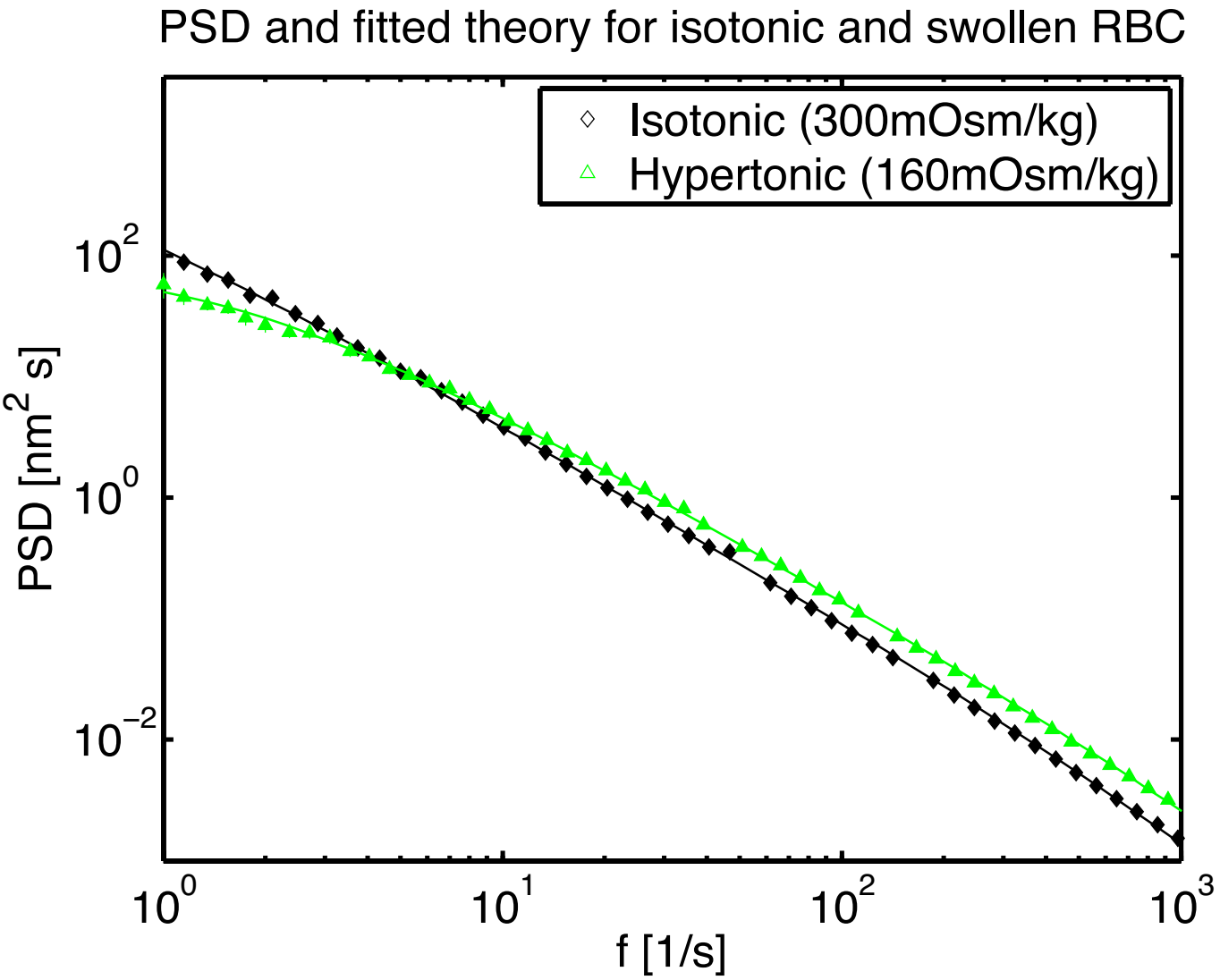

Fig. S2. To confirm the expected change of the PSD in osmotically swollen RBC, we merged the cells in a hypotonic medium with an osmolality of 160 mOsm/kg. In the osmotically swollen cells, the tension increased from normal tension: $\sigma_N = 6.5 \pm 2.1 \times 10^{-7}$N/m to swollen tension: $\sigma_s = 24.2 \pm 4.2 \times 10^{-7}$N/m. The internal viscosity was decreased from $\eta_N = 81 \pm 3.7 \times 10^{-3}$ Pa s to $\eta_s = 42 \pm 1.7 \times 10^{-3}$ Pa s consistent with the influx of water. The bending rigidity was almost unchanged between the normal cells $\kappa_N = 2.8 \pm 0.3 \times 10^{-19}$J and the swollen cells $\kappa_s = 2.4 \pm 0.3 \times 10^{-19}$J. These results further support our analysis method, as they yield the expected results of osmotic swelling.

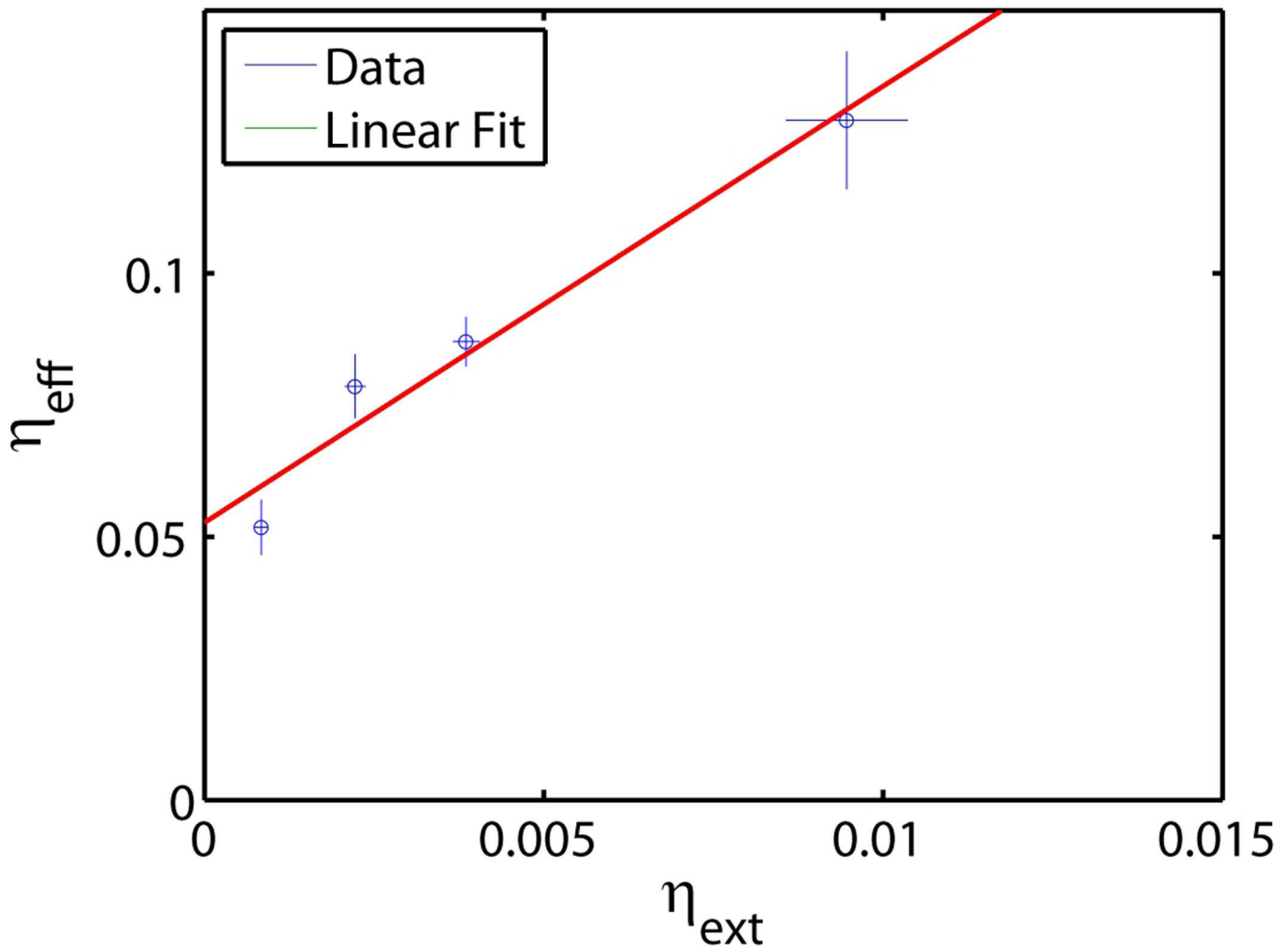

Fig. S3. Measured effective viscosity η_{eff} plotted as a function of the external viscosity η_{ext}. This phenomenological plot can be fitted by a simple linear function $\eta_{eff} = a \times \eta_{ext} + b$, yielding fit parameters of $a = 8.3 \pm 2.3$ and $b = 53 \pm 11 \times 10^{-3}$Pa s.

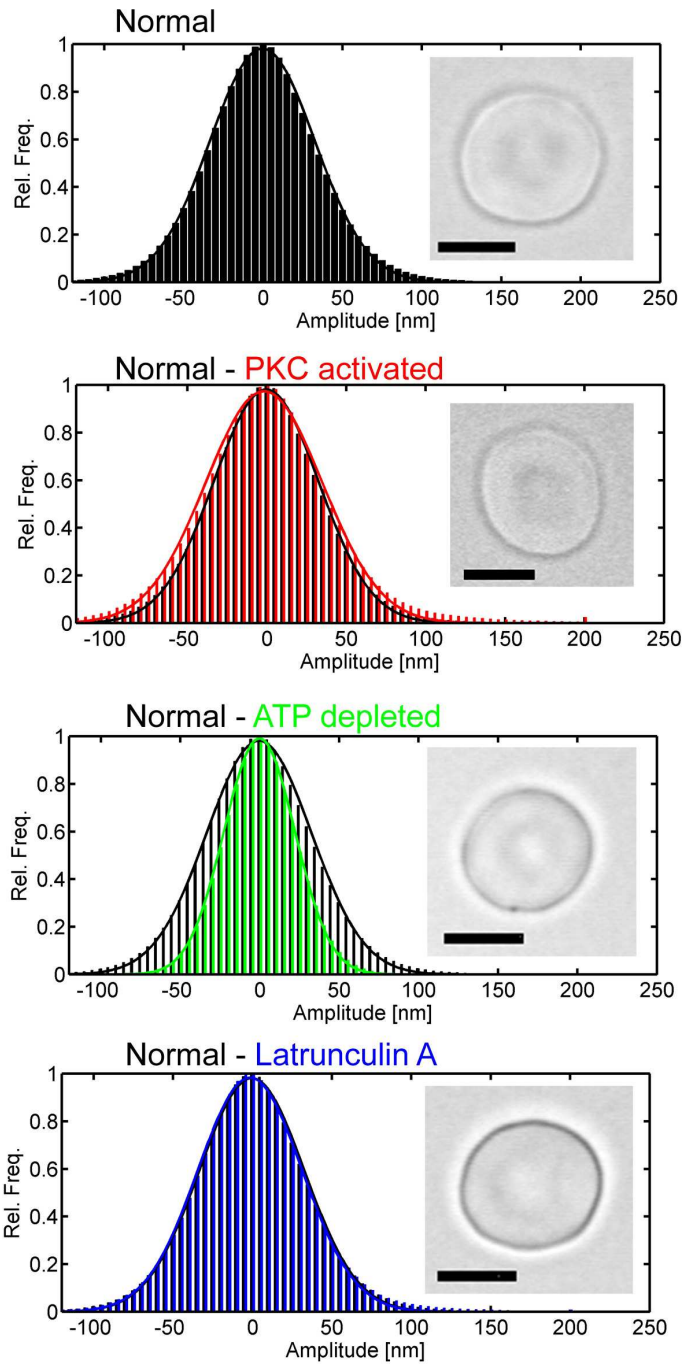

Fig. S4. Fluctuation amplitude histograms of normal (black), ATP-depleted (green), PKC-activated (red) and latrunculin A (blue)-treated cells. Straight lines present Gaussian fits of the respective histogram. The data shows that ATP-depleted cells have a significantly smaller fluctuation amplitude, whereas the fluctuations of PKC and LA-treated cells are similar.

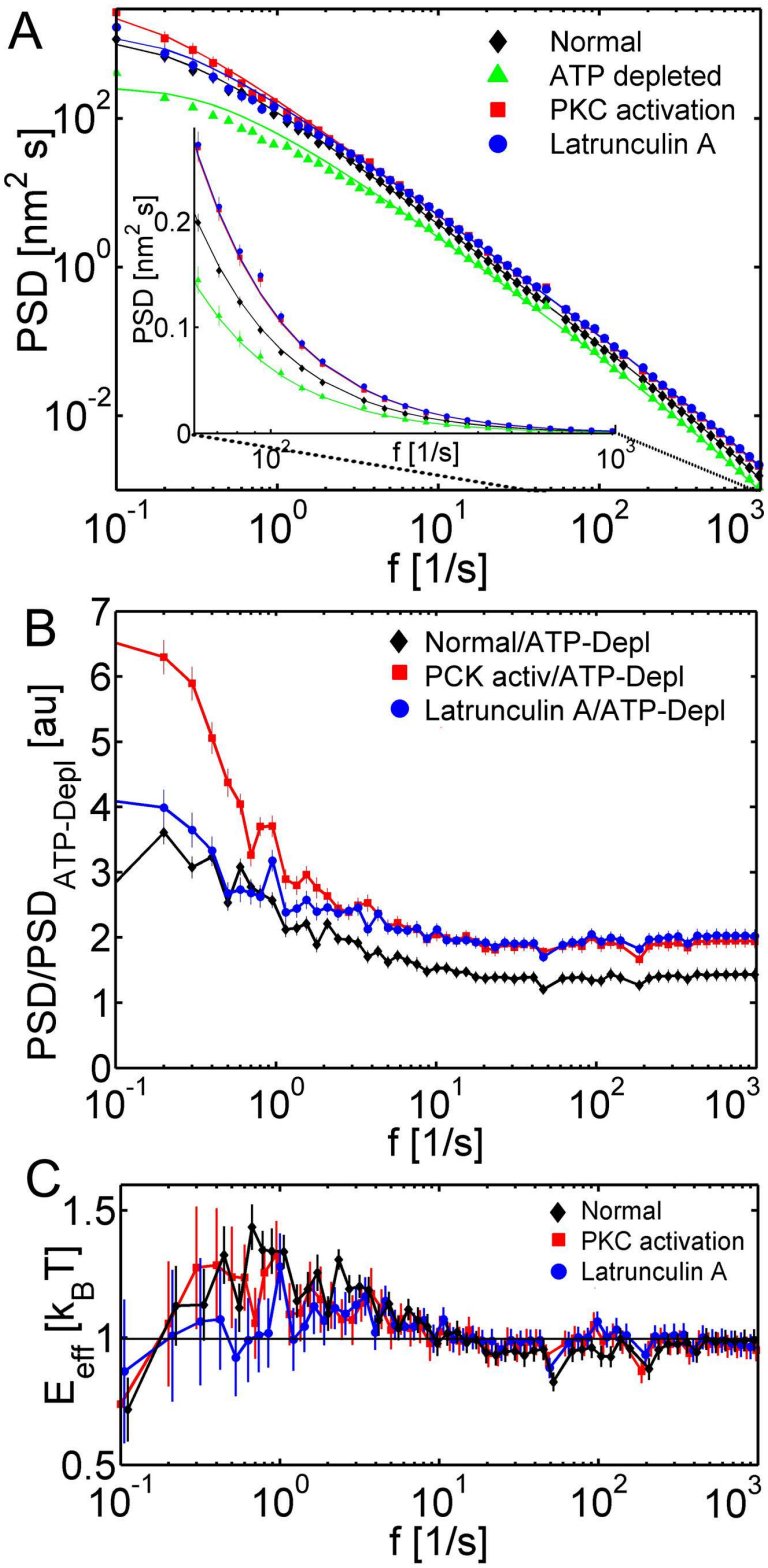

Fig. S5. Plots of the PDS as shown in Fig. 3 *A* and *B* and Fig. 4*A*, but including the data for the latrunculin A treated cells.

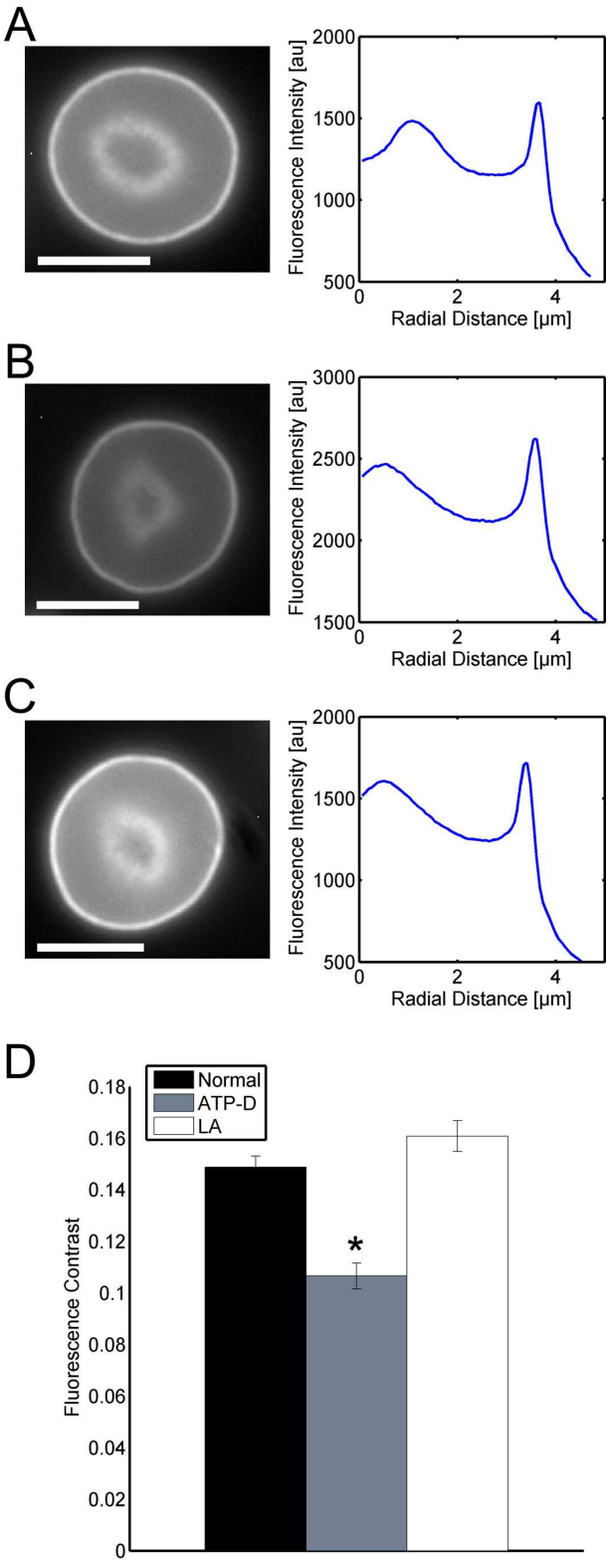

Fig. S6. (*A*) Fluorescence image of an F-actin stained normal RBCs. The radial intensity line as presented in the plot is averaged >100 center edge intensities. The contrast is determined by $c = M-m/(M + m)$, where M and m are the peak intensity at the rim and the minimal intensity in the cell, respectively. (*B*) Same as *A*, but for an ATP-depleted cell. (*C*) Same as *A*, but for a LA-treated cell. (*D*) Resulting contrast values for each 20 cells, giving a significantly reduced contrast in the ATP-depleted cells.

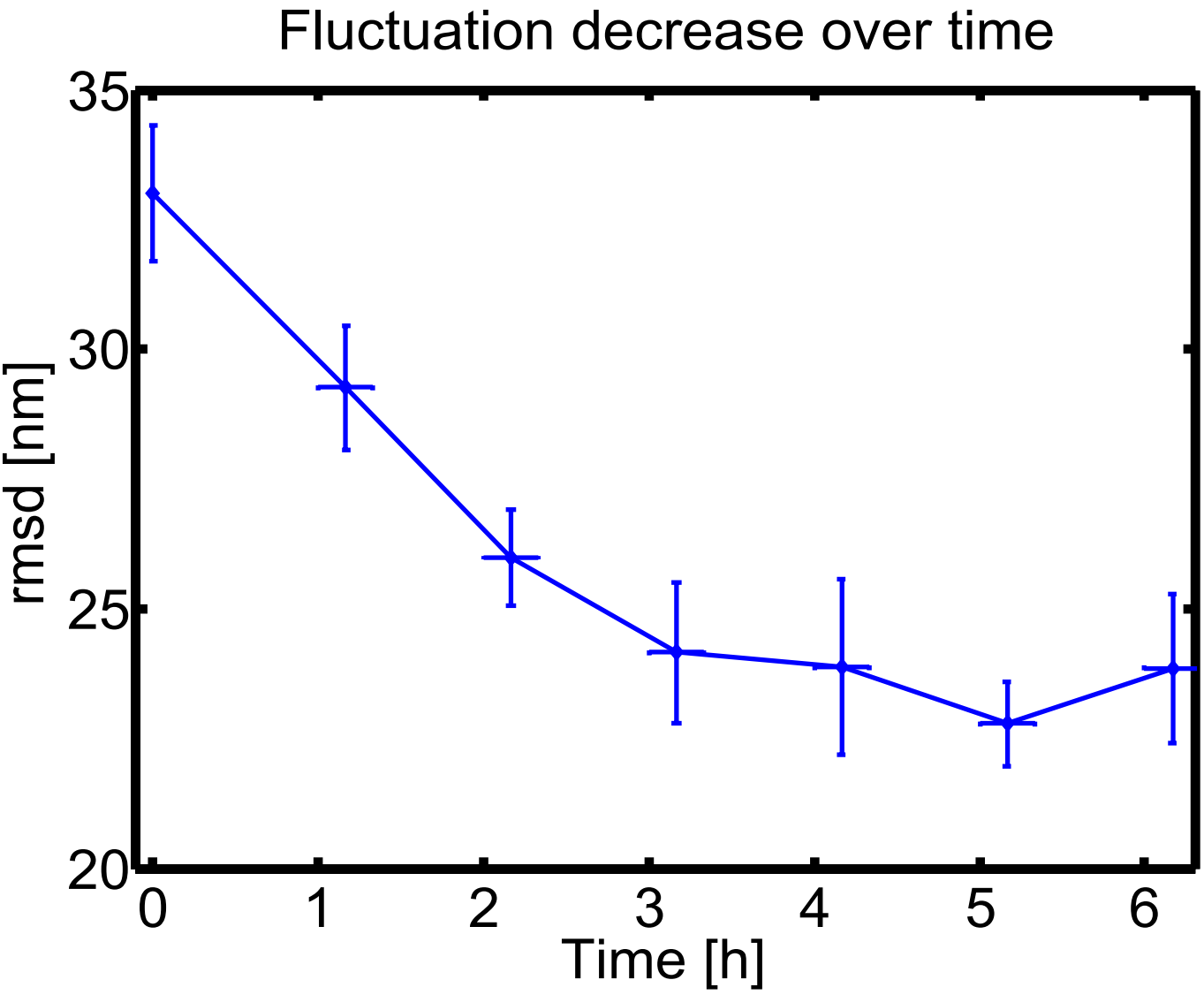

Fig. S7. Kinetic study of ATP-depletion effect. Rmsd as a function of the time during which the ATP-depletion buffer is applied. Each datapoint represents ≈50 experiments on usually 10 different cells. It should be noted that after 1 h the cells start to slowly deviate from the circular geometry, and after 6 h, most cells have turned into echinocytes. For the data acquisition, round and slightly deformed cells were mixed, but echinocytes were excluded. We record already after 1 h a significant reduction in fluctuation amplitude measured by the rmsd. After 3 h this reduction levels out, and after 6 h the measurement becomes impossible because almost all cells have deformed into echinocytes.

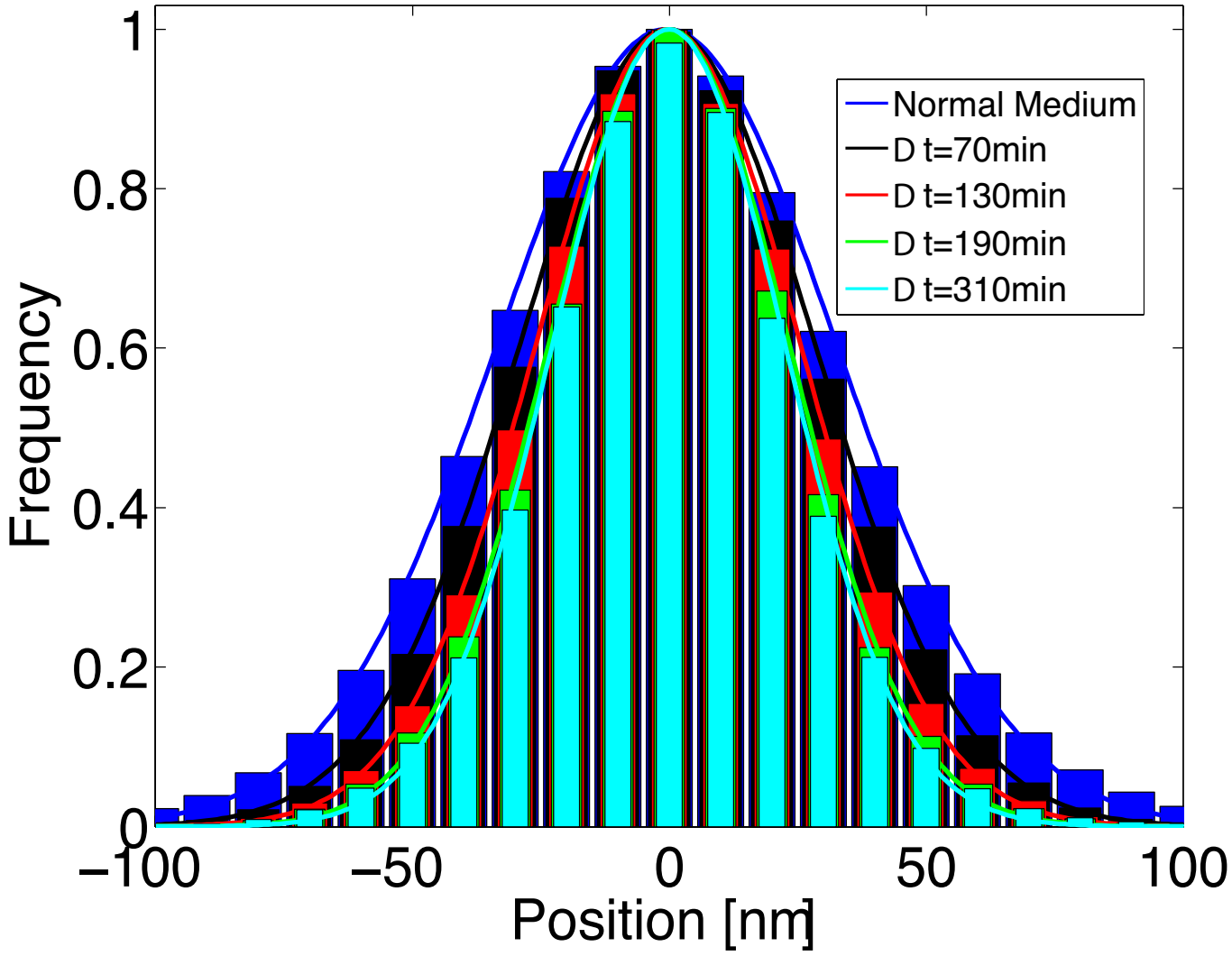

Fig. S8. Histogram of the edge fluctuation for the each ATP-depletion buffer application time. The figure overlays five time points, showing a steady decrease in fluctuation amplitude over time. All histograms represent the overlay of the ≈50 experiment at the given time of incubation (see legend). The histograms are well fitted by a Gaussian distribution.

Table S1. Collection of mechanical parameters of RBCs under various conditions, including the gamma term in the fit function

	Normal	ATP-depl.	PKC	LA
$rmsd_{ex}$ [nm]	33.0 ± 1.3	22.3 ± 0.6	36.7 ± 2.8	32.8 ± 2.2
κ^{stat} [10^{-19}J]	2.8 ± 0.3	6.1 ± 0.6	2.3 ± 0.2	2.8 ± 0.3
κ^{dyn} [10^{-19}J]	2.9 ± 0.3	3.9 ± 0.3	2.6 ± 0.2	2.7 ± 0.2
σ [10^{-7} N/m]	6.5 ± 2.1	19 ± 1	2.7 ± 1.1	4.7 ± 1.0
η_{eff} [10^{-3}Pa s]	81 ± 3.7	118 ± 11.7	57 ± 2.4	55 ± 4.0
γ [10^{-8}Jm^{-4}]	0.06 ± 0.04	4.9 ± 2	5.2 ± 2.0	6.6 ± 5.9

Other Supporting Information Files

SI Appendix (PDF)

ATP dependent mechanics of red blood cells – Betz *et al.*

Supplementary Information

1 Supplemental Information: Calculations

The power spectral density (PSD) was computed using Matlab as the square of the Fast Fourier Transform (FFT) of the recorded time series y:

$$Y = FFT(y) \tag{1}$$

$$PSD = \frac{Y \times Y^*}{ps}. \tag{2}$$

Here, Y^* denotes the complex conjugate of Y, p is the number of data points in y, and s is the sampling rate of y in Hz. Each value of the PSD corresponds to a frequency f spanning from 0 to the Nyquist frequency $s/2$ with an increment of $\Delta f = s/p$.

To extract the mechanical parameters, the recorded PSDs were fitted by a theoretical expression that is based on the classical Helfrich analysis (1). In the present study we extended previous results from flat membranes (2; 3) to spherical harmonics using expressions derived by Safran and Milner (4).

Plane Membranes The energy of a plane membrane fluctuation is described by a free energy functional:

$$F = \int \mathrm{d}A \left[\frac{1}{2}\kappa \left(\nabla^2 h\right)^2 + \frac{1}{2}\sigma(\nabla h)^2 \right], \tag{3}$$

where h is the extension of the membrane from its equilibrium position and the integral sums over the whole surface. Using the equipartition theorem the correlation function for the fluctuation reads:

$$\langle h_{\mathbf{q}} h_{\mathbf{q}'} \rangle = \frac{k_\mathrm{B}T}{\kappa q^4 + \sigma q^2}(2\pi)^2 \delta(\mathbf{q} + \mathbf{q}'), \tag{4}$$

A fluctuations of wavelength q relaxes at a rate $\omega(q) = (\kappa q^4 + \sigma q^2)/(4\eta q)$ for a impermeable membrane (5; 6), where η is the mean viscosity of the two fluids separated by the membrane. This yield the time dependent correlation function:

$$\langle h_q(t) h_{q'}(0) \rangle = (2\pi)^2 \delta(\mathbf{q} + \mathbf{q}') \langle h_q h_{q'} \rangle \exp[-\omega(q)t]. \tag{5}$$

Taking the Fourier transform and integrating over all q modes yields the PSD for a flat membrane:

$$PSD = \int \frac{\mathrm{d}^2\mathbf{q}}{(2\pi)^2} \int_{\infty}^{-\infty} \langle h_q(t) h_{-q}(0) \rangle \exp(i\omega t) \mathrm{d}t \tag{6}$$

$$= \frac{1}{\pi} \int_{0}^{-\infty} q \mathrm{d}q \langle h_q h_{-q} \rangle \frac{\omega(q)}{\omega(q)^2 + \omega^2} \tag{7}$$

$$= \frac{4\eta k_\mathrm{B}T}{\pi} \int \frac{\mathrm{d}q}{(\kappa q^3 + \sigma q)^2 + (4\eta\omega)^2}. \tag{8}$$

In the limiting cases of high and low frequency we find $PSD \underset{\omega\to\infty}{=} \frac{k_\mathrm{B}T}{12\pi(2\eta^2\kappa)^{1/3}\omega^{5/3}}$ and $PSD \underset{\omega\to 0}{=} \frac{k_\mathrm{B}T}{4\sigma\omega}$. It was suggested in Ref. (3) to include an additional term that reflects an elastic coupling between the membrane and the spectrin network , that extends Eq 3 as:

$$F = \int \mathrm{d}A \left[\frac{1}{2}\kappa\left(\nabla^2 h\right)^2 + \frac{1}{2}\sigma(\nabla h)^2 + \frac{1}{2}\gamma h^2\right], \tag{9}$$

where γ is harmonic coupling constant. This additional term changes the PSD expression to (3):

$$PSD = \frac{4\eta k_\mathrm{B}T}{\pi}\int_0^{-\infty} \frac{\mathrm{d}q}{(\kappa q^3 + \sigma q + \gamma/q)^2 + (4\eta\omega)^2}. \tag{10}$$

Spherical harmonics description The integral [8] is divergent in $\omega \to 0$. This is due to the fact that a flat membrane has fluctuations divergent in its size. In practice, this is limited by the finite size of the RBC which we take into account using spherical harmonics. This is an extension of previous work (4):

$$r(\Omega) = R(1 + \sum_{l,m} u_{lm} Y_{lm}(\Omega)), \tag{11}$$

where Ω is the solid angle, R is the mean radius of the sphere and Y_{lm} are the spherical harmonics (4). This expression leads to the mean squared amplitude for each fluctuation mode:

$$\langle |u_{lm}|^2 \rangle = \frac{k_\mathrm{B}T}{\kappa(l+2)(l-1)l(l+1) + \sigma R^2(l+2)(l-1)}. \tag{12}$$

As before we write the autocorrelation function:

$$\langle u_{lm}(t) u_{l'm'}(0)\rangle = \delta_{l,l'}\delta_{m,m'}\langle |u_{lm}|^2\rangle \exp(-\omega_l t), \tag{13}$$

where:

$$\omega_l = \frac{\kappa(l+2)(l-1)l(l+1) + \sigma R^2(l+2)(l-1)}{\eta R^3 Z(l)}, \tag{14}$$

with $Z(l) = \frac{(2l+1)(2l^2+2l-1)}{l(l+1)}$. Similar to the case of plane membranes, the Fourier transform of Eq. [13] yields the PSD as:

$$PSD = \int \mathrm{d}t \sum_{l=2,m=-l} \langle |u_{lm}|^2\rangle \exp(-\omega_l t)\exp(i\omega t) \tag{15}$$

$$= \sum_{l=2} \langle |u_{lm}|^2\rangle \frac{\omega_l}{\omega_l^2 + \omega^2}\frac{2l+1}{2\pi}. \tag{16}$$

This expression was used to fit the measured data in order to get the mechanical parameters κ and σ. The radius R is the average radius of all cells represented in the experimental data set, and the sum was evaluated numerically.

As used for the rescaling in the main text, we separate this expression into the energy source exiting the fluctuations (which we call effective energy $E_{eff}(f)$ in the general case). For the ATP-depleted cells we know that the system is purely passive, and hence we can identify $E_{eff}^{ATP-D} = k_\mathrm{B}T$. We write the PSD as product of the energy driving the fluctuations and a term describing the mechanics of the RBC:

$$PSD = E_{eff} \times g(\sigma, \kappa, \eta; f), \tag{17}$$

where:

$$g(\sigma,\kappa,\eta;f)=\sum_{l=2}\frac{1}{\kappa(l+2)(l-1)l(l+1)+\sigma R^2(l+2)(l-1)} \times\frac{\omega_l}{\omega_l^2+\omega^2}\frac{2l+1}{2\pi}. \tag{18}$$

We rescale the relative amplitude implying the full measured mechanics, thus collapsing all curves onto a master curve. This can be understood by expressing the relative PSDs analytically, where in the passive ATP depleted case, the effective energy is known to be $k_{\mathrm{B}}T$:

$$\frac{PSD_{N,P,L}}{PSD_{ATP-D}}=\frac{E_{eff}(f)}{k_{\mathrm{B}}T}\times\frac{g^{ATP-D}(\sigma,\kappa,\eta;f)}{g^{N,P,L}(\sigma,\kappa,\eta;f)}, \tag{19}$$

where the membrane mechanics are collected in the sum of function g. Hence, the frequency dependent effective energy $E_{eff}(f)$ in units of $k_{\mathrm{B}}T$:

$$\frac{E_{eff}(f)}{k_{\mathrm{B}}T}=\frac{PSD_{N,P,L}}{PSD_{ATP-D}}\times\frac{g^{N,P,L}(\sigma,\kappa,\eta;f)}{g^{ATP-D}(\sigma,\kappa,\eta;f)}. \tag{20}$$

As in the case of the infinite plane membrane, we extend the spherical harmonics expression of the PSD to include the harmonic membrane-spectrin interaction introduced in Ref. (3). This changes $\langle|u_{lm}|^2\rangle$ to:

$$\langle|u_{lm}|^2\rangle=\frac{k_{\mathrm{B}}T}{\kappa(l+2)(l-1)l(l+1)+\sigma R^2(l+2)(l-1)+\gamma R^4} \tag{21}$$

and the decay frequency ω_l:

$$\omega_l=\frac{\kappa(l+2)(l-1)l(l+1)+\sigma R^2(l+2)(l-1)+\gamma R^4}{\eta R^3 Z(l)}. \tag{22}$$

2 Supplemental Information: Viscosity correction

Since theory predicts that the effective viscosity should be the average of the internal and external viscosities

$$\eta_{eff}=1/2(\eta_{RBC}+\eta_{ext}) \tag{23}$$

we varied the external viscosity as presented in the results section. According to theory, η_{eff} should linearly increase with a slope of $1/2$ if plotted over the external viscosity η_{ext}. Our data, however, shows a slope of $a=8.3\pm2.3$ (SI-Fig S2) if fitted by a linear function. This experimental observation is thus inconsistent with the theory. From an phenomenological point of view, one may fix this by introducing a prefactor $\alpha=16.6\pm4.6$ which modifies the expression of the effective viscosity to:

$$\eta_{eff}=\alpha/2(\eta_{RBC}+\eta_{ext}). \tag{24}$$

Interestingly, applying this *ad hoc* modification allows to extract a corrected RBC viscosity $\eta^{\alpha}_{RBC}=6.4\pm1.9$ Pa s, which is consistent with previous measured values (7).

References

[1] Helfrich, W (1973) Elastic properties of lipid bilayers: theory and possible experiments. *Z Naturforsch C* 28:693–703.

[2] Helfer, E et al. (2001) Viscoelastic properties of actin-coated membranes. *Phys Rev E Stat Nonlin Soft Matter Phys* 63:021904.

[3] Gov, N, Zilman, AG, Safran, S (2003) Cytoskeleton confinement and tension of red blood cell membranes. *Phys Rev Lett* 90:228101.

[4] Milner, ST, Safran, SA (1987) Dynamical fluctuations of droplet microemulsions and vesicles. *Phys Rev A* 36:4371–4379.

[5] Prost, J, Manneville, JB, Bruinsma, R (1998) Fluctuation-magnification of non-equilibrium membranes near a wall. *The European Physical Journal B - Condensed Matter and Complex Systems* 1:465–480.

[6] Seifert, U (1994) Dynamics of a bound membrane. *Phys Rev E Stat Phys Plasmas Fluids Relat Interdiscip Topics* 49:3124–3127.

[7] Cokelet, GR, Meiselman, HJ (1968) Rheological comparison of hemoglobin solutions and erythrocyte suspensions. *Science* 162:275–7.

A Reaction-Diffusion Model of the Cadherin-Catenin System: A Possible Mechanism for Contact Inhibition and Implications for Tumorigenesis

Markus Basan,[†] Timon Idema,[‡] Martin Lenz,[†*] Jean-François Joanny,[†] and Thomas Risler[†]
[†]Laboratoire Physico-Chimie Curie, CNRS-UMR 168, Université Pierre et Marie Curie Paris VI, Institut Curie Centre de Recherche, Paris, France; and [‡]Instituut-Lorentz for Theoretical Physics, Leiden Institute of Physics, Leiden University, Leiden, The Netherlands

ABSTRACT Contact inhibition is the process by which cells switch from a motile growing state to a passive and stabilized state upon touching their neighbors. When two cells touch, an adhesion link is created between them by means of transmembrane E-cadherin proteins. Simultaneously, their actin filaments stop polymerizing in the direction perpendicular to the membrane and reorganize to create an apical belt that colocalizes with the adhesion links. Here, we propose a detailed quantitative model of the role of cytoplasmic β-catenin and α-catenin proteins in this process, treated as a reaction-diffusion system. Upon cell-cell contact the concentration in α-catenin dimers increases, inhibiting actin branching and thereby reducing cellular motility and expansion pressure. This model provides a mechanism for contact inhibition that could explain previously unrelated experimental findings on the role played by E-cadherin, β-catenin, and α-catenin in the cellular phenotype and in tumorigenesis. In particular, we address the effect of a knockout of the adenomatous polyposis coli tumor suppressor gene. Potential direct tests of our model are discussed.

INTRODUCTION

Before the establishment of cell-cell contacts, epithelial cells are in a motile and growing state. The polymerizing actin filaments create forces on the membrane that are responsible for the formation of lamellipodia and filopodia (1,2). Moreover, the actin filaments undergo continuous branching and growth resulting in dynamic extensions of the membrane (3). When cells are scarce and do not contact each other, E-cadherins are found both on the plasma membrane and in membrane vesicles within the cytoplasm, but their role is minimal: when located on the membrane, they quickly get endocytosed into cytoplasmic vesicles (4). After they have grown enough to cover the substrate in a confluent layer, epithelial cells become polarized perpendicular to the substrate. At this point, they no longer produce lamellipodia and filopodia, but instead reorganize their actin into a belt located near their apical side (see Fig. 1 *A*) (5). Simultaneously, the E-cadherins located in the plasma membrane link their extracellular domains with the cadherins of the neighboring cells and colocalize with the actin belt, forming what is known as the adhesion zone. The linkage of E-cadherins stabilizes their localization on the plasma membrane, effectively depleting them from the cytoplasm (4,6).

The reorientation of the actin filaments upon cell-cell contact indicates a reduced activity of branching proteins such as Actin-related proteins 2 and 3 (Arp2/3) and an increased activity of bundling proteins such as α-catenin dimers (see Fig. 1 *B*). When oriented parallel to it, the growing actin filaments no longer exert a force on the plasma membrane. Therefore, the cell downregulates both its motility and expansion pressure in response to reaching confluence, a process referred to as contact inhibition.

In 2005, Drees et al. (7) challenged the textbook view that α-catenin mechanically links the adhesion complex to the underlying actin cytoskeleton. They showed that α-catenin exists either as a monomer or as a dimer, and that the domain on an α-catenin monomer that binds to β-catenin overlaps with the domain that binds to another α-catenin monomer. Therefore, the formations of α-catenin dimers and α-catenin-β-catenin complexes are mutually exclusive (8). Dimeric α-catenin can bundle actin filaments and competes for actin binding sites with Arp2/3. According to these findings, a high concentration of α-catenin dimers therefore suppresses actin branching, growth, and expansion pressure (see reviews (9,10) and Fig. 1 *B*).

A loss of contact inhibition via epithelial-mesenchymal transition is an essential step for tumorigenesis (11). It has recently been proposed that an excess expansion pressure could be a characteristic trait of neoplastic tissues (12). A breakdown of the regulation mechanism discussed above might therefore lead to tumorigenesis. It is indeed well-known that the E-cadherin-β-catenin-α-catenin adhesion complex plays an important role in carcinomas (13,14). A reduced expression of E-cadherins—for example, due to DNA hypermethylation—is associated with a loss of cellular polarity and the acquisition of invasive characteristics (15). However, it has been shown that overexpression and reduced degradation of β-catenins also leads to cellular transformations that result in the cell's ability to grow in soft agarose gels and to overproliferate at high cell densities (16). Along the same lines, in cells that have undergone the epithelial-mesenchymal transition, E-cadherin expression is downregulated, whereas the production of β-catenin is increased (17). It has also been shown that the growth-inhibiting activity of E-cadherin is counteracted by an increased β-catenin activity (18). Finally, the concentration of β-catenins is regulated by the adenomatous polyposis coli (APC) protein,

Submitted October 26, 2009, and accepted for publication March 9, 2010.
*Correspondence: martin.lenz@curie.fr
Editor: Douglas Nyle Robinson.

0006-3495/10/06/2770/10 $2.00
doi: 10.1016/j.bpj.2010.03.051

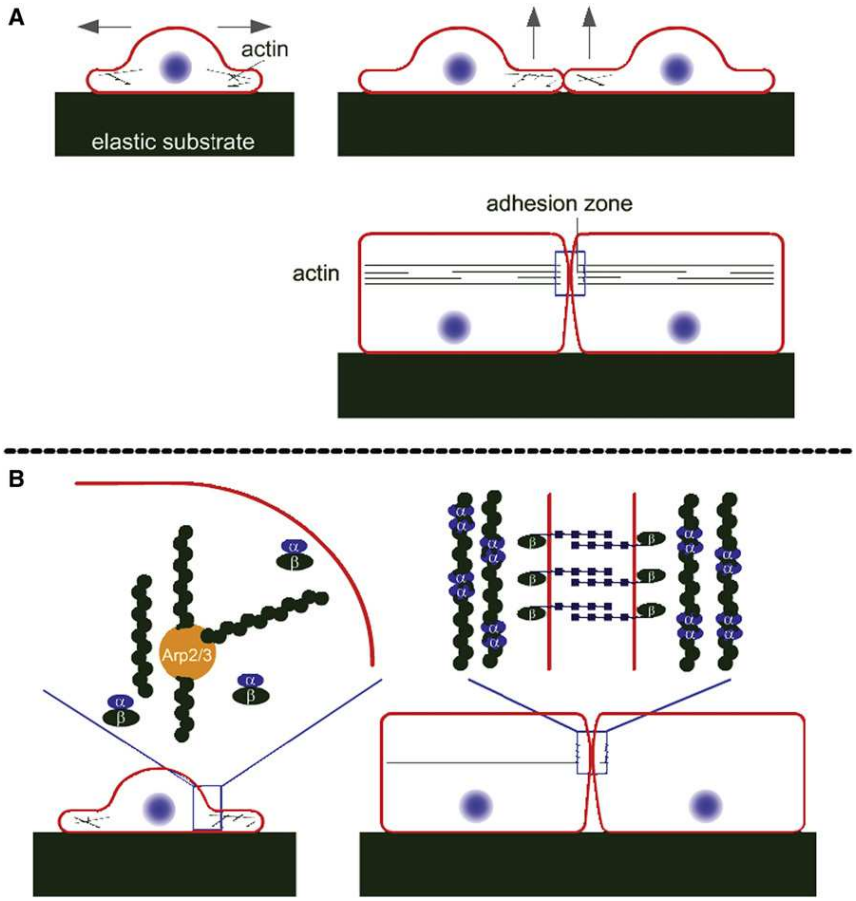

FIGURE 1 (*A*) Schematic illustration of the establishment of the epithelial cell-cell adhesion zone. After cells have spread via protrusions along the substrate and become confluent, they start growing upward and colocalize their actin belt while forming the adhesion zone. (*B*) Different organizations of cortical actin, α-catenin, and β-catenin-related complexes in epithelial cells during their spreading (*left*) and after the mature epithelial sheet is formed (*right*). Before cell-cell contact, β-catenin-E-cadherin complexes are present in the cytoplasm and therefore recruit α-catenin proteins before they can form dimers, which allows Arp2/3 complexes to branch the actin network. In the presence of a neighboring cell, however, β-catenin-E-cadherin complexes are mostly found at the cell membrane, a situation that favors the formation of α-catenin dimers in the cytoplasm. These dimers further bind strongly to actin, effectively excluding Arp2/3 complexes from the actin network and favoring parallel bundling.

a tumor suppressor protein that is known to label β-catenin for degradation (19). On the other hand, β-catenin-null cells show an unaffected or even decreased rate of expansion and proliferation (20,21). The important role of E-cadherin and β-catenin in the progression of cancer has been well studied, and several articles report that loss of α-catenin is an important prognostic factor for cancer, as reviewed in Benjamin and Nelson (22). For example, the ablation of α-catenin in the skin causes cellular hyperproliferation, occurrence of mitoses away from the basal layer, and defects in epithelial polarity (23). These phenotypes are remarkably similar to those obtained with a modified expression level of E-cadherin or β-catenin proteins.

Although there are strong indications that the influence of α-catenin on actin polymerization plays a role in contact inhibition, the functional details of this mechanism remain unclear. Important progress has been made in this direction by Drees and co-workers (7,8), who propose a picture in which cell-cell contact leads to an accumulation of E-cadherin-β-catenin-α-catenin complexes at the adhesion sites. They propose that the release of α-catenin monomers from these complexes into the cytoplasm provides an increase in α-catenin dimer concentration, favoring actin bundling and downregulating actin assembly and branching. In this work, we propose a model for the E-cadherin-β-catenin-α-catenin function that is based on a reaction-diffusion system. We show that the interplay between these three proteins results in a pathway for contact inhibition that downregulates actin polymerization in response to cell-cell contact.

Our mechanism relies on the fact that the binding of β-catenin to α-catenin limits α-catenin dimerization in the cytosol. When β-catenin-E-cadherin complexes are recruited to the cell membrane due to cell-cell contact, the cytosolic concentration of β-catenin drops, and α-catenin dimerization can take place. According to the work by the Nelson and Weis group (7), this in turn prevents Arp2/3-based actin branching and causes the cell to enter a quiescent state. Using the framework of our physical model, we investigate the effect of disruptions of this pathway and obtain results that are consistent with experimentally observed cellular transformations that lead to tumorigenesis.

RESULTS

Description

The mechanism of the pathway we propose is schematically illustrated in Fig. 2. Its main feature is that α-catenin-β-catenin binding competes with α-catenin dimerization: At high cytosolic concentrations of β-catenins, the majority of α-catenins enter α-catenin-β-catenin complexes. At low cytosolic

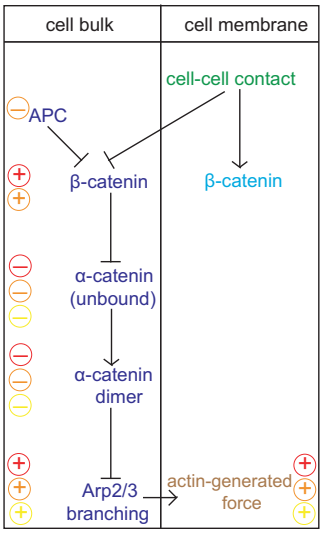

FIGURE 2 Schematic illustration of the proposed cadherin-catenin pathway for contact inhibition, as well as possible disruptions of the pathway. Arrows and T-bars between the different genes, proteins, or cell states of the diagram indicate induction and repression, respectively. Minus and plus signs of different colors illustrate how various events can lead to a breakdown of this pathway: reduced expression of E-cadherins (*red, upper signs*), mutation of the APC tumor suppressor gene (*orange, middle signs*), and reduced expression or mutations of α-catenin (*yellow, lower signs*). Minus signs indicate either decreased concentrations or complete impairment of the associated proteins, and plus signs indicate increased concentrations compared with the healthy cell state.

concentrations of β-catenins, however, α-catenins form dimers almost exclusively (7). Therefore, the organization and activity of the actin cortex of the cell depends on the presence of a neighboring cell according to the following mechanism. It is known that β-catenin quickly binds to E-cadherin after production at the Golgi apparatus of the cell (24). When the cell is in its growth phase, E-cadherin-β-catenin complexes are mostly found in vesicles in the cytoplasm (4), effectively creating a large concentration of β-catenin complexes in the cytosol. These complexes further recruit most of the α-catenin monomers that are present in the cytoplasm, leaving actin binding sites free for Arp2/3 complexes to bind. The structure of the actin cortex is therefore branched, and its activity is high. In contrast, when contact with a neighboring cell is established, the E-cadherins bind to the neighboring cell and accumulate at the membrane, effectively lowering their concentration in the cytosol (25). Since a large fraction of E-cadherins is bound to β-catenins, the establishment of cell-cell contacts also induces a redistribution of β-catenins to the plasma membrane. Indeed, the potent ability of E-cadherin to recruit β-catenin to the cell membrane has been observed in vivo (26). This β-catenin redistribution to the plasma membrane in turn favors the formation of α-catenin dimers in the cytosol, which further favors actin bundling rather than actin branching and polymerization. Note that other protein complexes could play a role similar to that of E-cadherins and transport β-catenin proteins to the cell membrane upon cell-cell contact, as proposed recently (27). In any case, the cell switches from an active state with high actin branching and polymerization activity when there is no cell-cell contact to a passive state characterized by reduced actin activity after cell-cell contact has been established.

Model equations

To model the cadherin-catenin system described above in a quantitative manner, we write a system of reaction-diffusion equations for the cytosolic concentrations of the different proteins involved. (Note that although active transport of these proteins may be involved, we do not expect the mechanism presented in this article to depend crucially on this aspect.) In this model, we treat all protein bindings as irreversible because binding affinities are high (typically with energies of many k_BT (28)). Assuming that the protein production rates and the configuration of neighboring cells are constant in time, we can focus on the steady-state dynamics of the system, which for the cytosol of the cell can be written as

$$D_\alpha \nabla^2 C_\alpha - k_{\alpha\beta} C_\alpha C_\beta - 2\, k_{\alpha\alpha} C_\alpha^2 - r_\alpha C_\alpha = 0 \qquad (1a)$$

$$D_\beta \nabla^2 C_\beta - k_{\alpha\beta} C_\alpha C_\beta - r_\beta C_\beta = 0 \qquad (1b)$$

$$D_{\alpha\alpha} \nabla^2 C_{\alpha\alpha} + k_{\alpha\alpha} C_\alpha^2 - \left(r_{\alpha\alpha} + \tilde{r}_{\alpha\alpha}\right) C_{\alpha\alpha} = 0 \qquad (1c)$$

$$D_{\alpha\beta} \nabla^2 C_{\alpha\beta} + k_{\alpha\beta} C_\alpha C_\beta - r_{\alpha\beta} C_{\alpha\beta} = 0. \qquad (1d)$$

These equations describe the diffusion dynamics of α-catenin, β-catenin, α-catenin dimers, and α-catenin-β-catenin complexes, respectively, in the cytoplasm. Here, C_α, C_β, $C_{\alpha\alpha}$, and $C_{\alpha\beta}$ are the cytoplasmic protein concentrations of α-catenin monomers, β-catenin monomers (bound to cytosolic E-cadherins), α-catenin dimers, and α-catenin-β-catenin complexes (bound to cytosolic E-cadherins), respectively; D_α, D_β, $D_{\alpha\alpha}$, and $D_{\alpha\beta}$ are the associated diffusion constants and r_α, r_β, $r_{\alpha\alpha}$, and $r_{\alpha\beta}$ the associated degradation rates; $k_{\alpha\alpha}$ and $k_{\alpha\beta}$ are the rates of α-catenin dimerization and α-catenin-to-β-catenin binding, respectively; and $\tilde{r}_{\alpha\alpha}$ is the rate of reaction of α-catenin dimers with actin. Note that since most β-catenins bind to E-cadherins immediately after production (24), we do not explicitly model the reaction-diffusion dynamics of E-cadherins but instead account for its important effect on the redistribution of β-catenin-E-cadherin complexes in the boundary conditions at the plasma membrane, as shown below. Modeling the diffusion and reactions of E-cadherins and β-catenins separately adds another layer of complexity to our model but would not qualitatively change our main results. Therefore, when we refer to β-catenin in our model, we mean the E-cadherin-β-catenin complex. Note also that the effect of the Wnt signaling pathway on β-catenin is taken into account effectively in the bulk degradation rate of this protein.

Production of these proteins in the vicinity of the cell nucleus, as well as their interactions with the plasma membrane, needs to be accounted for using appropriate boundary conditions. The production of α-catenin and β-catenin in the Golgi apparatus of the cell is taken into account by fixed influxes of proteins into the cytoplasm, denoted by j_α^0 and j_β^0, respectively. On the membrane, the concentrations of protein complexes are $C_\beta^{\mathrm{m,d}}$, $C_\beta^{\mathrm{m,a}}$, $C_{\alpha\beta}^{\mathrm{m,d}}$, $C_{\alpha\beta}^{\mathrm{m,a}}$—all bound to E-cadherin proteins—which can be either detached or attached to an adjacent cell via E-cadherin-E-cadherin homophilic binding, as indicated by superscripts d and a. Cytoplasmic concentrations at the membrane, denoted by C_β^{b}, C_α^{b}, and $C_{\alpha\beta}^{\mathrm{b}}$, correspond to the respective concentrations introduced in Eq. 1 at this particular location. β-catenin and α-catenin-β-catenin complexes—both bound to E-cadherin proteins—can go to the plasma membrane of the cell, where they are then in the detached state. We denote by k_β^{on} and k_β^{off} $\left(k_{\alpha\beta}^{\mathrm{on}}\right.$ and $\left.k_{\alpha\beta}^{\mathrm{off}}\right)$ the rates at which the protein complex β-catenin-E-cadherin (α-catenin-β-catenin-E-cadherin) goes to the plasma membrane of the cell, and note that only complexes in the detached state can move from the membrane to the cytoplasm. The two fluxes, j_β and $j_{\alpha\beta}$, of β-catenin and α-catenin-β-catenin complexes from the cytoplasm to the plasma membrane of the cell then read

$$j_\beta = k_\beta^{\mathrm{on}} C_\beta^{\mathrm{b}} - k_\beta^{\mathrm{off}} C_\beta^{\mathrm{m,\,d}}, \tag{2a}$$

$$j_{\alpha\beta} = k_{\alpha\beta}^{\mathrm{on}} C_{\alpha\beta}^{\mathrm{b}} - k_{\alpha\beta}^{\mathrm{off}} C_{\alpha\beta}^{\mathrm{m,\,d}}. \tag{2b}$$

Monomeric α-catenins can only go to the plasma membrane by forming α-catenin-β-catenin complexes via a reaction with β-catenin complexes that are already located on the membrane (either in the attached or detached state). The rates of these reactions are denoted by $k_{\alpha\beta}^{\mathrm{m,\,a}}$ and $k_{\alpha\beta}^{\mathrm{m,\,d}}$, respectively. Once formed, these complexes do not release pure α-catenins anymore. α-catenin dimeric complexes, on the other hand, cannot go to the membrane, since they do not attach directly to E-cadherins, nor can they bind β-catenin-E-cadherin complexes, because to do so they need to be in their monomeric form. Their flux therefore vanishes. We finally get

$$j_\alpha = k_{\alpha\beta}^{\mathrm{m,d}} C_\beta^{\mathrm{m,d}} C_\alpha^{\mathrm{b}} + k_{\alpha\beta}^{\mathrm{m,a}} C_\beta^{\mathrm{m,a}} C_\alpha^{\mathrm{b}}, \tag{3a}$$

$$j_{\alpha\alpha} = 0. \tag{3b}$$

To solve our system of equations, we must combine these boundary conditions with the cytosolic protein diffusion equations (Eqs. 1a–1d), which we can do thanks to the definition of diffusive fluxes ($j_A = -D_A \nabla C_A$). To do so, we need to eliminate the membrane protein concentrations from our system of equations. This is done by writing the balance of protein complexes located on the plasma membrane of the cell. In addition to the reaction rates introduced above, we introduce the rate k_{A-B}^{EE} for a given complex A linked to an E-cadherin molecule to attach to another complex B of the adjacent cell via cross-membrane E-cadherin homophilic binding. Also, all complexes are degraded with their specific rates, $r_A^{\mathrm{m,\,d}}$ and $r_A^{\mathrm{m,\,a}}$, on the membrane. For simplicity, we assume a completely symmetric, identical configuration of the neighboring cell, and thus identical protein concentrations on the membrane of the adjacent cell. Taking all of this into account, the protein concentrations on the cell membrane are determined by the following steady-state equations, a schematic representation of which is presented in Fig. 3:

$$\begin{aligned} k_\beta^{\mathrm{on}} C_\beta^{\mathrm{b}} - k_\beta^{\mathrm{off}} C_\beta^{\mathrm{m,\,d}} - k_{\alpha\beta}^{\mathrm{m,\,d}} C_\beta^{\mathrm{m,\,d}} C_\alpha^{\mathrm{b}} - k_{\beta-\beta}^{\mathrm{EE}} \left(C_\beta^{\mathrm{m,\,d}}\right)^2 \\ - k_{\alpha\beta-\beta}^{\mathrm{EE}} C_\beta^{\mathrm{m,\,d}} C_{\alpha\beta}^{\mathrm{m,\,d}} - r_\beta^{\mathrm{m,\,d}} C_\beta^{\mathrm{m,\,d}} = 0, \end{aligned} \tag{4a}$$

$$\begin{aligned} k_{\alpha\beta}^{\mathrm{on}} C_{\alpha\beta}^{\mathrm{b}} - k_{\alpha\beta}^{\mathrm{off}} C_{\alpha\beta}^{\mathrm{m,\,d}} + k_{\alpha\beta}^{\mathrm{m,\,d}} C_\beta^{\mathrm{m,\,d}} C_\alpha^{\mathrm{b}} - k_{\alpha\beta-\alpha\beta}^{\mathrm{EE}} \left(C_{\alpha\beta}^{\mathrm{m,\,d}}\right)^2 \\ - k_{\alpha\beta-\beta}^{\mathrm{EE}} C_\beta^{\mathrm{m,\,d}} C_{\alpha\beta}^{\mathrm{m,\,d}} - r_{\alpha\beta}^{\mathrm{m,\,d}} C_{\alpha\beta}^{\mathrm{m,\,d}} = 0, \end{aligned} \tag{4b}$$

$$\begin{aligned} - k_{\alpha\beta}^{\mathrm{m,\,a}} C_\beta^{\mathrm{m,\,a}} C_\alpha^{\mathrm{b}} + k_{\beta-\beta}^{\mathrm{EE}} \left(C_\beta^{\mathrm{m,\,d}}\right)^2 + k_{\alpha\beta-\beta}^{\mathrm{EE}} C_\beta^{\mathrm{m,\,d}} C_{\alpha\beta}^{\mathrm{m,\,d}} \\ - r_\beta^{\mathrm{m,\,a}} C_\beta^{\mathrm{m,\,a}} = 0, \end{aligned} \tag{4c}$$

$$\begin{aligned} k_{\alpha\beta}^{\mathrm{m,\,a}} C_\beta^{\mathrm{m,\,a}} C_\alpha^{\mathrm{b}} + k_{\alpha\beta-\alpha\beta}^{\mathrm{EE}} \left(C_{\alpha\beta}^{\mathrm{m,\,d}}\right)^2 \\ + k_{\alpha\beta-\beta}^{\mathrm{EE}} C_\beta^{\mathrm{m,\,d}} C_{\alpha\beta}^{\mathrm{m,\,d}} - r_{\alpha\beta}^{\mathrm{m,\,a}} C_{\alpha\beta}^{\mathrm{m,\,a}} = 0. \end{aligned} \tag{4d}$$

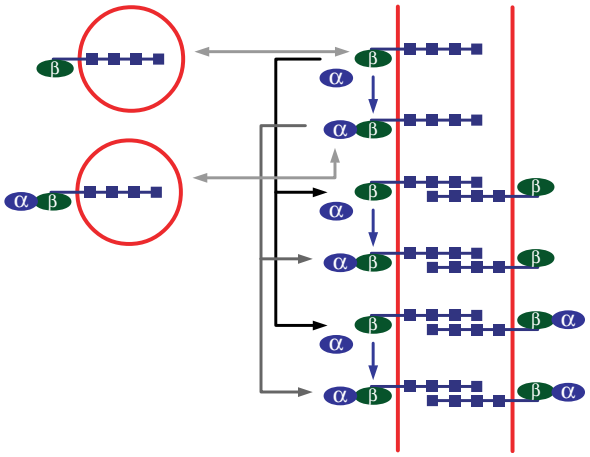

FIGURE 3 Schematic illustration of the reactions occurring at the cell membrane and leading to Eq. 4. E-cadherin vesicles, either bound to β-catenins alone or to α-catenin-β-catenin complexes, can merge with the membrane or be endocytosed. The two associated light gray arrows correspond to the four on and off rates in Eq. 4. In the presence of cell-cell contact, the E-cadherins on the membrane can bind to E-cadherins on the membrane of the adjacent cell, which is represented by the black arrows for β-catenin-associated complexes, and by the dark gray arrows for α-catenin-β-catenin-associated complexes. These correspond to all the reactions that have rates with an EE superscript in Eq. 4. In addition, α-catenin monomers can bind to E-cadherin-β-catenin complexes present on the membrane, whether or not they are bound to E-cadherins from the adjacent cell. This is represented by the blue vertical arrows and corresponds to the terms in Eq. 4 whose rates have an m,d or m,a superscript. Finally, all protein complexes located on the membrane can be degraded, which is taken into account by the rates labeled with the letter r in Eq. 4 (not represented). We assume a symmetric configuration of the adjacent cell.

Here, the first two equations describe the balance of β-catenin and α-catenin-β-catenin complexes, respectively, on the plasma membrane of the cell that are detached from the neighboring cell, and the last two equations do the same for the attached protein complexes. For example, in the first equation, β-catenin-E-cadherin complexes in the detached state can—in the order of the terms present in the equation—be replenished via attachment of β-catenin-E-cadherin complexes from the cytoplasm, disappear via endocytosis of β-catenin-E-cadherin complexes, form α-catenin-β-catenin-E-cadherin complexes, attach with other β-catenin-E-cadherin or α-catenin-β-catenin-E-cadherin complexes from the neighboring cell via cross-membrane E-cadherin-E-cadherin homophilic binding, and, finally, disappear via degradation. The terms in the second equation are of similar origin. The third and fourth equations for the attached states resemble the first two, except that there is no exchange of proteins directly with the cytoplasm in these cases.

Steady-state concentration profiles

To solve Eqs. 1–4, we now separate the two cases of the presence and absence of contact with a neighboring cell, for which we can separately eliminate the membrane concentrations from the boundary conditions given by Eqs. 2 and 3 thanks to Eq. 4. In the absence of cell-cell contact, the different rates k^{EE}_{A-B} vanish and all the proteins on the membrane are in the detached state. In this case, Eqs. 4c and 4d become irrelevant, and Eqs. 4a and 4b become

$$k^{\mathrm{on}}_{\beta}C^{\mathrm{b}}_{\beta} - k^{\mathrm{off}}_{\beta}C^{\mathrm{m,\,d}}_{\beta} - k^{\mathrm{m,\,d}}_{\alpha\beta}C^{\mathrm{m,\,d}}_{\beta}C^{\mathrm{b}}_{\alpha} - r^{\mathrm{m,\,d}}_{\beta}C^{\mathrm{m,\,d}}_{\beta} = 0, \quad (5a)$$

and

$$k^{\mathrm{on}}_{\alpha\beta}C^{\mathrm{b}}_{\alpha\beta} - k^{\mathrm{off}}_{\alpha\beta}C^{\mathrm{m,\,d}}_{\alpha\beta} + k^{\mathrm{m,\,d}}_{\alpha\beta}C^{\mathrm{m,\,d}}_{\beta}C^{\mathrm{b}}_{\alpha} - r^{\mathrm{m,\,d}}_{\alpha\beta}C^{\mathrm{m,\,d}}_{\alpha\beta} = 0. \quad (5b)$$

The first equation makes it possible to solve for $C^{\mathrm{m,\,d}}_{\beta}$ and then express j_α and j_β as a function of the cytosolic concentrations of α-catenin and β-catenin complexes only. Thus, we get a closed set of equations for these two quantities, in which we find the cytosolic equations (Eqs. 1a and 1b), as well as the expressions for the fluxes at the boundaries of the system, namely, the imposed fluxes j^0_α and j^0_β at the Golgi apparatus of the cell and the two fluxes at the cell membrane,

$$j_\beta = \frac{r^{\mathrm{m,d}}_{\beta} + k^{\mathrm{m,d}}_{\alpha\beta}C^{\mathrm{b}}_{\alpha}}{r^{\mathrm{m,d}}_{\beta} + k^{\mathrm{off}}_{\beta} + k^{\mathrm{m,d}}_{\alpha\beta}C^{\mathrm{b}}_{\alpha}}\,k^{\mathrm{on}}_{\beta}C^{\mathrm{b}}_{\beta}, \quad (6a)$$

$$j_\alpha = \frac{k^{\mathrm{m,d}}_{\alpha\beta}C^{\mathrm{b}}_{\alpha}}{r^{\mathrm{m,d}}_{\beta} + k^{\mathrm{off}}_{\beta} + k^{\mathrm{m,d}}_{\alpha\beta}C^{\mathrm{b}}_{\alpha}}\,k^{\mathrm{on}}_{\beta}C^{\mathrm{b}}_{\beta}. \quad (6b)$$

This system can be solved independently and then used to solve for the concentrations of α-catenin-β-catenin and α-catenin dimeric complexes in a second step, using the remaining equations.

In the presence of cell-cell contact, we assume, for simplicity, $k^{\mathrm{EE}} \to \infty$, meaning that all protein complexes on the membrane instantaneously bind to the neighboring cell. Therefore, the concentrations of unbound proteins on the membrane, $C^{\mathrm{m,\,d}}_{\beta}$ and $C^{\mathrm{m,\,d}}_{\alpha\beta}$, vanish. Similar to the previous case, the dynamics for α-catenin and β-catenin complexes decouples from the rest of the system, and the fluxes can be obtained from Eqs. 2. and 3 after we have solved for $C^{\mathrm{m,\,a}}_{\beta}$ using Eqs. 4a and 4c:

$$j_\beta = k^{\mathrm{on}}_{\beta}C^{\mathrm{b}}_{\beta}, \quad (7a)$$

$$j_\alpha = \frac{k^{\mathrm{m,a}}_{\alpha\beta}C^{\mathrm{b}}_{\alpha}}{r^{\mathrm{m,a}}_{\beta} + k^{\mathrm{m,a}}_{\alpha\beta}C^{\mathrm{b}}_{\alpha}}\,k^{\mathrm{on}}_{\beta}C^{\mathrm{b}}_{\beta}. \quad (7b)$$

The system of equations derived above can now be solved independently in the two configurations of the cell numerically, namely, in the presence or absence of contact with a neighboring cell. It consists of Eqs. 1a and 1b together with one of the boundary conditions (Eq. 6 or Eq. 7) at the plasma membrane and a constant protein influx given by j^0_α and j^0_β at the Golgi apparatus of the cell. We solve this system for the case of a spherical cell of radius R, whose Golgi apparatus is modeled as a sphere of radius r_0. In Fig. 4, we illustrate the difference in the concentrations of α-catenin, β-catenin, and α-catenin dimers with and without cell-cell contact. We see in Fig. 4 *C* that the overall concentration of α-catenin dimers presents a significant increase in the case of cell-cell contact, as compared to the case without contact, which provides an efficient switch between the two phenotypic states of the cell. Note that in both cases, there is a drop in the concentration of α-dimers away from the nucleus. If the diffusion constant is small enough (i.e., if $D_{\alpha\alpha}/[R^2(r_{\alpha\alpha} + \tilde{r}_{\alpha\alpha})] \ll 1$), this concentration drop is significant and could be relevant for the spatial organization of polymerized actin within the cell.

Scaling analysis

Let us now perform a scaling analysis of the total number of α-catenin dimers in the system as given by our model, comparing the two cases with and without cell-cell contact. In asymptotic limits in which the involved lengthscales separate, it is possible to solve our system of equations analytically. We thereby obtain a better physical understanding of the contact inhibition mechanism proposed in this article. We also derive a simple expression for the change in the total amount of α-catenin dimers, $N_{\alpha\alpha}$, in the cell between the contact and no-contact states, which dictates the amplitude of the switch. This final expression is given by Eq. 19, and one may want to skip to this equation and its associated comments directly. Later, this derivation also helps us to see in which biological conditions our mechanism can function, and to investigate the various possibilities that can lead to its breakdown. This is done in the next section.

We first identify the different characteristic lengths over which the concentrations of the different proteins vary as

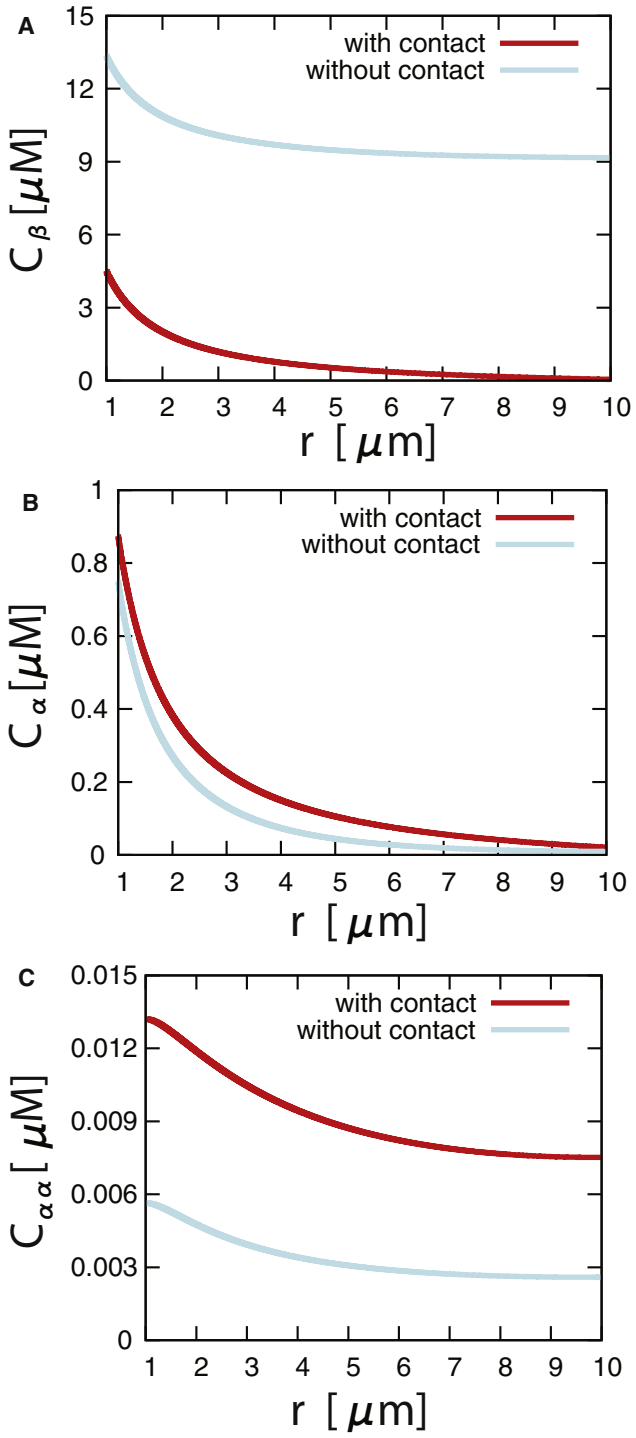

FIGURE 4 Cytosolic concentration profiles of β-catenin (*A*), α-catenin (*B*), and α-catenin dimers (*C*) resulting from the reaction-diffusion system described by Eqs. 1a–1d, with the boundary conditions without cell-cell contact (Eq. 6) or with cell-cell contact (Eq. 7), as functions of the distance from the center of a cell with spherical symmetry. The different parameters are as follows. The Golgi apparatus of the cell is located at $r_0 = 1$ μm and the total radius of the cell is $R = 10$ μm. The β-catenin influx is $j_\beta^0 = 5.0$ μm μM s^{-1}. The diffusion constants of α- and β-catenin are equal to 1 μm^2 s^{-1}, and the one for α-catenin dimers is 0.5 μm^2 s^{-1} (30). In these plots, the reaction rate of α-catenin with β-catenin is 0.01 μM^{-1} s^{-1}, and that of α-catenin with itself is 0.005 μM^{-1} s^{-1} (31). The protein degradation rates of α-catenin and β-catenin are equal to 10^{-3} s^{-1}, and the consumption and degradation rates of α-catenin dimers are 0.5×10^{-3} s^{-1}. Finally, the membrane binding and unbinding rates, k_β^{on} and k_β^{off}, of the β-catenin protein complex are equal to 1 μm s^{-1} and 1 s^{-1}, respectively.

each of the reactions is considered separately. For a given protein, the shortest of the characteristic lengths of the different reactions it enters determines its dominant reaction pathway. The characteristic length for the change in monomeric α-catenin concentration due to α-catenin dimer formation (α-catenin-to-β-catenin binding) is given by $l_{\alpha\alpha}^\alpha = \sqrt{D_\alpha/(k_{\alpha\alpha}C_\alpha)}$ $\left(l_{\alpha\beta}^\alpha = \sqrt{D_\alpha/(k_{\alpha\beta}C_\beta)}\right)$. In a similar way, the change in β-catenin concentration due to α-catenin-to-β-catenin binding is given by $l_{\alpha\beta}^\beta = \sqrt{D_\beta/(k_{\alpha\beta}C_\alpha)}$. Finally, the characteristic length due to monomeric α-catenin degradation (β-catenin degradation) is $l_\alpha = \sqrt{D_\alpha/r_\alpha}$ $\left(l_\beta = \sqrt{D_\beta/r_\beta}\right)$.

We first look at the case where $l_{\alpha\beta}^\alpha$ is the shortest of the lengthscales given above. As shown below, such a condition is realized as soon as the production of β-catenin at the Golgi apparatus of the cell is large enough, such that reactions with monomeric β-catenin proteins (bound to E-cadherins) are fast. In this case, α-catenin-to-β-catenin binding is dominant over α-catenin dimerization in the absence of cell-cell contact, such that our mechanism can be efficient. (Other limits are studied below.) The concentration of α-catenin at the cell membrane is always very low and the change in the steady-state concentration of α-catenin with and without cell-cell contact results from a redistribution of β-catenin inside the cell.

Within this limit, we can assume a quasiconstant concentration of β catenin in a region of length $l_{\alpha\beta}^\alpha$ around its source, which allows us to find analytical expressions for the reaction-diffusion system in a one-dimensional geometry with coordinate x, the protein source being at $x = r_0$ and the cell membrane at $x = R$. The solution for the α-catenin concentration is given by

$$C_\alpha \simeq C_\alpha^0 \exp\left(-(x - r_0)/l_{\alpha\beta}^\alpha\right), \tag{8}$$

with $C_\alpha^0 = l_{\alpha\beta}^\alpha j_\alpha^0/D_\alpha = j_\alpha^0/\sqrt{k_{\alpha\beta}C_\beta^0 D_\alpha}$, and where C_α^0 and C_β^0 are the concentrations of α-catenin and β-catenin complexes, respectively, at $x = r_0$. The solution for the β-catenin concentration is given by

$$C_\beta \simeq C_\beta^0 \cosh((x - r_0)/l_\beta) - \frac{j_\beta^0 - j_\alpha^0}{\sqrt{D_\beta r_\beta}} \sinh((x - r_0)/l_\beta) \tag{9}$$

From the boundary conditions, we can determine the expression for C_β^0:

$$C_\beta^0 \simeq f\,\frac{j_\beta^0 - j_\alpha^0}{\sqrt{D_\beta r_\beta}}, \tag{10}$$

where

$$f = \frac{1 + g\tanh(R/l_\beta)}{\tanh(R/l_\beta) + g} \quad \text{and} \quad g = \frac{r_\beta^{\mathrm{m,d}}}{k_\beta^{\mathrm{off}} + r_\beta^{\mathrm{m,d}}} \frac{k_\beta^{\mathrm{on}}}{\sqrt{D_\beta r_\beta}}. \quad (11)$$

It is now possible to translate our initial assumptions on the different characteristic reaction lengths into conditions directly on the concentration C_β^0 of β-catenin at $x = r_0$. For the three characteristic lengths $l_i = l_\alpha$, l_β, and R, the condition $l_{\alpha\beta}^\alpha \ll l_i$ reads

$$C_\beta^0 \gg \frac{D_\alpha}{k_{\alpha\beta}} \frac{1}{l_i^2}, \quad (12)$$

whereas the conditions $l_{\alpha\beta}^\alpha \ll l_{\alpha\beta}^\beta$ and $l_{\alpha\beta}^\alpha \ll l_{\alpha\alpha}^\alpha$, respectively, read

$$C_\beta^0 \gg \left[\frac{D_\alpha}{k_{\alpha\beta}}\left(\frac{j_\alpha^0}{D_\beta}\right)^2\right]^{1/3}, \quad (13)$$

and

$$C_\beta^0 \gg \frac{\left(2k_{\alpha\alpha} j_\alpha^0\right)^{2/3}}{k_{\alpha\beta}(D_\alpha)^{1/3}}. \quad (14)$$

Finally, there is an additional condition stating that the concentration of β-catenin is quasiconstant in a region of length $l_{\alpha\beta}^\alpha$ around the protein source:

$$C_\beta^0 \gg \frac{D_\alpha r_\beta}{k_{\alpha\beta} D_\beta} \frac{1}{f^2}. \quad (15)$$

Since $C_\beta^0 \propto j_\beta^0 - j_\alpha^0$, all of these conditions are satisfied for a sufficiently large influx, j_β^0, of β-catenins at the Golgi apparatus of the cell.

The amplitude of the switch is given by the change in the total amount of α-catenin dimers, $N_{\alpha\alpha}$, in the cell between the contact and no-contact states. The concentration in α-catenin dimers is given simply by

$$C_{\alpha\alpha} = \frac{k_{\alpha\alpha}}{r_{\alpha\alpha} + \tilde{r}_{\alpha\alpha}} C_\alpha^2 \quad (16)$$

if $l_{\alpha\beta}^\alpha$ is much smaller than the two other lengthscales given by Eq. 1c, namely $\tilde{l}_{\alpha\alpha}^\alpha = \sqrt{D_{\alpha\alpha} C_{\alpha\alpha}/(k_{\alpha\alpha} C_\alpha^2)}$ and $l_{\alpha\alpha} = \sqrt{D_{\alpha\alpha}/(r_{\alpha\alpha} + \tilde{r}_{\alpha\alpha})}$. Integrating the α-catenin dimer concentration over the size of the whole cell under this hypothesis, we obtain

$$N_{\alpha\alpha} \simeq \frac{k_{\alpha\alpha}\left(j_\alpha^0\right)^2}{2r_{\alpha\alpha}(k_{\alpha\beta})^{3/2}(D_\alpha)^{1/2}}\left(C_\beta^0\right)^{-3/2} \quad (17)$$

as a formal expression. The consistency check for this expression gives the following condition for C_β^0:

$$C_\beta^0 \gg \frac{D_\alpha k_{\alpha\beta}}{D_{\alpha\alpha}(r_{\alpha\alpha} + \tilde{r}_{\alpha\alpha})}, \quad (18)$$

which again is satisfied for a sufficiently large influx, j_β^0, of β-catenins at the Golgi apparatus of the cell. The results in the presence and absence of cell-cell contact can be obtained by switching the rates for detached membrane proteins with those for attached ones. In particular, the off-rate of β-catenin from the membrane, k_β^{off}, must be set to 0 in the case where there is contact with a neighboring cell. If all the other rates stay the same, we obtain a simple expression for the ratio of the total amounts of α-catenin dimers with and without cell-cell contact:

$$\frac{N_{\alpha\alpha}^{\mathrm{con}}}{N_{\alpha\alpha}^{\mathrm{nocon}}} \simeq \left(1 + \frac{k_\beta^{\mathrm{off,nocon}}}{r_\beta^{\mathrm{m,d}}}\right)^{3/2}, \quad (19)$$

which comes from the dependence of $N_{\alpha\alpha}$ on C_β^0, and where $k_\beta^{\mathrm{off,\ nocon}}$ is the off rate of β-catenin from the membrane when there is no cell-cell contact. Hence, for a protein degradation rate, $r_\beta^{\mathrm{m,\ d}}$, much smaller than the off rate, k_β^{off}, we expect a significant switch in the total amount of α-catenin dimers produced and, thus, a functional contact inhibition mechanism.

We now look at two cases where $l_{\alpha\beta}^\alpha$ may not necessarily be the smallest characteristic length in the system. First, it is possible that when there is cell-cell contact, $l_{\alpha\alpha}^\alpha$ becomes the shortest characteristic length, instead of $l_{\alpha\beta}^\alpha$ in the absence of contact. Indeed, when there is cell-cell contact, β-catenin proteins could be sufficiently depleted from the cell that most of the α-catenins form homodimeric complexes before reacting with β-catenins. In this case, the contact inhibition switch remains intact, and the previous ratio still scales as stated in Eq. 19.

Another limit corresponds to the case where the cell radius, R, is the shortest lengthscale in the system. In this case, the system of reaction diffusion equations—together with the corresponding boundary conditions—can be treated as a system without spatial extension. A substantial change in the β-catenin concentration between the two states of the cell can be achieved in this limit if the degradation rate of β-catenin in the cytosol, r_β, is much smaller than its degradation rate on the membrane, $r_\beta^{\mathrm{m,\ d}}$. The numerical solutions that correspond to this limit are shown in Fig. 5. In particular, Fig. 5 *B* shows that the switch is controlled by the ratio $r_\beta/r_\beta^{\mathrm{m,\ d}}$. As an alternative, the reaction rate $k_{\alpha\beta}^{\mathrm{m,\ a}}$ of membrane-bound β-catenin with α-catenin could be smaller than the corresponding reaction rate in the cytosol $k_{\alpha\beta}$. This would also yield a functioning contact inhibition switch.

Breakdown of contact inhibition

Let us now investigate the various possibilities that, according to our model, can lead to a breakdown of the contact inhibition pathway. To investigate what affects the production of α-catenin dimers, let us look at the total number of α-catenin dimers in the cell calculated from a numerical solution of our whole system of equations (Eqs. 1a–1d) together with the boundary conditions described by Eqs. 6 and 7, for the contact-free and contact-inhibited states (see Fig. 6). We first show the dependence on j_α^0 (Fig. 6 *A*), which is

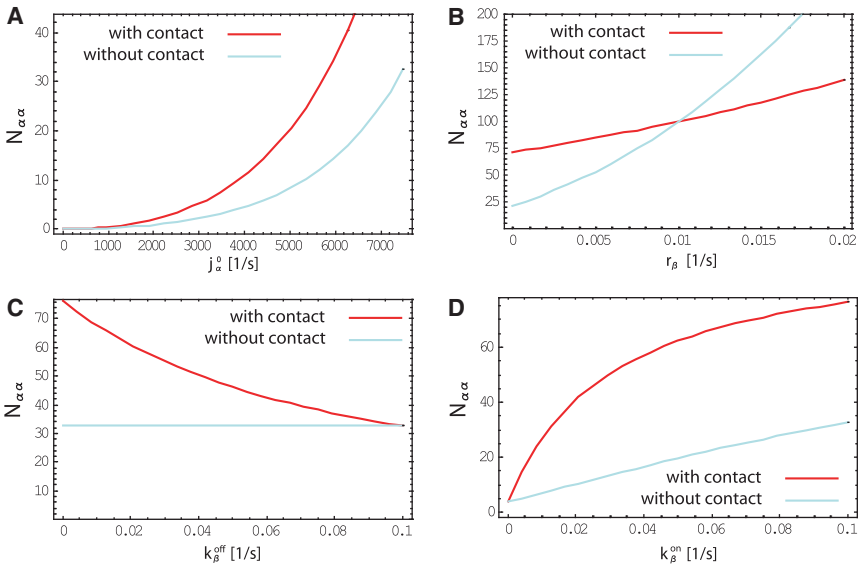

FIGURE 5 Numerical solutions for the total number of α-catenin dimers in the cell as a function of different parameters when the cadherin-catenin system is treated as a zero-dimensional reaction system. In this limit, the contact inhibition mechanism is based on a larger degradation rate on the membrane ($r_\beta^{m,\,d} = 10^{-2}\ s^{-1}$) than in the cytosol ($r_\beta = 10^{-3}\ s^{-1}$). The α-catenin degradation rate, r_α, is also assumed to be small ($10^{-3}\ s^{-1}$). The total production rates of α-catenin and β-catenin are equal to $7.5 \times 10^3\ s^{-1}$ and $14 \times 10^3\ s^{-1}$. Protein-protein reaction rates are $10^{-3}\ s^{-1}$, and on and off rates of the β-catenin protein complex to the cell membrane are $k_\beta^{on} = k_\beta^{off} = 0.1\ s^{-1}$. Note that for $r_\beta > r_\beta^{m,\,d}$, the switch is reversed.

proportional to the total production of α-catenin in the cell Golgi apparatus. As discussed above, many cancerous cells show mutations that impair the function or production of α-catenin proteins. From Eq. 17, we see that the total number of α-catenin dimers scales like $(j_\alpha^0)^2$, which is consistent with these experimental observations. For low values of j_α^0, the

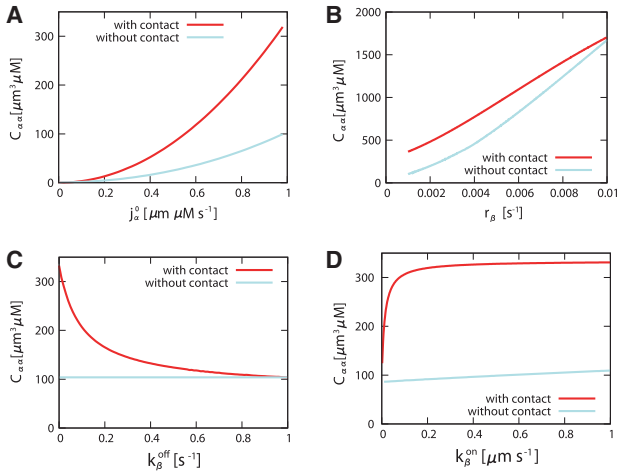

FIGURE 6 Integrated α-catenin dimer concentration over the cell volume from the numerical solution of the whole model. This quantity is plotted as a function of the α-catenin influx j_α^0 (A), the β-catenin degradation rate in the cytoplasm, r_β (B), and the rates of unbinding, k_β^{off} (C), and binding , k_β^{on} (D), of the β-catenin protein complex from and to the membrane. The same constants are used as in Fig. 4. In B, $r^{m,\,d}{}_\beta = r_\beta$ is assumed. Contact inhibition occurs when the concentration of α-catenin dimers, $C_{\alpha\alpha}$, is large. The contact inhibition breaks down for low production, j_α^0, of α-catenin (A) and for an increased degradation of β-catenin (B). It also breaks down for an increased membrane off rate (C), which corresponds to mutations of E-cadherins leading to less efficient formation of cell-cell E-cadherin bonds. This results in an insufficient trapping of β-catenins on the membrane in the presence of cell-cell contact. Finally, contact inhibition breaks down for small values of k_β^{on} (D), which could correspond to a less efficient binding of β-catenin to the membrane due to a decreased expression of E-cadherins.

difference between the contact-free and contact-inhibited state disappears, as has been observed experimentally (23). Next, we consider the effect of a knockout of the APC protein, which is known to label the β-catenin in the cytosol for degradation. From Eqs. 10, 11, and 17, we see that for a fast β-catenin degradation, the total amount of α-catenin dimers scales like $(r_\beta)^{3/4}$. Hence, contact inhibition becomes less effective for a lower cytosolic β-catenin degradation rate, as has been observed in experiments (19). As can be seen in Fig. 6 B, a low degradation rate of β-catenin—which corresponds to a knockout of APC—leads to a total concentration of α-catenin dimers in the cell that is low, even when there is cell-cell contact. Other defects frequently encountered for cancerous cells are downregulation or mutations of E-cadherins (15). In our picture, a malfunction of E-cadherins due to mutations corresponds to a less effective binding of E-cadherins to neighboring cells, and thereby a less efficient trapping of E-cadherins and β-catenins to the plasma membrane. Fig. 6 C shows that an increased off rate, k_β^{off}, in both states again leads to a failure of contact inhibition, since the difference between the contact and no-contact states disappears for large values of k_β^{off} in the contact state. Finally, a lower expression of E-cadherin results in a less effective binding of β-catenin to the plasma membrane, which can be modeled by a decreased on rate, k_β^{on}, as shown in Fig. 6 D. Similar results are obtained when R is the shortest lengthscale in the system. In this case, the solution of the system of equations is plotted in Fig. 5 as a function of the model parameters that simulate a breakdown of the contact inhibition mechanism. The breakdown of the switch is similar to the one discussed above.

DISCUSSION

In this article, we have proposed a reaction-diffusion model of the cadherin-catenin system in which the concentration of

α-catenin dimers increases in a confluent cell as compared to a cell without contact. We propose that this switch is due to a competition between mutually exclusive α-catenin dimerization and α-catenin-to-β-catenin binding in the cytosol of the cell. In the presence of cell-cell contact, intercellular E-cadherin bonds prevent endocytosis of E-cadherin complexes. This leads to a redistribution of unbound β-catenins to the cell membrane and thereby a significant increase in the amount of α-catenin dimerization. Hence, the cell shifts between an active state, combining high cellular expansion pressure with high cellular motility, to a quiescent state, where actin branching is inhibited.

From our analysis, we expect the contact-inhibition switch to function efficiently if β-catenin is sufficiently abundant in the cell to effectively compete with α-catenin dimerization. Therefore, there are three distinct possibilities that can lead to a functioning contact inhibition mechanism. First, the protein reaction rates could be sufficiently fast compared with protein diffusion to effectively separate two distinct pools of β-catenin proteins, cytosolic and membrane-bound β-catenins (both linked to E-cadherin proteins), respectively. Although β-catenins in the cytosol compete with α-catenin dimerization, β-catenins on the membrane cannot react with α-catenins anymore, because all α-catenins either bind β-catenins or form dimers before they get a chance to arrive at the membrane. In that case, the contact inhibition switch comes from a redistribution of β-catenin-E-cadherin complexes from the cytosol toward the cell membrane as a response to contact with a neighboring cell, effectively letting α-catenin dimers form in the cytosol before reaching the cell membrane, where a high concentration of β-catenin proteins is found. Second, the contact-inhibition switch could arise from depletion of β-catenins from the entire cell in the state with contact as compared to the state without contact. This is the case, for example, if the degradation rate of β-catenin is much larger on the membrane than it is in the cytosol, which is possible, since β-catenin degradation takes place via two distinct pathways in the cytosol and on the membrane of the cell. In this case, the mechanism works even for very slow reaction rates and fast protein diffusion, and the spatial structure of the cell can then be ignored or be treated as a zero-dimensional system. This case is illustrated in Fig. 5. Third, the switch could arise from a reaction of membrane-bound β-catenin with α-catenin that is much slower than the corresponding reaction rate in the cytosol. Depending on the state of the cell, β-catenin proteins are indeed located primarily either on the plasma membrane or in the cytosol, allowing α-catenin proteins to dimerize or not. This case also does not rely on slow diffusion and can be treated as a zero-dimensional system.

In addition to providing a mechanism for contact inhibition, the model qualitatively reproduces the effect of several mutations that are known to cause the breakdown of this mechanism and result in tumorlike phenotypes. As can be seen in Figs. 5 and 6, the model agrees with experimental observations in which the expression levels or the degradation rates of E-cadherin, β-catenin, or α-catenin are modified. These findings explain why a broad range of mutations leads to similar cancerous phenotypes. In particular, the effects of an increased β-catenin concentration on contact inhibition are explained by this model without implicating the Wnt-signaling pathway (18).

Although this work shows that the cadherin-catenin reaction-diffusion system could play the role of a contact-inhibition switch, it is impossible to determine whether it is the most relevant effect without further experimental studies. Experiments that would directly test this pathway are possible. We have already discussed how the cadherin-catenin mechanism reproduces the observed effects of a change in the production and degradation rates of different proteins. However, it might also be possible to inhibit only the interaction of any given pair of these proteins by phosphorylation of specific residues, and thereby to investigate directly every step in the proposed mechanism without interfering with other pathways like the Wnt-signaling pathway (18,29). For example, one experiment of particular interest would be to knock out β-catenin-to-α-catenin binding by phosphorylation without changing the level of expression of these proteins. This would distinguish our model from the picture proposed by Nelson et al. (7,8): indeed, within the reaction-diffusion model presented here, such a treatment would result in an increased concentration of α-catenin dimers, the inhibition of actin branching, and, thus, the contact-inhibited cell state even in the absence of a neighboring cell. In contrast, in the picture proposed by Nelson et al., failure of β-catenin to bind to α-catenin would lead to a disruption of the localization of α-catenin to the adhesion sites, and thereby to actin branching and polymerization even at confluence.

If the model presented here were to be confirmed experimentally, it could potentially ground the idea that different homeostatic growth pressures between neoplastic and healthy tissues are responsible for tumor growth (12). In particular, one could then test whether different disruptions of the cadherin-catenin pathway that are known to lead to tumorigenesis would affect the homeostatic pressures of the tissues under study. Such an observation could potentially give a direct explanation of the observed link between the cadherin-catenin system and neoplastic phenotypes.

We thank F. Amblard, J. Whitehead, E. Farge, and C. Storm for a critical reading of the manuscript and many helpful discussions. T.I. acknowledges financial support from the Foundation for Fundamental Research on Matter of the Netherlands Organisation for Scientific Research (NWO-FOM) within the program on Material Properties of Biological Assemblies (grant FOM-L2601M).

REFERENCES

1. Peskin, C. S., G. M. Odell, and G. F. Oster. 1993. Cellular motions and thermal fluctuations: the Brownian ratchet. *Biophys. J.* 65:316–324.

2. Vasioukhin, V., C. Bauer, …, E. Fuchs. 2000. Directed actin polymerization is the driving force for epithelial cell-cell adhesion. *Cell.* 100:209–219.
3. Pollard, T. D., and G. G. Borisy. 2003. Cellular motility driven by assembly and disassembly of actin filaments. *Cell.* 112:453–465.
4. Bryant, D. M., and J. L. Stow. 2004. The ins and outs of E-cadherin trafficking. *Trends Cell Biol.* 14:427–434.
5. Hirokawa, N., T. C. Keller, 3rd, …, M. S. Mooseker. 1983. Mechanism of brush border contractility studied by the quick-freeze, deep-etch method. *J. Cell Biol.* 96:1325–1336.
6. de Beco, S., C. Gueudry, …, S. Coscoy. 2009. Endocytosis is required for E-cadherin redistribution at mature adherens junctions. *Proc. Natl. Acad. Sci. USA.* 106:7010–7015.
7. Drees, F., S. Pokutta, …, W. I. Weis. 2005. α-catenin is a molecular switch that binds E-cadherin-β-catenin and regulates actin-filament assembly. *Cell.* 123:903–915.
8. Yamada, S., S. Pokutta, …, W. J. Nelson. 2005. Deconstructing the cadherin-catenin-actin complex. *Cell.* 123:889–901.
9. Gates, J., and M. Peifer. 2005. Can 1000 reviews be wrong? Actin, α-catenin, and adherens junctions. *Cell.* 123:769–772.
10. Lecuit, T., and P. F. Lenne. 2007. Cell surface mechanics and the control of cell shape, tissue patterns and morphogenesis. *Nat. Rev. Mol. Cell Biol.* 8:633–644.
11. Thiery, J. P. 2002. Epithelial-mesenchymal transitions in tumour progression. *Nat. Rev. Cancer.* 2:442–454.
12. Basan, M., T. Risler, …, J. Prost. 2009. Homeostatic competition drives tumor growth and metastasis nucleation. *HFSP J.* 3:265–272.
13. Hirohashi, S., and Y. Kanai. 2003. Cell adhesion system and human cancer morphogenesis. *Cancer Sci.* 94:575–581.
14. Conacci-Sorrell, M., J. Zhurinsky, and A. Ben-Ze'ev. 2002. The cadherin-catenin adhesion system in signaling and cancer. *J. Clin. Invest.* 109:987–991.
15. Hirohashi, S. 1998. Inactivation of the E-cadherin-mediated cell adhesion system in human cancers. *Am. J. Pathol.* 153:333–339.
16. Orford, K., C. C. Orford, and S. W. Byers. 1999. Exogenous expression of β-catenin regulates contact inhibition, anchorage-independent growth, anoikis, and radiation-induced cell cycle arrest. *J. Cell Biol.* 146:855–868.
17. Eger, A., A. Stockinger, …, R. Foisner. 2000. Epithelial mesenchymal transition by c-Fos estrogen receptor activation involves nuclear translocation of β-catenin and upregulation of β-catenin/lymphoid enhancer binding factor-1 transcriptional activity. *J. Cell Biol.* 148:173–188.
18. Stockinger, A., A. Eger, …, R. Foisner. 2001. E-cadherin regulates cell growth by modulating proliferation-dependent β-catenin transcriptional activity. *J. Cell Biol.* 154:1185–1196.
19. Korinek, V., N. Barker, …, H. Clevers. 1997. Constitutive transcriptional activation by a β-catenin-Tcf complex in APC$-/-$ colon carcinoma. *Science.* 275:1784–1787.
20. Posthaus, H., L. Williamson, …, E. Müller. 2002. β-Catenin is not required for proliferation and differentiation of epidermal mouse keratinocytes. *J. Cell Sci.* 115:4587–4595.
21. Fevr, T., S. Robine, …, J. Huelsken. 2007. Wnt/β-catenin is essential for intestinal homeostasis and maintenance of intestinal stem cells. *Mol. Cell. Biol.* 27:7551–7559.
22. Benjamin, J., and W. Nelson. 2008. Bench to bedside and back again: molecular mechanisms of α-catenin function and roles in tumorigenesis. *In* Seminars in Cancer Biology.. Elsevier, Amsterdam. 53–64.
23. Vasioukhin, V., C. Bauer, …, E. Fuchs. 2001. Hyperproliferation and defects in epithelial polarity upon conditional ablation of α-catenin in skin. *Cell.* 104:605–617.
24. Hinck, L., I. S. Näthke, …, W. J. Nelson. 1994. Dynamics of cadherin/catenin complex formation: novel protein interactions and pathways of complex assembly. *J. Cell Biol.* 125:1327–1340.
25. Le, T. L., A. S. Yap, and J. L. Stow. 1999. Recycling of E-cadherin: a potential mechanism for regulating cadherin dynamics. *J. Cell Biol.* 146:219–232.
26. Orsulic, S., O. Huber, …, R. Kemler. 1999. E-cadherin binding prevents β-catenin nuclear localization and β-catenin/LEF-1-mediated transactivation. *J. Cell Sci.* 112:1237–1245.
27. Maher, M. T., A. S. Flozak, …, C. J. Gottardi. 2009. Activity of the β-catenin phosphodestruction complex at cell-cell contacts is enhanced by cadherin-based adhesion. *J. Cell Biol.* 186:219–228.
28. Pokutta, S., and W. I. Weis. 2000. Structure of the dimerization and β-catenin-binding region of α-catenin. *Mol. Cell.* 5:533–543.
29. Clevers, H. 2006. Wnt/β-catenin signaling in development and disease. *Cell.* 127:469–480.
30. Konopka, M. C., I. A. Shkel, …, J. C. Weisshaar. 2006. Crowding and confinement effects on protein diffusion in vivo. *J. Bacteriol.* 188:6115–6123.
31. Schlosshauer, M., and D. Baker. 2004. Realistic protein-protein association rates from a simple diffusional model neglecting long-range interactions, free energy barriers, and landscape ruggedness. *Protein Sci.* 13:1660–1669.

Appendix E

Résumé de la thèse en français

Les cellules sont des structures d'une complexité remarquable, et il est essentiel pour leur survie que la matière vivante qu'elles contiennent soit confinée en leur sein. Pour cette raison, elles sont entourées d'une bicouche lipidique appelée membrane plasmique. Au cours de la vie de la cellule, cette membrane est sans cesse remodelée, notamment par des protéines, pour permettre les échanges au sein de la cellule et avec l'extérieur.

La présente thèse traite d'un type de structure impliqué dans un large éventail de situations où les protéines interagissent avec la membrane. Il s'agit des tubes de membrane, qui apparaissent à la base de vésicules en formation, d'invaginations de la membrane ou lorsque le cytosquelette exerce une force ponctuelle sur le bord de la cellule, ce qui résulte en une protrusion enveloppée de membrane. Notre travail est divisé en trois parties, qui traitent de trois géométries d'interactions protéines-membranes très répandues au sein de la cellule. Chacune de ces parties est construite autour d'un exemple concret de protéine participant à la déformation de la membrane, ce qui nous permet de systématiquement comparer nos résultats à des données expérimentales. Le premier de ces exemples est la dynamine, une protéine qui enveloppe la membrane et la contraint à adopter une forme tubulaire, puis la rompt grâce à l'énergie fournie par l'hydrolyse du GTP. Notre second exemple est le complexe protéique ESCRT-III, qui a un rôle similaire à celui de la dynamine à une différence notable près : il ne s'assemble pas *autour* des tubes de membrane, mais *à l'intérieur*. Enfin, nous nous intéressons aux stéréocils, qui sont des protrusions tubulaires que la cellule étend vers le monde qui l'entoure en poussant sa membrane vers l'extérieur au moyen de filaments d'actine.

E.1 Dynamine

La dynamine et ses analogues sont présents dans de nombreuses cellules eucaryotes, où ils participent au trafic intracellulaire. Plus spécifiquement, ils sont utilisées dans une large gamme d'événements de fission membranaire, au cours desquels deux compartiments membranaires distincts sont formés à partir d'un seul. Chez l'homme, des mutations liées à la dynamine ou à ses analogues sont à la source de maladies neurologiques, de myopathies et de déficiences visuelles.

Le mode d'opération de la dynamine est illustré dans la Fig. 2.2, qui présente son action lors de la fermeture des puits de clathrine. La clathrine est une protéine qui forme un

manteau courbé autour de la membrane, la contraignant à adopter une forme sphérique. Une fois la clathrine assemblée [Fig. 2.2(c)], il reste à couper le cou de membrane qui relie la vésicule à la membrane plasmique. Cette opération est coûteuse énergétiquement, car elle nécessite de courber la membrane fortement. C'est là qu'intervient la dynamine. La dynamine polymérise en forme d'hélice autour de la membrane [Fig. 2.2(d-f)], puis hydrolyse un carburant moléculaire, le GTP, une opération qui fournit l'énergie nécessaire à la rupture de la membrane [Fig. 2.2(g)].

Plusieurs travaux expérimentaux portant sur des systèmes *in vitro* mettant en jeu des protéines purifiées permettent de mieux comprendre l'action de la dynamine. En ajoutant de la dynamine seule à des vésicules ou à une phase lamellaire de membrane, on peut obtenir sa polymérisation autour de la membrane, à condition que cette dernière soit négativement chargée ou contienne le lipide PIP_2. Cette polymérisation résulte en la formation de longs (plusieurs milliers de tours d'hélice, soit quelques dizaines de micromètres) tubes, dont la structure et les dimensions sont représentées en Fig. 2.3. Du GTP peut maintenant être ajouté à ces tubes. Si ces tubes sont libres de se mouvoir en solution, la dynamine change de conformation (le rayon et le pas de l'hélice de dynamine diminuent), mais le tube ne casse pas. Si au contraire les tubes sont tenus par leurs extrémités, par exemple parce qu'ils sont adsorbés sur la surface d'une lamelle de microscope, on observe qu'ils deviennent très tendus lorsque du GTP est introduit, puis cassent en un point unique. Par ailleurs, il est possible d'attacher une bille de polystyrène à l'hélice de dynamine. Lors de l'introduction du GTP, on observe alors la rotation de la bille, ce qui prouve que l'hydrolyse du GTP par la dynamine engendre des couples en plus d'engendrer des forces. C'est l'action conjuguée de ces couples et forces qui provoque la rupture du tube.

Notre étude de la dynamine est divisée en deux chapitres, correspondant aux deux étapes de l'action de la dynamine : polymérisation et changement de conformation.

E.1.1 Polymérisation de la dynamine

Notre étude théorique de la polymérisation de la dynamine est réalisée en proche collaboration avec Aurélien Roux et Patricia Bassereau à l'Institut Curie. Nous commençons par présenter le dispositif expérimental utilisé, puis présentons une étude thermodynamique étayée par des résultats expérimentaux. Nous proposons ensuite des voies de recherche concernant la cinétique de nucléation du polymère de dynamine, ainsi que sa cinétique de croissance.

E.1.1.1 Montage expérimental

Les expériences présentées ici sont réalisées dans le cadre du dispositif représenté en Fig. 3.1. Une vésicule unilamellaire géante est maintenue en place par une pipette d'aspiration, qui permet de contrôler la tension de sa membrane. Une pince optique est également employée, qui permet d'approcher une bille recouverte de streptavidine de la vésicule. La membrane contient des lipides biotinylés, et adhère donc à la bille en raison de la formation de liens biotine-streptavidine. La bille est ensuite éloignée de la vésicule, ce qui résulte en la formation d'un tube de membrane reliant la vésicule à la bille. Au

cours de l'expérience, le tube de membrane peut être observé par microscopie confocale. Il contient en effet des lipides PIP_2 marqués par un fluorophore rouge.

Le rayon du tube ainsi formé est déterminé par la compétition entre deux effets. D'une part, la membrane a une certaine élasticité, caractérisée par son module de courbure, qui tend à lui faire adopter une configuration aussi plane que possible, et donc à faire augmenter le rayon du tube de membrane. D'autre part, la vésicule a une certaine tension imposée par la pipette d'aspiration. La conséquence en est que la membrane contenue dans le tube est tirée vers la vésicule. Cet effet tend à réduire le rayon du tube. Puisque nous contrôlons la tension de la membrane via l'intensité de l'aspiration exercée par la pipette, nous en contrôlons aussi le rayon, dans une gamme allant typiquement de 10 à 100 nm. De plus, la traction exercée par la vésicule sur le tube de membrane se répercute sur la bille, et tend à la déplacer du centre du piège optique dans lequel elle est maintenue. Ce déplacement est de faible amplitude devant la longueur du tube, mais peut être résolu optiquement. Ainsi, en observant le déplacement de la bille, nous pouvons inférer la force que le tube exerce sur elle. Dans le cas d'un tube de membrane seule, cette force est reliée à la tension de la membrane.

Le tube de membrane que nous tirons de la vésicule sert de substrat à la polymérisation de la dynamine. La dynamine peut être introduite dans le dispositif expérimental de deux manières différentes. Pour les faible concentrations de dynamine (440 nM ou moins), celle-ci est incorporée dans la solution de vésicules avant son introduction dans le microscope. Lorque des concentrations élevées sont employées (12 μM), une solution de dynamine est injectée en cours d'expérience par une pipette auxiliaire.

E.1.1.2 Étude thermodynamique

La première partie de notre étude consiste à déterminer dans quelles conditions la solution de dynamine forme une hélice autour du tube. La formation d'une telle hélice n'est pas anodine pour la membrane. En effet, elle voit au cours de ce processus sa courbure augmenter très significativement, car l'hélice de dynamine (qui est très rigide) impose à la membrane son rayon de courbure, égal à 10 nm. La membrane s'oppose à cette déformation, qui ne peut donc se produire que si le gain d'énergie lié à la formation de l'hélice est assez important. Nous adoptons ici ce point de vue énergétique et comparons l'énergie du tube de membrane nu et à celle du tube entouré d'une hélice pour conclure sur l'existence ou non de telles hélices. Dans cette approche thermodynamique initiale, nous ne nous soucions donc pas de l'existence d'éventuelles barrières cinétiques à la formation du polymère de dynamine.

Plusieurs effets ont une influence sur la stabilité de l'assemblage dynamine-membrane : l'affinité de la dynamine pour la membrane, le gain énergétique lié à la formation de liaisons chimiques lors de la polymérisation, l'abondance de la dynamine dans la solution, l'énergie de la membrane contrainte par l'hélice (qui est notamment liée à la tension de la membrane dans la vésicule, et donc au rayon du tube de membrane initial). Parmi ces facteurs, les plus faciles à contrôler sont la concentration de la solution de dynamine et la tension de la membrane. L'énergie de l'assemblage dynamine-membrane doit être comparée à celle du tube de membrane nu. Celle-ci dépend de la courbure de la membrane (en raison de son module de courbure) et de sa surface (en raison de la tension de la

vésicule). Ainsi que nous l'avons vu plus haut, l'une comme l'autre sont reliées au rayon du tube nu. Grossièrement parlant, un tube de grand rayon a une énergie plus basse qu'un tube de faible rayon. Si nous formons un tube de faible rayon, son énergie initiale est donc relativement élevée et la dynamine n'aura donc pas besoin de payer beaucoup plus d'énergie pour finir de le déformer.

Parmi les facteurs énumérés ci-dessus, ceux liés à la mécanique de la membrane ainsi qu'à la concentration de la solution sont bien connus, et nous pouvons sans peine évaluer l'énergie qui leur est associée. Par contre, ceux liés à l'énergie de polymérisation de la dynamine sont mal connus. Notre première expérience a pour but de déterminer l'amplitude de ces derniers. Nous nous plaçons dans un cas où la dynamine polymérise spontanément autour de la membrane. Une fois le tube complètement recouvert de dynamine, la croissance de celle-ci est bloquée par la bille maintenue dans le piège optique. En raison de sa tendance à polymériser, cependant, la dynamine est capable de déplacer la bille de sa position d'équilibre afin de libérer un peu d'espace de polymérisation supplémentaire. Nous pouvons formuler cette observation en termes de forces et dire que la polymérisation de la dynamine exerce une force au même titre que celle de l'actine ou des microtubules. Comme nous l'avons évoqué plus haut, notre montage de pinces optiques nous permet de mesurer cette force. Nous pouvons donc mesurer le gain d'énergie de la dynamine lors de sa polymérisation. La dynamine est un polymère de dimères, et ce gain s'élève à $3.8 k_B T$ par dimère lorsqu'une solution de dynamine de $12\,\mu$M est utilisée.

Nous sommes donc maintenant en possession d'informations quantitatives sur tous les effets déterminant la stabilité de l'hélice de dynamine. Nous pouvons les comparer et prédire pour quelles valeurs du rayon initial du tube de membrane et de la concentration de la solution la dynamine polymérisera. Cette prédiction est tracée sous la forme d'un diagramme de phases en Fig. 3.3(b), et nous la vérifions expérimentalement. Le bon accord entre expérience et théorie confirme notre image de compétition entre énergie de polymérisation de la dynamine et énergie de courbure de la membrane, et démontre donc que la polymérisation de la dynamine peut être contrôlée par la courbure initiale de la membrane. Cette observation a des conséquences intéressantes pour le rôle biologique de la dynamine, car elle suggère que le recrutement de la dynamine à la base des puits de clathrine est dépendant de leur courbure, ce qui est en accord avec plusieurs observations expérimentales. Qui plus est, le mécanisme décrit ici est assez général pour s'appliquer à d'autres protéines sensibles à la courbure de la membrane, et pourrait donc constituer un moyen générique pour la cellule de contrôler les interactions protéines-membranes.

E.1.1.3 Cinétique de nucléation

Lorsque des expériences de polymérisation décrites plus haut sont réalisées à faible concentration de dynamine (typiquement 440 nM), de courtes hélices de dynamine se forment sur le tube de membrane, puis croissent lentement jusqu'à le recouvrir. Ces noyaux d'hélice sont peu nombreux (quelques unités par tube), ce qui suggère que la nucléation d'une hélice de dynamine est un événement rare. Dans cette seconde partie de notre étude, nous nous intéressons aux causes de cette rareté et étudions les barrières cinétiques à la polymérisation de la dynamine. Nous formulons deux hypothèses quant à leur origine, dont découlent des prédictions pour la dépendance du taux de nucléation en la con-

centration de la solution et en la tension de la membrane. Ces deux hypothèses sont schématisées en Fig. 3.4. La validation de l'un de ces mécanismes (ou la preuve que les deux mécanismes ont un rôle à jouer) fournirait des informations intéressantes sur les détails microscopiques des interactions dynamine-membrane. Dans les deux cas, nous nous demandons avec quelle fréquence la dynamine est capable de former un oligomère encerclant la membrane et à partir duquel la croissance d'un long polymère peut débuter.

Notre première hypothèse [Fig. 3.4(b)] consiste à considérer que la membrane est beaucoup plus rigide que la dynamine[1]. Dans ce cas-là, les dimères de dynamine s'aggrègent aléatoirement à la surface d'un tube de courbure constante. Les oligomères qu'ils forment sont frustrés (et ont donc une énergie élevée), car leur rayon naturel est 10 nm, beaucoup plus petit que celui du tube. Lorsqu'au hasard du processus d'aggrégation de grands oligomères de dynamine se forment, l'énergie emmagasinée est telle qu'elle leur permet de courber la membrane et de former une hélice. Dans le cadre de cette hypothèse, la cinétique de nucléation de la dynamine est donc contrôlée par la cinétique d'aggrégation des dimères.

La seconde hypothèse est à l'extrême opposé de la première. Dans ce cas, les oligomères de dynamine sont beaucoup plus rigides que la membrane. Il ne pourront donc jamais polymériser sur un substrat ayant un rayon supérieure à 10 nm. Le seul moyen d'initier la polymérisation est donc que le rayon du tube de membrane soit abaissé jusqu'à atteindre la valeur requise. Au sein du système décrit ci-dessus, le seul type de déformations auxquelles est soumise la membrane provient de ses fluctuations thermiques. Nous assimilons donc le taux de nucléation des polymères de dynamine au taux de fluctuations du rayon du tube de membrane abaissant son rayon au-dessous de 10 nm assez longtemps pour permettre à la dynamine de l'encercler, et calculons ce taux.

E.1.1.4 Cinétique de croissance

Une étude approfondie de la croissance du polymère de dynamine après sa nucléation révèle plusieurs effets inattendus. Nous proposons deux origines possibles pour ces effets, et présentons des prédictions impliquant certaines caractéristiques microscopiques de l'assemblage dynamine-membrane, telles que les constantes d'adsorption, de désorption et de polymérisation de la dynamine, ou encore une friction effective caractérisant la dynamique des interactions dynamine-membrane. Ici encore, la vérification de nos prédictions permettrait une meilleure compréhension qualitative et quantitative des interactions dynamine-membrane.

Les effets inattendus mentionnés ci-dessus sont illustrés en Fig. 3.5. Premièrement, il est observé que les noyaux de dynamine mentionnés précédemment ne sont pas répartis au hasard sur le tube de membrane, mais tendent à être séparés par une distance caractéristique, si ce n'est à être agencés périodiquement. Deuxièmement, ces noyaux n'apparaissent qu'au début des expériences, puis ne font que croître sans qu'aucun nouvel événement de nucléation ne soit observé. Troisièmement, ces noyaux croissent initialement à vitesse constante, mais dans certaines expériences leur croissance semble ralentir lorsque le taux de couverture de la membrane par l'hélice s'approche de 1. Quatrièmement,

[1] Il est impossible de savoir si cette hypothèse est justifiée *a priori*, car les propriétés mécaniques des petits oligomères de dynamine, au contraire de celles des longs polymères, n'ont jamais été caractérisées.

il est parfois observé que la force mesurée par la pince optique diminue avant que l'hélice ne recouvre complètement le tube, ce qui suggère que l'hélice est capable d'exercer à distance une force sur la bille.

Notre première hypothèse permet d'expliquer les trois premiers effets. Elle consiste à supposer que la dynamine ne passe pas directement de la solution à l'état polymérisé, mais doit d'abord s'adsorber sur une partie du tube non recouverte par l'hélice. Dans ce cas-là, la formation d'un court polymère tend à appauvrir son voisinage en dynamine adsorbée, ce qui explique que d'autres noyaux ne peuvent pas se former à proximité. Cet appauvrissement peut s'étendre au tube tout entier, ce qui défavorise la nucléation de nouvelles hélices dès lors que quelques-unes sont déjà présentes. Enfin, si deux hélices croissent en direction l'une de l'autre, leur taux de croissance dépend du taux d'adsorption de la dynamine de la solution sur la section de membrane nue qui les sépare. Au fur et à mesure que la taille de cette section diminue, l'apport de dynamine depuis la solution est de plus en plus réduit et la croissance des hélices ralentit.

La seconde hypothèse est complémentaire de la première et rend compte des trois derniers effets. Elle consiste à remarquer que puisque le tube de membrane initial est plus large que celui enserré par l'hélice, la polymérisation de la dynamine dégage un excès de membrane, ainsi que d'eau contenue à l'intérieur de celle-ci. Dans le cas hypothétique où la dynamine commencerait à polymériser depuis la bille, ces excès n'influenceraient pas la dynamique de polymérisation car ils s'écouleraient rapidement en direction de la vésicule, où ils seraient absorbés. Imaginons maintenant qu'une autre hélice de dynamine se trouve sur leur chemin. En raison de son faible rayon et des interactions de l'hélice avec la membrane, celle-ci s'oppose à l'écoulement de l'eau et de la membrane. Ce phénomène peut être modélisé par une friction effective entre l'hélice et la membrane, et une autre entre la membrane et l'eau. Celles-ci s'accumulent donc, et le rayon des sections libres du tube augmente au fur et à mesure de la croissance des hélices. Il se peut ainsi qu'après une courte période de croissance des hélices, les sections libres du tube deviennent impropres à la nucléation de nouvelles hélices, ce qui constitue le second effet décrit plus haut. L'accumulation de membrane est évidemment défavorable à la croissance du polymère, ce qui explique que celle-ci ralentisse. Enfin, un excès de membrane induit une chute de sa tension, ce dont découle une décroissance de la force mesurée par la pince optique.

E.1.2 Action mécanochimique de la dynamine

La principale motivation de la plupart des études portant sur la dynamine est la compréhension de son rôle dans la rupture de tubes de membrane. Celle-ci se produit lorsque la dynamine est alimentée en GTP, ce qui engendre un changement de sa conformation. Dans le chapitre 4 de cette thèse, nous proposons une description théorique très générale de ce changement de conformation. Cette approche se fonde sur l'hydrodynamique généralisée, qui décrit le comportement aux longues échelles de temps de systèmes thermodynamiques faiblement hors d'équilibre de grande étendue spatiale.

E.1.2.1 Formalisme hydrodynamique pour la dynamine

L'hydrodynamique généralisée offre une description simple mais rigoureuse de systèmes potentiellement très compliqués. L'origine de cette grande simplicité est le fait qu'aux longues échelles de temps, il est légitime de ne prendre en compte la dynamique que des seules quantités conservées (c'est-à-dire soumises à une loi de conservation) du système. En effet, si le système est très étendu, sa relaxation aux longues échelles de temps sera dominée par le transport de la quantité conservée (par exemple le nombre de particules de soluté diffusant dans un solvant) d'une extrémité à l'autre du système. Ainsi que nous l'illustrons pour un exemple simple en Sec. 4.1, les symétries du système imposent alors la forme des équations du mouvement.

Dans le cadre de notre étude de la dynamine, il nous faut donc tout d'abord identifier les quantités conservées. Nous envisageons un long tube de membrane couvert de dynamine du type de ceux rencontrés dans les expériences *in vitro* décrites plus haut. Nous avons donc affaire à un sytème unidimensionnel avec une structure périodique due à l'empilement des tours d'hélice de la dynamine. Les quantités conservées dans le système sont la masse de dynamine et la masse de membrane (nous envisageons en effet des échelles de temps auxquelles aucun échange avec la solution environnante ne se produit), les densités de quantité de mouvement et de moment cinétique, et enfin un paramètre de symétrie brisée correspondant à la structure périodique de l'hélice.

Une fois identifiées ces quantités conservées, il nous est possible d'écrire la production d'entropie au sein d'un système faiblement hors d'équilibre. En appliquant des contraintes géométriques et thermodynamiques fondamentales telles que la positivité de la production d'entropie, nous pouvons en déduire les relations flux-forces décrivant la relaxation du tube.

Si les contraintes imposées par les lois de la physique nous permettent de dériver la forme des équations décrivant notre système, ces contraintes ne nous permettent pas de calculer la valeur des coefficients qu'elles font intervenir. Afin de mieux comprendre les équations que nous venons de formuler, ainsi que d'en acquérir une compréhension intuitive, nous discutons ces coefficients phénoménologiques et en donnons des estimations quantitatives. En particulier, l'un de ces coefficients décrit une friction effective entre l'hélice et la membrane. Cette friction est identique à celle évoquée lors de notre étude de la polymérisation de la dynamine.

En plus des effets liés à la relaxation passive de notre système décrits ci-dessus, il nous faut encore prendre en compte les effets de l'hydrolyse du GTP sur le changement de conformation de l'hélice. D'après les images de microscopie électronique de la dynamine, il est peu probable que l'hélice de dynamine soit polaire. De plus, l'injection d'une solution de GTP homogène ne peut pas briser cette symétrie. Il est donc nécessaire que l'hydrolyse du GTP se couple à nos relations flux-forces de façon non-polaire. Dans le cadre de nos résultats précédents, nous en déduisons que mettre le tube en présence de GTP est équivalent à exercer un couple et une force sur lui.

Enfin, nous regroupons les équations de conservation avec les relations flux-forces décrivant notre système, ce qui nous permet d'obtenir les équations du mouvement complètes. Dans le cas (toujours réalisé expérimentalement) où le tube est immergé dans un milieu aqueux, un transfert de quantité de mouvement et de moment cinétique est

possible entre ce milieu et le tube, ce qui implique que ces deux quantités ne sont pas conservées. Il reste donc trois quantités conservées, ce qui implique que la dynamique du tube peut être décomposée sur une base de trois modes hydrodynamiques. Tous trois sont de type diffusif.

E.1.2.2 Dynamique aux temps très longs

Grâce à notre étude quantitative des coefficients phénoménologiques impliqués dans la dynamique du tube, nous pouvons estimer les échelles de temps impliquées dans la relaxation de ces trois modes hydrodynamiques. Les deux premiers sont dominés par la friction de la dynamine contre l'eau environnante, et relaxent beaucoup plus vite que le troisième, qui implique la friction de l'hélice contre la membrane. Nous sommes donc en mesure d'écrire une théorie de perturbation prenant en compte le taux de relaxation du troisième mode comme un petit paramètre. Aux échelles de temps expérimentalement observables, qui sont beaucoup plus longues que les temps de relaxation des deux premiers modes, nous pouvons réduire les équations décrivant la dynamique du tube à une équation de diffusion unique [Éq. (4.41)] ne mettant en jeu que la seule dissipation provenant de la friction discutée plus haut, ainsi qu'une matrice de susceptibilité caractérisant l'élasticité de l'assemblage dynamine-membrane.

E.1.2.3 Description élastique de la dynamine

Ainsi, une fois estimé le coefficient de friction de la dynamine contre la membrane, il est donc possible de décrire la dynamique complète du tube à condition de connaître ses propriétés élastiques. Cette information est en principe accessible expérimentalement par des expériences de micromanipulation qui consisteraient à comprimer et tordre le tube de manière contrôlée, ainsi qu'à changer la tension de la membrane, et à observer combien ces opérations influencent la forme de l'hélice et de la membrane. Ces expériences sont malheureusement techniquement difficiles. Afin de contourner cette difficulté, nous proposons un modèle microscopique partiel du tube. Ce modèle ne concerne que les propriétés d'équilibre de la dynamine, et nous permet donc encore de tirer profit de notre description hydrodynamique concernant ses propriétés hors d'équilibre, dont la modélisation microscopique serait considérablement plus compliquée.

Notre modèle consiste à prendre la dynamine en compte comme un ressort, c'est-à-dire comme une hélice constituée d'un matériau homogène avec un certain module d'Young. Il nous est possible d'inférer la valeur de ce module d'Young à partir d'une mesure de la longueur de persistence de la dynamine. La membrane, d'autre part, est contrainte par l'hélice à adopter une forme approximativement cylindrique. Nous l'autorisons cependant à se courber entre deux tours d'hélice (cette déformation est illustrée en Fig. 4.3, et fait intervenir le module de courbure de la membrane), et prenons en compte son extensibilité. Le module de courbure de la membrane et son extensibilité étant bien caractérisés dans la littérature, nous pouvons donc calculer la matrice de susceptibilité du tube dans le cadre de ce modèle. Nous montrons à cette occasion que les écoulements d'eau à l'intérieur du tube sont une source de dissipation négligeable aux échelles de temps accessibles expérimentalement.

E.1.2.4 Prédictions concernant le changement de conformation

Maintenant que nous disposons des équations du mouvement décrivant la relaxation du tube sous l'effet d'une force et d'un couple, il nous faut déterminer les valeurs de la force et du couple équivalents décrivant l'introduction de GTP. Des données de microscopie électronique indiquant l'amplitude du changement de conformation de l'hélice nous permettent de les déterminer. En effet, connaissant l'élasticité de l'hélice, nous pouvons inférer les forces qui lui sont appliquées de l'ampleur de sa déformation. Nous exposons ces valeurs dans l'Éq. (4.65).

Grâce à ce résultat et à celui de la section précédente, nous sommes en mesure de faire la différence entre les effets mécaniques liés à l'hydrolyse du GTP par la dynamine et à son élasticité, et ceux liés à l'élasticité de la membrane. Nous pouvons ainsi modifier notre modèle de la membrane pour représenter non pas une membrane flexible, mais un bâtonnet solide sur lequel la dynamine viendrait s'assembler. Ce modèle pourrait rendre compte de certaines expériences sur le changement de conformation de la dynamine indiquant une augmentation du pas de l'hélice à rayon constant au lieu de la diminution de pas et de rayon présentée en Fig. 2.3. Moyennant que le module de torsion du filament hélicoidal de dynamine soit plus grand qu'une fois et demie son module de courbure, nous démontrons que les deux types de changement de conformation peuvent être obtenus dans des conditions expérimentales utilisant une dynamine et des nucléotides identiques, mais des membranes de rigidités différentes.

Enfin, nous regroupons nos résultats pour prédire le changement de conformation complet de la dynamine. En accord avec les évaluations réalisées plus haut, nous trouvons que les trois modes hydrodynamiques du tube relaxent à des échelles de temps très différentes. Seul le plus long (celui qui est dominé par la friction hélice-membrane) est observable expérimentalement. Nous n'en représentons pas moins nos prédictions théoriques pour la dynamique complète en Fig. 4.4.

E.1.2.5 Observation expérimentale du comportement hydrodynamique

Notre collaboration avec Patricia Bassereau et Aurélien Roux, ainsi qu'avec Sandrine Morlot de l'Institut Curie nous permet de comparer nos prédictions théoriques à des résultats expérimentaux. Les expériences en question mettent en jeu un système reconstitué impliquant une phase lamellaire de membrane, à laquelle est ajoutée de la dynamine, ce qui induit la formation de tubes. De multiples billes de polystyrène sont fixées à ces tubes, ce qui permet de visualiser la dynamique du changement de conformation de la dynamine non seulement en fonction du temps, mais aussi en fonction de la position de la bille sur le tube. L'expérience est observée en microscopie optique au moyen d'une caméra ordinaire et l'injection du GTP (qui déclenche le changement de conformation) prend quelques dixièmes de secondes, ce qui signifie que nous ne pouvons observer la relaxation que du mode de relaxation le plus long du tube. Notre formalisme nous permet de faire plusieurs prédictions dans ce domaine.

Premièrement, nous prédisons que le mode de plus grande longueur d'onde autorisé par les conditions aux limites voit son amplitude décroître exponentiellement au cours du temps. Puisque ce mode a également le temps de relaxation le plus long, nous nous attendons à ce que la relaxation de la rotation des billes portées par le tube aux temps

longs soit exponentielle. Cette prédiction est confirmée par les données de la Fig. 4.6(a).

Deuxièmement, l'effet du GTP est d'après notre formalisme identique à l'application d'une force et d'un couple sur le tube. À l'équilibre, nous nous attendons donc à ce que le tube se déforme de manière homogène, et donc à ce que le nombre de tours effectué par une bille fixée au tube dépende linéairement de sa distance au point d'attachement du tube, ce que nous montrons expérimentalement en Fig. 4.6(b).

Enfin, nous prédisons que la relaxation du tube est de type diffusif. Cela implique que le profil de vitesse le long du tube est sinusoïdal aux temps longs, ce que nous vérifions en Fig. 4.6(c). Le temps de relaxation le plus long du tube devrait de plus croître comme le carré de la taille du tube. Nous observons en effet en Fig. 4.6(d) que ce temps est une fonction croissante de la longueur, mais ne sommes pas capables de confirmer la dépendance parabolique. Plus d'expériences sont nécessaires pour juger de l'accord ou du désaccord de la théorie avec les expériences.

Bien qu'ils ne permettent pas de confirmer avec certitude toutes nos prédictions, ces résultats expérimentaux indiquent que notre approche hydrodynamique est justifiée. Cette approche hydrodynamique est à son tour intimement liée à l'idée que l'hélice garde sa cohésion lors de son changement de conformation. Réaliser des expériences similaires à celles-ci dans le cadre d'un montage de pinces optiques tel que celui de la Fig. 3.1 nous permettrait de clarifier certains de nos résultats et d'en apprendre plus sur le mécanisme de cassure du tube par la dynamine. En effet, ce nouveau montage permet de contrôler un grand nombre de paramètres de l'expérience, et notre formalisme permet d'inférer l'état local du tube à tout moment de la dynamique. En combinant ces outils théoriques et expérimentaux, il devrait donc être possible de formuler un critère heuristique (par exemple une tension critique de la membrane induisant la rupture) qui nous permettrait de mieux comprendre le phénomène déclencheur de la fission membranaire médiée par la dynamine.

E.2 ESCRT-III

Notre second sujet d'étude est un complexe proteique impliqué dans la formation des corps multi-vésiculaires, dans le bourgeonnement de certains virus enveloppés et agissant lors de la cytocinèse. Tous ces processus ont en commun qu'ils impliquent la formation et/ou la rupture de tubes de membrane dans une géométrie différente de celle envisagée lors de notre étude de la dynamine. En effet, dans chacun de ces cas les protéines ont accès à l'intérieur du tube de membrane, et non pas à l'extérieur comme précédemment.

Ici nous nous intéressons au rôle d'ESCRT-III dans la déformation de la membrane menant à la formation de tubes. Il est observé expérimentalement que l'une des protéines constitutives d'ESCRT-III, hSnf-7, forme des polymères courbés. Lorsque hSnf-7 est surexprimée dans des cellules COS-7, on observe qu'elle se lie à la membrane plasmique et forme des réseaux de forme circulaire [Fig. 5.1(a)]. Ces réseaux changent d'aspect lorsqu'une autre protéine d'ESCRT-III, VPS4, est modifiée. VPS4 est connue pour engendrer le désassemblage des filaments de protéines d'ESCRT-III et est une ATPase. La modification de VPS4 en question ici est une surexpression d'une forme de VPS4 déficiente dans l'hydrolyse de l'ATP. Lorsque cette protéine est surexprimée, les réseaux circulaires

de hSnf-7 ne sont plus plans comme précédemment, mais forment des tubes qui protrudent vers l'extérieur de la cellule [Fig. 5.1(b-c)]. Ici, nous supposons que de tels tubes se forment toujours, mais sont immédiatement coupés quand seul le VPS4 endogène à la cellule est présent. Nous concentrons notre attention sur la formation de ces tubes et proposons de décrire ce processus comme un phénomène physique apparenté au flambage d'une tige. Nous proposons également une expérience permettant de valider notre approche.

E.2.1 Description du processus de flambage

Notre proposition de mécanisme de flambage se fonde sur des considérations énergétiques simples, dont nous dérivons l'énergie libre présentée dans l'Éq. (5.1). Premièrement, nous décrivons la mécanique de la membrane par son module de courbure et sa tension. Nous introduisons également une énergie pour décrire les interactions attractives entre la membrane et les filaments de hSnf-7, ainsi qu'entre filaments de hSnf-7. Nous décrivons les polymères de hSnf-7 comme des filaments élastiques ayant une courbure spontanée, ce qui mène à leur assemblage sous forme de réseaux circulaires.

Ces ingrédients simples permettent de comprendre le mécanisme de flambage illustré en Fig. 5.2. Dans un réseau plan de filaments, les filaments intérieurs sont sur-courbés et ceux de l'extérieur sont sous-courbés. Si la membrane s'incurve vers le haut ou vers le bas, les filaments de l'intérieur peuvent relaxer en s'élargissant et ceux de l'extérieur peuvent se contracter. Une autre source de gain énergétique dans cette situation est le fait qu'un nombre plus important de filaments peut se lier à la membrane. D'un autre côté, la déformation de la membrane coûte de l'énergie de tension et de courbure. Selon la valeur des paramètres, soit le gain soit le coût énergétique sera plus important, ce qui déterminera la stabilité de la membrane habillée par des réseaux de hSnf-7.

E.2.2 Réseaux plans de filaments

Le premier phénomène que nous pouvons décrire à l'aide de notre modèle est la formation de réseaux plans de hSnf-7. Les clichés de microscopie électronique présentés en Fig. 5.1(a) suggèrent que leur rayon est bien défini. Notre modèle permet d'interpréter cette observation : imaginons un réseau circulaire de hSnf-7 de petite taille. De nouveaux filaments ont tendance à s'aggréger à sa périphérie en raison du gain énergétique associé aux interactions avec la membrane et avec les filaments déjà en place. Au fur et à mesure que le réseau s'élargit, cependant, le rayon de courbure des filaments nouvellement ajoutés devient de plus en plus grand, ce qui est défavorable énergétiquement. Le rayon d'équilibre des réseaux observés expérimentalement reflète une situation où ces deux effets se compensent.

E.2.3 Établissement d'un diagramme de stabilité

Nous envisageons maintenant la stabilité du réseau vis-à-vis de perturbations perpendiculaires au plan de la membrane. La forme de l'énergie libre introduite plus haut permet de dériver une équation décrivant l'équilibre des forces pour une membrane faiblement déformée (nous effectuons une analyse de stabilité linéaire). Des solutions de

cette équation obéissant aux conditions au bord n'existent que pour certaines valeurs des paramètres, définissant un seuil auquel la membrane devient instable.

D'un autre côté, nous pouvons envisager la stabilité de longs tubes de membrane cylindriques, qui permettent à tous les filaments de hSnf-7 qu'ils contiennent d'adopter une courbure proche de leur courbure spontanée. Nous trouvons que ces tubes sont stables pour toutes les valeurs des paramètres où la membrane est linéairement instable, ainsi que dans une partie de la région où la membrane est linéairement stable. Dans ce dernier cas, la membrane habillée de hSnf-7 est donc métastable, car elle est stable vis-à-vis de petites perturbations mais tombe dans un puits énergétique lorsqu'elle est fortement déformée.

En utilisant les valeurs expérimentalement observées du rayon des réseaux de hSnf-7 plans et des longs tubes de hSnf-7, nous estimons qu'il est possible que les cellules présentées en Fig. 5.1 soient soit dans le régime instable, soit dans le régime métastable.

E.2.4 Métastabilité et barrière énergétique

Nous continuons notre étude par une analyse plus poussée du régime métastable. Une question intéressante concerne la hauteur de la barrière énergétique séparant un réseau plan métastable de son état de long tube stable. Cette question implique de résoudre les équations mécaniques de la membrane habillée dans le régime fortement déformé. Ces équations sont donc non-linéaires, et nous ne pouvons les résoudre que numériquement. Nous déduisons du résultat de cette opération que si la membrane est métastable *in vivo*, la barrière énergétique la séparant de son état de long tube est beaucoup trop haute pour être traversée sous l'effet des seules fluctuations thermiques. Dans ce cas, le phénomène de déformation de la membrane par ESCRT-III doit être activé par un processus actif, par exemple la polymérisation de l'actine.

E.2.5 Proposition d'expérience

Au cours de cette étude nous avons montré que la seule aggrégation de filaments courbés interagissant entre eux et avec la membrane est susceptible d'engendrer la tubulation de celle-ci, et calculé la dépendance du seuil de tubulation en la tension de la membrane et le potentiel chimique d'hSnf-7 en solution. Des expériences où ces deux paramètres sont contrôlés sont relativement faciles à réaliser, par exemple au moyen d'une vésicule unilamellaire géante et d'un dispositif d'aspiration. Étant donné qu'il a récemment été démontré expérimentalement qu'hSnf-7 et quelques protéines associées sont suffisantes pour tubuler la membrane *in vitro*, les perspectives de vérification quantitative de notre modèle sont prometteuses.

E.3 Stéréocils

La troisième et dernière partie de cette thèse porte sur la morphogénèse des protrusions cellulaires à base d'actine, et en particulier sur les stéréocils. Les stéréocils sont des faisceaux de filaments d'actine enveloppés par la membrane plasmique qui émergent des cellules ciliées et forment des touffes ciliaires à leur surface [Fig. 6.1(b)]. Les cellules

ciliées sont localisées dans la cochlée, au coeur de l'oreille interne, et sont des composants essentiels du mécanisme de l'audition. En effet, le stimulus sonore se propage au travers des différentes régions de l'oreille sous la forme d'une onde mécanique [Fig. 6.1(a)] jusqu'à faire vibrer les touffes ciliaires des cellules ciliées, qui traduisent l'information sonore en un signal nerveux. Selon la hauteur du son, différentes régions de la cochlée entrent en résonance. De plus, la touffe ciliaire se comporte comme un composant actif et amplifie préférentiellement certaines fréquences, ce qui améliore considérablement la sensibilité fréquencielle de notre audition. Ce mécanisme d'amplification met en jeu de manière essentielle les propriétés mécaniques des stéréocils, car ces derniers pivotent autour de leur base lors de la vibration de la touffe ciliaire [Fig. 6.1(d)]. Dans ce chapitre, nous nous intéressons aux facteurs déterminant la forme, et donc les propriétés mécaniques, des stéréocils.

La structure interne des stéréocils est très ordonnée, et les filaments d'actine qu'ils contiennent sont si densément empaquetés qu'ils forment un paracristal hexagonal [Fig. 6.1(e)]. Dans cette étude, nous nous concentrons sur un facteur jusque-là négligé ou mal pris en compte dans la littérature théorique, mais cependant essentiel pour la cohésion des stéréocils : les liens transversaux entre filaments d'actine voisins, et en particulier ceux procurés par la protéine espine. Notons que cette protéine et d'autres liens transversaux sont présents dans d'autres protrusions à base d'actine, telles que les filopodes ou les microvillosités. Plusieurs études expérimentales ont montré qu'une modification de ces liens, qui sont indiqués par des flèches sur la Fig. 6.1(e), peut induire des changements de forme significatifs des stéréocils ainsi que la surdité chez la souris. Il convient enfin de noter que les stéréocils sont des structures éminemment dynamiques. En effet, l'actine et l'espine sont incorporées à leur extrémité supérieure, puis se déplacent vers le bas du stéréocil au fur et à mesure de sa croissance. Enfin, l'actine dépolymérise à la base du stéréocil [Fig. 6.1(f)].

E.3.1 Modèle

Nous étudions ici les effets sur la forme du stéréocil de la dynamique de polymérisation-dépolymérisation de l'actine et de son couplage avec la dynamique d'attachement-détachement de l'espine. En effet, nous remarquons que la tension de la membrane enveloppant les stéréocils est assez élevée pour enserrer les filaments et les mettre au contact les uns des autres. Ainsi, la surface de la section du stéréocil à une certaine distance de son extémité supérieure est toujours proportionnelle au nombre de filaments plus longs que cette distance. Nous notons de plus qu'aux échelles de temps pertinentes pour la morphogénèse des stéréocils, la diffusion de l'actine et de l'espine est très rapide et ne devrait donc pas jouer de rôle important.

Nous supposons que l'actine est polymérisée à vitesse constante à l'extrémité du stéréocil (le front de polymérisation) et que les espines y sont intégrées avec une probabilité donnée. Tant qu'elle est entourée de filaments d'actine, une espine peut se détacher et se rattacher stochastiquement. La dépolymérisation des filaments d'actine est supposée très rapide. Cependant, un filament d'actine lié à une espine ne peut dépolymériser au-dessus de cette espine tant qu'elle ne s'est pas détachée d'elle-même. Notre modèle est schématisé en Fig. 6.2.

E.3.2 Forme du stéréocil en l'absence de réattachement

Nous étudions tout d'abord le problème dans le cas où l'espine n'est incorporée qu'à l'extrémité du stéréocil. En d'autres termes, en-dessous du front de polymérisation l'espine ne peut que se détacher, pas se réattacher. Le problème est très simple dans ce cas, car il suffit de décrire la dynamique de détachement de l'espine sans se soucier de l'actine dans un premier temps. La dynamique de l'actine peut ensuite être déduite de cette étude, car elle est asservie à celle de l'espine.

Nous comparons les formes calculées dans ce cas aux formes de stéréocils observées en microscopie électronique. Nous sommes en mesure de reproduire la forme de trois stéréocils de la même touffe ciliaire en n'utilisant qu'un seul paramètre ajustable commun (Fig. 6.3). Notre modèle est en accord quantitatif avec des données expérimentales indiquant que la vitesse de polymérisation de l'actine est à peu près proportionnelle à la taille du stéréocil [Fig. 6.4(a)]. Enfin, nous rendons quantativement compte de l'allongement des microvillosités de cellules CL4 surexprimant l'espine [Fig. 6.4(b)].

E.3.3 Filament unique en présence de réattachement

Nous nous intéressons maintenant aux effets du réattachement de l'espine sur la forme du faisceau d'actine. Nous commençons par étudier un cas simplifié, celui d'un filament unique lié à un mur par des espines. Étant donné que les espines sont incorporées préférentiellement à l'extrémité du stéréocil, l'actine est plus densément liée à cet endroit. Lorsque l'on s'éloigne du front de polymérisation, l'espine est échangée avec le milieu environnant et tend vers une densité d'équilibre imposée par l'égalité des flux d'attachement et de détachement.

Nous formulons tout d'abord ce problème de filament unique sous la forme d'une équation maîtresse. Cette équation porte sur les probabilités que le système total soit dans une configuration du filament et de toutes les espines donnée. Nous montrons que la dynamique des espines situées au-delà de l'extrémité du filament se découple de la dynamique de dépolymérisation. Le problème peut donc être considérablement simplifié et transformé en un problème ne portant que sur la probabilité que le filament ait une longueur donnée.

Nous nous intéressons ensuite à la dynamique du filament dans la région où l'équilibre chimique entre les espines liées au filament et celles en solution est établi. Dans cette région, le problème spécifié ci-dessus peut être résolu exactement. Aux longues échelles de temps, l'extrémité du filament a une dynamique assimilable à une diffusion biaisée. Un argument simple permet de retrouver la vitesse moyenne de dépolymérisation.

E.3.4 Long filament stationnaire en présence de réattachement

Lorsque l'espine se réattache au filament avec un taux élevé, la dépolymérisation du filament est considérablement ralentie et son extrémité dépolymérisante ne rattrape jamais le front de polymérisation. Dans ce cas, le filament ne cesse de s'allonger, ou en d'autres termes a une longueur non-bornée. Lorsque l'espine se réattache au filament avec un taux faible, la concentration d'espine pour les filaments évoqués ci-dessus diminue et la

vitesse moyenne de dépolymérisation augmente. Si le filament dépolymérise plus vite qu'il ne polymérise, son extrémité dépolymérisante rattrape l'extrémité polymérisante. Lorsque le filament devient assez court, la concentration d'espine au niveau de l'extrémité dépolymérisante redevient élevée et la dépolymérisation ralentit. Le filament est donc stabilisé à une longueur finie. Nous appelons la transition d'un état de longueur non-bornée à un état de longueur finie la transition d'allongement.

Dans le reste de ce travail nous nous concentrons sur les filaments de longueur finie dont la longueur est grande devant l'espacement entre deux espines. Nous montrons que la vitesse de polymérisation doit être beaucoup plus grande que l'espacement entre deux espines fois la constante de détachement de l'espine pour obtenir de tels filaments. Dans ce cas, la valeur du taux de réattachement à la transition d'allongement est beaucoup plus faible que celle du taux de détachement.

Dans le cadre de longs filaments de ce type, nous pouvons utiliser une approximation continue soigneusement choisie pour représenter l'état stationnaire du processus de polymérisation-dépolymérisation. Nous appliquons cette approche à une forme généralisée de l'équation maîtresse dérivée plus haut permettant de décrire un filament lié à un nombre arbitraire de murs. La solution analytique de ce problème est présentée en Éq. (6.55).

E.3.5 Couplage entre filaments

Finalement, nous retournons au problème à plusieurs filaments, cette fois-ci en prenant en compte le réattachement des espines. L'abord de ce problème est difficile du point de vue analytique, et nous nous reposons donc sur des simulations numériques Monte-Carlo.

Notre premier résultat concerne l'existence d'une transition d'allongement dans le cas à plusieurs filaments. Le seuil de la transition correspond à celui attendu pour un filament unique lié à 2,5 murs. Ce nombre qui joue le rôle d'un nombre de voisins effectifs vu par chaque filament dans le cas à plusieurs filaments. Au-dessus de la transition, ce point de vue d'un nombre de voisins effectif rend très bien compte de la dépendance de la vitesse d'allongement du filament en fonction du taux de réattachement de l'espine [Fig. 6.8(b)]. En-dessous de la transition, l'accord est nettement moins bon [Fig. 6.8(a)]. En particulier, dans le cadre de la théorie à un seul filament la longueur stationnaire du filament diverge à la transition d'allongement comme l'inverse de la distance au seuil. Cette divergence existe également dans le cas de filaments couplés, mais une loi de puissance différente est observée [Éqs. (6.62) et (6.63)]. Il n'est pas évident à ce stade si cet exposant pourrait être décrit par une théorie de champ moyen plus raffinée que la description en termes de nombre de voisins effectifs ou si elle nécessite une approche plus élaborée.

Les résultats présentés ci-dessus suggèrent que les interactions entre filaments jouent un rôle important en-dessous de la transition d'allongement. Nous focalisons donc notre attention sur une description de ces interactions en termes des corrélations qu'elles induisent entre la longueur des filaments. Bien que la portée de ces corrélations augmente avec le taux de réattachement de l'espine, nous ne sommes pas encore en mesure d'affirmer qu'elle diverge à la transition d'allongement. Un argument d'échelle nous permet néanmoins d'écarter l'hypothèse selon laquelle l'interface aurait une géométrie auto-affine à la transition, ou encore une transition rugueuse.

Finalement, nous comparons les formes stationnaires de stéréocils obtenus grâce à

nos simulations numériques à celles déduites d'une théorie de filament unique. Les deux approches donnent des résultats identiques en l'absence de réattachement des espines et lorsque le nombre réel de voisins est utilisé, en accord avec notre solution exacte du problème sans réattachement. Lorsque le réattachement est introduit, cependant, la théorie de filament unique avec nombre de voisins réel subit rapidement une transition d'allongement, et une théorie de nombre de voisins effectifs semble plus appropriée. L'accord entre les formes numériques et celles tirées de la théorie de filament unique est cependant mauvais, ce à quoi notre étude précédente concernant la divergence de la longueur du stéréocil à la transition permettait de s'attendre. Nous confirmons donc par ce résultat que des efforts analytiques supplémentaires sont nécessaires pour mieux comprendre le problème multi-filament en présence de réattachement de l'espine.

References

[1] Joshua Zimmerberg and Michael M Kozlov. How proteins produce cellular membrane curvature. *Nat. Rev. Mol. Cell Biol.*, 7(1):9–19, 2006.

[2] Juan S Bonifacino and Benjamin S Glick. The mechanisms of vesicle budding and fusion. *Cell*, 116(2):153–66, January 2004.

[3] W Helfrich. Elastic properties of lipid bilayers: theory and possible experiments. *Z. Naturforsch. (C)*, 28(11):693–703, November-December 1973.

[4] J A Theriot. The polymerization motor. *Traffic (Oxford, U. K.)*, 1(1):19–28, January 2000.

[5] Wikipedia. Actin—Wikipedia, the free encyclopedia, 2009. Online; accessed 13-July-2009.

[6] Céline Revenu, Rafika Athman, Sylvie Robine, and Daniel Louvard. The co-workers of actin filaments: from cell structures to signals. *Nat. Rev. Mol. Cell Biol.*, 5(8):635–46, August 2004.

[7] Gerrit J K Praefcke and Harvey T McMahon. The dynamin superfamily: universal membrane tubulation and fission molecules? *Nat. Rev. Mol. Cell Biol.*, 5(2):133–147, February 2004.

[8] C Alexander, M Votruba, U E Pesch, D L Thiselton, S Mayer, A Moore, M Rodriguez, U Kellner, B Leo-Kottler, G Auburger, S S Bhattacharya, and B Wissinger. OPA1, encoding a dynamin-related GTPase, is mutated in autosomal dominant optic atrophy linked to chromosome 3q28. *Nat. Genet.*, 26(2):211–215, 2000.

[9] Stephan Zuchner, Maher Noureddine, Marina Kennerson, Kristien Verhoeven, Kristl Claeys, Peter De Jonghe, John Merory, Sofia A Oliveira, Marcy C Speer, Judith E Stenger, Gina Walizada, Danqing Zhu, Margaret A Pericak-Vance, Garth Nicholson, Vincent Timmerman, and Jeffery M Vance. Mutations in the pleckstrin homology domain of dynamin 2 cause dominant intermediate Charcot-Marie-Tooth disease. *Nat. Genet.*, 37(3):289–294, 2005.

[10] Marc Bitoun, Svetlana Maugenre, Pierre-Yves Jeannet, Emmanuelle Lacene, Xavier Ferrer, Pascal Laforet, Jean-Jacques Martin, Jocelyn Laporte, Hanns Lochmuller, Alan H Beggs, Michel Fardeau, Bruno Eymard, Norma B Romero, and Pascale

Guicheney. Mutations in dynamin 2 cause dominant centronuclear myopathy. *Nat. Genet.*, 37(11):1207–1209, 2005.

[11] Shawn M Ferguson, Gabor Brasnjo, Mitsuko Hayashi, Markus Wolfel, Chiara Collesi, Silvia Giovedi, Andrea Raimondi, Liang-Wei Gong, Pablo Ariel, Summer Paradise, Eileen O'toole, Richard Flavell, Ottavio Cremona, Gero Miesenbock, Timothy A Ryan, and Pietro De Camilli. A selective activity-dependent requirement for dynamin 1 in synaptic vesicle endocytosis. *Science*, 316(5824):570–574, April 2007.

[12] J H Koenig and K Ikeda. Disappearance and reformation of synaptic vesicle membrane upon transmitter release observed under reversible blockage of membrane retrieval. *J. Neurosci.*, 9:3844–3860, November 1989.

[13] Jean-Baptiste Fournier, Paul G Dommersnes, and Paola Galatola. Dynamin recruitment by clathrin coats: a physical step? *C. R. Biol.*, 326:467–476, January 2003.

[14] K Takei, P S McPherson, S L Schmid, and P De Camilli. Tubular membrane invaginations coated by dynamin rings are induced by GTP-γS in nerve terminals. *Nature (London)*, 374(6518):186–190, March 1995.

[15] Bruce Alberts, Dennis Bray, Alexander Johnson, Julian Lewis, Martin Raff, Keith Roberts, and Peter Walter. *Essential Cell Biology.* Garland, New-York, 1998.

[16] Sanja Sever, Hanna Damke, and Sandra L Schmid. Garrotes, springs, ratchets, and whips: Putting dynamin models to the test. *Traffic (Oxford, U. K.)*, 1(5):385–392, May 2000.

[17] Dganit Danino and Jenny E Hinshaw. Dynamin family of mechanoenzymes. *Curr. Opin. Cell Biol.*, 13(4):454–460, August 2001.

[18] L L Carter, T E Redelmeier, L A Woollenweber, and S L Schmid. Multiple GTP-binding proteins participate in clathrin-coated vesicle-mediated endocytosis. *J. Cell Biol.*, 120(1):37–45, 1993.

[19] A M van der Bliek, T E Redelmeier, H Damke, E J Tisdale, E M Meyerowitz, and S L Schmid. Mutations in human dynamin block an intermediate stage in coated vesicle formation. *J. Cell Biol.*, 122(3):553–563, August 1993.

[20] V I Slepnev and P De Camilli. Accessory factors in clathrin-dependent synaptic vesicle endocytosis. *Nat. Rev. Neurosci.*, 1(3):161–172, December 2000.

[21] J E Hinshaw and S L Schmid. Dynamin self-assembles into rings suggesting a mechanism for coated vesicle budding. *Nature (London)*, 374(6518):190–192, 1995.

[22] J F Carr and J E Hinshaw. Dynamin assembles into spirals under physiological salt conditions upon the addition of GDP and gamma-phosphate analogues. *J. Biol. Chem.*, 272(44):28030–28035, 1997.

[23] Koert N J Burger, Rudy A Demel, Sandra L Schmid, and Ben de Kruijff. Dynamin is membrane-active: Lipid insertion is induced by phosphoinositides and phosphatidic acid. *Biochemistry*, 39(40):12485 –12493, October 2000.

[24] Sharon M Sweitzer and Jenny E Hinshaw. Dynamin undergoes a GTP-dependent conformational change causing vesiculation. *Cell*, 93(6):1021–1029, June 1998.

[25] K Takei, V Haucke, V Slepnev, K Farsad, M Salazar, H Chen, and P De Camilli. Generation of coated intermediates of clathrin-mediated endocytosis on protein-free liposomes. *Cell*, 94(1):131–141, 1998.

[26] K Salim, M J Bottomley, E Querfurth, M J Zvelebil, I Gout, R Scaife, R L Margolis, R Gigg, C I Smith, P C Driscoll, M D Waterfield, and G Panayotou. Distinct specificity in the recognition of phosphoinositides by the pleckstrin homology domains of dynamin and Bruton's tyrosine kinase. *EMBO J.*, 15(22):6241–6250, November 1996.

[27] Peijun Zhang and Jenny E Hinshaw. Three-dimensional reconstruction of dynamin in the constricted state. *Nat. Cell Biol.*, 3(10):922–927, October 2001.

[28] Yen-Ju Chen, Peijun Zhang, Edward H Egelman, and Jenny E Hinshaw. The stalk region of dynamin drives the constriction of dynamin tubes. *Nat. Struct. Mol. Biol.*, 11(6):574–575, June 2004.

[29] Jason A Mears, Pampa Ray, and Jenny E Hinshaw. A corkscrew model for dynamin constriction. *Structure*, 15(10):1190–1202, October 2007.

[30] H S Shpetner and R B Vallee. Dynamin is a GTPase stimulated to high levels of activity by microtubules. *Nature (London)*, 355(6362):733–735, 1992.

[31] K Maeda, T Nakata, Y Noda, R Sato-Yoshitake, and N Hirokawa. Interaction of dynamin with microtubules: its structure and GTPase activity investigated by using highly purified dynamin. *Mol. Biol. Cell*, 3(10):1181–1194, 1992.

[32] P L Tuma, M C Stachniak, and C A Collins. Activation of dynamin GTPase by acidic phospholipids and endogenous rat brain vesicles. *J. Biol. Chem.*, 268(23):17240–17246, 1993.

[33] Dganit Danino, Kwan-Hoon Moon, and Jenny E Hinshaw. Rapid constriction of lipid bilayers by the mechanochemical enzyme dynamin. *J. Struct. Biol.*, 147(3):259–267, May 2004.

[34] Michael H B Stowell, Bruno Marks, Patrick Wigge, and Harvey T McMahon. Nucleotide-dependent conformational changes in dynamin: evidence for a mechanochemical molecular spring. *Nat. Cell Biol.*, 1(1):27–32, May 1999.

[35] Bruno Marks, Michael H B Stowell, Yvonne Vailis, Ian G Mills, Adele Gibson, Colin R Hopkins, and Harvey T McMahon. GTPase activity of dynamin and resulting conformational change are essential for endocytosis. *Nature (London)*, 410(6825):231–235, March 2001.

[36] Aurélien Roux, Katherine Uyhazi, Adam Frost, and Pietro De Camilli. GTP-dependent twisting of dynamin implicates constriction and tension in membrane fission. *Nature (London)*, 441:528–531, May 2006.

[37] T J Pucadyil and S L Schmid. Real-time visualization of dynamin-catalyzed membrane fission and vesicle release. *Cell*, December 2008.

[38] P V Bashkirov, S A Akimov, A I Evseev, S L Schmid, J Zimmerberg, and V A Frolov. GTPase cycle of dynamin is coupled to membrane squeeze and release, leading to spontaneous fission. *Cell*, December 2008.

[39] Aurelien Roux and Bruno Antonny. The long and short of membrane fission. *Cell*, 135(7):1163–1165, December 2008.

[40] Benoit Sorre, Andrew Callan-Jones, Jean-Baptiste Manneville, Pierre Nassoy, Jean-Francois Joanny, Jacques Prost, Bruno Goud, and Patricia Bassereau. Curvature-driven lipid sorting needs proximity to a demixing point and is aided by proteins. *Proc. Natl. Acad. Sci. U.S.A.*, 106(14):5622–5626, April 2009.

[41] Kohji Takei, Vladimir I Slepnev, Volker Haucke, and Pietro De Camilli. Functional partnership between amphiphysin and dynamin in clathrin-mediated endocytosis. *Nat. Cell Biol.*, 1(1):33–39, May 1999.

[42] Marileen Dogterom, Jacob W J Kerssemakers, Guillaume Romet-Lemonne, and Marcel E Janson. Force generation by dynamic microtubules. *Curr. Opin. Cell Biol.*, 17(1):67–74, February 2005.

[43] Aurelien Roux, Damien Cuvelier, Pierre Nassoy, Jacques Prost, Patricia Bassereau, and Bruno Goud. Role of curvature and phase transition in lipid sorting and fission of membrane tubules. *EMBO J.*, 24(8):1537–1545, April 2005.

[44] Matthew J Footer, Jacob W J Kerssemakers, Julie A Theriot, and Marileen Dogterom. Direct measurement of force generation by actin filament polymerization using an optical trap. *Proc. Natl. Acad. Sci. U.S.A.*, 104(7):2181–2186, 2007.

[45] Jean-Marc Allain, Cornelis Storm, Aurélien Roux, Martine Ben Amar, and Jean-François Joanny. Fission of a multiphase membrane tube. *Phys. Rev. Lett.*, 93:158104, October 2004.

[46] P G J van Dongen and M H Ernst. Kinetics of reversible polymerization. *J. Stat. Phys.*, 37(3–4):301–324, 1984.

[47] N G Van Kampen. *Stochastic Processes in Physics and Chemistry*. North-Holland, Amsterdam, 1992.

[48] Raymond Goldstein, Philip Nelson, Thomas Powers, and Udo Seifert. Front progagation in the pearling instability of tubular vesicles. *J. Phys. II France*, 6(5):767–796, 1996.

[49] D R Daniels and M S Turner. Diffusion on membrane tubes: a highly discriminatory test of the saffman-delbruck theory. *Langmuir*, 23(12):6667–6670, 2007.

[50] E Evans and A Yeung. Hidden dynamics in rapid changes of bilayer shape. *Chem. Phys. Lipids*, 73(1-2):39–56, September 1994.

[51] C S Peskin, G M Odell, and G F Oster. Cellular motions and thermal fluctuations: the brownian ratchet. *Biophys. J.*, 65(1):316–324, July 1993.

[52] Marileen Dogterom and Bernard Yurke. Measurement of the force-velocity relation for growing microtubules. *Science*, 278:856–860, October 1997.

[53] A Mogilner and George Oster. The polymerization ratchet model explains the force-velocity relation for growing microtubules. *Eur. Biophys. J. Biophys. Lett.*, 28(3):235–242, March 1999.

[54] G S van Doorn, C Tanase, B M Mulder, and M Dogterom. On the stall force for growing microtubules. *Eur. Biophys. J. Biophys. Lett.*, 29(1):2–6, 2000.

[55] Evgeny B Stukalin and Anatoly B Kolomeisky. Polymerization dynamics of double-stranded biopolymers: chemical kinetic approach. *J. Chem. Phys.*, 122(10):104903, 2005.

[56] Erdinc Atilgan, Denis Wirtz, and Sean X Sun. Mechanics and dynamics of actin-driven thin membrane protrusions. *Biophys. J.*, 90(1):65–76, 2006.

[57] Edward W Washburn. The dynamics of capillary flow. *Phys. Rev.*, 17(3):273–283, March 1921.

[58] A Jamila Newton, Tom Kirchhausen, and Venkatesh N Murthy. Inhibition of dynamin completely blocks compensatory synaptic vesicle endocytosis. *Proc. Natl. Acad. Sci. U.S.A.*, 103(47):17955–17960, November 2006.

[59] Eric Macia, Marcelo Ehrlich, Ramiro Massol, Emmanuel Boucrot, Christian Brunner, and Tomas Kirchhausen. Dynasore, a cell-permeable inhibitor of dynamin. *Dev. Cell.*, 10(6):839–850, June 2006.

[60] Adam Frost, Rushika Perera, Aurélien Roux, Kasimir Spasov, Olivier Destaing, Edward H Egelman, Pietro De Camilli, and Vinzenz Unger. Structural basis of membrane invagination by F-BAR domains. *Cell*, 132(5):807–817, March 2008.

[61] J Dai, H P Ting-Beall, and M P Sheetz. The secretion-coupled endocytosis correlates with membrane tension changes in rbl 2h3 cells. *J. Gen. Physiol.*, 110(1):1–10, July 1997.

[62] D Raucher and M P Sheetz. Membrane expansion increases endocytosis rate during mitosis. *J. Cell Biol.*, 144(3):497–506, February 1999.

[63] Sybren R De Groot and Peter Mazur. *Non-Equilibrium Thermodynamics*. Dover, New York, 1984.

[64] Pierre-Gilles de Gennes and Jacques Prost. *The Physics of Liquid Crystals*. Number 83 in International Series of Monographs on Physics. Oxford University Press, second edition, 1993.

[65] P C Martin, O Parodi, and P S Pershan. Unified hydrodynamic theory for crystals, liquid crystals, and normal fluids. *Phys. Rev. A*, 6:2401–2420, December 1972.

[66] L. D. Landau and E M Lifshitz. *Fluid Mechanics*, volume 6 of *Course of Theoretical Physics*. Pergamon Press, Oxford, second edition, 1987.

[67] Tom C Lubensky. Phenomenological dynamics: From Navier-Stokes to chiral granular gases. *Pramana-J. Phys.*, 64(5):727–742, May 2005.

[68] E Ben-Jacob, O Schochet, A Tenenbaum, I Cohen, A Czirok, and T Vicsek. Generic modelling of cooperative growth patterns in bacterial colonies. *Nature (London)*, 368(6466):46–49, March 1994.

[69] John Toner, Yuhai Tu, and Sriram Ramaswamy. Hydrodynamics and phases of flocks. *Ann. Phys.*, 318(1):170–244, July 2005.

[70] K Kruse, J F Joanny, F Jülicher, J Prost, and K Sekimoto. Generic theory of active polar gels: a paradigm for cytoskeletal dynamics. *Eur. Phys. J. E*, 16(1):5–16, January 2005.

[71] P M Chaikin and T C Lubensky. *Principles of Condensed Matter Physics*. Cambridge University Press, Cambridge, 1995.

[72] R Dimova, B Pouligny, and C Dietrich. Pretransitional effects in dimyristoylphosphatidylcholine vesicle membranes: optical dynamometry study. *Biophys. J.*, 79(1):340–356, 2000.

[73] L D Landau and E M Lifshitz. *Statistical Physics Part 1*, volume 5 of *Course of Theoretical Physics*. Pergamon Press, Oxford, third edition, 1980.

[74] R E Waugh. Surface viscosity measurements from large bilayer vesicle tether formation. II. experiments. *Biophys. J.*, 38(1):29–37, April 1982.

[75] W Rawicz, K C Olbrich, T McIntosh, D Needham, and E Evans. Effect of chain length and unsaturation on elasticity of lipid bilayers. *Biophys. J.*, 79(1):328–339, 2000.

[76] Étienne Guyon, Jean-Pierre Hulin, and Luc Petit. *Hydrodynamique Physique*. EDP Sciences & CNRS Éditions, Les Ulis & Paris, second edition, 2001.

[77] Claude Cohen-Tannoudji. *Mécanique Quantique*. Hermann, Paris, 1973.

[78] A E H Love. *A Treatise On The Mathematical Theory Of Elasticity*. Dover, New York, 1927.

[79] Michael M Kozlov. Dynamin: Possible mechanism of "pinchase" action. *Biophys. J.*, 77:604–616, July 1999.

[80] Derek Marsh. Elastic curvature constants of lipid monolayers and bilayers. *Chem. Phys. Lipids*, 114(2):146–159, November-December 2006.

[81] Aurélien Roux. (private communication).

[82] Zev Bryant, Michael D Stone, Jeff Gore, Steven B Smith, Nicholas R Cozzarelli, and Carlos Bustamante. Structural transitions and elasticity from torque measurements on DNA. *Nature (London)*, 424:338–341, May 2003.

[83] Frank Jülicher, Armand Ajdari, and Jacques Prost. Modeling molecular motors. *Rev. Mod. Phys.*, 69(4):1269–1281, October 1997.

[84] Christien J Merrifield, Morris E Feldman, Lei Wan, and Wolfhard Almers. Imaging actin and dynamin recruitment during invagination of single clathrin-coated pits. *Nat. Cell Biol.*, 4(9):691–698, 2002.

[85] M A McNiven, L Kim, E W Krueger, J D Orth, H Cao, and T W Wong. Regulated interactions between dynamin and the actin-binding protein cortactin modulate cell shape. *J. Cell Biol.*, 151(1):187–198, October 2000.

[86] Jian Liu, Marko Kaksonen, David Drubin, and George Oster. Endocytic vesicle scission by lipid phase boundary forces. *Proc. Natl. Acad. Sci. U.S.A.*, 103(27):10277–10282, July 2006.

[87] Sanja Sever, Amy B Muhlberg, and Sandra L Schmid. Impairment of dynamin's gap domain stimulates receptor-mediated endocytosis. *Nature (London)*, 398(6727):481–486, April 1999.

[88] Elena Smirnova, Dixie-Lee Shurland, Erin D Newman-Smith, Babak Pishvaee, and Alexander M van der Bliek. A model for dynamin self-assembly based on binding between three different protein domains. *J. Biol. Chem.*, 274(21):14942–14947, May 1999.

[89] Michael M Kozlov. Fission of biological membranes: Interplay between dynamin and lipids. *Traffic (Oxford, U. K.)*, 2:51–65, 2001.

[90] J Zheng, S M Cahill, M A Lemmon, D Fushman, J Schlessinger, and D Cowburn. Identification of the binding site for acidic phospholipids on the PH domain of dynamin: implications for stimulation of GTPase activity. *J. Mol. Biol.*, 255(1):14–21, 1996.

[91] Thomas Slagsvold, Krupa Pattni, Lene Malerod, and Harald Stenmark. Endosomal and non-endosomal functions of ESCRT proteins. *Trends Cell Biol.*, 16(6):317–326, June 2006.

[92] Roger L Williams and Sylvie Urbe. The emerging shape of the ESCRT machinery. *Nat. Rev. Mol. Cell Biol.*, 8(5):355–368, May 2007.

[93] Suraj Saksena, Ji Sun, Tony Chu, and Scott D Emr. ESCRTing proteins in the endocytic pathway. *Trends Biochem. Sci.*, 32(12):561–573, December 2007.

[94] James H Hurley. ESCRT complexes and the biogenesis of multivesicular bodies. *Curr. Opin. Cell Biol.*, 20(1):4–11, February 2008.

[95] Paul D Bieniasz. Late budding domains and host proteins in enveloped virus release. *Virology*, 344(1):55–63, January 2006.

[96] Jez G Carlton and Juan Martin-Serrano. Parallels between cytokinesis and retroviral budding: a role for the ESCRT machinery. *Science*, 316(5833):1908–1912, June 2007.

[97] Eiji Morita, Virginie Sandrin, Hyo-Young Chung, Scott G Morham, Steven P Gygi, Christopher K Rodesch, and Wesley I Sundquist. Human ESCRT and ALIX proteins interact with proteins of the midbody and function in cytokinesis. *EMBO J.*, 26(19):4215–4227, October 2007.

[98] Phyllis I Hanson, Robyn Roth, Yuan Lin, and John E Heuser. Plasma membrane deformation by circular arrays of ESCRT-III protein filaments. *J. Cell Biol.*, 180(2):389–402, 2008.

[99] Yuan Lin, Lisa A Kimpler, Teresa V Naismith, Joshua M Lauer, and Phyllis I Hanson. Interaction of the mammalian endosomal sorting complex required for transport (ESCRT) III protein hSnf7-1 with itself, membranes, and the AAA+ ATPase SKD1. *J. Biol. Chem.*, 280(13):12799–12809, April 2005.

[100] Sara Ghazi-Tabatabai, Suraj Saksena, Judith M Short, Ajaybabu V Pobbati, Dmitry B Veprintsev, R Anthony Crowther, Scott D Emr, Edward H Egelman, and Roger L Williams. Structure and disassembly of filaments formed by the ESCRT-III subunit Vps24. *Structure*, 16(9):1345–1356, 2008.

[101] Suman Lata, Guy Schoehn, Ankur Jain, Ricardo Pires, Jacob Piehler, Heinrich G Gottlinger, and Winfried Weissenhorn. Helical structures of ESCRT-III are disassembled by VPS4. *Science*, 321(5894):1354–1357, September 2008.

[102] Thomas Wollert, Christian Wunder, Jennifer Lippincott-Schwartz, and James H Hurley. Membrane scission by the ESCRT-III complex. *Nature (London)*, 458(7235):172–177, March 2009.

[103] Nir S Gov and Ajay Gopinathan. Dynamics of membranes driven by actin polymerization. *Biophys. J.*, 90(2):454–469, 2006.

[104] R Shlomovitz and N S Gov. Membrane waves driven by actin and myosin. *Phys. Rev. Lett.*, 98:168103, April 2007.

[105] L D Landau and E M Lifshitz. *Theory of Elasticity*, volume 7 of *Course of Theoretical Physics*. Butterworth Heinemann, Oxford, third edition, 1986.

[106] Milton Abramowitz and Irene A Stegun. *Handbook of Mathematical Functions*. Number 55 in Applied Mathematics Series. National Bureau of Standards, Washington D. C., 1972.

[107] Arpita Upadhyaya and Michael P Sheetz. Tension in tubulovesicular networks of golgi and endoplasmic reticulum membranes. *Biophys. J.*, 86(5):2923–2928, May 2004.

[108] F Julicher and U Seifert. Shape equations for axisymmetric vesicles: A clarification. *Phys. Rev. E*, 49(5):4728–4731, May 1994.

[109] Imre Derényi, Frank Jülicher, and Jacques Prost. Formation and interaction of membrane tubes. *Phys. Rev. Lett.*, 88(23):238101, May 2002.

[110] William H Press, Saul A Teukolsky, William T Vetterling, and Brian P Flannery. *Numerical recipes in C*. Cambridge University Press, New York, second edition, 1992.

[111] Shujuan Pan, Ruoning Wang, Xi Zhou, Guangan He, John Koomen, Ryuji Kobayashi, Le Sun, Joe Corvera, Gary E Gallick, and Jian Kuang. Involvement of the conserved adaptor protein alix in actin cytoskeleton assembly. *J. Biol. Chem.*, 281(45):34640–34650, November 2006.

[112] R Kwok and E Evans. Thermoelasticity of large lecithin bilayer vesicles. *Biophys. J.*, 35(3):637–652, September 1981.

[113] Brian C J Moore. *An Introduction to the Psychology of Hearing*. Elsevier Academic Press, Amsterdam, fifth edition, 2004.

[114] Robert Fettiplace and Carole M Hackney. The sensory and motor roles of auditory hair cells. *Nature Rev. Neurosci.*, 7(1):19–29, January 2006.

[115] Lars Chittka and Axel Brockmann. Perception space–the final frontier. *PLoS Biol.*, 3(4):e137, April 2005.

[116] A J Hudspeth. Making an effort to listen: mechanical amplification in the ear. *Neuron*, 59(4):530–545, August 2008.

[117] A C Crawford and R Fettiplace. The mechanical properties of ciliary bundles of turtle cochlear hair cells. *J. Physiol.-London*, 364:359–379, July 1985.

[118] Mette M Mogensen, Agnieszka Rzadzinska, and Karen P Steel. The deaf mouse mutant whirler suggests a role for whirlin in actin filament dynamics and stereocilia development. *Cell Motil. Cytoskeleton*, 64(7):496–508, 2007.

[119] Agnieszka K Rzadzinska, Mark E Schneider, Caroline Davies, Gavin P Riordan, and Bechara Kachar. An actin molecular treadmill and myosins maintain stereocilia functional architecture and self-renewal. *J. Cell Biol.*, 164(6):887–897, March 2004.

[120] K C Holmes, D Popp, W Gebhard, and W Kabsch. Atomic model of the actin filament. *Nature (London)*, 347(6288):44–49, September 1990.

[121] M Itoh. Preservation and visualization of actin-containing filaments in the apical zone of cochlear sensory cells. *Hear. Res.*, 6(3):277–289, April 1982.

[122] Uri Manor and Bechara Kachar. Dynamic length regulation of sensory stereocilia. *Semin. Cell Dev. Biol.*, 19(6):502–510, December 2008.

[123] Harrison W Lin, Mark E Schneider, and Bechara Kachar. When size matters: the dynamic regulation of stereocilia lengths. *Curr. Opin. Cell Biol.*, 17(1):55–61, 2005.

[124] Mark E Schneider, Inna A Belyantseva, Ricardo B Azevedo, and Bechara Kachar. Rapid renewal of auditory hair bundles. *Nature (London)*, 418(6900):837–838, 2002.

[125] Jacques Prost, Camilla Barbetta, and Jean-François Joanny. Dynamical control of the shape and size of stereocilia and microvilli. *Biophys. J.*, 93(4):1124–1133, August 2007.

[126] Agnieszka Rzadzinska, Mark Schneider, Konrad Noben-Trauth, James R Bartles, and Bechara Kachar. Balanced levels of espin are critical for stereociliary growth and length maintenance. *Cell Motil. Cytoskeleton*, 62(3):157–165, 2005.

[127] Inna A Belyantseva, Erich T Boger, Sadaf Naz, Gregory I Frolenkov, James R Sellers, Zubair M Ahmed, Andrew J Griffith, and Thomas B Friedman. Myosin-XVa is required for tip localization of whirlin and differential elongation of hair-cell stereocilia. *Nat. Cell Biol.*, 7:148–156, February 2005.

[128] Felipe T Salles, Raymond C Jr Merritt, Uri Manor, Gerard W Dougherty, Aurea D Sousa, Judy E Moore, Christopher M Yengo, Andrea C Dose, and Bechara Kachar. Myosin IIIa boosts elongation of stereocilia by transporting espin 1 to the plus ends of actin filaments. *Nat. Cell Biol.*, 11(4):443–450, April 2009.

[129] M S Tilney, L G Tilney, R E Stephens, C Merte, D Drenckhahn, D A Cotanche, and A Bretscher. Preliminary biochemical characterization of the stereocilia and cuticular plate of hair cells of the chick cochlea. *J. Cell Biol.*, 109(4):1711–1723, October 1989.

[130] L Zheng, G Sekerkova, K Vranich, L G Tilney, E Mugnaini, and J R Bartles. The deaf jerker mouse has a mutation in the gene encoding the espin actin-bundling proteins of hair cell stereocilia and lacks espins. *Cell*, 102(3):377–385, August 2000.

[131] L G Tilney, E H Egelman, D J DeRosier, and J C Saunder. Actin filaments, stereocilia, and hair cells of the bird cochlea. II. packing of actin filaments in the stereocilia and in the cuticular plate and what happens to the organization when the stereocilia are bent. *J. Cell Biol.*, 96(3):822–834, March 1983.

[132] G Sekerkova, L Zheng, P A Loomis, E Mugnaini, and J R Bartles. Espins and the actin cytoskeleton of hair cell stereocilia and sensory cell microvilli. *Cell. Mol. Life Sci.*, 63(19-20):2329–2341, October 2006.

[133] B Chen, A Li, D Wang, M Wang, L Zheng, and J R Bartles. Espin contains an additional actin-binding site in its N terminus and is a major actin-bundling protein of the sertoli cell-spermatid ectoplasmic specialization junctional plaque. *Mol. Biol. Cell*, 10(12):4327–4339, December 1999.

[134] J R Bartles, L Zheng, A Li, A Wierda, and B Chen. Small espin: a third actin-bundling protein and potential forked protein ortholog in brush border microvilli. *J. Cell Biol.*, 143(1):107–119, October 1998.

[135] Kirstin R Purdy, James R Bartles, and Gerard C L Wong. Structural polymorphism of the actin-espin system: a prototypical system of filaments and linkers in stereocilia. *Phys. Rev. Lett.*, 98(5):058105, February 2007.

[136] Patricia A Loomis, Alexander E Kelly, Lili Zheng, Benjarat Changyaleket, Gabriella Sekerkova, Enrico Mugnaini, Adriana Ferreira, R Dyche Mullins, and James R Bartles. Targeted wild-type and jerker espins reveal a novel, WH2-domain-dependent way to make actin bundles in cells. *J. Cell Sci.*, 119(Pt 8):1655–1665, April 2006.

[137] F Donaudy, L Zheng, R Ficarella, E Ballana, M Carella, S Melchionda, X Estivill, J R Bartles, and P Gasparini. Espin gene (ESPN) mutations associated with autosomal dominant hearing loss cause defects in microvillar elongation or organisation. *J. Med. Genet.*, 43(2):157–161, February 2006.

[138] Patricia A Loomis, Lili Zheng, Gabriella Sekerkova, Benjarat Changyaleket, Enrico Mugnaini, and James R Bartles. Espin cross-links cause the elongation of microvillus-type parallel actin bundles in vivo. *J. Cell Biol.*, 163(5):1045–1055, December 2003.

[139] Lewis G Tilney, Patricia S Connelly, Linda Ruggiero, Kelly A Vranich, and Gregory M Guild. Actin filament turnover regulated by cross-linking accounts for the size, shape, location, and number of actin bundles in drosophila bristles. *Mol. Biol. Cell*, 14(10):3953–3966, October 2003.

[140] Ikuko Fujiwara, Shin Takahashi, Hisashi Tadakuma, Takashi Funatsu, and Shin'ichi Ishiwata. Microscopic analysis of polymerization dynamics with individual actin filaments. *Nat. Cell Biol.*, 4(9):666–673, September 2002.

[141] Huawei Li, Hong Liu, Steve Balt, Sabine Mann, C Eduardo Corrales, and Stefan Heller. Correlation of expression of the actin filament-bundling protein espin with stereociliary bundle formation in the developing inner ear. *J. Comp. Neurol.*, 468(1):125–134, January 2004.

[142] Gabriella Sekerkova, Lili Zheng, Enrico Mugnaini, and James R Bartles. Differential expression of espin isoforms during epithelial morphogenesis, stereociliogenesis and postnatal maturation in the developing inner ear. *Dev. Biol.*, 291(1):83–95, March 2006.

[143] Gabriella Sekerkova, Lili Zheng, Patricia A Loomis, Benjarat Changyaleket, Donna S Whitlon, Enrico Mugnaini, and James R Bartles. Espins are multifunctional actin cytoskeletal regulatory proteins in the microvilli of chemosensory and mechanosensory cells. *J. Neurosci.*, 24(23):5445–5456, June 2004.

[144] Moshe Naoz, Uri Manor, Hirofumi Sakaguchi, Bechara Kachar, and Nir S Gov. Protein localization by actin treadmilling and molecular motors regulates stereocilia shape and treadmilling rate. *Biophys. J.*, 95(12):5706–5718, December 2008.

[145] Lior Haviv, Nir Gov, Yaron Ideses, and Anne Bernheim-Groswasser. Thickness distribution of actin bundles in vitro. *Eur. Biophys. J. Biophys. Lett.*, 37(4):447–54, April 2008.

[146] Bechara Kachar. (private communication).

[147] Christoph Erlenkämper. Stochastische Beschreibungen dynamischer Biopolymere. Master's thesis, Universität des Saarlandes, 2008.

[148] D. T. Gillespie. A general method for numerically simulating the stochastic time evolution of coupled chemical reactions. *J. Comput. Phys.*, 22:403, 1976.

[149] Timothy Halpin-Healy and Yi-Cheng Zhang. Kinetic roughening phenomena, stochastic growth, directed polymers and all that. Aspects of multidisciplinary statistical mechanics. *Phys. Rep.-Rev. Sec. Phys. Lett.*, 254(4-6):215–414, March 1995.

[150] Albert-László Barabási and H Eugene Stanley. *Fractal Concepts in Surface Growth*. Cambridge University Press, Cambridge, 1995.

[151] Phillipe Nozières. *Solids Far from Equilibrium*. Cambridge University Press, Cambridge, 1992.

[152] Ariane Dimitrov, Mélanie Quesnoit, Sandrine Moutel, Isabelle Cantaloube, Christian Poüs, and Franck Perez. Detection of GTP-tubulin conformation in vivo reveals a role for GTP remnants in microtubule rescues. *Science*, 322(5906):1353–6, November 2008.

[153] Vladimir Varga, Jonne Helenius, Kozo Tanaka, Anthony A Hyman, Tomoyuki U Tanaka, and Jonathon Howard. Yeast kinesin-8 depolymerizes microtubules in a length-dependent manner. *Nat. Cell Biol.*, 8(9):957–62, September 2006.

[154] K Farsad, N Ringstad, K Takei, S R Floyd, K Rose, and P De Camilli. Generation of high curvature membranes mediated by direct endophilin bilayer interactions. *J. Cell Biol.*, 155(2):193–200, October 2001.

[155] François David. *Statistical Mechanics of Membranes and Surfaces*, volume 5 of *Jerusalem Winter School for Theoretical Physics*, chapter Geometry and Field Theory of Random Surfaces and Membranes, pages 157–223. World Scientific, Singapore, first edition, 1989.

[156] Jean-Baptiste Fournier and Paolo Galatola. Critical fluctuations of tense fluid membrane tubules. *Phys. Rev. Lett.*, 98(1):018103, January 2007.

[157] Igal Szleifer, Diego Kramer, Avinoam Ben-Shaul, William M Gelbart, and S A Safran. Molecular theory of curvature elasticity in surfactant films. *J. Chem. Phys.*, 92(11):6800–6817, June 1990.

[158] R D Kamien. The geometry of soft materials: a primer. *Rev. Mod. Phys.*, 74(4):953–971, October 2002.

[159] Jonathan Howard. *Mechanics of Motor Proteins and the Cytoskeleton*. Sinauer Associates, Sunderland, MA, 2001.

[160] Scott T Milner and S A Safran. Dynamical fluctuations of droplet microemulsions and vesicles. *Phys. Rev. A*, 36(9):4371–4379, November 1987.

Abstract

Membrane remodeling events are essential for the life of the cell, and involve membrane tubes shaped by proteins. We study three different configurations where such tubes appear. We first focus on the helical dynamin polymer, which encircles membrane tubes and severs them upon GTP hydrolysis. Dynamin recruitment is shown to depend on the membrane's curvature. We formulate hypotheses and propose experiments to understand the nucleation of the dynamin polymer and its interactions with the membrane. Dynamin's GTP-induced concerted conformational change is described using generalized hydrodynamics and seemingly contradictory experimental results are reconciled through mechanical arguments. The long-time dynamics of the dynamin-membrane tube is diffusive and dominated by an effective dynamin/membrane friction, which experiments confirm. Our second topic is the ESCRT-III complex, which tubulates flat membranes and assembles inside of them. We account for this deformation with a novel buckling instability arising when sticky curved filaments bind to the membrane. This hypothesis could be verified experimentally. A metastable regime for the flat membrane is uncovered, which the cell could use to quickly generate tubes. Thirdly, we turn to stereocilia, which are actin-based cellular protrusions essential for hearing. We predict their shape from the detachment dynamics of actin cross-linkers, which accounts for experimental data. If the cross-linkers are allowed to reattach, our model yields a dynamical phase transition towards unbounded growth and numerical simulations suggest an anomalous power-law divergence of the protrusion length.

Résumé

La cellule remodèle sa membrane en permanence, ce qui entraîne la formation de tubes de membrane façonnés par des protéines. Nous étudions trois cas impliquant de tels tubes. Le premier est le polymère hélicoïdal de dynamine, qui enveloppe les tubes de membrane puis les coupe en hydrolysant le GTP. Nous montrons que le recrutement de la dynamine dépend de la courbure de la membrane. Nous formulons des hypothèses et proposons des expériences pour comprendre la nucléation du polymère de dynamine et ses interactions avec la membrane. Nous donnons une description hydrodynamique généralisée du changement de conformation coopératif de la dynamine induit par le GTP et réconcilions des résultats expérimentaux apparemment contradictoires par des arguments mécaniques. La dynamique aux temps longs de l'assemblage dynamine-membrane est diffusive et dominée par une friction effective entre dynamine et membrane, ce qui est confirmé expérimentalement. Notre second sujet est le complexe ESCRT-III, qui tubule les membranes planes de l'intérieur. Nous expliquons cette déformation par une instabilité de flambage inédite se produisant lorsque des filaments courbés qui s'attirent se lient à la membrane. Cette hypothèse peut être vérifiée expérimentalement. Un régime métastable pour la membrane plane est mis en évidence, et pourrait être utilisé par la cellule pour former des tubes rapidement. Troisièment, nous nous tournons vers les stéréocils, des protrusions cellulaires à base d'actine essentielles pour l'audition. Nous expliquons leur forme par la dynamique de détachement de protéines liant l'actine, et rendons compte de résultats expérimentaux. Si ces protéines sont autorisées à se réattacher, notre modèle prévoit une transition de phase dynamique vers un état de croissance non-bornée, et des simulations numériques suggèrent que la longueur des protrusions diverge en loi de puissance avec un exposant anormal.